



HAL
open science

Combined effects of radiation and temperature on silica-based optical fibers

Cosimo Campanella

► **To cite this version:**

Cosimo Campanella. Combined effects of radiation and temperature on silica-based optical fibers. Optics [physics.optics]. Université Jean Monnet - Saint-Etienne, 2022. English. NNT : 2022STET0031 . tel-04189802

HAL Id: tel-04189802

<https://theses.hal.science/tel-04189802>

Submitted on 29 Aug 2023

HAL is a multi-disciplinary open access archive for the deposit and dissemination of scientific research documents, whether they are published or not. The documents may come from teaching and research institutions in France or abroad, or from public or private research centers.

L'archive ouverte pluridisciplinaire **HAL**, est destinée au dépôt et à la diffusion de documents scientifiques de niveau recherche, publiés ou non, émanant des établissements d'enseignement et de recherche français ou étrangers, des laboratoires publics ou privés.



N°d'ordre NNT : 2022STET0031

**THÈSE de DOCTORAT
DE L'UNIVERSITÉ JEAN MONNET SAINT-ÉTIENNE**

Membre de l'Université de LYON

**Ecole Doctorale N° 488
(SCIENCES, INGÉNIERIE, SANTÉ)**

Spécialité / discipline de doctorat :
Optique, Photonique et Hyperfréquences

Soutenue publiquement le 27/10/2022, par :
Cosimo CAMPANELLA

**Combined effects of radiation and temperature on
silica-based optical fibers**

Devant le jury composé de :

Skuja, Linards	Prof.	University of Latvia	Rapporteur
Buscarino, Giampiero	Prof.	University of Palermo	Rapporteur
Girard, Sylvain	Prof.	Institution	Examineur
Morana, Adriana	MCF	Institution	Examinatrice
Boukenter, Aziz	Prof.	Institution	Directeur de thèse
Mady, Frank	Prof.	Institution	Co-directeur de thèse
Robin, Thierry	CTO	iXblue Photonics	Invité

Table of Contents

TABLE OF CONTENTS	1
LIST OF ACRONYMS	5
INTRODUCTION	7
1. CHAPTER 1	11
1.1. OPTICAL FIBERS: MAIN PARAMETERS AND GUIDED MODES MODELLING	11
1.1.1. GUIDED MODES INSIDE AN OPTICAL FIBER: GEOMETRIC APPROACH ACCORDING TO RAY OPTICS	12
1.1.2. GUIDED MODES INSIDE AN OPTICAL FIBER: MODAL APPROACH ACCORDING TO ELECTROMAGNETIC OPTICS	13
1.2. OF MANUFACTURING PROCESS	17
1.2.1. MODIFIED CHEMICAL VAPOR DEPOSITION (MCVD)	17
1.2.2. DRAWING OF THE PREFORM INTO AN OPTICAL FIBER	20
1.3. RADIATION EFFECTS ON OPTICAL FIBERS	23
1.3.1. MACROSCOPIC EFFECTS OF RADIATION ON SILICA-BASED OFs (RIA, RIRIC, RIL)	23
1.3.1.1. Radiation-induced Attenuation (RIA)	24
1.3.1.2. Radiation-Induced Emission (RIE)	24
1.3.1.3. Radiation-Induced Compaction (RIC)	25
1.3.1.4. Radiation-Induced Refractive Index Change (RIRIC)	25
1.3.2. PARAMETERS AFFECTING RIA LEVELS AND KINETICS	26
1.3.2.1. Signal wavelength (or energy range)	26
1.3.2.2. Irradiation conditions: nature of particles	26
1.3.2.3. Irradiation conditions: total ionizing dose (TID)	26
1.3.2.4. Irradiation conditions: dose-rate	27
1.3.2.5. Irradiation conditions: irradiation temperature	28
1.3.2.6. Injected light power	29
1.3.2.7. Manufacturing process: glass stoichiometry	29
1.3.2.8. Manufacturing process: impurities and fictive temperature	30
1.3.2.9. Pre-treatments: hydrogenation and pre-irradiation	31
1.3.2.10. Optical fiber composition	32

Table of Contents

1.3.3. RADIATION-INDUCED POINT DEFECTS: WHAT WE KNOW ABOUT THEIR NATURE AND PROPERTIES	33
1.3.3.1. Pure silica: intrinsic point defects	34
1.3.3.1.1. SiE' center ($\equiv \text{Si} \bullet$)	34
1.3.3.1.2. Oxygen deficient center type I (ODC(I), $\equiv \text{Si} - \text{Si} \equiv$)	35
1.3.3.1.3. Oxygen deficient center II (ODC(II), $> \text{Si}:$)	35
1.3.3.1.4. Peroxy Linkage (POL, $\equiv \text{Si} - \text{O} - \text{O} - \text{Si} \equiv$)	35
1.3.3.1.5. Peroxy Radical (POR, $\equiv \text{Si} - \text{O} - \text{O} \bullet$)	36
1.3.3.1.6. Non-Bridging Oxygen Hole Center (NBOHC, $\equiv \text{Si} - \text{O} \bullet$)	36
1.3.3.1.7. Self-Trapped Holes (STH)	37
1.3.3.2. Pure silica: extrinsic point defects	38
1.3.3.2.1. Hydroxyl (OH) groups	38
1.3.3.2.2. Cl-related defects	39
1.3.3.2.3. Doping-related point defects	39
Germanium	40
Phosphorus	41
Aluminium	43
1.4. THESIS OBJECTIVES	45
2. CHAPTER 2	47
2.1. THE CERTYF METHODOLOGY	47
2.2. OFS USED FOR THE INVESTIGATION	48
2.2.1. CERTYF SAMPLES	48
2.2.2. TESTED OFS FROM OTHER MANUFACTURERS	49
2.2.2.1. P-doped samples	49
2.2.2.2. Al-doped sample	50
2.2.2.3. Ge-doped sample	50
2.2.2.4. GeP-doped sample	51
2.2.2.5. Pure-silica core samples	51
2.3. IRRADIATION TOOLS	52
2.3.1. X-RAY IRRADIATORS: MOPERIX, LABHX	52
2.3.2. γ -RAY IRRADIATOR: IRMA	55
2.3.3. CONTROLLING THE IRRADIATION TEMPERATURE: THERMAL PLATES	56
2.3.4. OF HYDROGENATION	57
2.4. X-γ RESULTS COMPARISON	58

2.5. RIA CHARACTERIZATION METHODS	58
2.5.1. SPECTRAL/MONOCROMATIC TRANSMISSION MEASUREMENTS	58
2.5.2. PHOTBLEACHING MEASUREMENTS	60
2.5.3. OTDR MEASUREMENTS	61
2.5.4. CUT-BACK TECHNIQUE	63
2.5.5. TECHNICAL ANALYSIS: SPECTRAL DECOMPOSITION	64

3. CHAPTER 3 **67**

3.1. COMBINED TEMPERATURE AND RADIATION EFFECTS ON THE MONOCROMATIC RIA OF RADIATION-SENSITIVE OFs AT TELECOMMUNICATION WAVELENGTHS.	68
3.1.1. RIA TEMPERATURE SENSITIVITY	71
3.1.1.1. Al-doped samples	71
3.1.1.2. P-doped samples	72
3.1.1.3. GeP-codoped samples	73
3.1.1.4. Combined impact of temperature and irradiation time	75
3.2. AL-DOPED OFs RIA TEMPERATURE DEPENDENCE	77
3.2.1. EVOLUTION OF UV-VIS AND NIR-RIA AT RT	77
3.2.2. TEMPERATURE INFLUENCE ON VIS- AND NIR-RIA	78
3.3. P-DOPED OFs RIA TEMPERATURE DEPENDENCE	85
3.3.1. EVOLUTION OF UV-VIS AND NIR-RIA AT RT	85
3.3.2. TEMPERATURE INFLUENCE ON THE UV-VIS AND NIR RIA	88
3.4. OPERATING TEMPERATURE RANGE OF P-DOPED OF DOSIMETERS EXPLOITING NIR-RIA	93
3.4.1. TEMPERATURE EFFECTS ON THE RADIATION SENSITIVITY OF P-DOPED OFs	94
3.4.2. DOSE-RATE EFFECTS ON THE RADIATION SENSITIVITY OF P-DOPED OFs AT DIFFERENT TEMPERATURES	98
3.4.3. TEMPERATURE EFFECTS ON THE NIR RIA SPECTRUM	99
3.5. SUMMARY	102

4. CHAPTER 4 **103**

4.1. EFFECT OF THE PROBING LIGHT POWER LEVEL ON THE RIA OF Ge-DOPED OFs AT TELECOMMUNICATION WAVELENGTHS	103
4.1.1. IRRADIATIONS AT 0.4 Gy s^{-1}	104
4.1.2. IRRADIATIONS AT 6 Gy s^{-1} FOR TID AT MGY LEVELS	106
4.1.3. MODELLING OF THE EXPERIMENTAL RIA KINETICS	107

Table of Contents

4.1.4. SPECTRAL NIR RIA AT HIGH DOSES	109
4.2. TEMPERATURE EFFECT ON THE RIA OF THE CORNING SMF-28E⁺ OF AT TELECOMMUNICATION WAVELENGTHS	114
4.2.1. 1310 NM AND 1550 NM RIA KINETICS AT 0.6 GY S⁻¹	114
4.2.2. EFFECT OF THE DOSE-RATE ON THE RIA AT DIFFERENT IRRADIATION TEMPERATURES	116
4.2.3. RIA KINETICS MODELLING	117
4.3. COMBINED EFFECTS OF TEMPERATURE AND RADIATION ON THE VIS/NIR RIA OF A CANONICAL MM GE-DOPED OF	122
4.3.1. SPECTRAL RIA AT RT	122
4.3.2. TEMPERATURE EFFECT ON THE SPECTRAL RIA	123
4.4. SUMMARY	131
5. CHAPTER 5	133
5.1. RADIATION EFFECTS ON PSC MM OFs: INFLUENCE OF OH GROUPS	133
5.1.1. ONLINE SPECTRAL RIA DURING AND AFTER THE IRRADIATION	135
5.1.2. RIA SPECTRAL DECOMPOSITION	137
5.2. SUMMARY	145
CONCLUSIONS	147
LIST OF PUBLICATIONS	151
ARTICLES PUBLISHED ON PEER-REVIEWED JOURNALS AS PRIMARY AUTHOR:	151
ARTICLES PUBLISHED ON PEER-REVIEWED JOURNALS AS CO-AUTHOR:	151
CONFERENCES CONTRIBUTION	153
INTERNATIONAL CONFERENCES:	153
NATIONAL CONFERENCES:	153
REFERENCES	155

List of Acronyms

ANDRA	National Agency for Radioactive Waste Management
C. A.	Commercially available
CERTYF	Combined Effects of Radiation, Temperature and hYdrogen on optical Fibers
COTS	Commercial-Off-the-Shelf
CRN	Continuous Random Network
DID	Drawing-Induced Defects
EPR	Electron Paramagnetic Resonance
FWHM	Full-Width at Half Maximum
GLPC	Germanium Lone Pair Center
HACC	Hole-assisted carbon-coated
INPHYNI	Physics Institute of Nice
IRSN	Radioprotection and Nuclear Safety Institute
LD	Laser Diode
LNT	Liquid Nitrogen Temperature
MCVD	Modified Chemical Vapor Deposition
MM	Multi-Mode
NA	Numerical Aperture
NBOHC	Non-Bridging Oxygen Hole Center
NIR	Near-Infrared
ODC	Oxygen Deficient Center
OF	Optical Fiber
OTDR	Optical Time-Domain Reflectometer
PM	Power Meter
POHC	Phosphorous-Oxygen Hole Center
POL	Peroxy Linkage
POR	Peroxy Radical
PSC	Pure-Silica Core
RIA	Radiation-Induced Attenuation
RIC	Radiation-Induced Compaction
RID	Radiation-Induced Defects
RIE	Radiation-Induced Emission
RIL	Radiation-Induced Luminescence
RIRIC	Radiation-Induced Refractive Index Change
SM	Single-Mode

List of Acronyms

STH	Self-Trapped Hole
TD	Transient Defect
TID	Total Ionizing Dose
TIR	Total Internal Reflection
UV	Ultra-Violet
vis	Visible
WLS	White Light Source

Introduction

Nowadays, Optical Fibers (OFs) are used in a variety of fields such as the high-bandwidth data communication, medical surgery, diagnostic and point or distributed sensing. Most of these applications take advantage of their low attenuation in the telecommunication wavelength range, immunity to most electromagnetic perturbation, low intrusiveness and a radiation resistance that can be enhanced during the manufacturing process. For this reason, OF and their derived sensors are also more and more considered for the employment in environments involving ionizing and non-ionizing radiations, e.g. space, high-energy physic facilities, fusion- and fission-related facilities and nuclear waste dismantling.

It is well known that radiation affects the macroscopic properties of the OF in a very complex way. One of the most limiting changes is the Radiation-Induced Attenuation (RIA), a wavelength and time-dependent phenomenon corresponding to a decrease in the transmitted signal caused by the generation of radiation-induced point defects inside the OF silica-based matrix. Numerous studies have been devoted to the investigation and understanding of the phenomena at the origin of RIA, revealing that its levels and kinetics depend on the nature and concentration of these point defects that, in turn, are influenced by intrinsic (OF composition, OF manufacturing process, etc.) and extrinsic (operating wavelength, irradiation characteristics, etc.) parameters.

Harsh environments are usually characterized by the presence of several other constraints than radiations, such as the variation of temperature over a wide range and the presence of various gases. When these environmental constraints are combined, the understanding of the degradation mechanisms at the origin of the RIA becomes even more complex and cannot be predicted by using the empirical laws or kinetics models discussed in literature, appropriate to reproduce the impact of each unique parameter. This lack of understanding, together with the difficulty to access facilities able to reproduce simultaneously the desired constraints, clearly limit the integration of OF-based systems in severe mixed environments.

Up to date, the OF radiation vulnerability in a given application and in mixed environments was usually evaluated through a series of separated tests. For example, for application involving environments combining radiation and temperature, the OF was initially exposed to radiation and, subsequently, to a thermal treatment. Such method is clearly not adapted to reproduce the environment to investigate. Indeed, for an adequate study of the combined effects, a proper reproduction of the final environment would be necessary, where all the constraints are simultaneously applied to the system under test. For this reason, the CERTYF consortium was created. CERTYF, acronym for Combined Effects of Radiation,

Introduction

Temperature and hydrogen on optical Fibers, is a fundamental research project aiming at improving the current knowledge on basic mechanisms responsible for the OF degradation when exposed to harsh environment characterized by the presence of ionizing radiations up to $\text{MGy}(\text{SiO}_2)$ dose levels, temperatures ranging from room temperature to about 300°C and presence of hydrogen. Those constraints are those faced by ANDRA (Agence Nationale pour la gestion des Déchets Radioactifs – National Agency for Radioactive Waste Management), the founder of the project, in the framework of the CIGEO (Centre Industriel de stockage Géologique – Industrial geological storage center) project, shown in Figure I.1, a French underground repository for high- and intermediate-level long-lived radioactive wastes. Here, OF-based diagnostic networks will be deployed for the monitoring of environmental parameters, namely strain, temperature, radiation and hydrogen concentration.

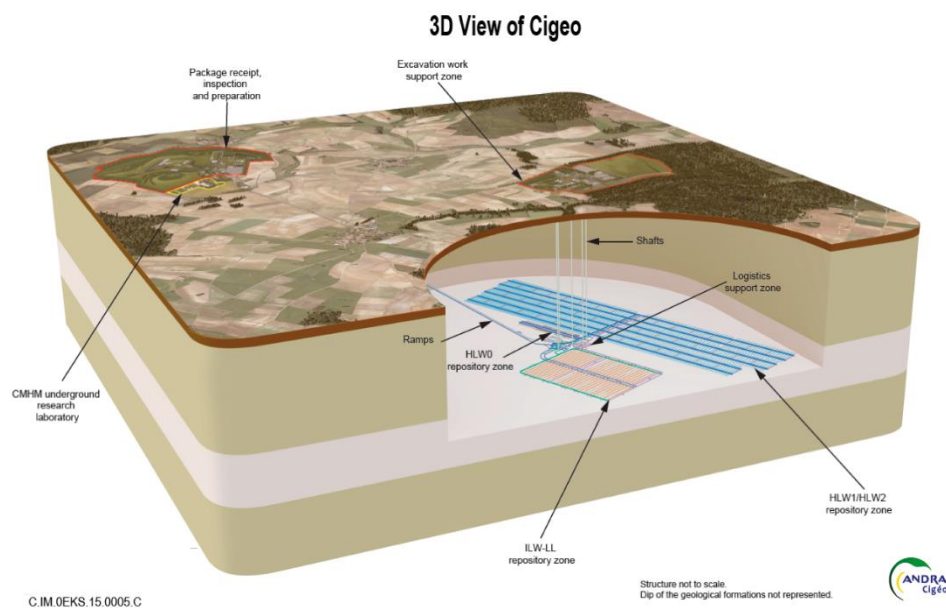


Figure I.1 Preliminary design of Cigéo, the underground repository for high level and intermediate level long-lived radioactive wastes. Taken from [1].

The partners involved in the project are:

- Inphyni Laboratory, Côte d’Azur University (Nice, France). With more than 30 years of experience in the manufacturing of the various OF classes, the Inphyni laboratory is in charge of the sample manufacturing (from the preform deposition to the final OF drawing) and the development of physical models permitting to reproduce and predict the OF behavior in mixed harsh environments.
- Hubert Curien Laboratory, Jean-Monnet University (Saint-Etienne, France). A recognized international leader in the subject of radiation effects in optical materials, is in charge for the characterization of the OF during and after the exposition to X-rays at various temperatures and with/without hydrogenation;

- IRSN (Institute for Radiological Protection and Nuclear Safety) (Gif-sur-Yvette, France). The French national public expert in nuclear and radiological risks, is providing tests with Gamma-ray irradiation at its IRMA facility.

The CERTYF project has been conceived in two phases. The first one dedicated to the fabrication of the different classes of OFs (radiation-hardened, radiation-tolerant and radiation-sensitive) and a systematic study on the parameters influencing their signal transmission in mixed environments. Subsequently, the second phase focuses on the consolidation of the physical models and on the exploitation of the acquired knowledge to the conception of optimized OFs for the employment in the mixed environments.

In line with the objectives established by the CERTYF project, this thesis focuses on the study of the role of radiation, temperature, OF composition and other parameters on the Radiation Induced Attenuation (RIA) of OFs. The first chapter of the thesis covers the theoretical background of the light propagation inside OFs, the OF manufacturing process, the effects of radiation on silica-based OFs and the main parameters affecting the RIA levels. The second chapter reports the materials and methods used for the characterization of the OFs under test. The third, fourth and fifth chapters are dedicated to the presentation and the discussion of the experimental results obtained on radiation-sensitive, radiation-tolerant and radiation-hardened OFs, respectively.

Chapter 1: Background on optical fibers and radiation effects

1.1. Optical Fibers: main parameters and guided modes modelling

An optical fiber (OF) is a cylindrical dielectric waveguide able to propagate electromagnetic waves at the optical frequencies, ranging from the ultra-violet (UV)/visible (vis) range to the near-infrared (NIR) one. Besides telecommunications, which is the field that has contributed the most to their worldwide diffusion, OFs are also exploited for sensing and other scientific applications.

The basic structure of an OF is shown in Figure 1.1. From the outside to the inside, it is constituted by:

- one (sometimes two) external layer(s), the **coating**, composed by polymers (usually acrylate or polyimide, depending on the application) that essentially ensure the mechanical protection of the inner glass structure;
- an intermediate layer, the **cladding**, made of pure or doped silica, with refractive index n_g ;
- an inner layer, the **core**, made of pure or doped silica, with refractive index n_c ($> n_g$).

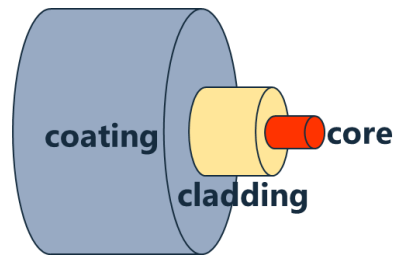


Figure 1.1 Basic structure of an optical fiber, composed by three concentric layers: the core, the cladding and the coating (from inside to outside).

1.1.1. Guided modes inside an optical fiber: geometric approach according to ray optics

To ensure that a waveguide is capable of guiding light, the total internal reflection (TIR) condition must be satisfied. In particular, referring to Figure 1.2, where is shown the OF cross-section, a ray propagating inside the core is completely reflected at the core-cladding interface only if $\vartheta_i > \vartheta_c$, where ϑ_i represents the angle of incidence and ϑ_c is the critical angle, defined by the Snell's law as

$$\vartheta_c = \arcsin\left(\frac{n_g}{n_c}\right) \quad (1.1)$$

Consequently, the same ray will be reflected at the opposite interface under the same condition, and so on.

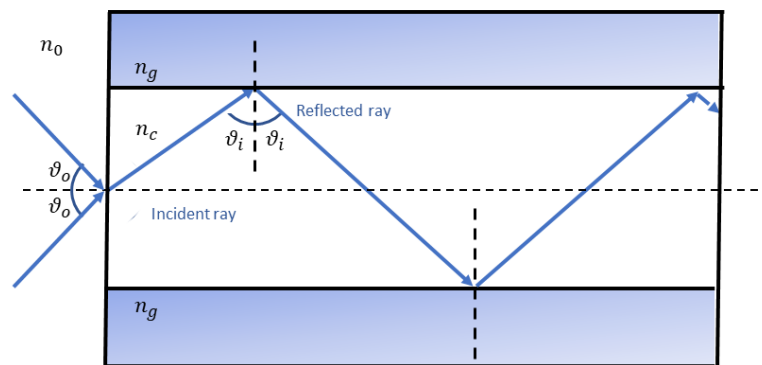


Figure 1.2 Cross-section of an optical fiber. The incident ray is totally reflected only if $\vartheta_i > \vartheta_c = \arcsin\left(\frac{n_g}{n_c}\right)$.

The angle ϑ_i depends on ϑ_o , the angle the incident ray creates with respect to the fiber axis. The “acceptance cone” is defined as the largest angle $\vartheta_{0,max}$ an incident ray can have to ensure the total internal reflection at the core-cladding interface.

All incident rays at an angle larger than $\vartheta_{0,\max}$ will be partially reflected at the core-cladding interface and partially transmitted, with the result of being dissipated in the cladding or in the coating and introducing prohibitive propagation losses. From the angle $\vartheta_{0,\max}$, it is possible to define the numerical aperture (NA), which constitutes a fundamental parameter of the OF and is defined as:

$$NA = n_0 \sin \vartheta_{0,\max} = \sqrt{n_c^2 - n_g^2} \cong n_c \sqrt{2\Delta} \quad (1.2)$$

where n_0 is the refractive index of the medium surrounding the optical fiber ($n_0 = 1$ in the case of air) and Δ is the relative index contrast between the OF core and cladding ($\Delta = \frac{n_c - n_g}{n_c} = \frac{\Delta n}{n_c}$). Typical values of Δn for single-mode¹ (SM) OF are in the order of 4×10^{-3} ($NA = 0.11$) and of 10^{-2} for multi-mode (MM) OF ($NA = 0.17$) [2], while values of n_c depend on the wavelength, but are approximately around 1.46. It is easier to couple light in a MM-OF rather than a SM-OF, because the core size is larger (tens of μm for SM-OFs compared to $\sim 50 \mu\text{m}$ or more for MM-OFs).

However, the theory of guided modes above described by the geometrical approach applies to OFs propagating many guided modes (and, therefore, over-dimensioned with respect to the wavelength). This approach has the advantage of being simple but fails to explain more complex phenomena, such as cladding losses and evanescent modes, for which electromagnetic concepts remain indispensable, especially to explain the theory behind SM-OFs.

1.1.2. Guided modes inside an optical fiber: modal approach according to electromagnetic optics

In order to define the guided modes in an OF it is necessary to start from Maxwell's equations. Considering the OF as an isotropic dielectric medium without charge, loss-free and non-magnetic, the Maxwell's equations and the constitution relations applicable for such environments are the following:

$$\vec{\nabla} \times \vec{E} = -\frac{\partial \vec{B}}{\partial t} \quad (1.3)$$

$$\vec{\nabla} \times \vec{H} = \vec{J} + \frac{\partial \vec{D}}{\partial t} \quad (1.4)$$

¹ When referring to SM OFs, we usually refer to OF operating in the IR domain, unless otherwise specified.

$$\vec{\nabla} \cdot \vec{B} = 0 \quad (1.5)$$

$$\vec{\nabla} \cdot \vec{D} = 0 \quad (1.6)$$

$$\vec{B} = \mu_0 \vec{H} \quad (1.7)$$

$$\vec{D} = \epsilon \vec{E} = \epsilon_0 n^2 \vec{E} \quad (1.8)$$

where \vec{E} and \vec{H} are respectively the electrical and magnetic field, \vec{B} is the magnetic flux density, \vec{D} is the density of electrical displacement, \vec{j} is the current density, ρ is the electrical charge density, μ_0 is the vacuum magnetic permeability of a non-magnetic medium ($\mu_0 = 4\pi \times 10^{-7}$ H m⁻¹), ϵ_0 is the vacuum dielectric permittivity ($\epsilon_0 = 8.84 \times 10^{-12}$ F m⁻¹) and n is the refractive index. The particular solutions of these equations have to satisfy the boundary conditions, constituted by the continuity, at the interfaces between media, of the normal and tangential component of the electric and magnetic field, the electric displacement current and the magnetic flux density.

Thanks to the cylindrical symmetry of OFs, the Maxwell's equations, as well as their solutions for the OFs, have to be expressed in cylindrical coordinates (r, φ, z), being r the radial position, φ the angular position and z the axial position. Consequently, this process makes it possible, by using the technique of separation of variables, to factorize the solution in two parts: a radial and an angular one. The radial part of the problem has to solve the following equation, both in the core and in the cladding of the optical fiber:

$$\frac{d^2 R}{dr^2} + \frac{1}{r} \frac{dR}{dr} + \left(n^2 k_0^2 - \beta^2 - \frac{m^2}{r^2} \right) R = 0 \quad (1.9)$$

where m is the separation constant, β is the wave propagation constant and $k_0 = 2\pi/\lambda$ is the free-space wave number. Equation (1.9) is a well-known differential equation for the Bessel functions. Its general solution in the core and cladding regions is given by

$$R(r) = \begin{cases} AJ_m(\kappa r) + A'Y_m(\kappa r) & , \text{if } r \leq a \\ CK_m(\gamma r) + C'I_m(\gamma r) & , \text{if } r > a \end{cases} \quad (1.10)$$

where A, A', C and C' are constants, J_m, Y_m, K_m, I_m are different kinds of Bessel and Hankel functions (characterized by the index m) and a is the core radius. Finally, $\kappa^2 = n_c^2 k_0^2 - \beta^2$ and $\gamma^2 = \beta^2 - n_g^2 k_0^2$ are the transverse propagation constants in the core and in the cladding, respectively. By applying the conditions that the electrical field of the guided mode must be finite for $r = 0$ and must decay to zero for $r = \infty$, equation (1.10) gives rise to the general solution for the electrical field E_z :

$$E_z(r, \varphi, z) = \begin{cases} AJ_m(\kappa r)e^{im\varphi}e^{i\beta z} & , \text{if } r \leq a \\ CK_m(\gamma r)e^{im\varphi}e^{i\beta z} & , \text{if } r > a \end{cases} \quad (1.11)$$

The components mentioned so far represent the electromagnetic field in the core and cladding of an OF. The same method can be used to obtain H_z , while the other components (E_r , E_φ , H_r and H_φ) can be expressed in terms of E_z and H_z by using Maxwell's equations. By ensuring the continuity of \vec{E} and \vec{H} and their derivatives at the core-cladding interface, the characteristic equation is obtained, which, in the particular case where $m = 0$ (corresponding to the case in which a symmetry of revolution for the modal solution exists), results:

$$\left[\frac{J'_0(\kappa a)}{(\kappa a)J_0(\kappa a)} + \frac{K'_0(\gamma a)}{(\gamma a)K_0(\gamma a)} \right] = 0 \quad (1.12)$$

where $(\kappa a)^2 + (\gamma a)^2 = V^2$, V being the normalized frequency. V can be expressed also as $V = \frac{2\pi}{\lambda} a \sqrt{n_c^2 - n_g^2}$.

From (1.12) is possible to calculate, for each value of V , the number of guided modes and their associated propagation constant. Those results are summarized in Figure 1.3, that gives for each mode (in the "weak guidance approximation" [3], i.e. $n_c \cong n_g$) the evolution of its effective refractive index (defined as $\frac{\beta}{k_0}$) with V .

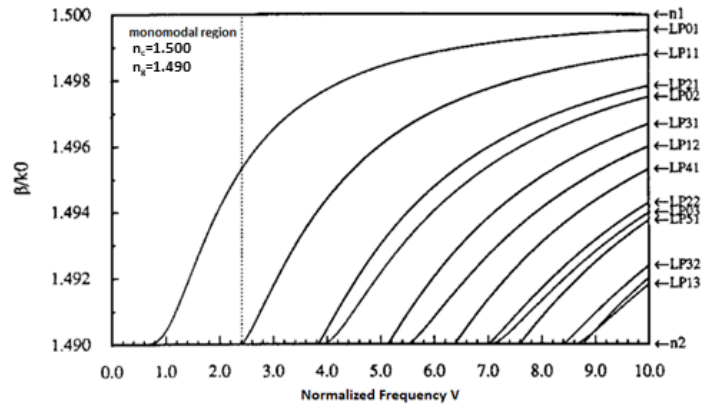


Figure 1.3 Evolution of the effective refractive index ($\frac{\beta}{k_0}$) as a function of the normalized frequency V for each guided mode in a step-index optical fiber with $n_c = 1.500$ and $n_g = 1.490$. Adapted from [2].

Figure 1.3 highlights that, for $V < 2.4$, only one solution exists to the characteristic equation, represented by the fundamental mode (LP_{01}). Indeed, the OF results SM for $V < 2.4$, whereas, for higher values of the normalised frequency, the OF becomes MM. The longest wavelength for which a mode is propagated in the OF is called cut-off wavelength (λ_c).

Figure 1.4 shows the radial distribution of the transverse component of the electrical field of guided modes from LP_{01} to LP_{12} . From the figure it is possible to observe the continuity of the Bessel and Hankel functions at the core-cladding interface.

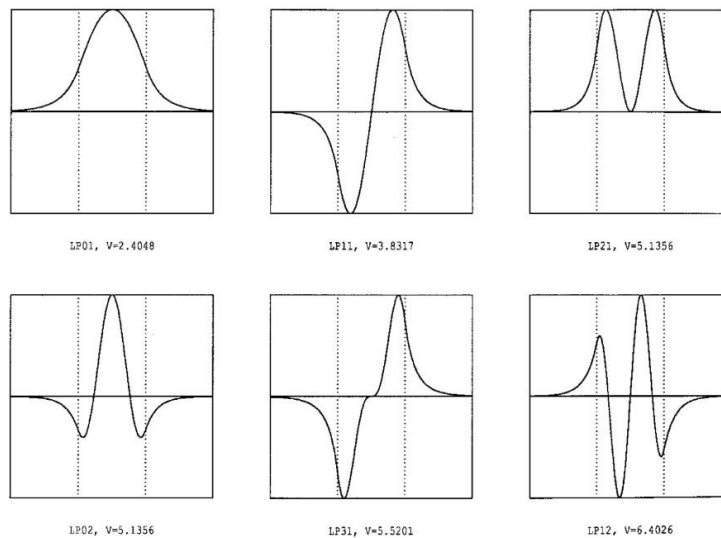


Figure 1.4 Radial distribution of the transverse components of the fields of the different LP modes. Vertical dashed lines represent the core-cladding interfaces. Adapted from [2].

By calculating the Poynting vector, it is possible to determine the power carried by each of the propagating modes. The fraction of power contained in the core with respect to the total power carried by the mode is called “confinement factor” and is denoted with Γ . In Figure 1.5 the confinement factor as a function of the normalised frequency is represented, for the first guided modes in the OF.

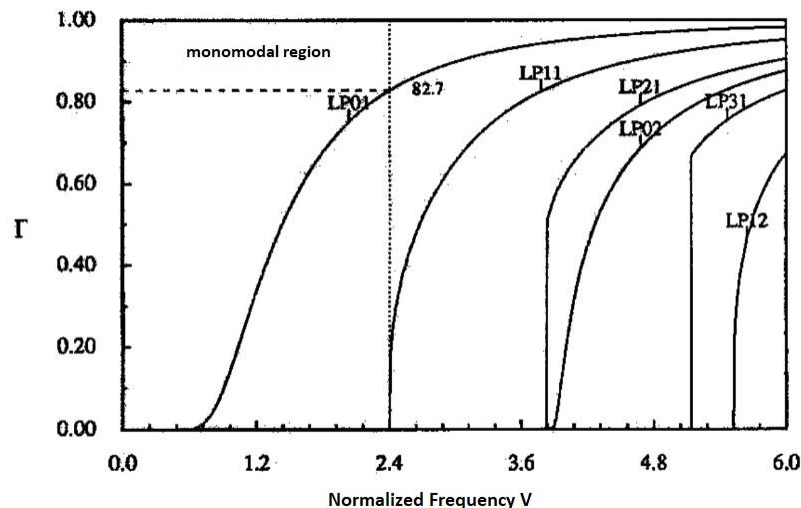


Figure 1.5 Confinement factor Γ as a function of the normalised frequency V determined for the first guided modes in the OF, from the fundamental mode LP_{01} to the LP_{12} . Adapted from [2].

It can be observed that, when the mode appears at its cut-off frequency, its power is almost entirely contained in the cladding of the OF. At higher frequencies, instead, the power is mostly contained in the core. For instance, at the first bi-mode cut-off frequency ($V = 2.4$), only 82.7% of the power of the fundamental mode LP_{01} is confined in the core.

1.2. OF Manufacturing process

An OF is obtained by the drawing process of a cylindrical bar of silica having a diameter of few centimeters, called preform. The drawing process is meant to reduce the diameter of the preform, while its radial distribution of dopants and, consequently, the radial refraction index profile, is maintained. However, some dopants, especially fluorine, can be subjected to a chemical diffusion process that can slightly modify the preform index profile.

The preform, being the homothetic reproduction in larger scale of the optical fiber, needs to have the specific radial index profile required by the manufacturer. Since, as already seen in section 1.1.1, the region inside the fiber where the light propagates is the inner one (the core and the inner part of the cladding), this has to be made of high-quality glass, i.e. with a low concentration of impurities that are associated with absorption losses. Indeed, for most cases, are recommended OH-groups and metallic ions (both typical impurities that can be found in OFs) concentrations of the order of some ppb. These requirements are achieved through synthesis processes involving ultra-pure reagents that are very expensive. Therefore, in order to contain the production costs, the preform is usually made following a two-stage process. In the first stage, a small preform (called “primary”) is realized with an elevated optical quality. The primary preform will constitute the region where the light will propagate inside the fiber. In the second stage, the outer diameter of the preform is increased through a quicker and less expensive process. Many different fabrication methods can be used to obtain the primary preform, each one differing in the way the silica is deposited: outside a rod or inside a hollow tube. Here, we will focus only on one of them, the Modified Chemical Vapor Deposition (MCVD), since this is the one used by the INPHYNI Laboratory in Nice to produce the OF samples studied in this thesis.

1.2.1. Modified chemical vapor deposition (MCVD)

The MCVD, initially developed by Corning, is today one of the most common OF manufacturing processes, since it enables to easily control the radial profile of the refractive index and leads to a high purity level of silica [4]–[6]. This fabrication method allows to synthesize and deposit different layers of pure or doped silica on the inner surface of a rotating hollow tube, which will be part of the final preform. In the first place, the synthesis phase takes place through the oxidation, at high temperatures, of ultra-pure gaseous reagents: $SiCl_4$, $GeCl_4$, SiF_4 or $POCl_3$. These gases are simultaneously introduced with molecular oxygen (O_2)

in the support tube. A temperature increase (up to 1400-1600 °C), made by an external moving torch H_2O_2 , creates a hot zone where the oxidation of the reagents occurs, producing a soot of pure or doped-silica that is initially deposited on the inner layer of the tube and, after, is sintered to form the amorphous glass. The chemical reactions happening inside the hollow tube are the following:



In Figure 1.6a and b, this first deposition/vitrification phase is illustrated. By controlling the gases concentration in the tube, this process allows controlling the radial preform composition from the outer layer of the cladding to the inner part of the core. Moreover, the oxidation reaction, occurring in a chlorine-rich environment, allows to reduce the OH groups concentration in the produced silica. Once the deposition phase is finished, a progressive reduction of the tube internal hole is performed, in order to reduce the preform diameter. This is accomplished by slowly moving the torch along the tube at higher temperatures (1800-2000°C). In this way, the viscosity of the glass is lowered and the increase of the surface tension allows a reduction of the internal hole. Simultaneously to this second phase, an aspiration of the residual gasses is performed in order to avoid the deposition of impurities. At the end of this phase, illustrated in Figure 1.6c, a preform with the radial index profile targeted for the final OF is obtained.

The MCVD platform at the INPHYNI Laboratory in Nice, where the samples for the CERTYF project have been manufactured, can produce pure-silica, Ge-doped, F-doped, P-doped and Al-doped preforms. However, if for the formers the dopants are introduced in gaseous form, as described above, the Al-doping is produced by soaking the preform into an aqueous or alcoholic solution containing this element. Figure 1.7 shows some steps of the MCVD process during the fabrication of an OF preform at the INPHYNI laboratory.

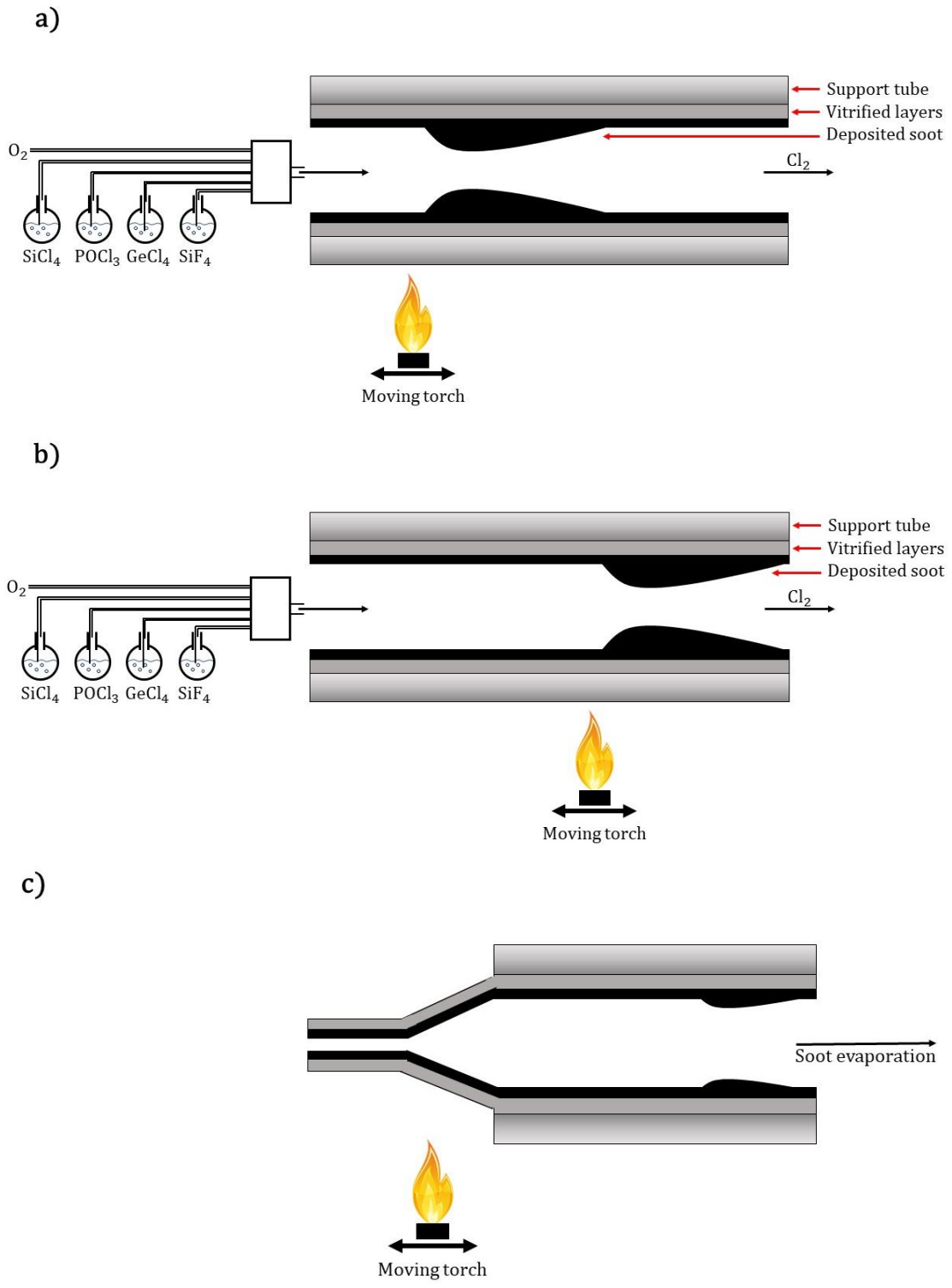


Figure 1.6 Modified chemical vapor deposition process: (a-b) deposition/vitrification phase of the pure- or doped-silica soot on the inner surface of the rotating hollow tube; (c) diameter reduction phase, also called collapsing phase, leading to the final preform creation.

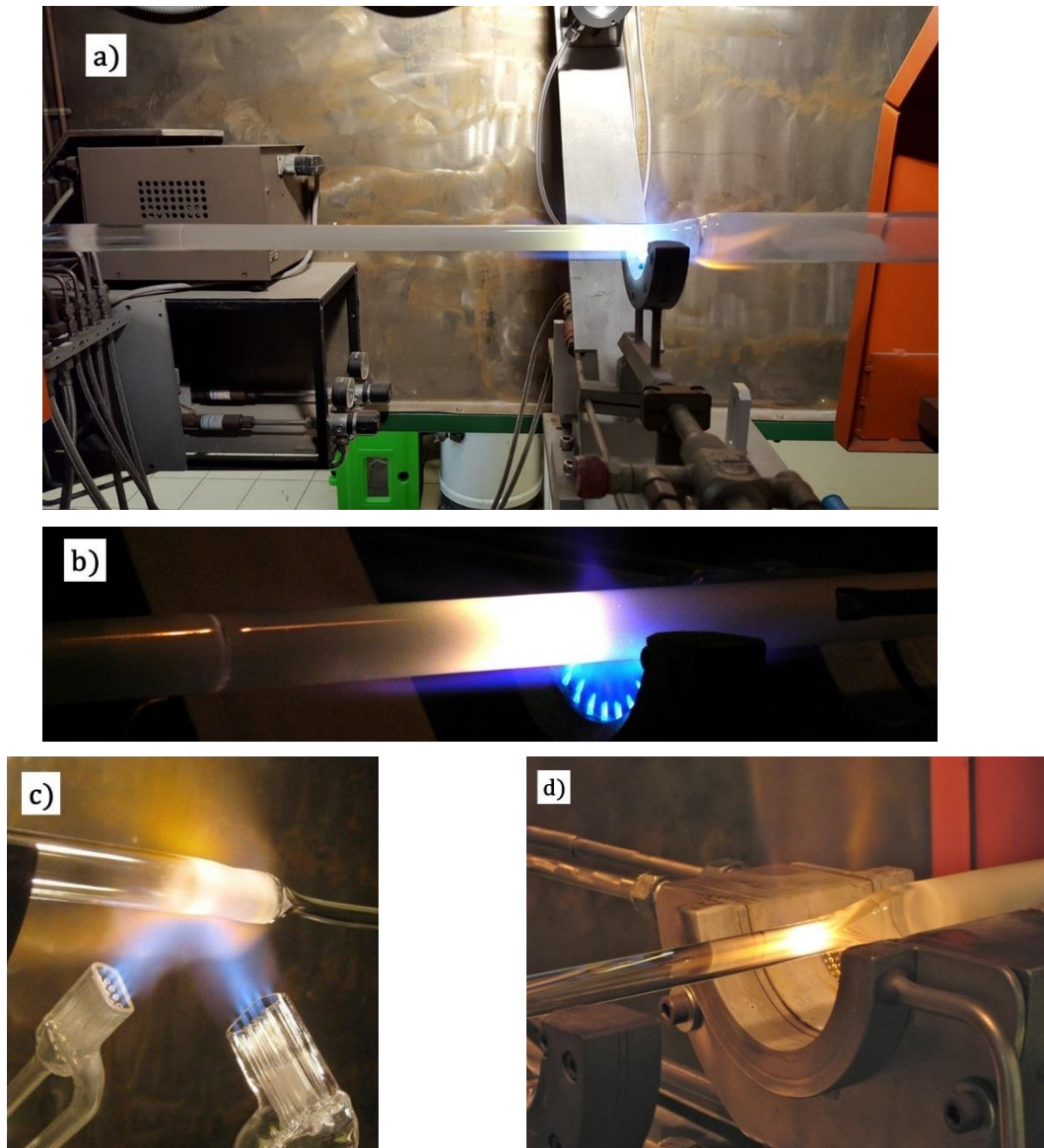


Figure 1.7 Manufacturing of an OF preform through the MCVD process at INPHYNI laboratory: **a)** soot deposition/vitrification phase, **b)** details of the deposition phase, **c)** H_2O_2 moving torch, **d)** collapsing phase of the preform, where its diameter is reduced.

1.2.2. Drawing of the preform into an optical fiber

The drawing process is meant to transform the preform into the final optical fiber. This process is carried out through the use of a “drawing tower”, which scheme is given in Figure 1.8.

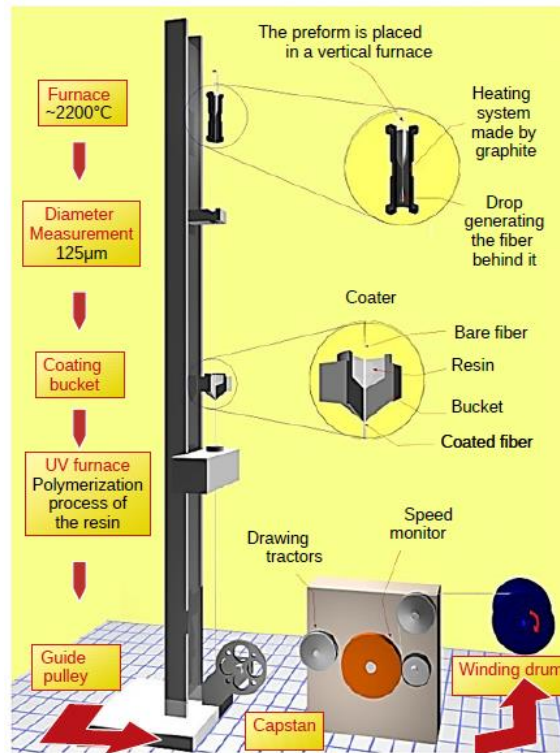


Figure 1.8 Schematic representation of a OF drawing tower. Taken from [7].

The preform is placed at the top of the tower in a vertical furnace, where temperatures reach around 2200°C. In this way the preform is melt and a drop falls down the tower, driven by gravity, creating a filament that has the same radial index profile of the preform but with a smaller diameter (typically ~125 µm). This is monitored by a device placed right after the furnace at the top of the tower. Then, the OF is cooled-down and is passed through a coating bucket where a polymer resin is applied to the outside of the fiber, forming the coating. The role of the coating is to protect chemically and mechanically the OF. After this procedure, the external diameter of the OF is typically around 250 µm (for an acrylate coating). Finally, a series of pulleys are used to transport the fibre to the spool. During the drawing process, many parameters have to be controlled in order to fulfil the OF design specifications, as the diameter, the drawing speed (between ~10 m/min and ~1000 m/m) and the drawing tension (from 5g to 200g), the furnace temperature as well as the preform descent speed into the furnace. In Figure 1.9, a part of the drawing tower in the INPHYNI laboratory is shown.



Figure 1.9 Drawing tower used at the INPHYNI laboratory.

1.3. Radiation effects on optical fibers

A radiation environment can involve the presence of one or more types of radiation:

- high energy photons (γ -rays and X-rays);
- particles (protons, neutrons, electrons and heavy ions).

Radiation excites electron-hole pairs present in the dielectric material, most of which are divided and recombined in a picosecond timescale. This process is called “geminate recombination” [8], and cannot be observed except with high-performance instruments. The particles that escape this initial recombination are the ones that contribute to the changes in the material properties and will be considered in the present thesis.

Depending on how they interact with matter, radiations can be classified as ionizing or non-ionizing. The first type interacts mostly causing ionization processes: an electron, originally located in the valence band, is excited to the conduction band with a given kinetic energy (depending on the energy transferred by the incoming particle), generating a hole in the valence band. The electron-hole pair created in this way can recombine both radiatively, by emitting photons (luminescence), or non-radiatively, by dissipating the energy through the creation of phonons or by secondary radiolitic processes that can lead to the generation of point defects. However, if the incoming particle is able to transfer a sufficient amount of energy to the silica matrix, displacement damage could occur. This is, for example, what happens in case of neutron exposures. The displacement threshold energy is 10 eV for O and 18 eV for Si [9]. In this case, the radiation causes direct atomic displacements, known also as knock-on damage [10].

Some of the environments featuring these two types of radiation are natural, such as space, while others are man-made, as the case of nuclear power plants, high-energy physics facilities and nuclear waste repositories.

1.3.1. Macroscopic effects of radiation on silica-based OFs (RIA, RIRIC, RIL)

When OFs are exposed to a radiation environment, four macroscopic effects can be observed:

- Radiation-Induced Attenuation (RIA);
- Radiation-Induced Emission (RIE);
- Radiation-Induced Compaction (RIC);
- Radiation-Induced Refractive Index Change (RIRIC).

The relative impact of these phenomena for a given application significantly depends on several parameters as the tested fiber material composition and its manufacturing process.

1.3.1.1. Radiation-induced Attenuation (RIA)

RIA consists of a decrease in the transmission properties of an OF when this is exposed to radiations. This phenomenon is largely the most studied among the radiation-involving processes because it is the most limiting one, especially for those applications where OFs are used for signal transmission. However, RIA can also be exploited for the development of fiber-based detectors for dosimetry applications [11], [12].

RIA is caused by the generation of radiation-induced point defects in the OF silica-based matrix. These point defects, also called color centers, are created by either ionization or displacement damage processes, depending on the nature of the radiation, and introduce additional energy levels within the silica bandgap. These “new” energy levels enable the trapping of radiation released electrons and holes. In this way, signals that were initially transmitted throughout the whole OF length before irradiation can be absorbed by the material.

On a microscopic level, the amorphous silica is a Continuous Random Network (CRN) constituted by SiO_4 tetrahedron units, characterized by the same Si-O bond length, O-Si-O angles than in the quartz crystalline structure [13], [14], but with a different Si-O-Si angles. Because of the radiation or the OF drawing process, some bonds can be broken, giving rise to intrinsic point defects. Furthermore, during the manufacturing process, can also be introduced, accidentally or voluntarily (in order to create the refractive-index contrast between the core and the cladding), impurities and/or dopants perturbing the CRN and creating extrinsic defects. Radiation-induced point defects can be generated from the unperturbed matrix of the silica or from pre-existing defects, named “precursors”.

Each defect is characterized by one or more optical absorption bands (in most cases, Gaussian ones) [10].

1.3.1.2. Radiation-Induced Emission (RIE)

RIE is the process by which light is generated inside the OF when it is exposed to radiations. This can happen through two different phenomena: the Cerenkov emission or the Radiation-Induced Luminescence (RIL). The first one occurs when a charged particle propagates through a dielectric medium at a speed greater than the speed of light in that medium [16]. Due to the electric field of the charged particle, the molecules of the material being traversed by the charged particle become polarised. When their initial state is re-established, they are discharged by emitting a short pulse of electromagnetic radiation into the visible light. The second phenomenon, the RIL, consists of light emission from pre-existing or radiation-induced point defects, excited by the radiation itself. As already said, the radiation

excites carriers from the valence band to the conduction band. While they come back to their ground state, they can be trapped in energy levels linked to point defects (already present in the pristine sample or created during the irradiation) and then, when they are released from the trapping states, they can emit a luminescence signal. Therefore, the intensity of the RIL phenomenon is the result of a competition between the speed at which the carriers are trapped and released from the trap states which, in turn, are two dose-rate depending processes. Thanks to this dependence, the RIL can be used for the real-time monitoring of the dose-rate in high-energy physics facilities or for medical applications [17].

1.3.1.3. Radiation-Induced Compaction (RIC)

When a glass is exposed to radiation, its density can change in proportion to the total accumulated dose, according to the following power law:

$$\frac{\Delta\rho}{\rho} \propto D^k$$

where $\Delta\rho$ is the density change, ρ is the density, D is the dose and k is a parameter depending on the irradiation nature. In particular, k is approximately 1 for fast neutrons and 2/3 for γ -rays [18]. This phenomenon is called Radiation Induced Compaction (RIC).

1.3.1.4. Radiation-Induced Refractive Index Change (RIRIC)

Both RIA and RIC originate the Radiation-Induced Refractive Index Change (RIRIC):

- the first one, through the Kramers-Kronig relation:

$$\Delta n(\lambda) = \frac{\lambda^2}{2\pi^2} \int_0^\infty \frac{\Delta\alpha(\lambda')}{\lambda^2 - \lambda'^2} d\lambda'$$

where Δn is the refractive index change, $\Delta\alpha$ is the variation of the absorption band and λ is the wavelength;

- the second one, through the Lorentz-Lorenz equation:

$$\Delta n(\lambda) = \frac{(n^2 + 2)(n^2 - 1)}{6n} \left(\frac{\Delta\rho}{\rho} + \frac{\Delta R}{R} \right)$$

where Δn is the refractive index change, $\Delta\rho$ is the density change, ΔR is the molar refractivity change, ρ is the density, R is the molar refractivity and n is the refractive index of the material.

This phenomenon can affect the guided properties of OF, the response of optical fiber sensors and also of the optical systems, e.g. the image blurring in a camera due to the lens RIRIC [19]. However, in most of cases this phenomenon is negligible compared, for example,

to the refractive-index change induced by temperature variation. Indeed, very sophisticated systems are needed to detect it.

1.3.2. Parameters affecting RIA levels and kinetics

RIA is dependent on many parameters. Hereafter, we review the most influencing ones.

1.3.2.1. Signal wavelength (or energy range)

As already pointed out, when a material is exposed to radiation, optical absorption bands are generated. These bands are peaked at different energy values and have different Full Width at Half Maximum (FWHM), depending on the specific point defect to which they are associated. For this reason, the operating wavelength of the application is one of the most important parameters because, depending on its proximity to absorption bands, RIA values and kinetics may differ significantly. Typically, RIA is higher at short wavelengths since most of the point defects absorb in the UV/vis range [15], [20].

1.3.2.2. Irradiation conditions: nature of particles

As mentioned in 1.3, a radiation environment can involve the presence of different types of radiations: high-energy photons (such as γ - and X-rays) and/or different types of particles (protons, neutrons, electrons and heavy ions). Depending on the nature and energy of the incident radiation, the OF response may vary as a result of a different relative contribution between ionisation processes and displacement damages [10], [21], [22]. With regard to OFs, the main phenomenon contributing to the RIA is the ionisation process, dominating the generation processes of radiation-induced point defects. However, for environment involving high neutron fluence or heavy ions, a specific displacement damage process contribution can be observed [23]–[25].

Figure 1.10 summarizes the different processes involved in the creation of point defects in amorphous silica depending on the type of incident radiation.

1.3.2.3. Irradiation conditions: total ionizing dose (TID)

Existing radiation environments are characterized by different levels of TIDs and dose-rates (Figure 1.11).

Usually, at higher TIDs correspond higher RIA values. This is dependent on the material constituting the OF but, generally, by examining RIA kinetics it can be seen that the RIA rapidly increases during the first part of the irradiation (up to few kGy) and then continues growing with a lower slope as the dose increases. This behavior could be explained by the fact that, at the beginning of the irradiation, the “weakest” sites present in the material, called precursor sites, are quickly transformed in optically-active defects by the radiation. Once these are

exhausted, the RIA increase is due to the generation of radiation-induced point defects originating from regular bonds. Since this generation process is less efficient than the one where the defects are generated from precursor sites, once these are exhausted, the RIA grows with a slower slope as the dose increases.

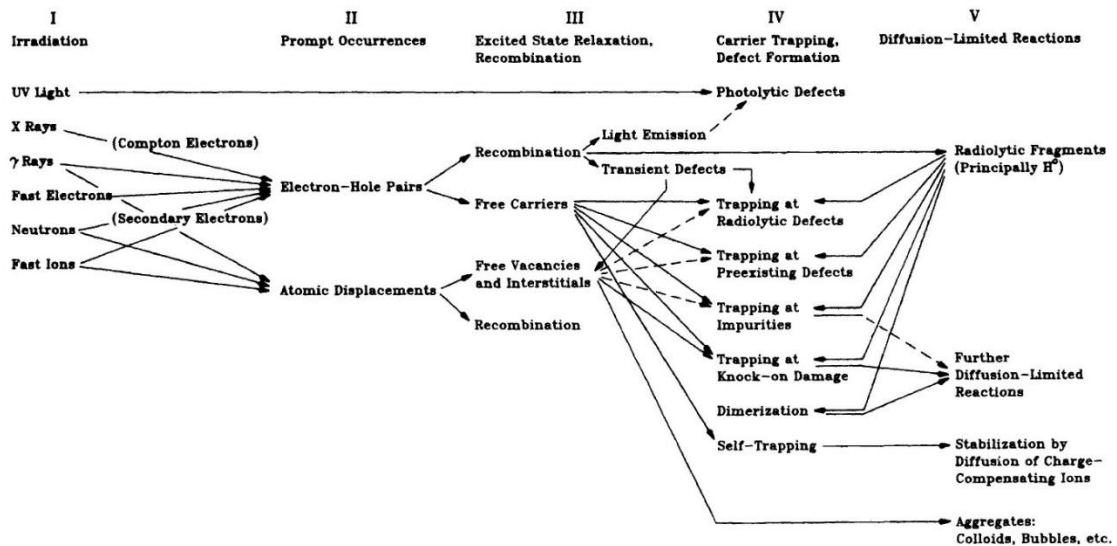


Figure 1.10 Different generation processes of point defects in amorphous silica depending on the type of incident radiation. Taken from [10].

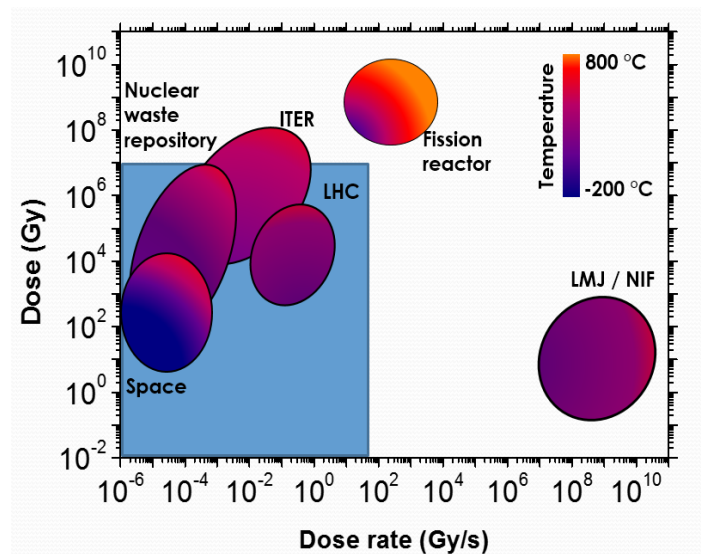


Figure 1.11 Various radiation environments as a function of the total ionizing dose and dose-rate. Taken from [20].

1.3.2.4. Irradiation conditions: dose-rate

The dose-rate at which the irradiation is performed can also have a big impact on the RIA. Several studies can be found in literature highlighting that no univocal dependency exists and that its influence is strictly related to the OF composition. In general, for a given TID, at higher dose-rates correspond higher RIA values. This is notably the case of pure-silica core [20], [26], [27] and Ge-doped OFs [28]–[31]. Indeed, at higher dose-rates, the same TID is

attained in a shorter irradiation run, leaving radiation-induced point defects less time to recombine (as a consequence, a lower portion of them will be annealed). On the other hand, it has been already reported the NIR-RIA insensitivity to dose-rate variations of P-doped OFs [12], [29] and also of Al-doped OFs [32], which is one of the main features that make this type of OFs suitable for dosimetry applications.

1.3.2.5. Irradiation conditions: irradiation temperature

From literature it is known that the irradiation temperature (i.e. the temperature at which the irradiation is performed) affects both generation and bleaching processes of radiation-induced point defects and, as a result, affects both the RIA growth and recovery kinetics [33], [34]. Usually, a higher temperature accelerates the bleaching process of the radiation-induced point defects (this phenomenon is also known as “thermal bleaching”) [20], [35]–[37]. However, a higher irradiation temperature is not always associated with a RIA reduction, as temperature can increase the generation efficiency of point defects and, also, can promote the conversion from a point defects to another with a higher thermal stability that can potentially have a negative impact on the signal transmission. This is the case of heavily-doped germanosilicate OFs, which showed a higher RIA at higher temperatures, for wavelengths lower than 1300 nm: this phenomenon has been associated with the increasing in the absorption of the GeX center due to thermal decay of the Ge(1) center [38]. Another example of temperature-driven conversion occurs during the thermal treatment (the temperature is increased only after the end of the irradiation) of P-doped OFs, where the temperature increase promotes the conversion of the phosphorus oxygen hole centers (POHC), absorbing in the UV/visible domain, into the P1 defect, absorbing in the third telecom window [39], [40].

Furthermore, it must be considered that the effect of the irradiation temperature is also dependent on the time. Right after the irradiation start there is a transient period in which the defect generation/bleaching is not stable and so the temperature effect could have no significant impact. After this first phase, when a more stationary regime is attained, the temperature effects can constantly affect RIA levels and kinetics.

To date, numerous works have been devoted to the study of the thermal stability of point defects in bulk samples [41]–[45]. Even though these studies are relevant for understanding the nature of defects and their interconversion processes, they are not sufficient to predict the complex role of temperature in defect generation and recombination during the irradiation, as these investigations are limited to the temperature effects on those defects that are stable at the irradiation temperature. For this reason, *in situ* measurements at the different temperatures are mandatory to provide a full picture of OFs vulnerability in environments combining temperature and radiation constraints.

1.3.2.6. Injected light power

Obviously, in order to perform attenuation measurements in an OF, a probing signal must be transmitted. It has been demonstrated that the power level of the probing signal can strongly affect the RIA levels of the tested sample through the activation of two opposite phenomena: photobleaching and photodarkening. Photobleaching can be explained by the possible recombination of some metastable radiation-induced point defects that could be assisted by the energy provided by the guided light. In this way, the RIA levels can be reduced and RIA recovery kinetics can be accelerated [46]. This phenomenon is hard to predict because it is very dependent on the type of point defect, but it has been demonstrated to be efficient for Ge-doped OFs [47] and pure-silica core OFs [46], [48]. Photodarkening, instead, is a phenomenon in which the probing light generates by itself point defects, thus increasing the attenuation of the OF. Photodarkening occurs only at high pumping power and not in all type of matrix. It can be very important for high power OF laser, in which the core of the OF consists in an aluminosilicate or phosphosilicate host matrix doped with rare-earth ions [49].

As a consequence, standard irradiation tests on OFs have to be performed with low levels of the probing signal ($<1 \mu\text{W}$) in order to measure the “real” RIA or at least to evaluate the worst-case scenario. However, depending on the target application, injected powers can vary from few microwatts to tens of Watts. Furthermore, photobleaching can contribute to make radiation constraints less restrictive, lowering the radiation-induced losses, as well as, from an applicative point of view, it can be used for the “reset” of OF dosimeters [50].

Photobleaching is a phenomenon that is expected to be temperature-dependent. This was already reported by Henschel et al., who proved that injection of light of about $\sim 800 \text{ nm}$ wavelength can increase the radiation hardness of Ge-doped OFs at low temperatures [51]. However, since photobleaching depends on many parameters (OF length, temperature and photobleaching wavelength), to evaluate its efficiency in each OF type is required an experimental approach in which every parameter can be controlled.

1.3.2.7. Manufacturing process: glass stoichiometry

The stoichiometry of the deposited silica can be tuned during the fiber manufacturing process, in particular by controlling the O_2 concentration in the vapor-gas mixture during the preform deposition [5]. It has been found that mostly for pure-silica core and fluorine-doped OFs, the oxygen concentration can change the nature and population of the point defects responsible for the fiber degradation. Indeed, in an oxygen-deficient OF the presence of defects as ODC(I) and ODC(II) is strongly enhanced, whereas in an oxygen-loaded OF an abundance of peroxy linkages is found [52]. Consequently, depending on the stoichiometry, the RIA levels and kinetics are significantly affected. For example, in PSC or F-doped OFs, it has been demonstrated [53] that an excess of oxygen during the core fabrication can limit the

incorporation of chlorine into the silica matrix, reducing the Cl^0 centers induced by radiation and absorbing in the UV. Moreover, the excess of oxygen also permits the reduction of the glass network strain, by the creation of peroxy linkages, and then the suppression of non-monotonic RIA behaviour due to self-trapped holes (STH_1 and STH_2) [53], [54].

1.3.2.8. Manufacturing process: impurities and fictive temperature

Impurities in the core and cladding of OFs are related to concentration of hydroxyl groups (Si-OH) and chlorine-related species. Those impurities are introduced into the OF during the manufacturing process and govern the fictive temperature [55] of the material which, in turn, impacts the losses due to the Rayleigh scattering. In general, to a fictive temperature decrease corresponds a decrease of Rayleigh losses [56], giving rise to an optical fiber with a lower attenuation especially in the UV-vis domain.

The relative amount of OH groups and Cl impurities in the material are anti-correlated and can be tuned during the preform deposition varying the manufacturing parameters. On this basis, two groups of OFs can be manufactured: “dry” fibers (low-OH content, high-Cl content) and “wet” fibers (high-OH content, low-Cl content). Dry fibers are more suitable for transmission in the NIR domain, whereas wet fibers are more appropriated for operating in the UV-visible domain, because of the high absorption related to OH groups and their overtones (one of the most impacting for telecommunication applications being peaked at 1380 nm).

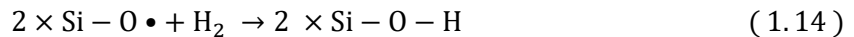
The fiber drawing process can also induce defects from the glass impurities, the so-called Drawing-Induced Defects (DID), whose structure is the same of some radiation-induced defects, e.g. Non-Bridging Oxygen Hole Centers (NBOHCs). DIDs are mostly present in dry optical fibers [57].

Under irradiation, wet OFs are characterized by a strong RIA in the visible range caused by the generation of NBOHCs, which absorption band is peaked at 630 nm. In dry fibers, instead, the NBOHC contribution is strongly reduced because of less precursor sites, but Cl-related defects, as the Cl_2 point defect, which absorption bands are peaked at 328 nm and 539 nm, and the Cl^0 species, with absorption peaked at 340 nm and 380 nm [58], [59], increase the RIA in the UV domain.

A third class of optical fiber, with low-OH and low-Cl content, has also been produced [60]. On this class of fiber, the radiation induces a reduced concentration of NBOHCs and Cl-related defects, but, on the other hand, a strong generation of STHs, causing the reduction of the fiber transmission in the visible domain, with their absorption bands peaked at 475 nm, 574 nm, 660 nm and 760 nm [15], [61]. For this specific defect class, the glass structure plays a key role and, in particular, its fictive temperature. Indeed, higher fictive temperatures lead to higher STH-related absorption [61]–[63].

1.3.2.9. Pre-treatments: hydrogenation and pre-irradiation

When it comes to RIA evaluation, the OF history can have a major effect. Indeed, the resistance to radiation can be changed by pre-treating the OF through gas loading or pre-irradiations. Both pre-treatments have the effect of reducing the number of precursor sites and, as a consequence, of the radiation-induced point defects. Since pre-treatments are essentially made to enhance the radiation-resistance, most of the studies are made on PSC optical fibers, as this class of fibers is the most suited to resist to steady-state irradiation (covering most of the application cases). It has been demonstrated that loading OF with gases, in particular with hydrogen or deuterium, changes the fiber response to radiation [64], [65]. Indeed, the gas quickly reacts with the radiation-induced point defects, passivating them. Those gases, being light elements, efficiently diffuse into material with kinetics depending on the temperature and on the optical fiber geometry [66]. Their addition reduces significantly the NBOHC concentration [67], and consequently the absorption in the visible domain. However, the benefits in the visible derived from the hydrogenation are counterbalanced by an increasing of the attenuation in the NIR domain caused by the increase of the hydroxyl groups concentration (in case of H₂ loading), which NBOHCs are converted into, through the following process:



In addition, hydrogen loading worsens the UV transmission by increasing the concentration of point defects absorbing in the UV domain, as the H(I) and H(II) centers. As a consequence, hydrogenation is only useful for OFs operating in the visible spectrum.

One of the major issues of loading fiber with hydrogen is that, at room temperature, it can quickly out-diffuse from the fiber, leading to a gas deficiency already after few days. Because of this, several solutions have been found to mitigate this problem, such as carbon- or metal-coated optical fibers [68]–[70].

To further increase the radiation resistance, also the use of micro-structured OF has been considered, as the hole-assisted carbon-coated (HACC) OFs [71]. Since the incorporation of the carbon coating (thickness of the order of tens of nm) requires high temperatures treatments (>300°C), if this operation is done in a gas-loaded OF, the high temperatures would accelerate the gas out diffusion during the process. In HACC OF, the presence of holes (created at the preform manufacturing stage) inside the OF allows an efficient and homogeneous gas loading of the OF after the deposition of the hermetic carbon coating. HACC OFs report a reduction of the out diffusion of the gas of about 100 times compared to non-carbon-coated ones [71].

As already said in 1.3.2.7, oxygen excess, obtained by varying the fiber manufacturing process, can change the point defect nature and kinetics under irradiation, with a potential

positive impact on the RIA depending on the signal wavelength. An oxygen excess, however, can also be obtained with direct O₂-loading; moreover, oxygen being a bigger molecule than hydrogen, it is not mobile at room temperature and it does not diffuse out from the fiber, allowing a constant gas concentration over long periods [72].

Besides gas loading, pre-irradiation represents another pre-treatment allowing to modify the RIA response of the optical fiber. This method, typically performed through consecutive X-ray irradiations, has the effect to convert precursor sites into active point defects. Applying, successively, thermal treatments or hydrogenation to the fiber, it is possible to bleach the defects created via the first irradiation, leaving, for the second irradiation, an OF with a lower precursor population and, then, a lower radiation response [73].

1.3.2.10. Optical fiber composition

Both core and cladding composition can significantly affect the RIA levels of OFs. Depending on the dopant used to define the refractive index profile, OFs can be classified in three main classes based on their response to steady-state irradiation, as listed below.

- **Radiation-sensitive**: OFs presenting a very high sensitivity to radiations, in both visible and NIR domains, e.g. reaching RIA levels of ~40000 dB/km at few hundreds of kGy at the telecommunication wavelengths. To this class belong OFs doped with Al or P in either core or cladding [74]–[76] or, as shown recently, doped with lanthanum (La) or thulium (Tm) [77]. Radiation-sensitive OFs should be avoided for data transfer applications in radiation-rich environments, but are very promising candidates for radiation detection and dosimetry.
- **Radiation-tolerant**: this OF type presents an intermediate response to radiation, with RIA levels approximately of 100 dB/km at few hundreds of kGy [15]. To this class belong Ge-doped OFs without phosphorus co-doping in their core or cladding. They are used for short length data links and in radiation environment where the attained doses are lower than 100 kGy. Other applications include distribute sensing or fiber Bragg gratings inscription.
- **Radiation-hardened**: this type of OFs presents the lowest level of radiation-induced losses under steady-state exposure, in the order of ~10 dB/km at few hundreds of kGy at the telecommunication wavelengths. F-doped and pure silica core OFs, both doped with fluorine in their cladding (in such a way to obtain a positive refractive-index contrast), are included in this class. They are suitable for high-dose level environments, such as ITER [78], nuclear waste repositories [1], nuclear industry [79] and high energy physics facilities [80], [81]. Recently, however, an extreme sensitivity of a commercial ultra-low loss (ULL) PSC OF to steady-state [27], [82] and pulsed X-ray [83] irradiations has been reported, exceeding levels of ~3000

dB km⁻¹ (~2000 dB km⁻¹) at 1310 nm (1550 nm) at the limited dose of 2 kGy. The same OF demonstrated to be more sensitive to radiation than P-doped OFs at the dose of ~500 Gy, dose-rate being of 175 mGy s⁻¹.

1.3.3. Radiation-induced point defects: what we know about their nature and properties

For the purpose of this thesis, the study of silica related point defects results of practical interest, as these defects affect the absorption and luminescence properties of the material. Point defects are defined as a local distortion of the atomic structure that lead to a rearrangement of the silica matrix. Amorphous silica is characterized by a short-range order limited to a few atomic bonds, contrary to crystalline silica, where the basic structural unit creates a periodic network. This structural unit is constituted by a SiO₄ tetrahedron, in which the silicon atom occupies the central position and the oxygen atoms are placed at the extremities. A theoretical model was initially proposed by Zachariasen [14], as already discussed in section 1.3.1.1.

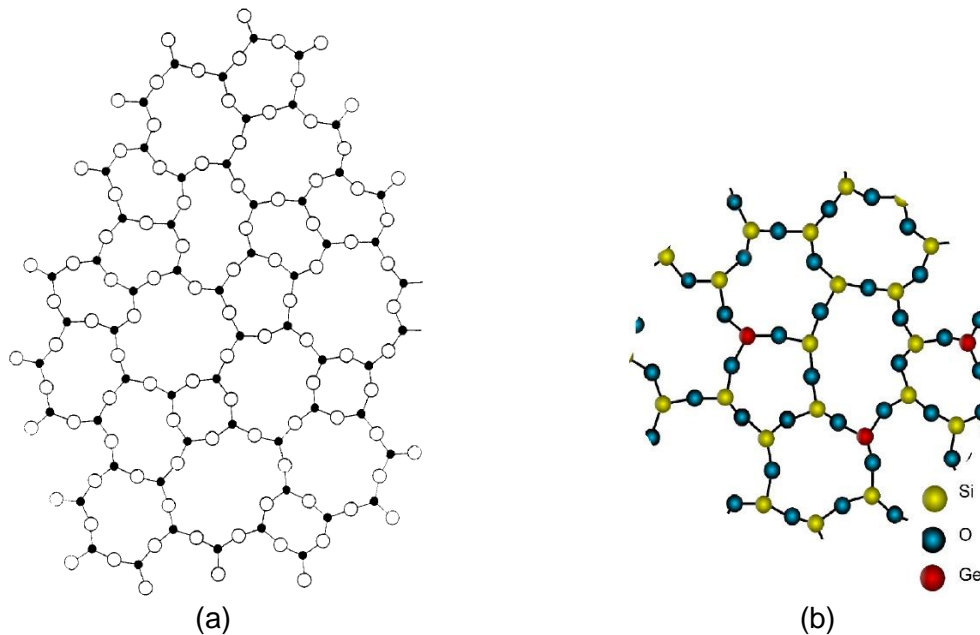


Figure 1.12 (a) Two-dimensional continuous random network (CRN) of amorphous silica. The black dots and white circles represent silicon and oxygen atoms, respectively. In the ideal silica matrix, each oxygen atom is bound to two SiO₄ tetrahedra. Figure taken from [14]. **(b)** CRN of a Ge-doped silica. The Ge atoms take the place of some Si atoms in some tetrahedron units, creating an extrinsic point defect. Adapted from [85].

Figure 1.12a illustrates, as an example, the bidimensional CRN for an ideal pure-silica. In the ideal silica matrix, each oxygen atom is bound to two SiO₄ tetrahedra but, in reality, this is not the case due to the presence of point defects. These can be classified into two types: intrinsic and extrinsic. The first are related to alteration in the base matrix involving O or Si

atoms, e.g. the presence of vacancies (missing atoms) or interstitial atoms (added atoms), double or broken bonds, trapped charges or under-coordinated atoms. On the other hand, extrinsic point defects are caused by the presence of “foreign” atoms other than Si and O, that can be either substitutional (replacing original atoms, as shown in Figure 1.12b) or interstitial. While substitutional extrinsic point defects are usually attributed to dopants, interstitial extrinsic point defects are generally associated with impurities [84].

Furthermore, point defects can be classified based on their electronic configuration: defect structures containing unpaired electrons are paramagnetic, otherwise they are diamagnetic defects. Paramagnetic defects, having a non-zero magnetic moment, are responsible for the magnetic resonance absorption and are, then, detectable by Electron Paramagnetic Resonance (EPR) [86].

In the following sub-sections we report an overview on the radiation-induced point defects concerning pure- and doped-silica OFs.

1.3.3.1. Pure silica: intrinsic point defects

In the following sections, the symbols \equiv and $>$ denote, respectively, three and two bonds with oxygen atoms, whereas the symbol \bullet denotes an unbound electron.

1.3.3.1.1. SiE' center ($\equiv \text{Si} \bullet$)

The E' center, shown in Figure 1.13, consists of a silicon dangling bond with an unpaired electron in the silicon sp^3 orbital [87] and, consequently, it is a paramagnetic defect. Different types of E' defect have been proposed in [10], being the E'_γ the only one stable at room temperature and characterized by a gaussian absorption band peaked at 5.8 eV (~214 nm) with a FWHM of 0.7 eV. These defects can be created both during the irradiation or the drawing of the preform into the fiber. In addition, their generation efficiency also depends on the hydroxyl groups concentration. Literature reports that E' defects can be destroyed with a temperature increase above ~80°C [21], [88].

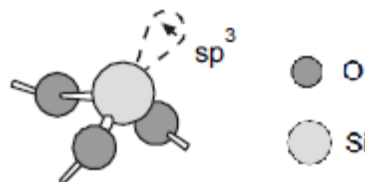


Figure 1.13. Atomic structure of the E' defect. Taken from [89].

1.3.3.1.2. Oxygen deficient center type I (ODC(I), $\equiv \text{Si} - \text{Si} \equiv$)

ODC(I) can be mostly found in unirradiated oxygen-deficient silica [90]. It is a diamagnetic defect consisting in two adjacent silicon atoms bonding together, as shown in Figure 1.14. It is characterized by an optical absorption band centered at 7.6 eV (~163 nm) with a FWHM of 0.5-0.6 eV [15].

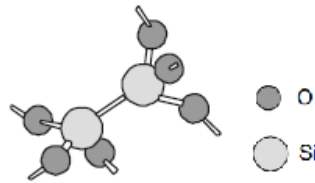


Figure 1.14. ODC(I) defect structure. Taken from [89].

1.3.3.1.3. Oxygen deficient center II (ODC(II), $> \text{Si}:$)

The ODC(II), also called “divalent Si”, is characterized by a twofold coordinated Si atom with two electrons that are not involved in any bonds [91], [92]. The ODC(II) structure is shown in Figure 1.15. The ODC(II) gives rise to three absorption bands centered at 5.05 eV (~246 nm), 3.15 eV (~394 nm) and 6.9 eV (~180 nm) with FWHM of 0.32 eV, 0.3 eV and 0.4 eV [15], respectively.

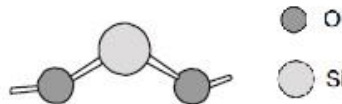


Figure 1.15. ODC(II) defect structure. Taken from [89].

1.3.3.1.4. Peroxy Linkage (POL, $\equiv \text{Si} - \text{O} - \text{O} - \text{Si} \equiv$)

The POL, also called “interstitial oxygen”, is composed by two Si atoms bonded by two O atoms (Figure 1.16). It is a diamagnetic center that, on the basis of simulation results, is associated with three absorption bands centered at 3.8 eV (~326 nm), 4.2 eV (~295 nm) and between 7.3 (~166 nm) and 7.5 eV (~165 nm) [15].

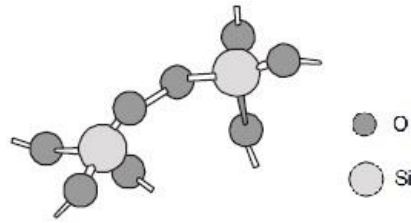
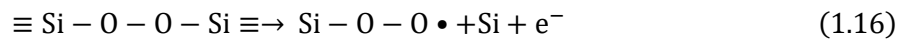


Figure 1.16. POL defect structure. Taken from [89].

1.3.3.1.5. Peroxy Radical (POR, $\equiv \text{Si} - \text{O} - \text{O} \bullet$)

The POR, which structure is shown in Figure 1.17, consists of a Si atom bonded to an O molecule and it is a paramagnetic defect [88], [93], [94]. It can be generated both during the OF drawing process or irradiation by the same processes, described below:

- from a POL:



- by the interaction of an E' center with an O₂ molecule:



- by the recombination of NBOHC centers with an oxygen atom:



Absorption bands centered at 7.6 eV (~163 nm), 4.77 eV (~260 nm) and 2 eV (~620 nm) are associated to the POR centers [15].

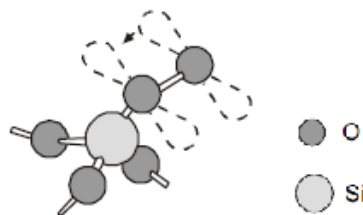


Figure 1.17. POR defect structure. Taken from [89].

1.3.3.1.6. Non-Bridging Oxygen Hole Center (NBOHC, $\equiv \text{Si} - \text{O} \bullet$)

The NBOHC center is a paramagnetic defect constituted of an O atom having a single bond with a Si atom and a hole on a 2p orbital, as identified by its EPR signal in [88], [93]. The NBOHC structure is shown in Figure 1.18.

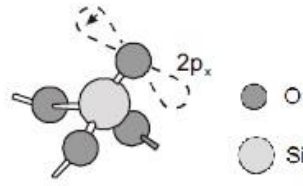
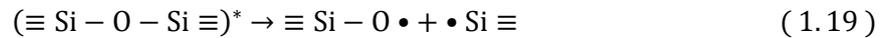


Figure 1.18. Atomic structure of the NBOHC defect. Taken from [89].

NBOHCs can be generated during the optical fiber drawing process and/or by radiations:

- by breaking strained Si-O bonds:



- by breaking network-bound hydroxyl groups $\equiv \text{Si} - \text{OH}$, a process that results more or less efficient depending on OH-groups concentration in the material:



- from a POL:



NBOHCs absorption dominates the visible and near-UV spectral region. To them are related different absorption bands: one centered around 2 eV (~620 nm) and characterized by an asymmetric shape and two other absorption bands at 4.5 eV (~275 nm) and 7.5 eV (~165 nm). Furthermore, concerning the 2 eV centered NBOHC absorption band, it has been demonstrated by Morana et al. [95] that it can be described by the sum of three gaussian bands centered at 1.95 eV (~636 nm), 2.04 eV (~608 nm) and 2.21 eV (~561 nm) with a fixed relative amplitude ratio.

1.3.3.1.7. Self-Trapped Holes (STH)

Depending on the irradiation conditions, STHs can represent one of the main contribution concerning the optical absorption of pure-silica core OFs [15]. Being paramagnetic defects, in [96] with EPR measurements Griscom has been able to distinguish two different types: the STH_1 , made of a hole positioned over a non-bonding p-orbital of a single bridging O atom (Figure 1.19a), and the STH_2 , which consists of a hole on non-bonded p-orbitals of two adjacent bridging O atoms forming the same SiO_4 tetrahedron (Figure 1.19b). The STH_1 is responsible of a broad (FWHM~1.2 eV) absorption band centered at 2.61 eV (~475 nm), while

the STH_2 generates an absorption band peaked at 2.16 eV (~574 nm). Strained Si-O-Si bonds have been supposed to be STHs precursors. In addition, STHs are characterized by a metastable nature and are not stable at room temperature, which allows them to quickly recombine after the end of an irradiation.

A singular feature of these two point defects lies in the fact that their stretched variants have been observed in optical fibers: the strain-assisted (s-a) STH_1 and strain-assisted STH_2 , having absorption bands centered at 1.88 eV (~660 nm) and 1.63 eV (~760 nm), respectively [98]–[100].

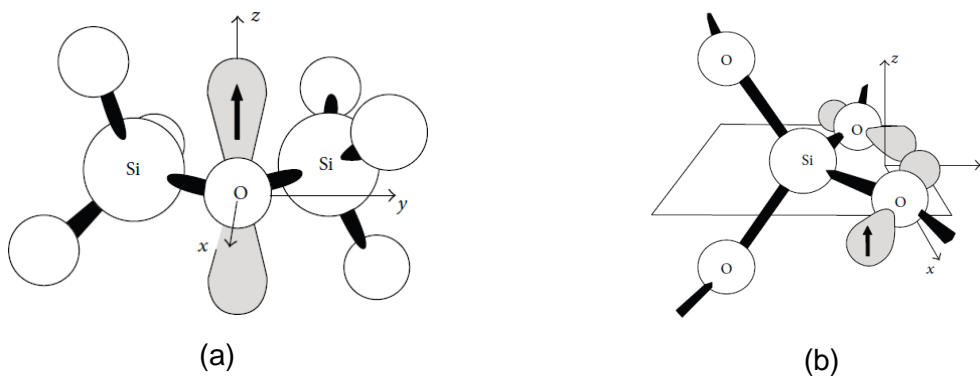


Figure 1.19 Models of self-trapped holes (STH): STH_1 (a) and STH_2 (b). The shaded orbitals represent the ones of the unpaired electron spins (denoted by vertical arrows). Figure taken from [97].

1.3.3.2. Pure silica: extrinsic point defects

1.3.3.2.1. Hydroxyl (OH) groups

The presence of hydrogen in pure or doped silica is difficult to avoid, since traces of hydrogen are present in the synthesis environment (in the raw substances or in the reagents used) and also because it has a very high capacity to diffuse into the silica (i.e. from the external “contaminated” region towards the OF core). Hydrogen enables the formation of OH groups, leading to absorption losses caused mainly by the excitation of the vibrational modes of OH groups.

In the case of Si-OH groups, the fundamental absorption band is peaked at a wavelength of 2.73 μm , whereas its first and second harmonics are peaked at 1.38 μm and 0.95 μm , respectively. In addition, coupling effects with the vibrational modes inherent to the silica matrix are responsible of several supplementary absorption bands. In Table 1.1 are listed the spectral positions and the absorptivity of the various principal and supplementary absorption bands along with corresponding vibrational mode (corresponding literature studies: [101]–[107]).

The vibrational overtones, in particular the first one (peaked at 1.38 μm), are of practical importance when it comes to OF transmission because they give rise to significative losses in the NIR domain, precluding their deployment in this spectral region. The impact of this particular absorption band can be easily calculated: less than 0.01 ppm_w of OH are enough to duplicate the OF losses at 1.38 μm .

Table 1.1 Peak wavelength, absorptivity and associated vibrational modes of the absorption bands related to OH overtones. Adapted from [2].

Optical absorption band peak [μm]	Absorptivity [$\text{dB km}^{-1} \text{ppm}_{\text{wOH}}^{-1}$]	Vibrational mode assignment
2.72	6000 – 10000	$\nu_3^1[\text{SiO-H}]$
2.22	160 – 260	$\nu_3^1[\text{SiO-H}] + \nu_1[\text{SiO}_4]$
1.90	6.2 – 10	$\nu_3^1[\text{SiO-H}] + 2\nu_1[\text{SiO}_4]$
1.38	30 – 80	$2\nu_3^1[\text{SiO-H}]$
1.24	1.7 – 3	$2\nu_3^1[\text{SiO-H}] + \nu_1[\text{SiO}_4]$
1.12	0.05 – 0.1	$2\nu_3^1[\text{SiO-H}] + 2\nu_1[\text{SiO}_4]$
1.03	~0.006	$2\nu_3^1[\text{SiO-H}] + 3\nu_1[\text{SiO}_4]$
0.95	0.6 – 2	$3\nu_3^1[\text{SiO-H}]$

1.3.3.2.2. Cl-related defects

As already reported in section 1.2.1, during the OF preform manufacturing process the gases, that constitutes the raw substances needed to synthetize the silica, are introduced in the form of chlorides. As a consequence, chlorine is the main impurity leftover in the silica matrix and gives rise to chlorine-related point defects, in particular the Cl^0 and Cl_2 centers [15]. The Cl^0 defect is paramagnetic and is characterized by a very large (FWHM=1.2 eV) optical absorption band peaked at 3.26 eV (~380 nm), whereas the Cl_2 is diamagnetic and its absorption band is centered at 3.78 eV (~328 nm), with a FWHM of 0.6 eV.

1.3.3.2.3. Doping-related point defects

As far as concerns OFs, dopants are combined to silica during the manufacturing process in order to change its refractive index profile. In this section, we will focus on point defects related to Germanium, Phosphorus, Aluminum, as these are the main dopants of optical fibers considered in the framework of this thesis.

Germanium

Concerning Ge-doped silica OFs, it has been demonstrated that the generation of Ge-related point defects is more significant compared to the silica-related ones, which are still present but have a minor contribution in terms of signal attenuation. Germanium, belonging to the same column of silicon in the periodic table, has the same number of valence electrons and so it can substitute the silicon atom in the atomic network of the material, creating the same bonds with the surrounding oxygen atoms. For this reason, in germanosilicate OFs is possible to find defects that are analogous to the ones already existing in pure silica fibers but with a substitutional germanium atom occupying the silicon slot, this is the case of the Ge-NBOHC and GeE'.

Germanium Lone Pair Centers (GLPC) are the germanosilicate-analogous of ODC(II) and, therefore, are constituted by a two-fold coordinated Ge atom [108]. As the ODC(II), GLPCs are diamagnetic defects. GLPCs are characterized by three different optical absorption bands, centered at 3.7 eV (~335 nm), 5.2 eV (~238 nm) and 6.8 eV (~182 nm) [20]. OFs sensitivity and properties during irradiation are strictly associated to GLPC concentration, as this class of defects (observed in pristine optical fibers and preforms[109], [110]) behave as precursor sites for the Ge(1) and Ge(2) defects [111], [112].

Ge(1), Ge(2) and GeE' are paramagnetic radiation-induced point defects that are already well documented in literature and characterized by absorption bands peaked at 4.4 eV (~282 nm), 5.8 eV (~214 nm) and 6.2 eV (200 nm), respectively [15], [20], [108], [113], [114]. While the GeE' center is structurally identical to the SiE', with the only difference of having a substitutional Ge atom occupying the silicon slot [113], [115], the Ge(1) defects consist of an unpaired electron trapped on four-fold coordinated Ge atom [113], as identified by EPR measurements in [116]. As far as concerns the Ge(2) point defect, Griscom described it as a variant of the Ge(1) [113], however recent simulation results indicate that this defect is a particular variant of E' defect [115].

Since RIA in OFs is usually evaluated in the 400-2000 nm range, the GeE' and Ge(2) defects have no significant contribution, as their absorption bands are peaked at much shorter wavelengths. The visible-RIA is almost entirely explained by the combination of absorption bands related to Ge(1), Ge-NBOHC and GeX, this one being a point defect absorbing around 2.61 eV (~475 nm) which atomic structure is still unknown [108], [117]. Studies on the irradiation temperature effects in the UV-visible domain report a RIA decrease, with the increasing temperature, at wavelengths shorter than 470 nm (region where the Ge(1) and GeX are the main responsible for the absorption) and almost no effect at longer wavelengths, where the GeX contributes more [36], [118]. This lets us suppose that is the Ge(1) concentration that decreases by increasing the irradiation temperature, as it was confirmed by post-irradiation

EPR measurements [118]. Moreover, it has been reported that, at low doses the temperature is ineffective, becoming relevant at higher irradiation doses (i.e. longer heating periods) [36].

As far as concerns the NIR domain, two classes of point defect have been identified as the major contributors to the RIA: the GeY, absorbing at 1.38 eV (~900 nm) and which structure is still unknown [38], and the Ge-STH, absorbing at 0.54 eV (~2296 nm) [119]. However, these two point defects are not sufficient to fully reproduce the steady-state NIR-RIA, indicating that some other attenuation contributions in this domain are still missing [120]. Contrary to the steady-state irradiation case, the RIA of Ge-doped OFs exposed to pulsed irradiation is fully explained by the existing aforementioned point defects and the introduction of a “transient defect” (TD), characterized by a broad absorption band peaked at 3.26 eV (~380 nm) with a 1.4 eV FWHM [15], [121], [122].

A linear correlation between the decay kinetics of the GeX and GeY has been observed under pulsed X-ray irradiations at both RT and liquid nitrogen temperature [122], suggesting that the two defects could be generated from the same precursor site and could also recombine together, or that the two absorption bands could be related to the same defect structure. However, recently, Kashaykin et al. demonstrated that the RIA temperature dependences for light and heavy Ge-doped OFs are different [38]. In particular, OFs with a high (>19 mol%) GeO₂ concentration in the core exhibited a RIA increase with the increasing temperature at wavelengths shorter than 1300 nm, due to an increase of the GeX point defect associated with a thermal decay of the Ge(1) center [108]. The GeY colour center proved to have a different dependence with respect to the irradiation temperature and Ge-content from the GeX: its concentration decreases when the temperature and the Ge-doping increases. While for heavily-doped OFs the absorption due to the GeY defect is marginal, for lightly doped OFs, such as those used for telecommunications (as the Corning SMF-28, with a GeO₂ doping of about 3.5 mol% in the core), the GeY-related absorption band is one of the main contributors to the RIA at the telecommunication wavelengths.

Phosphorus

It has been demonstrated that, before irradiation, P-doped OFs exhibit lower attenuation in the UV domain than their Ge-doped counterpart, for this reason they are deployed in applications operating below 400 nm, as LMJ diagnostic [121], [123], [124]. As far as concerns their RIA, a pioneer study conducted by Griscom [39] reported that, in the visible and NIR range, the absorption is due to a variety of radiation-induced point defects: the phosphorus-oxygen hole centers (POHCs), which can be stable or metastable depending on their thermal dependence, and the P1, P2 and P4 centers.

The P1, P2 and P4 centers correspond to a P atom bonded to 3, 4 or 2 O atoms, respectively, with absorption bands peaked at 0.79 eV (~1570 nm), 4.5 eV (~275 nm) and 4.8

eV (~258 nm). Metastable and stable POHCs consist of an unpaired electron located on a non-bridging O atom (absorption band peaking at 2.2 eV and 2.5 eV), or shared by two non-bridging O atoms (absorption band peaking at 5.3 eV and 3.1 eV), respectively. The structures of the aforementioned defects, as well as their corresponding precursor sites, are shown in Figure 1.20.

However, if the knowledge on the defects causing the visible RIA is adequate, the single P1 center is still not sufficient to explain all the losses in the NIR domain [15].

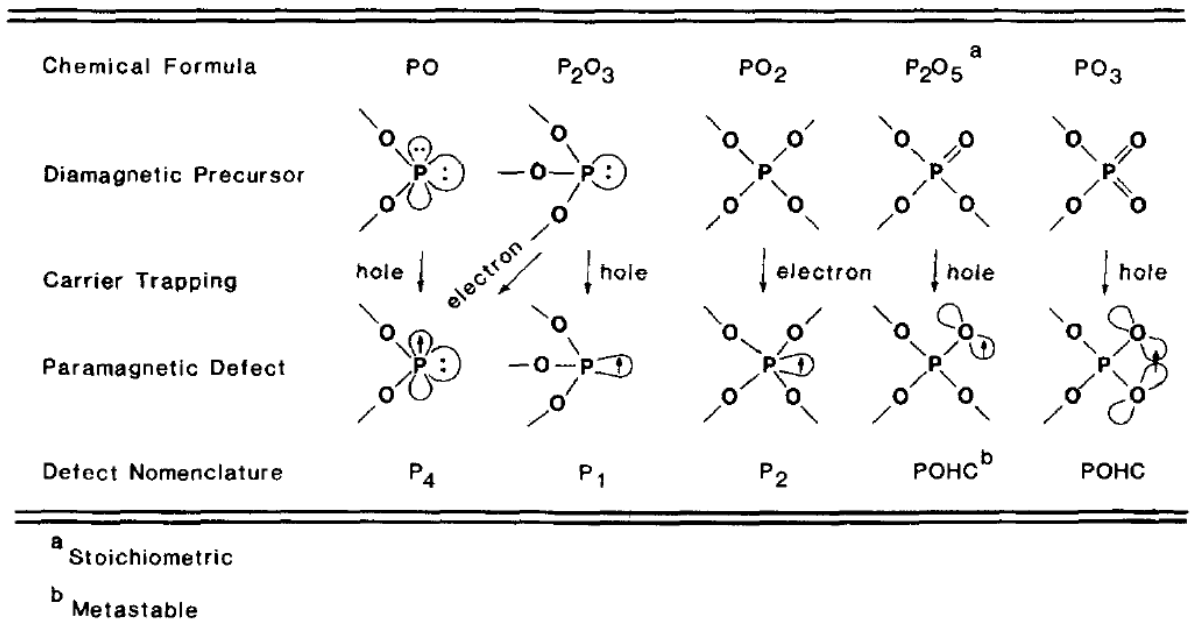


Figure 1.20 Summary of radiation-induced point defects in P-doped silica. Taken from [39].

From literature, it is well established that phosphosilicate OFs exhibit a significantly higher radiation sensitivity than most of other doped OFs [15], [20]. This feature, combined with the fact that at room temperature the P1 defect is not thermal- or photo-bleached (with an infrared probing signal) after the end of the irradiation, make phosphosilicate fibers suitable for dosimetry applications [12], [50], [125], [126]. In addition, P-doped silica can be used as host matrix for active optical fibers, in order to increase rare-earth concentration preventing rare-earth clusters.

With regard to the combined effects of temperature and radiation on P-doped OFs, several interesting insights can be found in literature. During steady-state irradiation, it was observed that the shape of the NIR RIA spectrum remains unchanged when measured at RT and at the liquid nitrogen temperature (LNT), suggesting a similar P1 defect generation at the two temperatures [127]. On the contrary, the RIA in the visible domain at the same temperatures changes significantly, revealing an increase of the s-POHC and m-POHC

contribution at LNT. Furthermore, a completely different RIA shape was observed after the exposition to pulsed X-rays [120]. For temperatures higher than RT, it was reported that the relative concentrations of defects change with the irradiation temperature but, in any case, no new band or no total bleaching of those observed at RT has been reported [36]. The same study shows that m-POHC contribution increases with the increasing temperature up to 150°C, then decreases at higher T. This result agrees with the definition of m-POHC defects, which are already considered unstable with temperature. In addition, EPR measurements confirmed the concentration decrease of m-POHC in samples irradiated at high temperatures [128]. A small increase in the UV/vis RIA when increasing the temperature up to 100°C has been also reported in [128]. In addition, the RIA shape at wavelengths lower than 300 nm is not affected by the temperature at least up to 200°C, after which RIA begins to decrease at higher temperatures. At 650 nm, it was reported that RIA is only slightly affected by the temperature (up to 300°C), demonstrating that only high-temperature stable POHCs contribute to the RIA at this wavelength.

As far as the NIR spectral domain is concerned, the effect of irradiation temperature has highlighted an increase of the P1 defect concentration for temperature higher than 100°C [128]. This phenomenon is nowadays reliably attributed to a conversion process of POHC into P1 centers [39], and it is also possible to observe in the 1550 nm recovery kinetics of P-doped OFs.

Aluminium

Even though the understanding of Al-related point defects responsible for the RIA in the UV-visible domain is adequate, still a significant amount of effort needs to be done to clarify the origin of the absorption of this type of OFs in the NIR region, where most of today's technologies operate. It has been proven in literature that, in the NIR range of spectrum, Al-doped OFs are the most sensitive in terms of RIA [129]–[131], making them very attractive for detecting low radiation dose levels. Furthermore, the aluminosilicate OFs potential use relies on the linear growth of the RIA levels as a function of the dose up to ~2 kGy, both in the visible and at telecommunication wavelengths. In particular, literature reports a linear RIA growth at room temperature in the range 0-2 kGy up to 2000 dB/m at 530 nm [76] and up to 8 dB/m at 1550 nm [32]. Moreover, this type of OFs revealed no dependence of the RIA on the Al-content (within 2 and 4.5 wt% range), core size, drawing parameters, preform deposition processes and dose-rate [32], [76].

It is worth pointing out also that Aluminium is often used as co-dopant in rare-earth (RE) doped OFs, since it has been demonstrated that it has a key role in the optimization of optical amplifiers performances, by increasing Er solubility and reducing clustering [132], [133].

Chapter 1: Background on optical fibers and radiation effects

Nowadays, the two known Al-related defects are the Al-OHC and the AlE'. The former consists in a hole trapped in an oxygen bridging an Al and a Si atom, responsible for optical absorption bands peaked at a 2.3 eV (539 nm) and 3.2 eV (388 nm) [134]–[136]. The AlE' is analogous to the SiE' defect but with an Al atom at the place of a Si atom, and give rise to an absorption band centred around 4.1 eV (302 nm) [134]. Both Al-OHC and AlE' are paramagnetic centers.

1.4. Thesis objectives

The main purpose of the CERTYF project is to improve the knowledge of basic mechanisms of RIA in silica-based OFs, in particular as regards the combined effect of temperature, radiation and hydrogen loading. The motivation is to reach a level of physical understanding allowing to design well-justified models that will be validated against accelerated and sequential tests before being used to achieve proper extrapolation of the OF vulnerability in the harsh conditions targeted by ANDRA, in particular when it comes to the optimization of radioactive dismantling waste's management.

The main objective of the present thesis is to increase the understanding of the role of radiation, temperature, fiber composition and other parameters on the RIA of OFs.

The thesis is organised as follows:

- chapter 2 reports the materials and methods used for the characterization of the OFs under test;
- chapter 3 focuses on the results obtained on radiation-sensitive OFs. The comparison of the RIAs measured at different TIDs and irradiation temperatures in CERTYF samples and in a set of commercially available counterparts containing the same dopants is reported. In addition, dedicated studies on the spectral features of the P- and Al-doped CERTYF samples are proposed;
- chapter 4 covers experiments conducted on germanosilicate OFs, including results on the effects of the probing light power and irradiation temperature at the telecom wavelengths obtained on commercial and CERTYF samples, as well as a dedicated study on the variation of the spectral RIA with respect to the irradiation temperature;
- chapter 5 deals with radiation-hardened OFs and, in particular, reports results based on the impact of the OH-group content on the RIA.

As far as concerns the impact of investigation parameters on the measured RIAs, Table 1.2 reports a more complete picture of what is required by the CERTYF project and what has been done in the framework of this thesis.

Table 1.2 Comparison of what expected from the CERTYF project and what has been done in the framework of the present thesis on the impact of the various impacting parameters on the measured RIA of OFs.

Parameters affecting the RIA	Objectives of study in the framework of the CERTYF project	Study carried out in this thesis
Wavelength (energy range)	NIR, as the main applications targeted by Andra (data transfer, fiber sensing, dosimetry) are focused in this spectral domain.	UV/VIS and NIR: for our experiments, we focused mainly on the NIR domain. Although, in some studies we extended the investigation to the UV/vis domain for a

Chapter 1: Background on optical fibers and radiation effects

		better comprehension of the physical phenomena underlying certain observed results.
Nature of particles	x-rays and γ-rays.	This thesis reports only results concerning x-rays irradiations. This is not a limitation since, as will be shown, γ - and x-ray irradiations give rise to the same RIA kinetics in OFs. We plan to publish results coming from γ -irradiations (at IRMA facility in Saclay, France) in future works, since some interesting phenomena have been observed.
TIDs	From few to ~100 kGy .	Depending on the investigation and, especially, on the class of the OF, we varied the attained TID range from some hundreds of Gy, to kGy and some MGy levels.
Temperature	From RT to 300°C .	All our investigations include the temperature range envisaged by the CERTYF project. In addition, for Ge- and P-doped OFs, temperature ranges below RT (down to -100°C) were also investigated.
Injected light power	Not defined	A dedicated study on the effect of the probing light power (from few nW to ~mW levels) on the RIA of Ge-doped OFs has been carried out.
Manufacturing processes	MCVD	MCVD
Impurities	Not defined	A dedicated study on how the OH-groups content affects the RIA of PSC MM OFs has been carried out.
H ₂ effect	From 0 to fiber saturation with H ₂ .	Chapter 5 reports the results obtained on a PSC OF subjected to a hydrogen loading treatment before the irradiation. However, in the course of the present thesis we did not focus too much on this aspect since, as already reported in literature, the use of carbon-coated OFs solve the problem of hydrogen diffusion within the OF.
OF composition	Radiation-sensitive, telecom-grade and radiation-hardened OFs.	In the context of this thesis, RIA investigations on all three classes of OFs were carried out. In particular, chapters 3, 4 and 5 report the results obtained on radiation-sensitive, telecom-grade and radiation-hardened OFs.

Chapter 2: Samples and experimental setups

In the first part of this second chapter we introduce all the OFs investigated in this PhD thesis manuscript. We first describe the CERTYF samples manufactured at INPHYNI lab for this project in terms of their main geometric and optical characteristics. We then discuss some of their commercial-off-the-shelf (COTS) available counterparts, with comparable composition but made for the Telecom or sensor markets. During the course of the thesis, the performances of both OF classes will be compared, to see how the results on the CERTYF OFs can be extrapolated to COTS OFs. The second part of this chapter deals with the descriptions of the facilities used for the irradiations and the associated instruments used for controlling the irradiation temperature. Finally, the various methods for the characterization and the spectral decomposition of the RIA are discussed.

2.1. The CERTYF methodology

As already mentioned in the introduction, the aim of the CERTYF project is to gain a better understanding on the combined effects of radiation, temperature and hydrogen on OFs and, more generally, on silica-based materials. The project made it possible to work on the material production scale (thus providing a clear overview on the composition and properties of the samples) other than the experimental procedure used for its optical characterization. As a result, the acquired knowledge will be used to better quantify the vulnerability of an OF,

exposed to a complex environment, for a given application. Some practical examples where the acquired information could be exploited are:

- the design of radiation-hardened OFs able to operate in radioactive waste storage facilities (such as CIGEO) mostly for sensing applications;
- the design of radiation-tolerant OFs used for data-link communications;
- the design of radiation-sensitive OFs that can be used into the field of the radiation detection and/or dosimetry.

To this end, a variety of samples representing the three main class of OFs (radiation-hardened, radiation-tolerant and radiation-sensitive) was provided by the INPHYNI laboratory. Being these samples manufactured by one of the CERTYF consortium partner, their characteristics are fully known. Furthermore, in parallel to CERTYF samples, a set of OFs from various other manufacturers (including iXblue [137], Corning [138], Samsung [139]) were also tested in our investigations, in such a way to make comparison of their performances with the ones of CERTYF OFs.

2.2. OFs used for the investigation

2.2.1. CERTYF samples

Table 2.1 lists the main geometrical and optical characteristics of some of the samples provided by the INPHYNI laboratory² that were tested during this thesis and that will be discussed in details in this manuscript. The core-cladding refractive index contrasts and cut-off wavelengths reported in the table were measured at the INPHYNI laboratory [7], while the core/cladding dopant concentrations were obtained from energy dispersive X-ray measurements (EDX) carried out at the Nova Gorica University (Slovenia).

Table 2.1 List of the CERTYF samples provided by the INPHYNI laboratory that are discussed in this thesis. Their main composition, geometrical and optical characteristics are listed.

INPHYNI identification code	Dopants		Core diameter [μm]	Dopant concentration [wt%]	Δn	λ_c [nm]
	Core	Cladding				
Q07-01	Ge	P	5	3.5 Ge / 1.2 P	3.3×10^{-3}	~1160
R27-03	Ge	none	5.9	9 Ge ¹	8.3×10^{-3}	~1130
K04-01	Al	none	11.3	2 Al	4.8×10^{-3}	~1490
L28-01	P	none	8.9	4.5 P	$3-4 \times 10^{-3}$	~1150

¹The concentration value was estimated from the refractive index contrast, under the assumption that no impurity or other dopant is present in the core region.

² In the framework of the CERTYF project, much more samples have been produced and characterized, but it was not possible to incorporate all the results in this manuscript.

All the samples have an acrylate coating. Moreover, as it can be observed from the table, all the considered OFs are single-mode in the IR region, for wavelengths longer than ~ 1100 nm (except for the Al-doped OF). As far as concerns the GeP-doped sample, the Ge-doped core (~ 5 μm diameter) is surrounded by an outer layer (~ 3.3 μm thick), where the P-doping is incorporated. In Figure 2.1 the doped OF regions of the GeP-, Al- and P-doped CERTYF samples are highlighted and their corresponding dopant concentration profiles are shown. Finally, the results of chemical analysis from EDX revealed traces of chlorine (concentration ~ 0.1 at%) homogeneously distributed in the cross section of all samples.

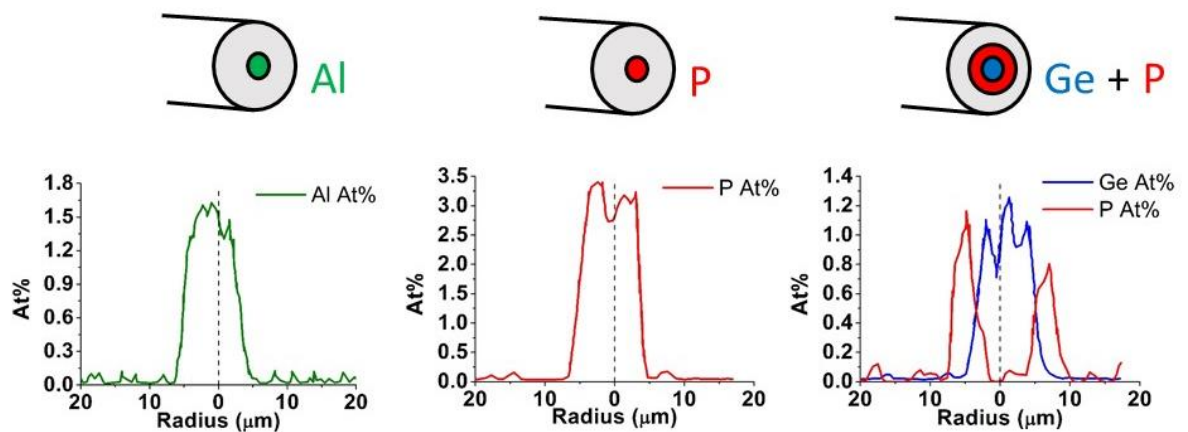


Figure 2.1 Dopant concentration profiles of CERTYF OFs doped with Al, P and GeP.

2.2.2. Tested OFs from other manufacturers

2.2.2.1. P-doped samples

Besides the CERTYF sample, two other P-doped OFs were tested, both manufactured by iXblue Photonics through MCVD process and optimized for dosimetry applications. The first one, provided with an acrylate coating, is close to the one implemented at CERN [140]. The second sample, instead, was drawn from a similar preform but under different conditions, with a polyimide coating. Generally, for acrylate-coated OFs the drawing speed and tension are higher than 100 m/min and 200 g, respectively, whereas for their polyimide-coated counterparts these parameters are in the order of 20 m/min and 50 g. As far as concerns the composition, both samples have a P-doped core, with P concentration of about 10 wt%, and a weak fluorine doping at the core/cladding interface, introduced to tailor its light guiding properties. Finally, residual Cl impurities have been detected in the order of 0.2 wt% and are homogeneously distributed along the OF cross section. The effect of such different manufacturing parameters on the OF refractive index profile will be illustrated in Chapter 3. As far as concerns the acrylate-coated sample, in [129], the influence of the modal propagation

on its NIR RIA has been discussed, with the assumption of the P1 point defects being homogeneously distributed in the OF core.

Table 2.2 Main geometrical and optical characteristics of the two iXblue P-doped OFs.

OF coating	Dopants		Core diameter [μm]	Dopant concentration [wt%]	Δn	λ_c [nm]	Losses @1550 nm [dB/km]
	Core	Cladding					
Acrylate	P	F	6	10 P	1×10^{-2}	~1120	2
Polyimide	P	F	9	10 P	8.3×10^{-3}	1250	1.85

2.2.2.2. Al-doped sample

The Al-doped sample considered for our measurements is manufactured by iXblue Photonics and is constituted by an Al-doped core, a pure silica cladding and an acrylate coating with diameters of ~6.6 μm , 125 μm and 250 μm , respectively. It is single-mode in the IR spectral region, its cut-off wavelength being at 1226 nm. The dopant concentration in the core was not declared by the manufacturer. Table 2.3 reports the main known characteristics of this sample.

Table 2.3 Geometrical and optical parameters of the iXblue Al-doped OF.

Dopants		Core diameter [μm]	Dopant concentration [wt%]	Δn	λ_c [nm]	Losses @1550 nm [dB/km]
Core	Cladding					
Al	none	6.7	--	--	1226	7.2

2.2.2.3. Ge-doped sample

Two commercially available Ge-doped OFs have been tested during the thesis. The first one is the Corning SMF-28e⁺, the enhanced version of the standard SMF-28, a long-standing industry benchmark for telecommunication in the 1.3-1.5 μm wavelength region. The SMF-28e⁺ presents very low losses at the telecom wavelength, in particular 0.34 dB/km at 1310 nm and 0.20 dB/km at 1550 nm, both values affected by a maximum of 0.05 dB/km variation in the -60°C / +85°C temperature range. Furthermore, this fiber has a refractive index contrast of 5.3×10^{-3} at 1550 nm and core/cladding diameters of 8.2 μm /125 μm . More information can be found in the OF datasheet [141].

The second tested sample is a canonical MM OF, manufactured by iXblue Photonics. It is composed by a double-core Ge-doped region, a pure-silica cladding and a polyimide coating.

A summary of the OFs characteristics is proposed in Table 2.4.

Table 2.4 Main geometrical and optical characteristics of the Ge-doped OFs.

OF name	Dopants		Coating	Core diameter [μm]	Dopant concentration [wt%]	Δn	λ_c [nm]	Losses @1550 nm [dB/km]
	Core	Cladding						
Corning SMF-28e ⁺	Ge	none	acrylate	8.2	4 Ge	10×10^{-3}	1260	≤ 0.2
Canonical MM	Ge	none	polyimide	42.5	6 Ge ¹	9×10^{-3}	--	5
				61.5	3 Ge ¹	4×10^{-3}		

¹The concentration value was estimated from the refractive index contrast, under the assumption that no impurity or other dopant is present in the core region.

2.2.2.4. GeP-doped sample

The commercial GeP-doped sample was manufactured by Samsung and, similarly to the CERTYF sample, is composed by Ge-doped core region (diameter 9.3 μm) surrounded by a ~ 3 μm thick P-doped region in the cladding (~ 125 μm) and an acrylate coating (~ 250 μm). The sample is SM in the NIR domain. Information about this sample is summarized in Table 2.5.

Table 2.5 Main geometrical and optical characteristics of the commercial GeP-doped sample.

Core	Dopants		Coating	Core diameter [μm]	Dopant concentration [wt%]	Δn	λ_c [nm]	Losses @1550 nm [dB/km]
	Cladding							
GeP	none		acrylate	~ 13	--	--	--	~ 2.5

2.2.2.5. Pure-silica core samples

Three different multi-mode OFs with pure-silica cores, F-doped cladding and polyimide coatings were drawn by iXblue from three distinct preforms characterized by different contents of OH-groups bonded to the silica network (Si-OH). The OH content was of 0.41 ppm (derived by the attenuation peak at 1385 nm), 27 ppm and 873 ppm (from the peak at 1240 nm). In the present thesis, these OFs will be referred to as *low*-, *medium*- and *high*-OH, respectively. The spectral overall losses of the three pristine samples, obtained by cut-back measurements (see section 2.5.4), are shown in Figure 2.2. Each sample has a numerical aperture of 0.22 and a diameter of 125 μm for the cladding and 250 μm for the coating, while the core diameter is 105 μm for the *low*- and *high*-OH samples, and 112 μm for the *medium*-OH one. Table 2.6 summarises the main characteristics of the three OFs.

As already said in section 1.3.2.8, the OH groups concentration affects the transmission properties due to the fundamental OH absorption band at 2.72 μm and its corresponding overtones, whose major absorption peaks are located at 1.38 μm and 0.94 μm . It is known from literature that, as far as the 0.94 μm overtone, the OH content affects the attenuation in the order of 1-2 dB km⁻¹ ppm⁻¹ [142]–[145]. Furthermore, in Figure 2.2 it is possible to observe

the absorption band centered at 630 nm due to DID NBOHCs [15] for both the *low*- and *medium*-OH OFs. This band is absent in the *high*-OH sample due to the excess of hydrogen atoms that passivate these defects.

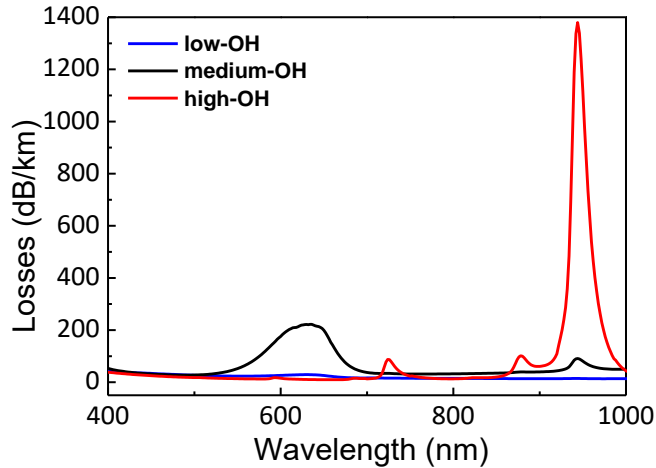


Figure 2.2 Spectral losses of the three PSC MM OFs, obtained by cut-back measurements.

Table 2.6 Geometrical characteristics and information about the OH content of the three PSC MM OFs.

Sample	Core diameter [μm]	Cladding / Coating diameters [μm]	OH content ¹ [ppm]
<i>low</i> -OH	105		0.41
<i>medium</i> -OH	112	125 / 150	27
<i>high</i> -OH	105		873

¹ Derived at 1385 nm for the *low*-OH sample and at 1240 nm for the *medium* and *high*-OH samples.

2.3. Irradiation tools

In this thesis, all accumulated doses and dose-rates will be expressed in Gy(SiO₂).

2.3.1. X-ray irradiators: MoperiX, LabHX

X-ray irradiation tests have been performed at the Hubert Curien laboratory (LabHC) with the two irradiation machines managed by the Mopere group: the MoperiX and the LabHX. Both facilities, illustrated in Figure 2.3, feature similar X-ray tubes having a tungsten target (inclined at a 30° angle to the incident electron beam) and an inherent filtration (4 mm and 2 mm of Beryllium, respectively for the LabHX and the MoperiX) that enables to eliminate low-energy photons. All the results reported in this thesis have been obtained supplying the tube with 100 kV. Under this condition, the tubes generate photons, whose spectrum is shown in Figure 2.4 and with mean energy ~40 keV.



Figure 2.3 X-ray machines utilized for the irradiation tests: **a)** MoperiX (taken from [146]) and **b)** LabHX.

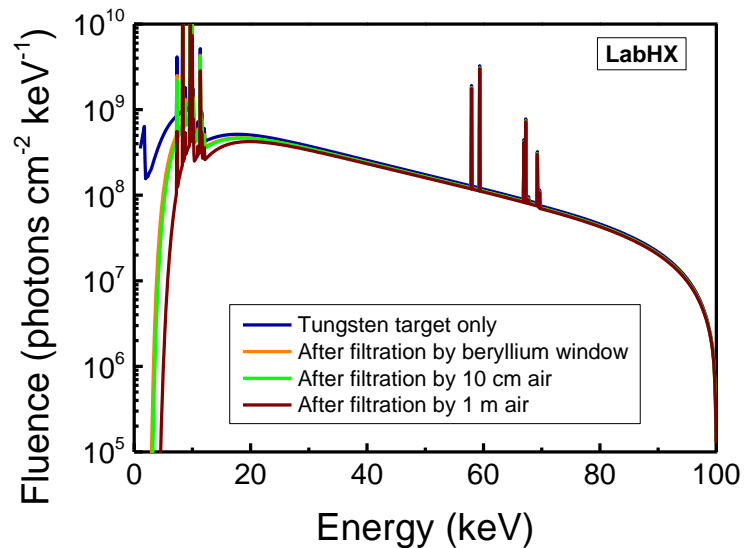


Figure 2.4 Expected X-ray spectrum generated by the tubes in our operating conditions (simulation conducted with Spekpy [147], [148]).

The broad band highlighted in Figure 2.4 is due to the “braking” of electrons accelerated by the 100 kV voltage, when entering into the tungsten target. This phenomenon is known as Bremsstrahlung. The peaks, instead, are due to electron transitions typical of the tungsten target. Indeed, the incident X-ray radiation enables a core electron of the atom to be ejected, leaving a vacancy in the inner-shell. As a consequence, another electron from a higher energy level can fill the vacancy, resulting in a release of energy. The described process is shown in Figure 2.5.

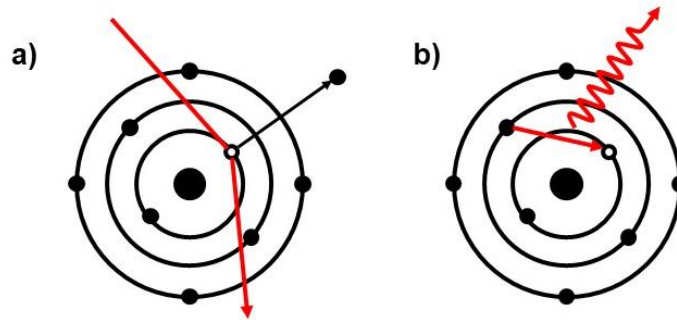


Figure 2.5 a) The incident radiation collides with an electron in the 1s level, creating a vacancy. **b)** An electron from the 2s level fills the vacancy, releasing radiative energy.

The dose-rate of the performed irradiation is changed either by changing the distance between the samples and the X-ray tube, either by modifying the tube current. The total accumulated dose (TID) is controlled by the exposure time. It is worth noticing that the dosimetry for all tests has been conducted with a soft 0.02 cm³ X-rays ionization chamber, with a precision of about 10%.

Since the energy of the X-rays generated under our experimental conditions is less than 100 keV, they may not be able to penetrate thick materials. In this regard, it is possible to determine the portion of X-rays penetrating a specific material by means of the following equation [149]:

$$\frac{I}{I_0} = e^{-\frac{\mu}{\rho}\rho t} \quad (2.1)$$

where I is the X-ray intensity after a thickness t , I_0 the initial intensity, μ/ρ is the mass attenuation coefficient of the material and ρ is its density. Figure 2.6 shows our scenario, where X-rays with 40 keV energy penetrate an OF, composed mainly of pure silica and with an acrylate coating. The parameters values of equation (2.1) were obtained from the NIST website [150] and are reported in Table 2.7.

It is possible to observe that, for a ~125 μm thickness (diameter of most of OFs, without coating), about 98 % of X-rays are penetrating inside the material. In addition, the acrylate coating layer, usually around 62.5 μm thick, allows almost 100% of X-rays to pass through. For all our irradiations, samples have been always spooled in a monolayer spiral, ensuring the beam to invest homogeneously the OF thickness along the entire length (Figure 2.7).

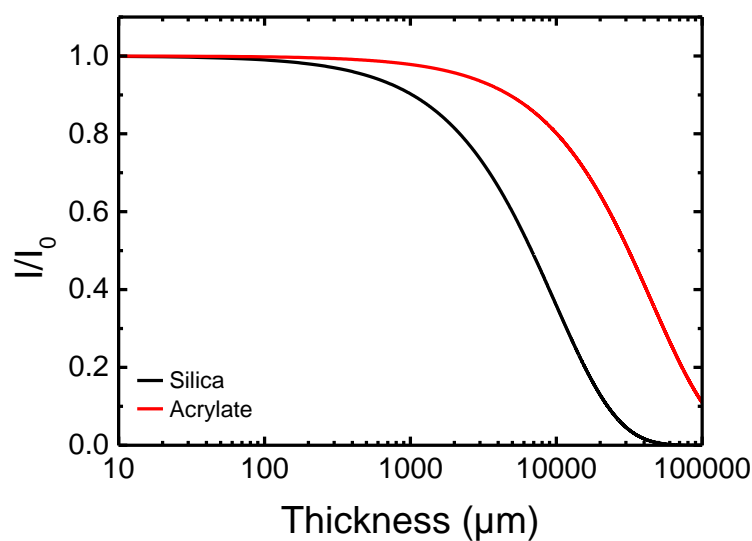


Figure 2.6 X-rays (energy of 40 keV) attenuation as a function of the silica (black curve) or acrylate (red curve) thickness.

Table 2.7 Parameters used for the calculation of the X-rays penetration depth, reported in equation (2.1)

Material	X-ray mass attenuation coefficient ¹ [cm ² g ⁻¹]	Density [g cm ⁻³]
Silica (SiO ₂)	0.465	2.20
Acrylate (C ₅ O ₂ H ₈)	0.235	0.94

¹ Derived for a 40 keV energy X-ray beam.

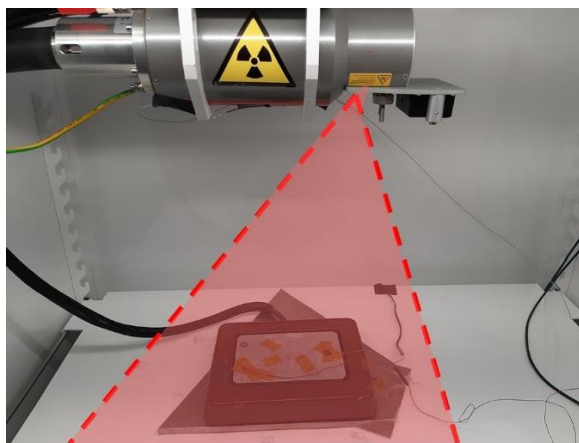


Figure 2.7 X-ray tube (on the top) with a sample placed on a thermal plate (on the bottom). The cone of X-ray generated by the tube is also highlighted.

2.3.2. γ -ray irradiator: IRMA

As far as concerns γ irradiations, these have been carried out at the IRMA facility at the IRSN in Saclay (France), exploiting the radiation produced by four independent ⁶⁰Co cylindrical

sealed sources. When not in use, the sources are stored in a 30 cm thick lead cask and, at the time of irradiation, are extracted one at a time. The facility allows irradiations with dose-rates from 5 $\mu\text{Gy/h}$, which is the background radiation present in the cell when the sources are enclosed in the lead cask, to 25 kGy/h , which is the value obtained at a distance of 10 cm when all the four sources are placed in the holder³. A photo of the irradiation cell entrance and the table where the sources are placed are shown in Figure 2.8.

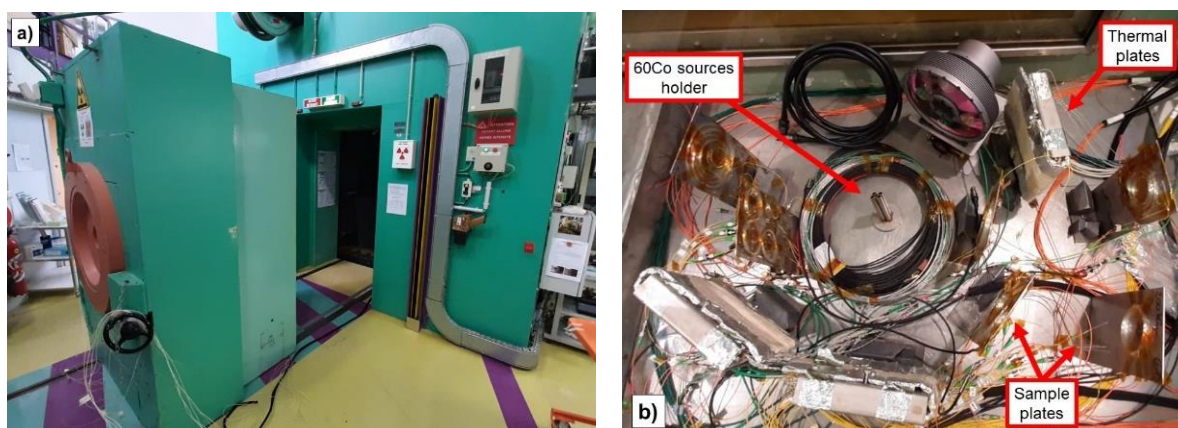


Figure 2.8 IRMA facility at IRSN: **a)** irradiation chamber door and entrance; **b)** top-view of the table where ⁶⁰Co sources and samples are placed.

2.3.3. Controlling the irradiation temperature: thermal plates

In order to control the irradiation temperature, the samples were placed in contact with thermal plates. For our tests, two different plates have been used: the Instec HCP204SC heating/cooling plate, allowing a temperature stability within a range of 0.1°C, and the BT Electronics thermal plate, having an accuracy of $\pm 1\%$ with respect to the selected temperature (Figure 2.9). Furthermore, for all experiments, a thermalization time of ~20 or 30 minutes before starting the irradiation has been always considered.

Since all the irradiated samples were prepared in the form of a monolayer spool and were carefully placed completely in contact with the thermal plate surface, it was possible to assume a homogeneous temperature over the entire sample. For all our experiments, the temperature is constantly monitored by two K-type thermocouples placed on the thermal plate and close to the sample under test.

³ At the time when the CERTYF experiments have been done.

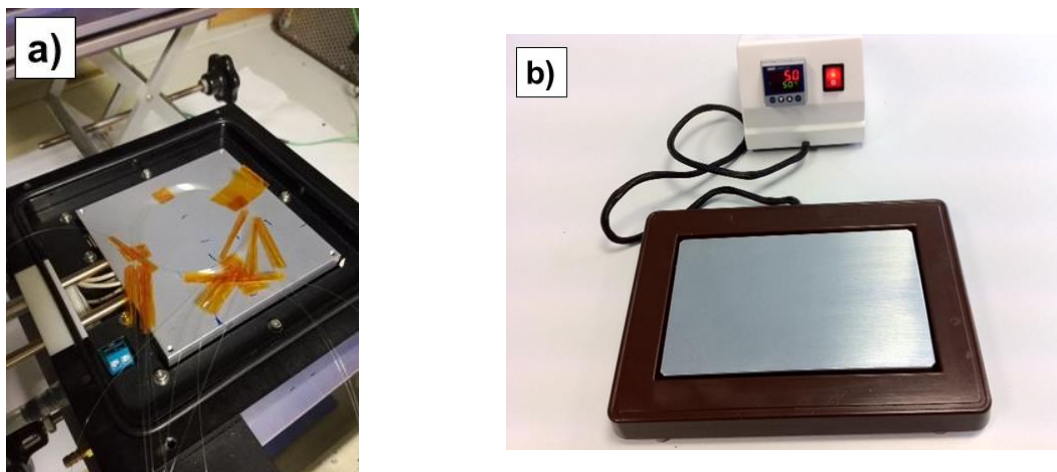


Figure 2.9 Thermal plates used for the studies: **a)** the Instec HCP204SC (with OFs samples placed on top) and **b)** the BT Electronics (photo taken from the datasheet).

2.3.4. OF hydrogenation

For the OFs hydrogenation (see section 1.3.2.9) we used a typical high-pressure reactor, its schematic representation is shown in Figure 2.10. After coiling the fibers on a 5 cm diameter cylinder, this is installed inside the vessel of the reactor, which is properly closed and then loaded with H₂ up to a pressure of 120 bars. In order to accelerate the diffusion process of the gas inside the OF, the reactor temperature can be increased to 60°C by placing an adapted thermal belt around the vessel. In this way, the saturation of the OF core with molecular hydrogen is obtained after a period of ~80 hours. It is worth noticing that, once the gas-loaded sample is removed from the reactor and is placed in the air, the hydrogen that failed to bond with the silica material gradually diffuses out, a process that is promoted with the increase of the temperature [151].

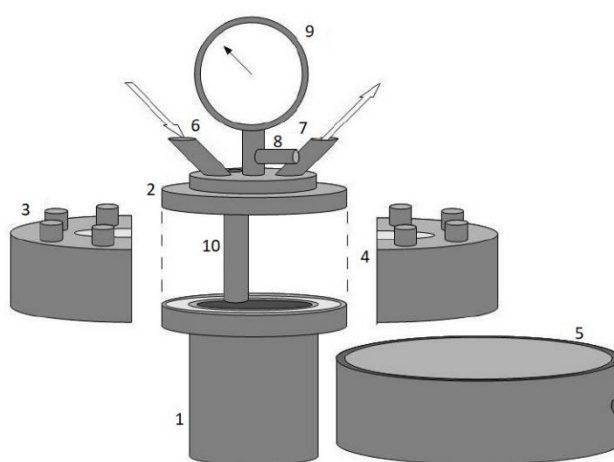


Figure 2.10 Schematic representation of a high-pressure reactor employed for loading the OFs with molecular hydrogen. OFs are coiled and then installed inside the vessel (1), then its cover (2) is properly closed and tightened by two steel half-rings (3 and 4) and an additional safety steel ring (5). Afterwards, the gas input (6) and output (7) valves are used for the gas loading, which pressure can be controlled with the transducer (8) and an analogical pressure gauge (9). In order to monitor the temperature of the reaction, a thermocouple is placed in the well (7).

2.4. X- γ results comparison

In order to check whether the results obtained with the two different types of irradiation are comparable, we plotted on the same graph the online RIA obtained on the two CERTYF radiation-sensitive OFs, the P-doped (L28-01) and Al-doped (K04-01), at telecommunication wavelengths during irradiations performed at 50 Gy/min and RT.

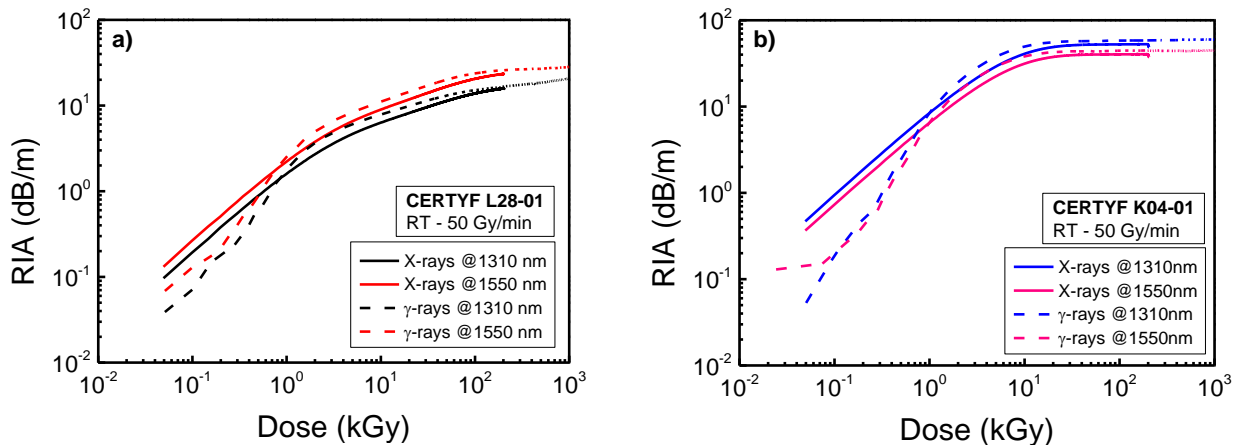


Figure 2.11 Online RIA kinetics as a function of the dose at 1310 nm and 1550 nm for **a)** the CERTYF P-doped and **b)** Al-doped OFs, during an irradiation with X-rays (continuous line) and γ -rays (dashed line). Irradiations have been performed at the same temperature and dose-rate.

From the figure it is possible to observe that both OFs show similar RIA kinetics, with a constant growth slope at low doses and a tendency to reach a saturation value at higher doses. Focusing on the X- γ comparison, one may notice that the γ -rays results present strong RIA fluctuations at low doses. This is due to the extraction time of the four ^{60}Co sources from their lead storage cask. Indeed, the sources are positioned successively and individually in the holder at the center of the table (Figure 2.8), which results in a very unstable dose-rate at the very low doses of irradiation. Once this settling-in time has passed, RIA values at one wavelength are very close for the two irradiation types, showing that the nature of the radiation does not affect the RIA. For this reason, in the present thesis we will mainly show results concerning X-ray irradiations, as these are easier for us to reproduce.

2.5. RIA characterization methods

2.5.1. Spectral/monochromatic transmission measurements

Figure 2.12 shows the experimental setup used for the spectral RIA characterization both in the UV-vis and NIR domain. The samples, one for each spectral region, are placed in contact with the thermal plate inside the irradiation chamber and are connected, via radiation-hardened OFs, to a white light source on one end and to a spectrometer to the other end.

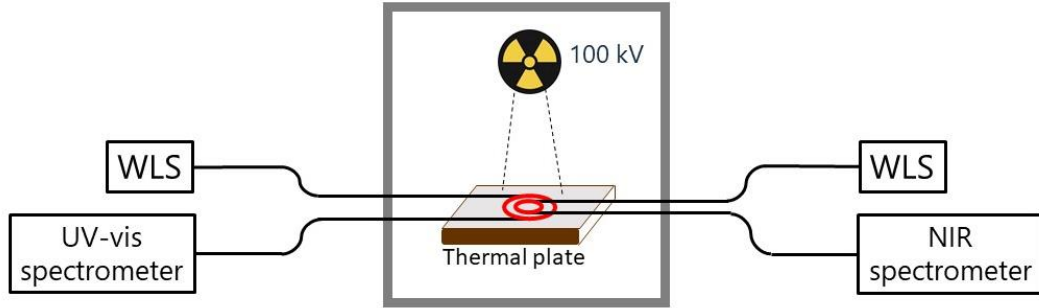


Figure 2.12 Experimental setup used for the spectral RIA characterization in both the UV-vis and NIR domain. The samples (represented in red), one for each spectral domain, are placed in contact with the thermal plate and connected by radiation-hardened OFs to the instruments.

We used the Ocean Optics DH-2000 (deuterium/halogen lamp with average power level of tens of μW) as white light sources, the Ocean Optics QE65000 or Maya 2000 Pro as spectrometers in the UV-vis range, and the Ocean Optics Nirquest as spectrometer in the NIR. This setup makes it possible to perform *in-situ* or “on-line” RIA measurements, allowing to observe not only the defects that are stable at the temperature of the experiments (the ones that could be observed also in post-mortem measurements), but also the transient defects that are unstable or metastable at this temperature. The results are in the form of spectral RIA kinetics as a function of time (or, correspondingly, of the dose). In order to obtain the online RIA spectra, a reference spectrum of the sample (with a known length L) is acquired before the start of the irradiation, then the RIA is calculated as:

$$\text{RIA}(\lambda, t) = -\frac{10}{L} \log_{10} \left(\frac{I(\lambda, t) - I_{\text{noise}}(\lambda)}{I(\lambda, t_0) - I_{\text{noise}}(\lambda)} \right) \quad (2.2)$$

where I represents the intensity of the transmitted spectrum when the light source is on ($I(\lambda, t)$) or off ($I_{\text{noise}}(\lambda)$), t_0 is the time when the irradiation starts, λ and t are the wavelength and the time, respectively.

We performed also monochromatic online RIA measurements. In this case, the white light source is replaced with a laser diode (LD) and the spectrometer with a photodetector (PD), making possible to measure the transmitted intensity of the sample only at the laser wavelength and to calculate the RIA from the same equation (2.2). With the instruments available at LabHC, we implemented a setup that allowed us to measure the online monochromatic RIA of several samples (up to six) simultaneously and at two different wavelengths (1310 nm and 1550 nm), as illustrated in Figure 2.13. The developed system is composed on an optical coupler, an Agilent 8163B power meter and a Thorlabs Pro 8000-4 rack where the two laser sources and three optical switches are incorporated. The whole setup is controlled by an implemented Labview interface with a variable sampling time, dependent on the number of actual tested samples (1 min of sampling time in the case of six samples).

Six channels are used to test the samples while the seventh one constitutes the reference line, allowing to monitor the laser fluctuations in such a way to remove their impact on the RIA.

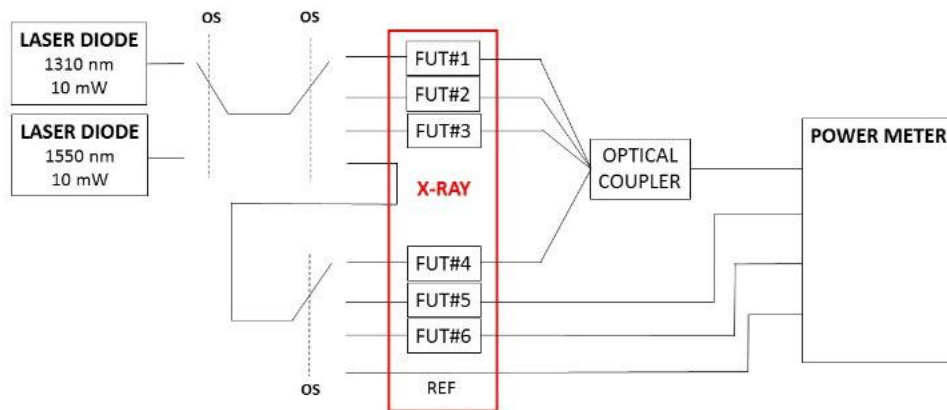


Figure 2.13 Setup for online monochromatic RIA measurement allowing to test up to six samples. Three optical switches (OS) and an optical coupler have been used for propagating the signal provided by the two laser diodes through the different fibers under test (FUT) to the power meter.

2.5.2. Photobleaching measurements

Figure 2.14 shows the experimental setup used to investigate the possible existence of the photobleaching phenomenon on the measured RIA (section 1.3.2.6). The light signal at 1310 nm (1550 nm), originated from a Thorlabs PRO8 DFB laser diode module with a nominal power level of 10 mW, is injected into a 1×4 single-mode IR optical coupler, which equally distributes the light power among its four different channels. Successively, each channel is subjected to a different attenuation controlled by the inserting a given length of a pre-irradiated P-doped single-mode OF manufactured by iXblue Photonics. We chose this type of fiber as attenuator mainly because it shows no recovery phenomena after the end of the irradiation, as already reported in [130], [140], so its overall NIR losses remain constant over time. Also, by recording the reference signals for several days before the start of the irradiation, no fluctuation in signal power levels has been observed, ensuring that this type of irradiated OF is not affected by photobleaching at the considered wavelengths. The pre-irradiation of the attenuators was performed at 6 Gy/s up to a TID of 7 kGy (online-RIA kinetic at 1550 nm shown in Figure 2.15), allowing to obtain overall losses of 9.7 dB/m and 12.7 dB/m at 1310nm and 1550 nm, respectively (spectral losses, measured through the cut-back technique, are shown in the inset of Figure 2.15). Depending on the desired attenuation, different lengths of P-doped OF have been spliced along the signal path of each channel, except for the fourth one, which was used as reference channel. Finally, radiation-hardened OFs were used to connect the FUTs, placed inside the Moperix irradiator, to the attenuators and to an Agilent 8163B power meter controlled by an implemented Labview interface. This setup allowed to measure the RIA with different probing signal levels, from hundreds of nanowatts to some milliwatt. During the irradiation and after its end, the probing light was continuously propagating into the samples.

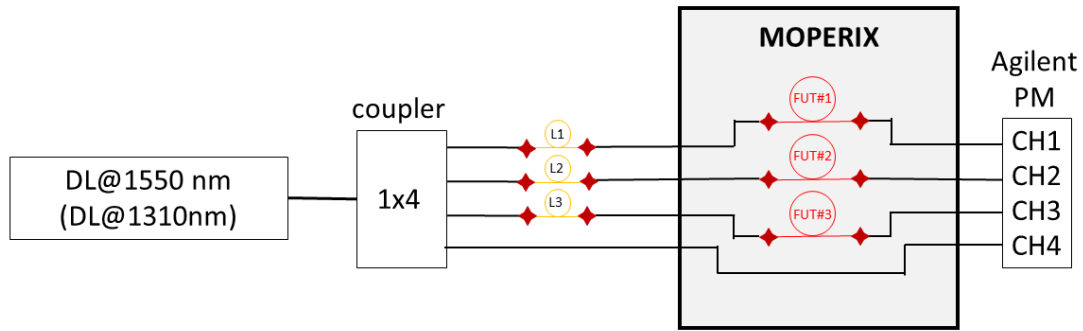


Figure 2.14 Experimental setup used for photobleaching tests at 1310 nm or 1550 nm. The signal originated from a LD is distributed into four channels by a NIR optical coupler. The first three output channels of the coupler are individually attenuated with a different length of a pre-irradiated P-doped OF (yellow circles denoted with L1, L2, and L3), the fourth one is used as a reference monitor. Radiation-hardened OFs are used to send the signal into and out of the FUTs, as well as for the transmission of the reference signal. The transmitted signal at the end of each channel is then recorded with an Agilent 8163B power meter (PM).

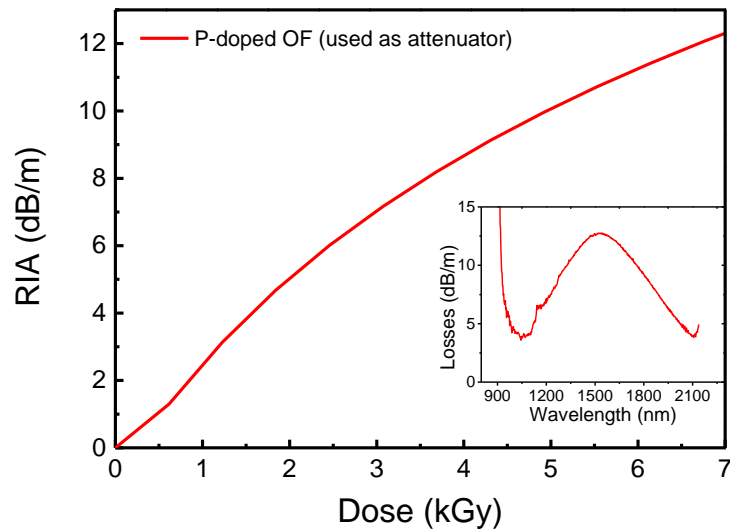


Figure 2.15 RIA kinetic measured at 1550 nm of the iXblue P-doped OF used as attenuators, irradiated up to a TID of 7 kGy and at 6 Gy/s. The inset shows the IR losses measured with the cut-back technique after the end of the irradiation.

2.5.3. OTDR measurements

Another method that allows to measure the online RIA consists in using an optical time domain reflectometer (OTDR) [152], [153]. This device injects a short probe pulse signal at wavelength λ_0 into the sample and, from the same launching end, it acquires the backscattered Rayleigh signal. The OTDR, by associating the intensity of the backscattered light with the time of flight it takes to return from the point it was reflected to the point where the signal was injected, permits to measure the backscattered intensity as a function of the fiber length, by the following equation:

$$I(\lambda_0, z, t) = I(\lambda_0, z_0, t) e^{-\alpha(\lambda_0)2z} \quad (2.3)$$

where I is the backscattered signal intensity, z_0 and z are respectively the fiber launching end (where the signal was injected) and the distance from it, λ_0 is the wavelength of the investigation, t is the time and α is the overall attenuation. Since the light pulse propagates twice along the distance z , it is subjected twice to the OF attenuation and so a factor 2 is necessary to the exponent of equation (2.3).

The probing light, traveling down the OF, loses intensity along its way due to the different attenuations. By evaluating the slope of the curve resulting from the measurement, during or after the irradiation, it is possible to determine the value of the attenuation of the OF. Furthermore, since the OTDR considers the overall attenuation and not only that induced by radiation, the losses of the pristine sample must be subtracted from the one measured in order to calculate the RIA. For the results presented in this thesis, we used an OTDR manufactured by VIAVI solutions, operating at 1310 nm and 1550 nm.

As example, Figure 2.16 reports some OTDR traces acquired at 1550 nm during an irradiation at 0.6 Gy s^{-1} and -40°C , of the SMF-28e⁺ OF (a comprehensive discussion of these results is reported in section 4.2). In this case, the spatial resolution was set at 20 cm (by fixing the pulse width at 2 ns) and the acquisition time was 1 min long.

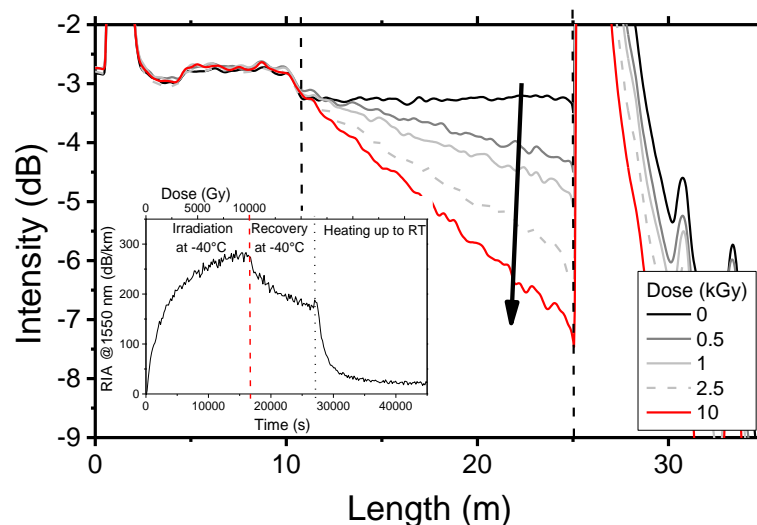


Figure 2.16 Intensity of the backscattered probing signal at 1550 nm coming from the OTDR as a function of the length, during the irradiation of the SMF-28e⁺ OF at 0.6 Gy s^{-1} at -40°C . The dashed vertical lines delimit the sample region, while the arrow indicates the increasing dose. The big peak after the end of the sample (length $\sim 25 \text{ m}$) is due to the reflections at the OF end. The inset reports the 1550 nm RIA kinetics: the dashed vertical red line indicates the irradiation end, while the black one indicates the end of the 3 hours recovery at the irradiation temperature.

Being the OF under test the trace between the two vertical dashed line, it is possible to observe that the intensity of the backscattered probing signal decreases as the accumulated dose increases. The RIA is represented by the opposite of the trace slope along the sample, and is calculated by performing a linear fit on the sample trace region for each acquisition period. In this way, the RIA as a function of the time (or, consequently, of the dose) is derived

by subtracting the measured attenuation from the reference one (acquired before the irradiation start), that considers the pristine losses of the OF as well as the bending losses. The inset of Figure 2.16 illustrates an example of RIA kinetic at 1550 nm obtained from the traces reported in the same figure. From the kinetic, three phases can be distinguished: the irradiation, the recovery at the irradiation temperature and the recovery during the heating of the temperature up to RT.

Using the OTDR as measurement tool for RIA calculation offers some advantages, such as the potential to perform distributed measurements and to work with very long samples (unlike transmission measurements). Although, it must be kept in mind that the probe signal can have power levels of some milliwatts, causing, in some cases, phenomena such as photobleaching or photodarkening.

A more in-depth theoretical coverage of how an OTDR works can be found in [154].

2.5.4. Cut-back technique

The cut-back technique [155] is the only case of “passive” measurement performed during this thesis. Using this method, the OF losses are measured on the pristine sample or only after the end of the irradiation. This is why it is also possible to refer to this type of measurements as “post-mortem” measurements.

The cut-back technique allows measuring the overall losses of the OF and, since it is not carried out during irradiation, it makes possible to evaluate only the permanent attenuation. Indeed, this method is unable to detect any transient effects of RIA occurring during the irradiation and, moreover, does not permit the investigation of fast recovery processes after the end of the irradiation. Therefore, when using this technique, the measured RIA can be smaller than the “real” one experienced by the OF during irradiation.

The spectral attenuation is measured by calculating the ratio of the transmission spectra of two different sample lengths, a longer (L) and a shorter (l) ones, acquired by using a white light source and a spectrometer (that, for our measurements, are the same cited in section 2.5.1). A schematic of the experimental setup is shown in Figure 2.17. To ensure that the losses evaluation is not perturbed by the setup, it is fundamental to maintain the same injection conditions during the measurements. For this reason, after the acquisition of the transmitted spectrum of the longer sample, a length $\Delta L=L-l$ is removed from it and the remaining shorter sample is reconnected to the spectrometer by splicing it to the transport fiber. In this way, the operator can obtain the shorter sample without touching the connections. In addition, to avoid that the insertion losses due to the splice are also considered as losses of the material, the splicing process should be repeated few times, in order to assess the reproducibility of the transmitted spectrum.

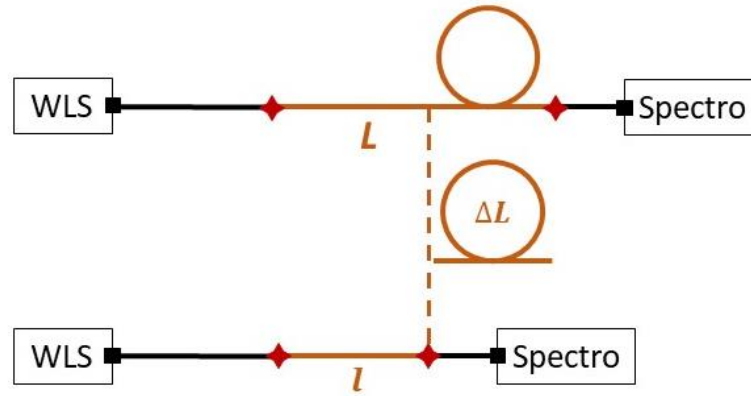


Figure 2.17 Schematic of the cut-back technique. The black squares indicate the signal injection and detection points, which must never be touched by the operator, whereas the red stars represent the splices. Transport OFs (shown in black) are not mandatory if the sample under test is longer than few meters.

The overall spectral losses (α) are obtained by the formula:

$$\alpha(\lambda) = -\frac{10}{\Delta L} \log_{10} \left(\frac{I_L(\lambda) - I_{\text{noise}}(\lambda)}{I_l(\lambda) - I_{\text{noise}}(\lambda)} \right) \quad (2.4)$$

where $I_L(\lambda)$ and $I_l(\lambda)$ are, respectively, the spectral intensities of the long and short sample, $I_{\text{noise}}(\lambda)$ is the noise spectrum, acquired when the white light signal is turned off. I_{noise} is mainly due to the spectrometer electronic noise and can be reduced by lowering the temperature of the detector. Indeed, some spectrometers are equipped with thermo-electric coolers that enable to control the operative temperature of the sensor. Finally, the radiation-induced losses (α_{RIA}) are obtained by subtracting the attenuation of the pristine sample (α_0) from those of the irradiated one:

$$\alpha_{\text{RIA}}(\lambda) = \alpha(\lambda) - \alpha_0(\lambda). \quad (2.5)$$

2.5.5. Technical analysis: spectral decomposition

Given a RIA spectrum, this can be defined as the sum of the optical absorption bands associated with the various point defects existing in the OF. Although, it has to be considered that changes in the propagation conditions of guided modes within the OF can affect the RIA evaluation, especially for those OFs that are single-mode in the IR domain [129].

The absorption bands of most known defects are characterized by a Gaussian shape (when RIA is represented as a function of the energy of the probing light). An exception is represented by the NBOHC absorption band peaked around 1.9 eV, which has been proved to have a non-Gaussian and non-symmetrical shape (see section 1.3.3.1.6) but which can still be described as the sum of three Gaussians with a fixed amplitude ratio [95].

The equation of a Gaussian is defined as:

$$G(E) = \frac{A}{\sqrt{2\pi\sigma^2}} e^{-\frac{(E-E_C)^2}{2\sigma^2}} \quad (2.6)$$

where E is the energy, A and E_C are respectively the area and the center of the band, σ is the standard deviation, that is related to the FWHM by the relation:

$$\text{FWHM} = 2\sqrt{2\ln 2}\sigma. \quad (2.7)$$

Once the RIA profile is acquired, its spectral decomposition consists of performing a fitting routine based on the minimum set of absorption bands available in literature. For the present thesis, most of the parameters of the absorption bands were taken from [15]. During the fitting routine, the center and FWHM of the bands are fixed, while the area is the only free parameter. By knowing the value of the absorption band area and the oscillator strength of a specific point defect, it is possible to estimate its concentration for a given dose, dose-rate, temperature, etc. In addition, if a spectral online measurement has been carried out, this technique enables to investigate the kinetics of single point defects as a function of the dose (or time), by performing the decomposition at different irradiation time periods.

Chapter 3: Combined radiation and temperature effects on radiation-sensitive optical fibers

In this chapter, the results concerning radiation-sensitive OFs will be presented and discussed. The chapter is divided into four sections:

- study of the irradiation temperature effects on the monochromatic RIA at telecommunication wavelengths of the CERTYF P-, Al- and GeP-doped OFs and their C.A. counterparts;
- study of the irradiation temperature effects on the vis and NIR RIA of the CERTYF Al-doped sample;
- study of the irradiation temperature effects on the vis and NIR RIA of the CERTYF P-doped sample;
- study of the operating temperature range of the CERTYF P-doped OF and two other C.A. samples with different coatings for dosimetry applications.

3.1. Combined temperature and radiation effects on the monochromatic RIA of radiation-sensitive OFs at telecommunication wavelengths.

The combined effects of temperature and radiation have been investigated on three different types of radiation-sensitive OFs: Al-doped, P-doped and GeP co-doped. For each type of dopant, two samples were considered: the CERTYF one and one of its corresponding commercially available (C.A.) counterparts. Information about the samples under test can be found in chapter 2, while Table 3.1 recalls OF names with their core/cladding dopant concentration (expressed in wt%) as well as the sample length used for our experiments.

Table 3.1 List of radiation-sensitive OFs tested with their dopant concentration and lengths.

Sample	Core dopant concentration [wt%]	Length [m]
CERTYF Al (K04-01)	2 Al	0.2
CERTYF P (L28-01)	4.5 P	0.2
CERTYF GeP (Q07-01)	3.5 Ge / 1.2 P	1
C.A. Al	NA	0.2
C.A. P	10 P	0.2
C.A. GeP	NA	1

NA= not available

In Table 3.2 are reported the irradiation conditions for this study. The dose-rate of 10 Gy s^{-1} (uniformity within 5%) was essentially chosen to optimize the irradiation time, since the RIA of both the phosphosilicate and aluminosilicate OFs is almost insensitive to the dose-rate [32], [76], [126], whereas, with regard to GeP OFs, studies on the subject are underway at LabHC. For each irradiation run, new pristine samples have been used.

Table 3.2 Irradiation details.

Dose-rate	Total Ionizing Dose in Gy(SiO ₂)	Temperature
		-40°C
		0°C
10 Gy/s	100 kGy	24°C (RT)
		75°C
		150°C

The monochromatic online RIA was measured using the setup described in section 2.5.1 (Figure 2.13). In order to assess the reproducibility of the obtained results, the

measurements were repeated up to three times. Table 3.3 illustrates, for each sample, the relative uncertainties, calculated as the ratio of the maximal RIA variation over the associated mean value at the only dose of 100 kGy, for the two investigated wavelengths (1310 and 1550 nm) and at the considered irradiation temperatures.

Table 3.3 Relative errors, in percentage, of the RIA at 1310 nm and 1550 nm (in brackets).

Sample Temperature	CERTYF Al		C.A. Al		CERTYF P		C.A. P		CERTYF GeP		C.A. GeP	
	-40°C											
0°C	0.7 (0.4)		1.8		4 (4)		3 (0.5)		2 (8)		4 (8)	
24°C	1 (0.3)		1.5 (0.8)		3 (7)		4 (5)		7 (4)		6 (2)	
75°C	2 (6)		1.8		0.8 (4)		0.3 (0.9)		3 (3)		1.4	
150°C												

Overall, a relative uncertainty less than 8% has been evaluated, highlighting an excellent reproducibility of the results. In both cases of irradiation temperature of -40°C and 150°C, only one measurement has been performed.

Figure 3.1 shows the online RIA during and after the irradiation performed at RT and at both investigated wavelengths for the CERTYF and the C.A. OFs. In this figure, the kinetics for all three irradiation runs are shown. The results that will be presented at other temperatures are, instead, the average of the irradiation runs done with the same conditions.

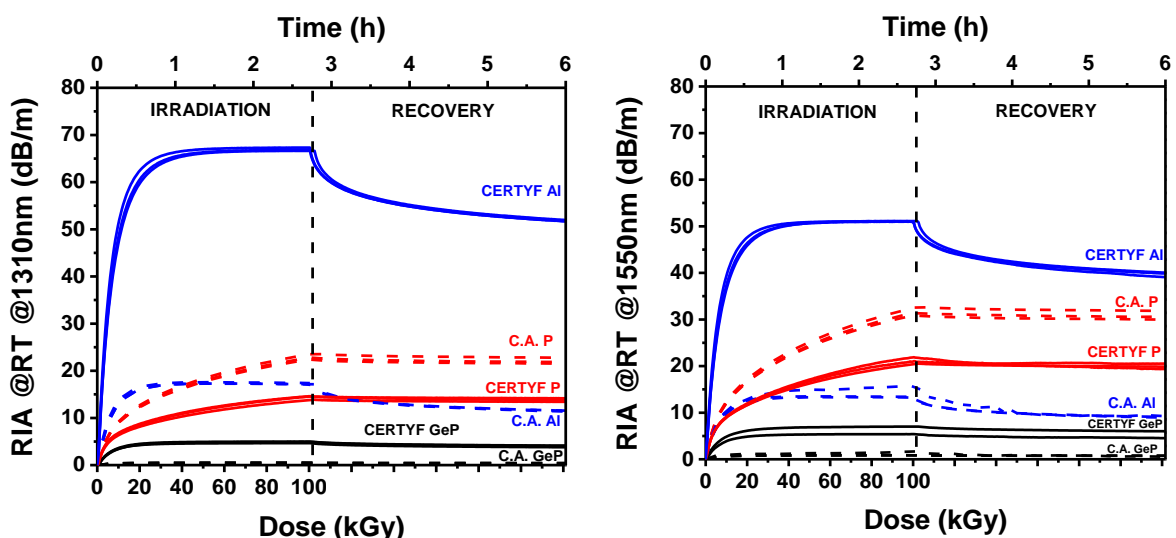


Figure 3.1 Online 1310 nm (left) and 1550 nm (right) RIA kinetics at RT during and after 100 kGy irradiation (dose-rate being 10 Gy/s) for the CERTYF samples and their corresponding C.A. OFs.

It is possible to observe that, for all the samples, right after the beginning of the irradiation, the RIA linearly increases with respect to the dose with different slopes, depending on the type of dopants and their concentration: the Al-doped samples show the steepest slope, the Ge/P-codoped ones reveal to be the least sensitive to radiations, while the P-doped ones have an intermediate sensitivity compared to the two other types. Moreover, at higher doses, the RIA of the Al-doped and Ge/P-codoped OFs reaches a saturation value, whereas for the P-doped samples it continues to increase but with a lower trend. As far as concerns the RIAs after the end of the irradiation, Table 3.4 reports the percentage of the recovered RIA (respect to the RIA at 100 kGy) ~3h after the end of the irradiation.

Table 3.4 Recovered RIA (~3 after the end of the irradiation) of the six investigated samples at 1310 and 1550 nm.

Wavelength	Sample					
	CERTYF Al	C.A. Al	CERTYF P	C.A. P	CERTYF GeP	C.A. GeP
1310 nm	22%	34%	4%	2%	20%	20%
1550 nm	22%	21%	3%	3%	15%	13%

It is possible to observe that there is almost no recovery for the P-doped samples. This feature, in addition to the fact that phosphosilicate OF RIA has a linear dependence up to a dose of ~500 Gy [140], make this type of fibers suitable for applications such as dosimetry. On the other hand, Al-doped samples are the ones that exhibited the largest recovery 3h after the end of the irradiation.

Figure 3.1 also shows that, at both wavelengths, the CERTYF Al-doped and GeP-codoped samples exhibit a higher RIA compared to the one of their C.A. counterparts, by a factor of 4 and 10, respectively. Instead, in the case of the P-doped sample, the sensitivity of the CERTYF sample is lower by a factor 3 compared to the one of its corresponding C.A.. This is probably due to the smaller P concentration, as reported in Table 3.1. In the case of Al-doped OFs, the losses at 1310 nm are higher than ones at 1550 nm, coherently with the shape of the spectral RIA found in literature [15], [32], [129]. Instead, the presence of the P-codoping in the GeP sample gives rise to an absorption band peaked around 1550 nm associated with the P1 point defect, resulting in a higher attenuation at this wavelength compared to 1310 nm.

In order to verify that the measured RIA is the “real” one (i.e. there is no perturbation due to the experimental setup) and no effect of the probe signal power is present, Figure 3.2 compares the RT RIA kinetics of the CERTYF Al-doped sample when measured with an experimental setup constituted by a laser diode and a power meter (the one used for the present study) with the ones obtained with a white light source and a NIR spectrometer (Figure 2.12). It is possible to observe that no dependence of the RIA on the probing light power exists, indicating that photobleaching has a negligible impact at the power levels we use. Same

conclusions can be made for P-doped OFs [140], [156]. Moreover, as far as concerns with Ge doped OF, it has been demonstrated that photobleaching with IR lasers is very weak at RT (but can have a significant impact at low temperatures, e.g. at -55°C as the particular case of [51]).

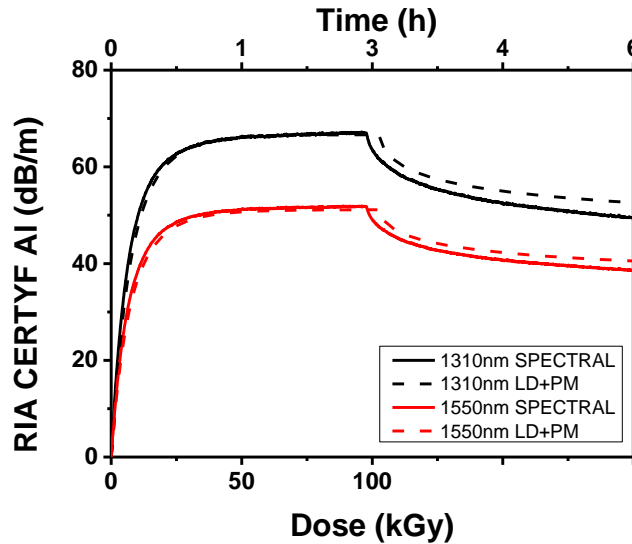


Figure 3.2 Comparison of RT RIA kinetics at 1310 nm and 1550 nm measured with two different experimental setups: white light source and spectrometer (continuous lines), laser diode and power meter (LD+PM) (dashed lines).

3.1.1. RIA temperature Sensitivity

3.1.1.1. Al-doped samples

Figure 3.3 reports the dependence of the RIA on the dose at the investigated irradiation temperatures for both the CERTYF and C.A. Al-doped samples, measured at 1310 nm and 1550 nm. The results highlight a clear dependence: when the irradiation temperature increases, the RIA decreases. A lower RIA implies a lower concentration of point defect(s) responsible for the attenuation at these wavelengths. This means that, as the temperature increases, point defects have been either less efficiently generated under irradiation, more efficiently annealed (de-trapping of carriers from those trapped-states forming point defects), or more efficiently recombined.

Besides the fact that the CERTYF sample presents a much higher RIA than the C.A. (~4 times higher at all temperatures and at both wavelengths), it must be pointed out that the temperature has no significant effect on the kinetics shapes. Therefore, at the moment, it is not possible to discriminate whether the temperature influences one particular aspect between the generation or recombination of the point defects, or whether it acts on both at the same time. However, for the C.A. sample, the RIA measured in the range between -40°C and RT is

within the experimental uncertainty reported in Table 3.3, meaning that the measured variations are not significant.

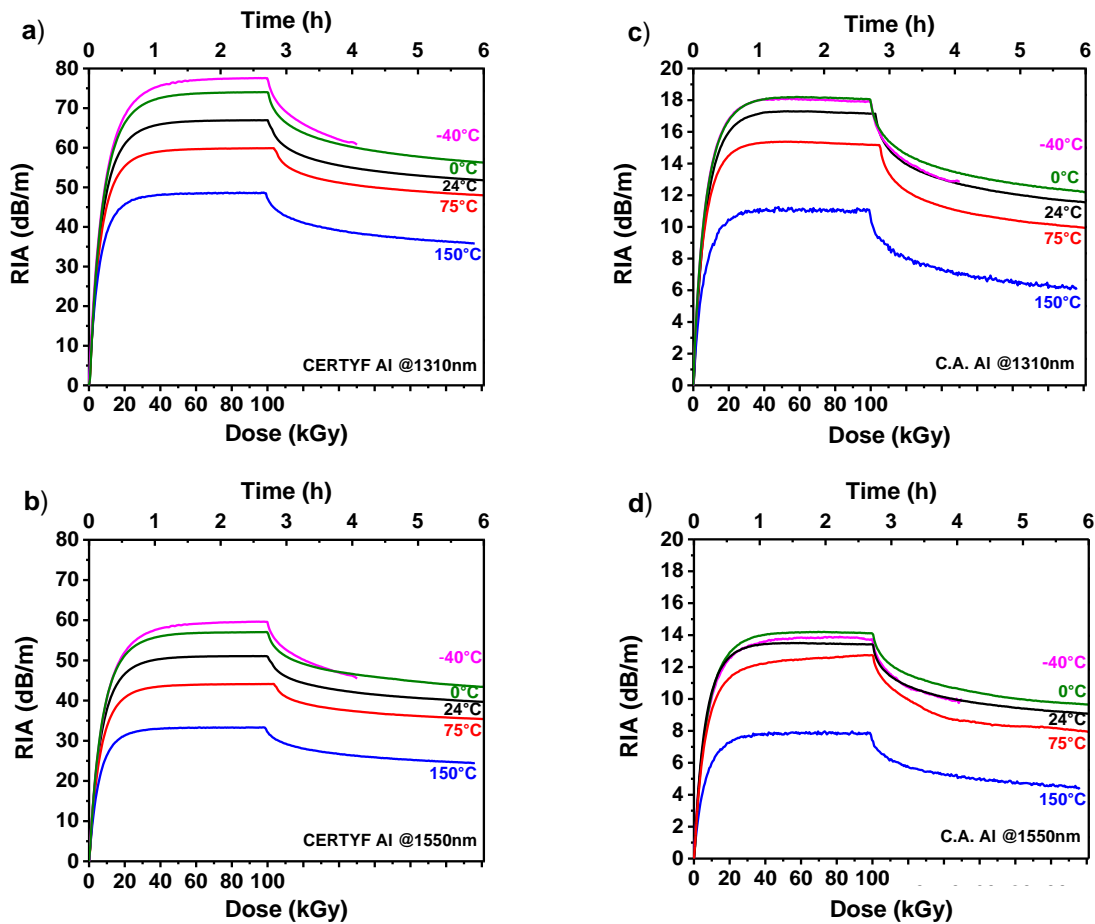


Figure 3.3 Online RIA, during and after a 100 kGy irradiation, for the CERTYF Al-doped sample at 1310 nm (a) and 1550 nm (b) and for the C.A. Al-doped sample at 1310 nm (c) and 1550 nm (d) at different irradiation temperatures.

3.1.1.2. P-doped samples

The results concerning the P-doped samples are shown in Figure 3.4. Compared to the Al-doped OFs, these fibers present a different behavior. The 1310 nm RIA of both samples increases as the irradiation temperature increases. At 1550 nm, instead, the two OF show different trends: the RIA of the CERTYF sample is marginally influenced (<4%) by the irradiation temperature, whereas in the C.A. sample the temperature influence is about 20% at the maximum dose of 100 kGy.

For phosphosilicate OFs, the induced losses at 1550 nm are related to the P1 defect. Instead, at 1310 nm, the attenuation is due to the tail of the P1 defect and to another unknown optical absorption band that should be peaked around ~ 1.23 eV (~ 1008 nm), as discussed in more detail in [15].

An interesting feature is observed in the C.A. sample at both wavelengths: the RIA increases in the range from -40°C to 75°C , and then decreases at 150°C (Figure 3.4c and d).

A similar tendency can be noticed also for the CERTYF sample, but only at 1310 nm (Figure 3.4a); however, the RIA at 150°C is higher than the one measured at 75°C, and the recovery is enhanced at 150°C than a 75°C.

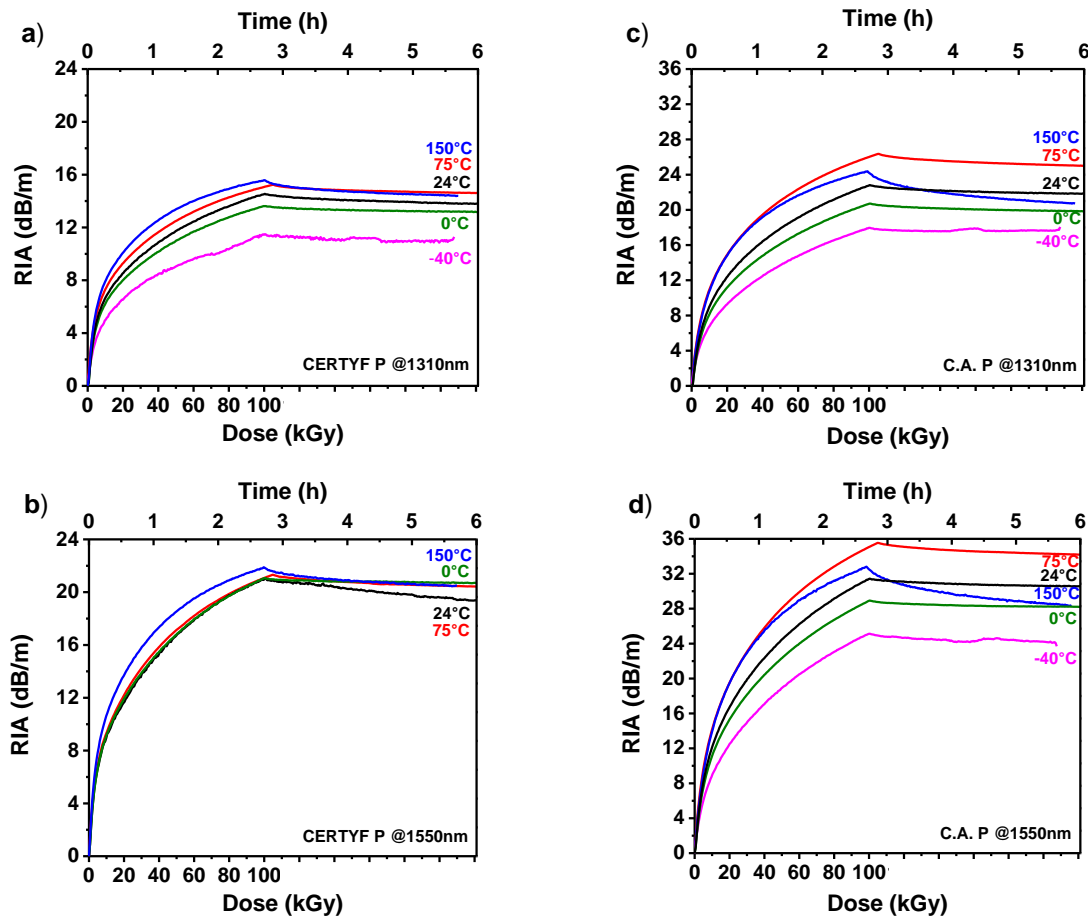


Figure 3.4 Online RIA, during and after a 100 kGy irradiation, for the CERTYF P-doped sample at 1310 nm (a) and 1550 nm (b) and for the C.A. P-doped sample at 1310 nm (c) and 1550 nm (d) at different irradiation temperatures.

3.1.1.3. GeP-codoped samples

As it can be seen in Figure 3.5, the RIA of the C.A. sample decreases at higher temperatures. However, in general, the RIA kinetics trends depend on Ge and P concentrations and on their localization in the OF section. Moreover, it has been proven in literature that Ge-related point defects are more sensitive with respect to the temperature than P-related ones [157]. Looking at the kinetics of the CERTYF sample, a complex behaviour is found. At 1310 nm, the observed variations on the RIA are within the experimental uncertainty of the measurements performed at RT, so it is possible to conclude that no significative dependence on the temperature exists. However, at 150°C, is observed a clear decrease of the RIA compared to the one measured at other temperatures.

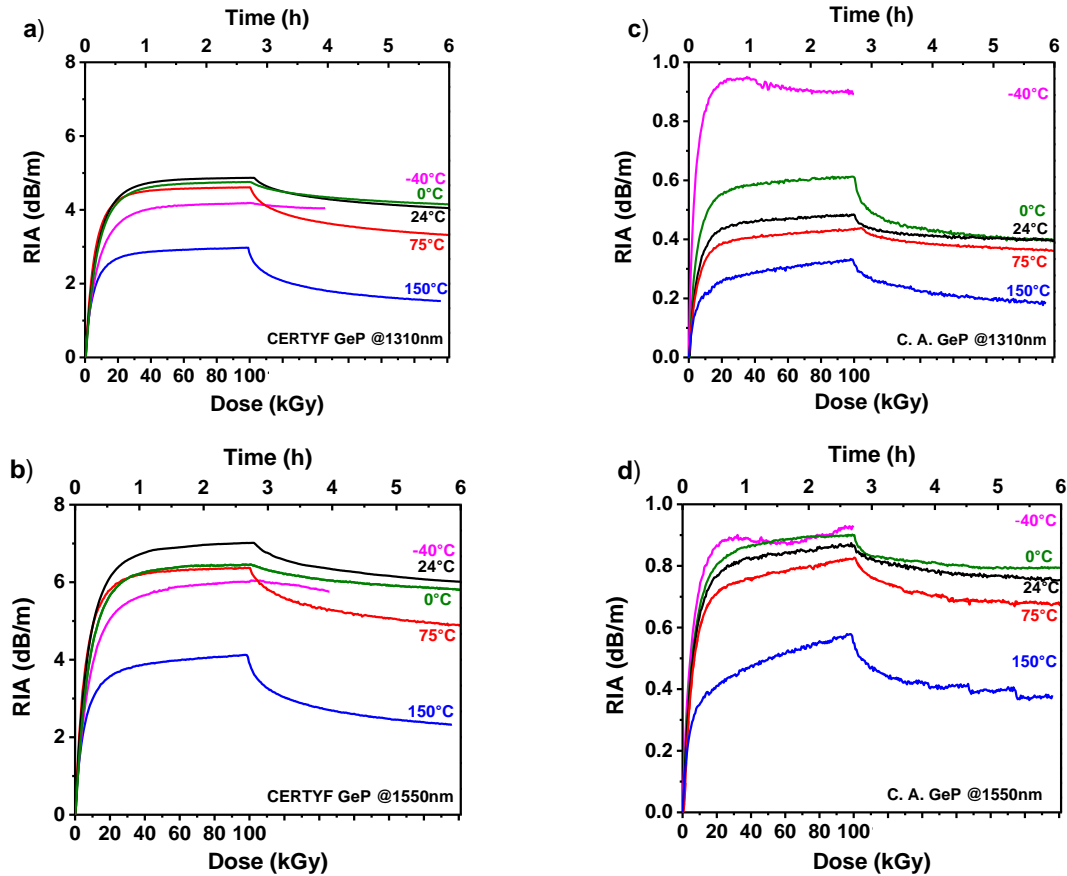


Figure 3.5 Online RIA, during and after a 100 kGy irradiation, for the CERTYF GeP-codoped sample at 1310 nm (a) and 1550 nm (b) and for the C.A. GeP-codoped sample at 1310 nm (c) and 1550 nm (d) at different irradiation temperatures. The break observed in kinetics at -40°C is due to a source shutdown.

With regard to the post-irradiation period, by normalizing the kinetics to the value at the maximum dose, it is possible to observe that the RIA is recovered more efficiently as the temperature increases, as shown in Figure 3.6 (case of the CERTYF sample). This allows us concluding that temperature affects the recombination rate of defects absorbing at these wavelengths, increasing its efficiency as the temperature increases.

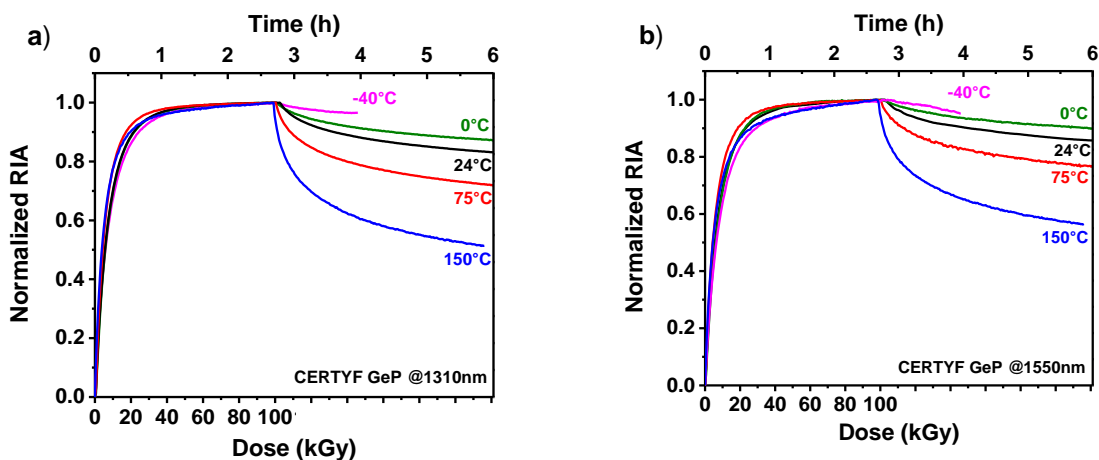


Figure 3.6 RIA kinetics, normalized to the maximum dose value, at 1310 nm (a) and 1550 nm (b) for the CERTYF GeP-doped sample.

3.1.1.4. Combined impact of temperature and irradiation time

In order to focus on the impact of the irradiation temperature, the measured RIAs have been normalized to their respective values at RT and calculated for multiple elapsed times during the irradiation (corresponding, in turn, to different accumulated doses). In Figure 3.7 is shown the case of the CERTYF Al sample at 1550 nm (the same behaviour has been observed at 1310 nm). In general, when the value of the normalized RIA is greater than 1, it means that the temperature has an overall negative impact on the radiation effects, i.e. a higher RIA is measured at a temperature T (different from RT) compared to the one measured at RT. On the contrary, when the normalized RIA has a value lower than 1, a positive impact of temperature is reported on the RIA. Furthermore, it can be appreciated that the impact of the temperature on the normalized RIA strongly depends on the accumulated dose or, more precisely, on the irradiation time. The figure highlights that, for temperature of -40°C and 0°C, an increase in the total accumulated dose results in a higher normalized RIA. On the other hand, at 75°C and 150°C, the normalized RIA has lower values for longer irradiation periods, proving that at these temperatures the thermal-bleaching is more efficient (despite an overall higher RIA for higher doses, as already shown in Figure 3.3b). The same behaviour has also been observed by studying the graph concerning the C.A. Al-doped sample (not reported here).

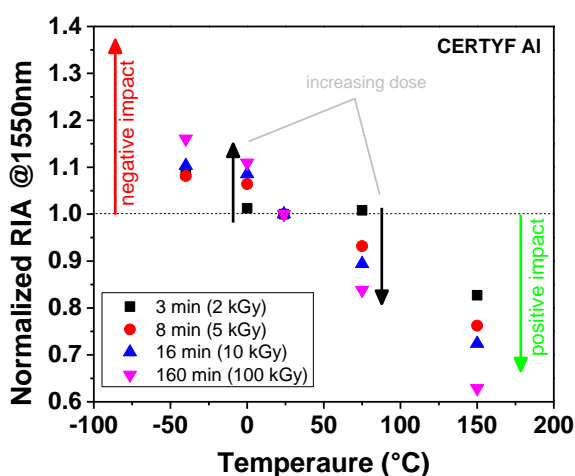


Figure 3.7 Normalized RIA with respect to its value at RT for the CERTYF Al sample at 1550 nm and at different irradiation times.

In Figure 3.8 is shown the same type of graph but for the C.A. P-doped sample. In this case, a different behaviour than the one observed in the Al-doped sample is found. At temperatures lower than RT, the normalized RIA has values lower than 1, possibly due to a lower conversion rate from phosphorus oxygen hole centers (POHCs) precursor centers into P1 defects [39]. Furthermore, at lower temperatures, no significant variation exists in relation

to the dose increase. Finally, at higher temperatures the normalized RIA results higher than 1 and decreases as the irradiation time increases.

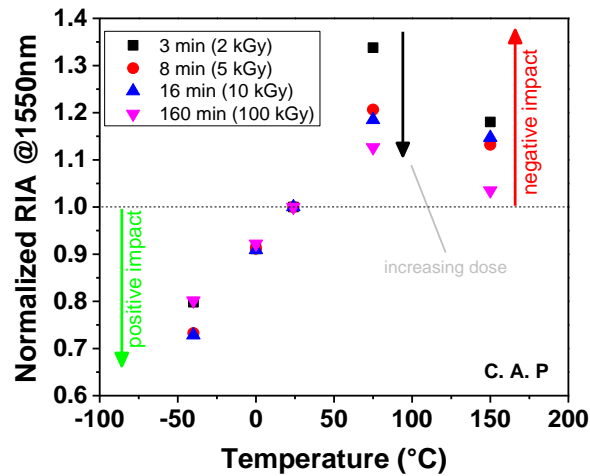


Figure 3.8 Normalized RIA with respect to its value at RT for the C. A. P-doped sample at 1550 nm and at different irradiation times.

The analysis of the C.A. GeP-codoped sample is shown in Figure 3.9. A similar temperature dependence to that of Al-doped samples has been observed, i.e. the normalized RIA decreases with the increasing temperature. However, in this case, the figure shows a different trend of the RIA with the dose at low temperatures. For example, at -40°C the normalized RIA decreases as the dose increases. One possible explanation could be that, the longer the duration of the irradiation, the higher the probability that the generated defect can recombine because of the photobleaching. This phenomenon is not significant at higher temperatures probably because other phenomena, such as thermal bleaching, become predominant.

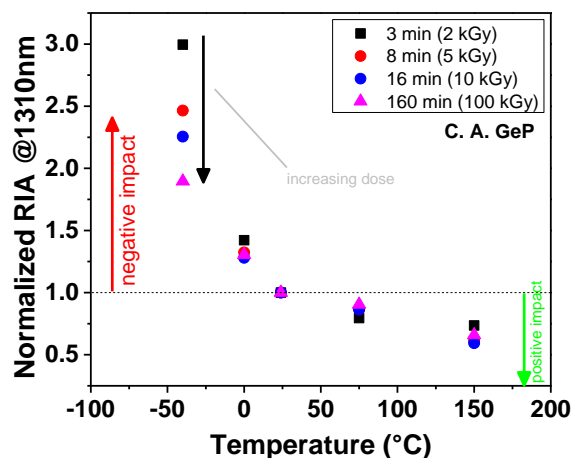


Figure 3.9 Normalized RIA with respect to its value at RT for the C. A. GeP-codoped sample at 1310 nm and at different irradiation times.

3.2. Al-doped OFs RIA temperature dependence

In the present section, the results about the influence of the irradiation temperature on the vis and NIR RIA of the CERTYF Al-doped OF (K04-01) will be presented. Experiments were carried out with the experimental setup described in section 2.5.1 (Figure 2.12).

Table 3.5 reports the irradiation details for this study. For each experiment, once the target temperature is reached, a thermalization time of about 20 minutes has been considered before starting the irradiation. Since the radiation induced expected losses in the visible and in the NIR differ by several orders of magnitude, two samples of different lengths (1 cm long for the UV/vis and 15 cm long for the NIR) have been tested simultaneously for each irradiation run.

Table 3.5 Irradiation details.

Dose-rate	Total Ionizing Dose in Gy(SiO ₂)	Temperature
1 Gy/s	10 kGy	25°C (RT)
		50°C
		100°C
		150°C
		200°C
		250°C
		300°C

3.2.1. Evolution of UV-vis and NIR-RIA at RT

Figure 3.10 shows the online UV-vis and NIR RIA measured at RT and at different TIDs (up to 10 kGy). One can see that the losses increase across the whole spectrum as the dose accumulates. However, the growth rate of the RIA decreases as the dose increases, which leads us to assume that, at doses greater than 10 kGy, the losses should eventually saturate. Furthermore, RIA levels are much higher in the visible domain than the ones measured at longer wavelengths, accordingly to what already reported in literature [76]. Indeed, in the visible domain, the RIA is due to two wide optical absorption bands, peaked around 390 nm and 540 nm, both attributable to Al-OHCs [15], [76]. These bands are responsible for most of the optical losses at shorter wavelengths, making it possible to consider Al-OHCs the main contributor to the vis-RIA. In addition, from the spectra at 100 Gy and 200 Gy is also possible to appreciate the shape of the UV-RIA and the contribution of the optical absorption band related to AlE' point defect, centered around 300 nm [15]. As far as concerns the NIR-RIA, for wavelengths longer than 1000 nm there is no evidence of optical absorption band peaks and also a homogeneous increase over the spectrum with the dose, suggesting that, in this region, the

RIA is due to a single absorption defect or to several point defects that are generated simultaneously, as already pointed out in [32].

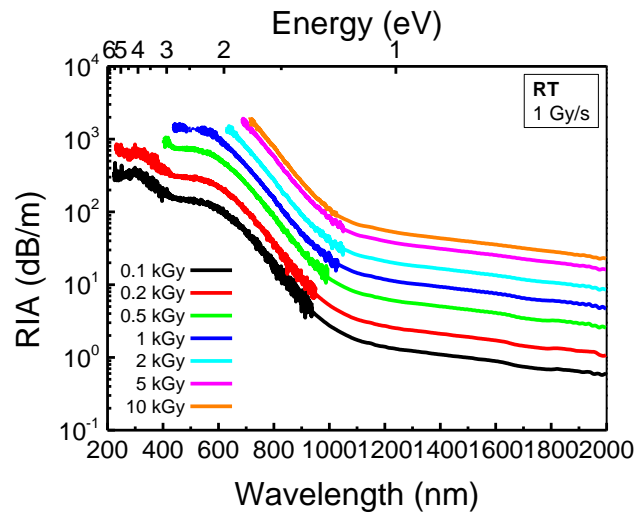


Figure 3.10 UV-vis and NIR online RIA of the Al-doped sample measured at RT for different TIDs, up to 10 kGy. No particular optical absorption band is identified in the NIR range of the spectrum. Also, the contribution of the Al³⁺ OA band, peaked at 300 nm, can be observed up to 200 Gy.

3.2.2. Temperature influence on vis- and NIR-RIA

Figure 3.11 shows the vis- and NIR-RIA at the maximum attained dose of 10 kGy and at the various investigated irradiation temperatures. It is possible to observe that, for wavelengths shorter than ~1100 nm, the RIA spectra are superimposed up to 200°C, proving that the RIA levels are not affected by the temperature in this spectral range. On the contrary, at longer wavelengths, the temperature increase leads to a RIA decrease. Indeed, the RIA decreases as the temperature increases and this trend becomes more and more relevant as higher temperatures are reached. The different behavior of the visible and NIR RIA with respect to the temperature indicates that the absorbers in the NIR and the ones in the visible (Al-OHCs) have different thermal stabilities. Finally, at 300°C the influence of the temperature is significant across all the spectrum, reducing the attenuation by a factor of ~6 and ~4 (compared to the RIA at RT) respectively at 800 nm and 1550 nm.

Figure 3.12 shows the ratio between the NIR RIA at the investigated temperatures and the one at RT, recorded at 10 kGy. It can be noticed that, for wavelengths longer than 1100 nm and up to 150°C, the temperature has a limited effect, in particular the RIA is within ±20% of its RT value. Furthermore, at 800 nm and 1200 nm the RIA ratio is approximately 1 in the temperature range RT-200°C. This feature makes it possible to state that, at these two wavelengths, the RIA is independent from the temperature, making this OF very appealing for applications such as dosimetry or, in general, radiation sensing.

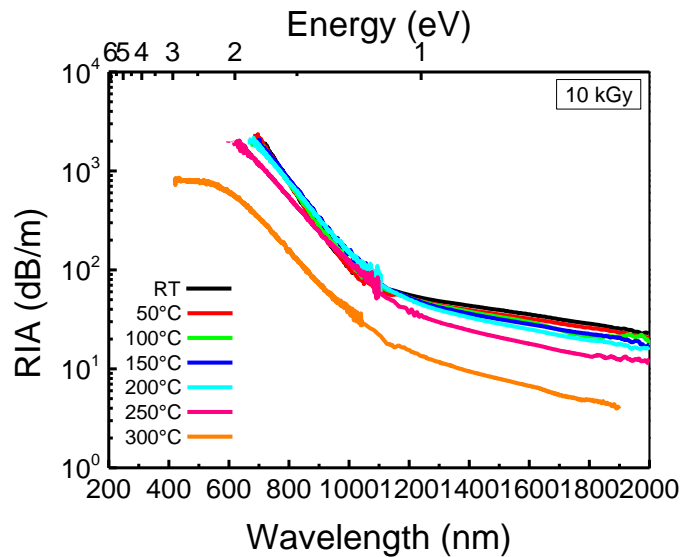


Figure 3.11 Vis- and NIR-RIA at the maximum dose (10 kGy) and at different irradiation temperatures. The effects of the temperature become significant above 200°C in the visible domain, whereas, in the NIR, the RIA decreases with the increasing temperature.

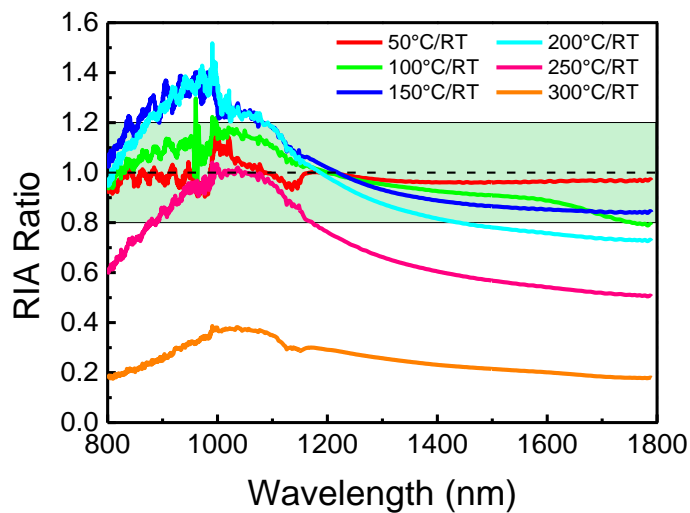


Figure 3.12 Ratio between the RIAs at the investigated temperatures and the one at RT, both for a 10 kGy TID. The 800 nm and 1200 nm wavelength stand out as temperature-independent in the range between RT and 200°C.

In order to evaluate the Al-OHCs contribution in the measured RIA spectra, a fitting routine has been performed for the acquired experimental data at the maximum dose and at all temperatures. As the shortest measured wavelength at the highest TID is around 700 nm, it was sufficient to consider only the Al-OHC band centred at 2.3 eV (540 nm) to describe the RIA in the 700-1000 nm region. This Al-OHC optical absorption band has been considered as a Gaussian band with a 0.9 eV full width at half maximum, consistently with [15]. Figure 3.13 shows the quality of the obtained fit and enables to observe that, in the 700 – 1000 nm range (~1.24 – 1.77 eV), the 2.3 eV band, associated with Al-OHCs, can be approximately considered as the only contribution to the RIA.

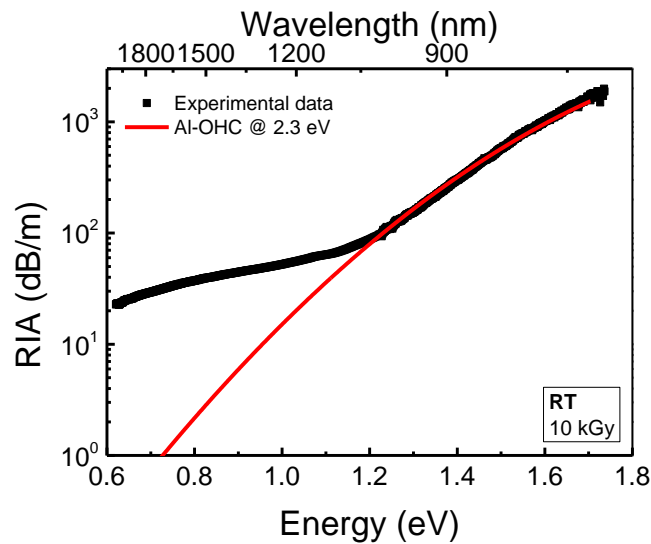


Figure 3.13 Spectral RIA measured at RT and 10 kGy and optical absorption band due to Al-OHCs peaked at 2.3 eV. In the 1.24 – 1.77 eV range, this band can be considered as the only contribution to the RIA.

From the aforementioned considerations it follows that, by analysing RIA kinetics at 800 nm during and after the end of the irradiation (as reported in Figure 3.14) it is possible to investigate the combined effects of temperature and radiation on Al-OHCs. From Figure 3.14a it can be observed that, independently from the temperature, RIA levels grow monotonically with the same behaviour during the irradiation and without reaching the saturation level up to 200°C. Above 200°C, the temperature effect becomes significant and an equilibrium state between the defect generation and recombination processes is attained before a TID of 10 kGy. Here, RIA reaches lower steady-state levels as the temperature increases. From Figure 3.14b, where the same kinetics are represented in a double logarithmic scale, it is also possible to notice that the growth trend is the same up to ~5 kGy for irradiation temperatures up to 200°C, moreover with a linear slope up to ~2 kGy and with a sensitivity of ~170 dB km⁻¹ Gy⁻¹. Figure 3.14c shows the RIA recoveries normalized to RIA values at 10 kGy: RIAs have also the same recovery trend (within the measurement uncertainty) up to 200°C. Instead, at 250°C and 300°C, it is possible to observe that the recovery is more efficient with the increasing temperature.

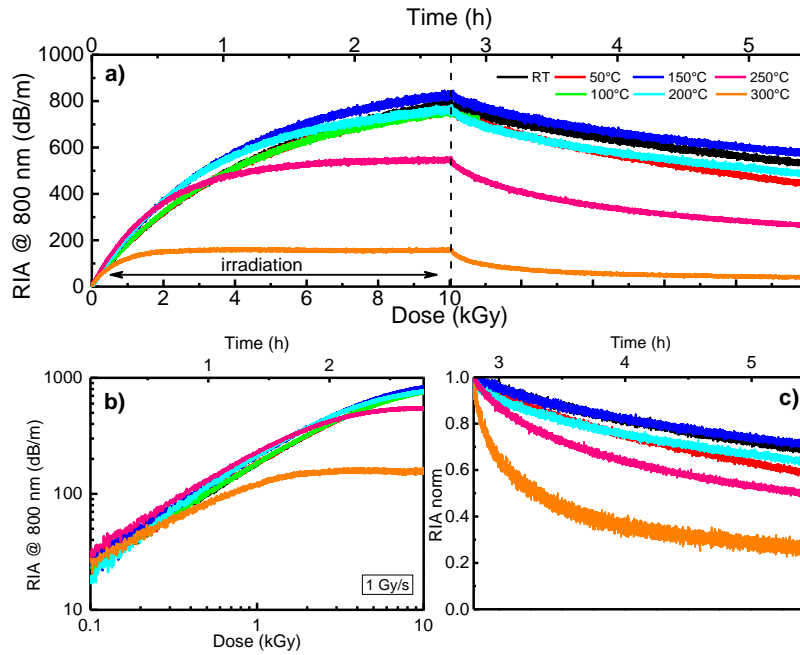


Figure 3.14 a) Online RIA kinetics measured at 800 nm during and after the irradiation up to 10 kGy at the different investigated temperatures. The RIA values at 250°C and 300°C are significantly lower compared to the ones up to 200°C. **b)** Online RIA growth kinetics at 800 nm in double logarithmic scale. **c)** Recovery kinetics up to ~3 hours after the end of the irradiation, normalized to the RIA value obtained at 10 kGy, at the different temperatures.

The same type of analysis has been carried out for kinetics at 1550 nm (Figure 3.15). From the figure it is possible to observe that, at all temperatures, the RIA grows as the dose increases and then decreases after the end of the irradiation. In addition, while at lower temperature the kinetics do not reach the saturation for TID up to 10 kGy, at higher temperatures the curves begin to flatten, showing a steady-state behaviour at 300°C for doses above 2 kGy. Also, from Figure 3.15b it can be highlighted that, for accumulated doses lower than 300 Gy, temperature has no significant effect at the investigated dose-rate, whereas, at TIDs higher than 300 Gy, the temperature influences the RIA with a definite trend: the higher the temperature, the lower the RIA. The RIA grows linearly with the dose for TID ranges that are smaller as the temperature increases, indeed if at RT it can be assessed that up to ~2 kGy exists a linear growth of the RIA (sensitivity of about $8 \text{ dB km}^{-1} \text{ Gy}^{-1}$), at 300°C the RIA changes its slope at about 300 Gy. Finally, in Figure 3.15c, the recovery kinetics normalized to the RIA value at 10 kGy show that defect recovery is more efficient when the temperature increases.

It has been possible to fit the RIA growth kinetics at 1550 nm with a single exponential contribution, defined by the following equation:

$$RIA(D, T) = a_{eq}(T) \left(1 - e^{-\frac{D}{D_{eq}(T)}} \right) \quad (3.1)$$

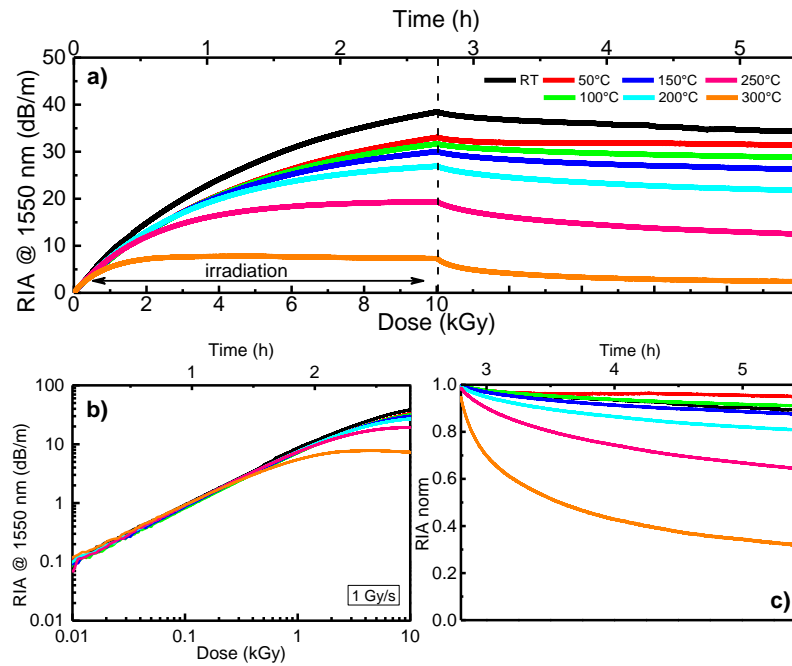


Figure 3.15 a) Online RIA kinetics measured at 1550 nm during and after the irradiation up to 10 kGy at the different investigated temperatures. The RIA progressively starts to decrease as the temperature increases. **b)** Online RIA growth kinetics at 1550 nm in double logarithmic scale. **c)** Recovery kinetics up to ~3 hours after the end of the irradiation, normalized to the RIA value at 10 kGy, at the investigated temperatures.

where a_{eq} and D_{eq} indicate respectively the level and dose at which equilibrium between defect generation and annealing is reached, whereas D is the dose and T the temperature. The quality of the obtained fits for the 1550 nm wavelength is shown in Figure 3.16a. From the fit parameters, it has been observed that, by increasing the irradiation temperature, both the equilibrium level and dose change following a monotonic decreasing trend. In particular, by representing the coefficient a_{eq} as a function of D_{eq} , as shown in Figure 3.16b, it is possible to notice a linear correlation, e.g. by increasing the equilibrium dose, the equilibrium RIA (and, consequently, the concentration of the corresponding defect) increases by the same factor. This linear relationship is an indication that the defect absorbing at 1550 nm is generated by a direct process, i.e. there is no “intermediate” state involved. If this was the case, we should have observed a change in the relationship at some point since the activation of another generation channel (for example an intermediate defect different from the final one) would correspond to a different activation energy.

Previous studies have reported that, in the case of aluminosilicate OFs, the NIR-RIA at RT is not dose-rate dependent (within 15%) [32]. However, a deeper analysis on the dependence of the parameters a_{eq} and D_{eq} on dose-rate variations remains a key point for future studies in order to provide more insights about the generation of the defects responsible for the absorption at these wavelengths.

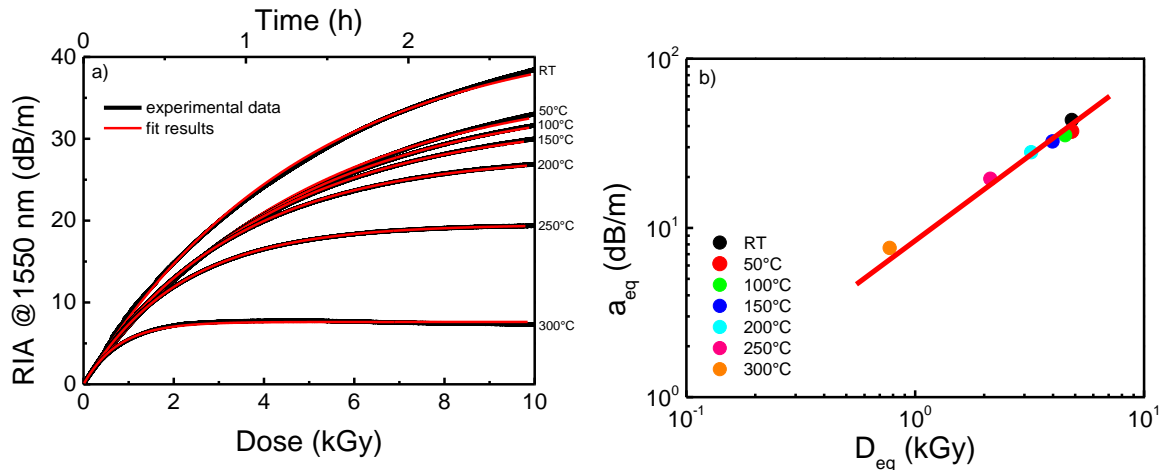


Figure 3.16 a) Results of the fit routine, performed with Eq. (3.1), on the 1550 nm RIA growth kinetic at the different investigated temperatures. b) Equilibrium level (a_{eq}) as a function of the equilibrium dose (D_{eq}) of RIA kinetics at 1550 nm at the different investigated temperatures. The red line is a guide for the reader to remark the linear dependence.

By comparing the RIA growth at 800 nm and 1550 nm for each given temperature (Figure 3.14b and Figure 3.15b) it can be noticed that they are characterized by the same equilibrium doses. At both wavelengths, we can observe that: D_{eq} is between 4 and 5 kGy for $RT < T < 200^\circ\text{C}$, $D_{eq} \approx 2$ kGy at $T = 250^\circ\text{C}$ and $D_{eq} \approx 700$ Gy at $T = 300^\circ\text{C}$. This finding allows to assume that the two defects responsible for the absorption in the two spectral domains are generated from the same precursor, which opens up the possibility that could exist a possible recombination channel between Al-OHCs and defects absorbing in the NIR. Instead, with regard to the recoveries (Figure 3.14c and Figure 3.15c), we observe that kinetics at 800 nm have a faster decay-rate than the ones at 1550 nm. As already said, since the two defects come from the same precursor, it is possible that they could recombine together. But since the recovery kinetics differ, Al-OHCs appear to have multiple recombination channels: one with defects in the NIR and at least an additional one (not yet identified).

Once the behaviour of RIA kinetics at 1550 nm has been studied, it was found interesting to investigate RIA in the entire NIR spectral region, as no evidence of optical absorption bands but a more extended absorption was found here (as already pointed out with Figure 3.10 and Figure 3.11). In order to do so, the RIA in the NIR spectral region has been isolated by subtracting the 2.3 eV peaked Al-OHC contribution (obtained from the fitting routine performed on the spectral RIA, which results for the case at RT are shown in Figure 3.13). The normalization makes it possible to compare the shape of the spectral RIA at all the investigated temperatures. The results of the normalization are shown in Figure 3.17.

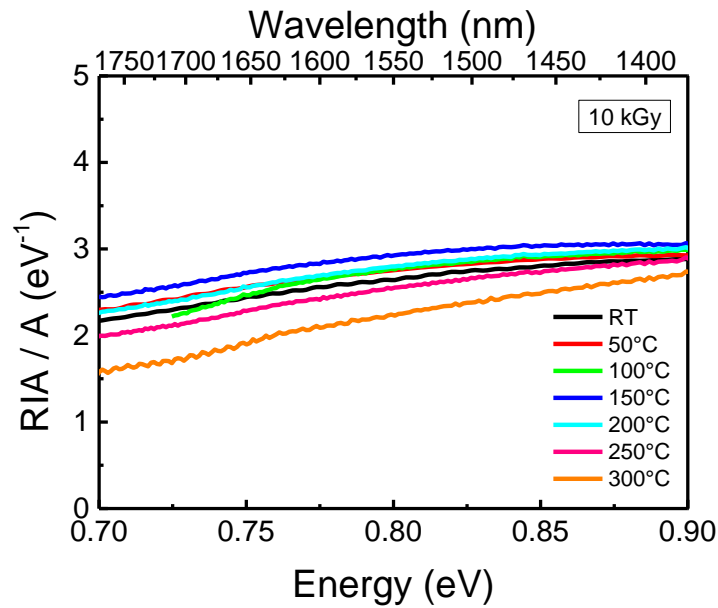


Figure 3.17 Isolated NIR RIA contribution for all the investigated temperatures and at 10 kGy as a function of the energy, determined by subtracting the 2.3 eV peaked Al-OHC contribution to the total measured RIA and normalizing the result to the area (A) underneath the experimental RIA curves in the 0.7-1.1 eV energy region.

It can be noticed that the shape of the obtained curves does not change significantly up to a temperature of 250°C (the small fluctuations, evaluated to be within 10%, can be due both to a change in the guiding properties of the sample as the temperature changes and to the experimental uncertainty of the measures) suggesting that, in the NIR region, the RIA is due to a single absorption component. Furthermore, the flat shape of the NIR RIAs (Figure 3.10 and Figure 3.11) allows us to assume that the absorption component is characterized by a continuum of absorption states. Indeed, the presence of a not clearly defined absorption band suggests a transition between electronic states that are not well localized and characterized by a high degree of dispersion.

Since it has been argued that the defects responsible for the absorption in the two spectral regions could be generated by the same precursor and can, eventually, recombine together, it is possible that the defect in the NIR could be an electron trap, being the one in the UV-vis domain a hole center. In addition, looking both at the shape and nature of the NIR-defects, these could be ascribed to “Anderson localized states” below the conduction band. However, future experiments are needed to confirm this hypothesis.

3.3. P-doped OFs RIA temperature dependence

This section reports the results obtained on the CERTYF P-doped OF (L28-01). We measured the spectral online RIA in the UV-vis and NIR domain during and up to 3 hours after the end of an irradiation at 1 Gy s^{-1} and up to a TID of 10 kGy, by using the experimental setup illustrated in 2.5.1. In order to investigate the combined effects of temperature and radiation, several irradiation runs were performed, each at different irradiation temperature in the range from 25°C (RT) up to 300°C. Before each irradiation, the thermal stabilization of the heating plate, where the OF sample were placed on, was reached before the acquisition of the reference signal and the start of the irradiation.

Table 3.6 reports the details of the irradiation runs. Since the expected attenuations in the considered spectral domains can vary by several orders of magnitude, the chosen sample lengths are approximately 1 cm in the UV-vis range and 20 cm in the NIR. In addition, in order to have better dynamics in the UV-vis domain, for some experiments two UV-vis spectrometers were used to record the transmitted spectra of samples with different lengths.

Table 3.6 Irradiation details of the CERTYF P-doped OF.

Dose-rate	Total Ionizing Dose in Gy(SiO ₂)	Temperature
1 Gy/s	10 kGy	25°C (RT)
		50°C
		100°C
		150°C
		200°C
		250°C
		300°C

3.3.1. Evolution of UV-vis and NIR-RIA at RT

Figure 3.18 reports the spectral growth of the RIA in the UV-vis and NIR domain measured at RT. In the UV-vis range, it is possible to distinguish the contribution of several known point defects, as the P2, with a narrow absorption band peaked at ~280 nm, and the stable and metastable-POHCs, contributing to the absorption in the 400-600 nm spectral range. As far as the NIR spectral range is concerned, the RIA is on average two orders of magnitude less than the one recorded in the vis domain, with the main contribution of the optical absorption band due to the P1 point defect. From the figure it can be noticed, also, that the RIA grows with the accumulated dose without reaching the saturation at any of the investigated wavelengths, up to the maximal dose of 10 kGy.

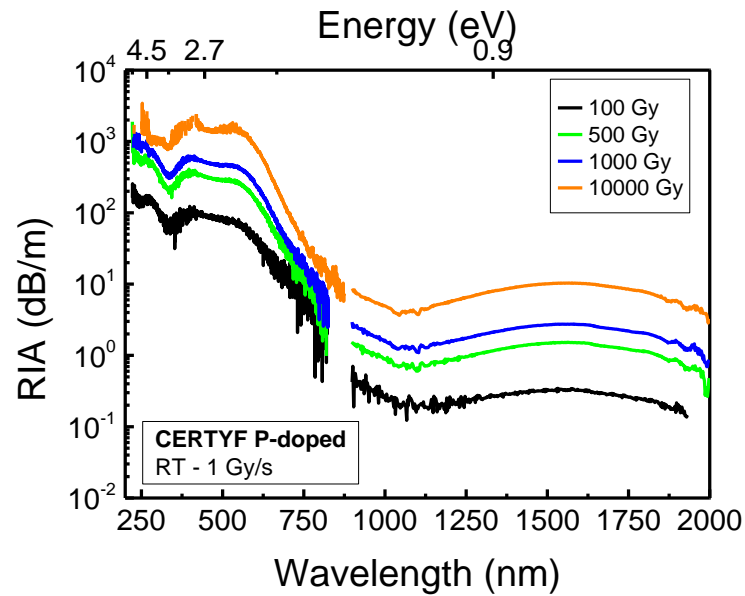


Figure 3.18 Evolution of the UV-vis and NIR RIA of the CERTYF P-doped sample measured at RT for the selected TIDs of 100, 500, 1000 and 10000 Gy.

As already said, the RIA is due to the absorption bands of the radiation-induced point defects. Figure 3.19 shows, as an example, the spectral decomposition of the RIA recorded at RT and at 10 kGy TID, with the single contribution of each point defect. The experimental data are well described by the absorption bands of the known defects, except for the 0.9 – 1.9 eV energy range where, as already known from literature [15], the contribution to the RIA is still difficult to attribute to a single or multiple absorption bands. Moreover, it is worth pointing out that, in this energy range, the effects of the propagation conditions of the different guided modes into the OF should be first considered when operating with SM OFs. In our case, being the cut-off wavelength of the sample under test around 1150 nm (~ 1.08 eV), the measured RIA for energies above 1.08 eV may be more impacted by the point defects that are present in the pure-silica cladding or more probably at the core-cladding interface, since a significant part of the optical power, that is guided into the OF, results distributed over propagation modes that more “illuminate” the cladding region than at lower energies. In literature have been recently reported cases of SM P-doped OF in which, to properly fit the RIA under steady-state radiation and in the energy range around ~ 1.6 eV, absorption bands related to s-a STHs have been introduced [127]. The same group also studied the RIA decay in the 1 – 2 eV energy range after a pulsed X-ray irradiation, observing a relevant contribution of the s-a variant of STH in the RIA of P-doped OFs [158]. However, in our case, the introduction of this type of color center was not supported by a RIA decay after the irradiation end (typical of s-a STHs) in the same energy range, then the RIA has to be attributed to other unknown contributions.

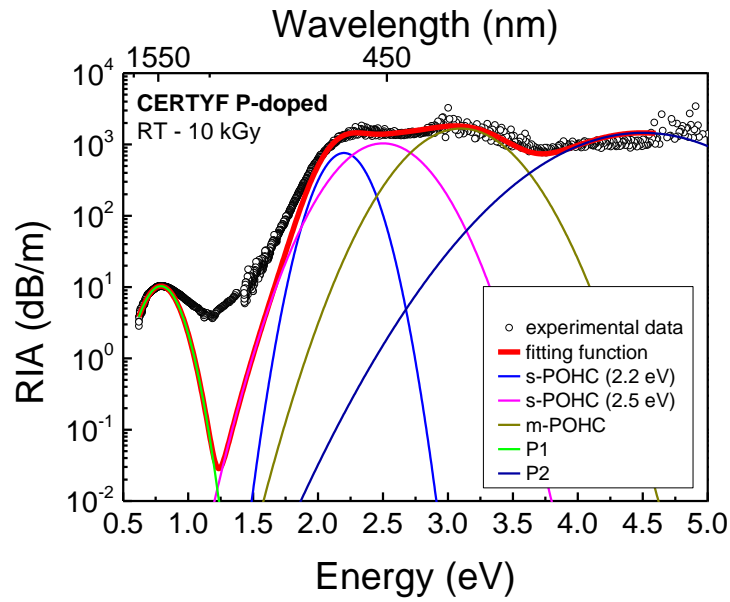


Figure 3.19 Spectral decomposition performed on the RIA at 10 kGy and at RT of the CERTYF P-doped sample, with considered Gaussian optical absorption bands of the color centers.

As far as recoveries are concerned, Figure 3.20 shows the RIA in the two investigated spectral domains up to ~3 hours (10000 s) after the end of the irradiation. In the UV-vis range, a significant reduction of the RIA is recorded as the recovery time increases. In particular, we distinguish a decrease of the POHC-related absorption bands, while the P2 color center appears more stable after the end of the irradiation. In the NIR range, the RIA is a lot more stable after the end of the irradiation: it should be pointed out a slight RIA increase (~2%) after ~3h from the irradiation end, a phenomenon related to the growth of the P1 absorption band, an already well documented process due to the conversion of POHC centers into P1 [39], [128].

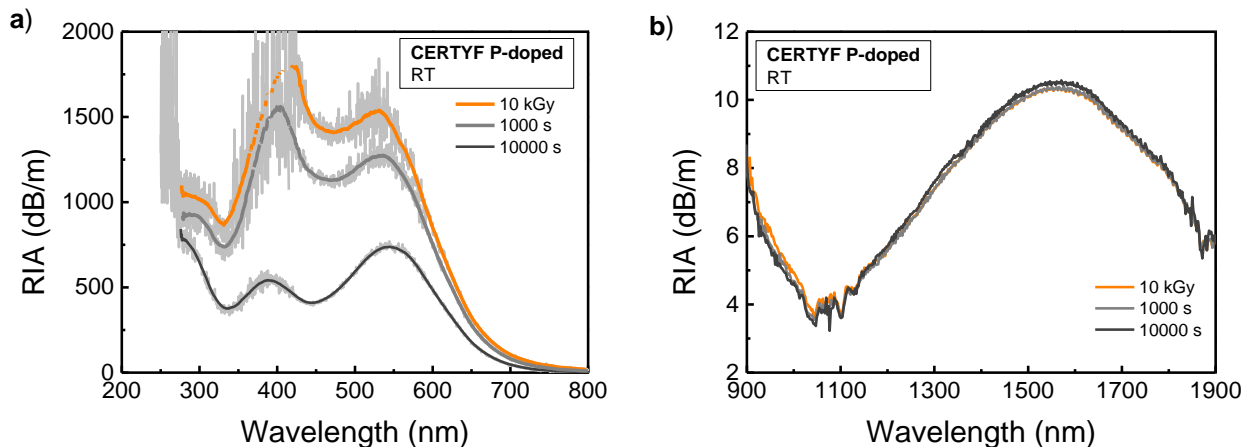


Figure 3.20 UV-vis (a) and NIR (b) RIA of the CERTYF P-doped sample, measured at the maximum TID (10 kGy), 1000 s and 10000 s after the end of the irradiation. This time the double linear scale was chosen to better highlight the different recovery behaviour in the two spectral domains. A smoothing function has been applied to the UV-vis data in order to remove fluctuations due to the noise (reported with the grey continuous line).

3.3.2. Temperature influence on the UV-vis and NIR RIA

Figure 3.21 reports the measured RIA at the maximum attained dose and at seven different irradiation temperatures, ranging from RT to 300°C. The figure highlights that the RIA peak around ~400 nm decreases with the increasing temperature, consistently with results reported in [33] and [115], a phenomenon that has been attributed to a lower generation rate (or higher conversion rate) of the m-POHCs at high temperatures. Furthermore, for temperatures higher than 100°C, we observe a decrease of the absorption peak around ~590 nm. Even though the combined contribution of the two s-POHC bands is significant in this spectral region, the observed RIA decrease could be due to the bleaching of the band peaked at 400 nm. Moreover, the temperature increase has no major impact in the 600-700 nm range, whereas a clear decreasing trend with the increasing temperature is observed in the 800-1100 nm region. At longer wavelength, the absorption band centered at about 1600 nm, and associated with P1 centers, appears to be not influenced by the irradiation temperature up to 200°C, then decreases at higher temperatures.

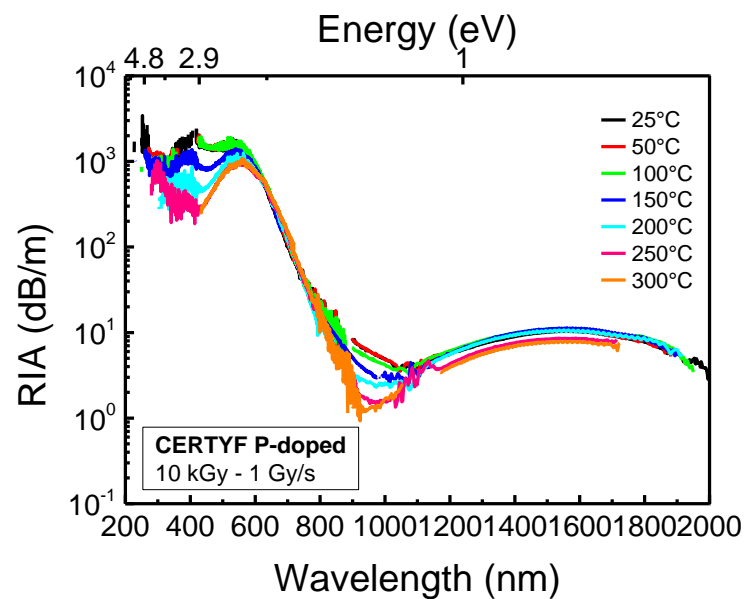


Figure 3.21 Spectral RIA of the CERTYF P-doped sample measured at the maximum TID of 10 kGy and at different irradiation temperatures.

To better investigate variations in the NIR, we subtracted the RIA spectrum at 25°C from the ones measured at the other temperatures. The measured RIAs were fitted with a high-degree polynomial function, this step allowed to remove fluctuations in the subtraction process. The results, reported in Figure 3.22, show the presence of a band centered between 1.7 and 1.8 eV. The shift of the band peak could not be significant, since it must be considered that in this spectral region several color centers contribute to the RIA and, moreover, their contributions can vary depending on the propagation condition of the guided modes. The spectral position of the detected band could lead to consider the s-a STHs as point defects

responsible for this absorption, but, since the band is stable even long time after the end of irradiation, we excluded this hypothesis. Furthermore, a negative contribution appears around 1.4 eV as the temperature increases.

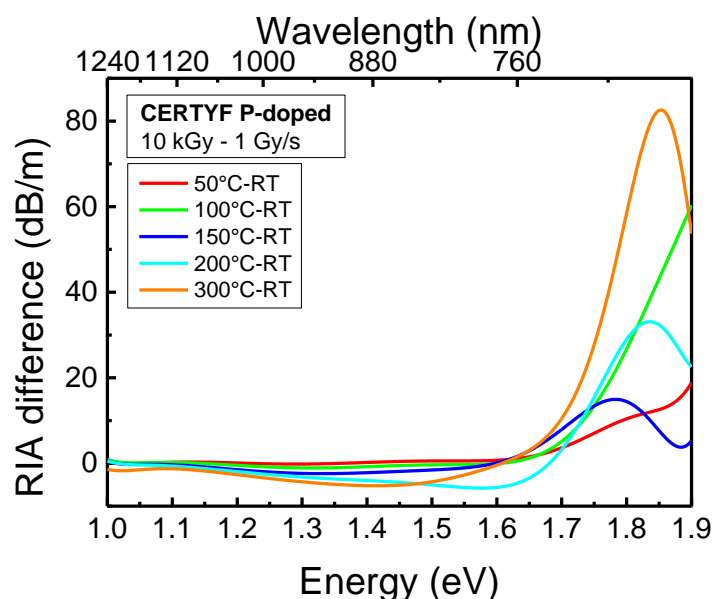


Figure 3.22 Results of subtraction between NIR RIA spectra measured at various temperatures and that measured at RT. To remove the fluctuations, the experimental data were approximated with a high-degree polynomial function.

To better highlight the combined effects of temperature and radiation on the RIA, Figure 3.23 reports separately the RIA in the UV/vis and NIR domains at 25°C, 150°C and 300°C, both at 10 kGy and ~3 hours after the end of irradiation. From the figure it is possible to observe that m-POHCs, which absorption is centered around ~400 nm, are very sensitive to the temperature increase, indeed their amplitude results maximum at RT, decreases significantly at 150°C and is almost zero at 300°C. Furthermore, the same absorption peak decreases after the end of the irradiation, reaching almost the same level at both 25°C and 150°C irradiation temperatures after ~3h from the irradiation stop. Also the absorption peak centered around 550 nm, which main contribution is due to s-POHC absorption bands (centered at ~500 and ~560 nm), revealed a sensitivity to the irradiation temperature. Indeed, its amplitude decreases by increasing the temperature. As far as concerns the NIR domain, the absorption band due to the P1 center results slightly increased at 150°C compared to the one measured at RT but, while during the recovery at RT it remains stable, at 150°C decreases of ~10% after ~3 hours from the irradiation stop. At 300°C, the same absorption band results ~30% lower than the one measured at RT but exhibits a very low recovery.

Same observations can be made by observing the RIA growth and recovery kinetics at the three selected wavelengths, as shown in Figure 3.24. Wavelengths of 400 nm, 550 nm and

1550 nm were chosen in such a manner to highlight, respectively, the metastable and stable POHCs, as well as the P1 color centers.

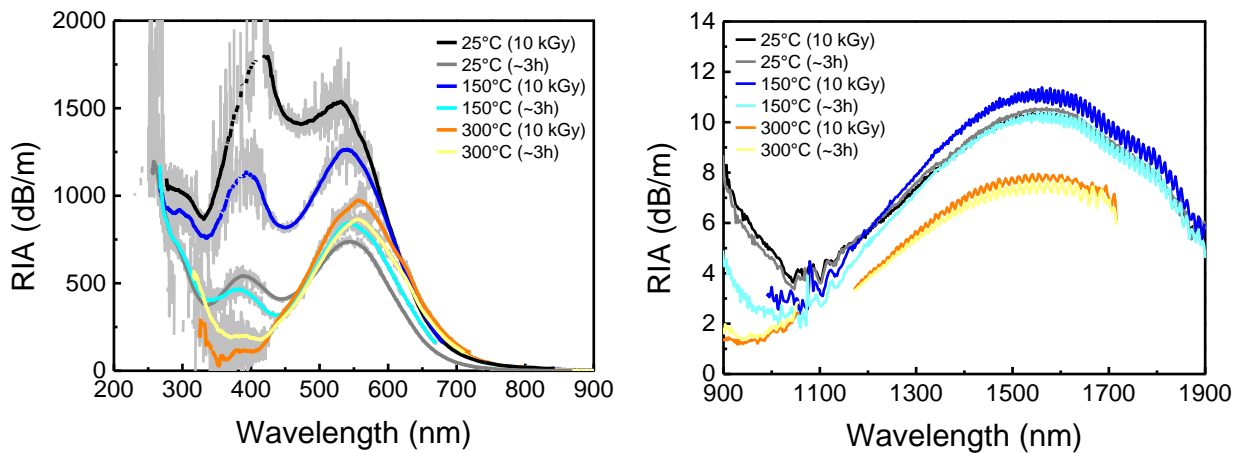


Figure 3.23 UV/vis (left) and NIR (right) RIA of the CERTYF P-doped sample recorded at 25°, 150 °C and 300°C, at 10 kGy and after ~3 hours from the irradiation end. A smoothing function has been applied to the UV-vis experimental data (reported with grey curves) in order to remove fluctuations due to the noise. In the NIR domain, the artifacts reported around ~1100 nm are probably due to the change of propagation conditions in the OF, from MM to SM.

The RIA growth kinetics at 400 nm shows a slight increase at 100°C (~18% at 2 kGy) with respect to the one at RT, in line with what reported in [36]. Above 100°C, 400 nm kinetics show lower RIA levels, growing with a sub-linear slope right after the irradiation start and reaching saturation levels at lower TIDs as the temperature increases. At 550 nm, the RIA reduces when increasing the temperature above 100°C and up to 250°C. The temperature increase above 250°C has no influence on the measured RIA at this wavelength, indicating that only high-temperature stable POHCs contribute to the attenuation. Furthermore, the slight RIA increase at 100°C results not significant (~5% higher than the values measured at RT and 50°C for a TID of 2 kGy, within the error associated with our measurements). At 1550 nm, RIA kinetics are superimposed up to ~2 kGy in the RT – 200°C temperature range, whereas, at higher doses the POHC into P1 conversion process becomes relevant (at 10 kGy, ~9% RIA increment at 100°C with respect to the one at RT). Finally, RIAs at 250°C and 300°C are significantly lower than the ones measured at all others temperatures, denoting a clear thermal-bleaching process of the P1 absorption centers.

Finally, we investigated the effect of the irradiation time (i.e. accumulated dose) on the measured RIA at the different temperatures. To this end, Figure 3.25 shows the ratio between the RIA values at several wavelengths (550 nm, 650 nm and 1550 nm) at all the investigated temperatures and the one at RT, and different TIDs during the irradiation. At 550 nm, increasing the temperature up to 100°C has a slight negative impact (ratio >1) on the measured RIA, at most increasing it by 10 % (at 100°C and 10 kGy).

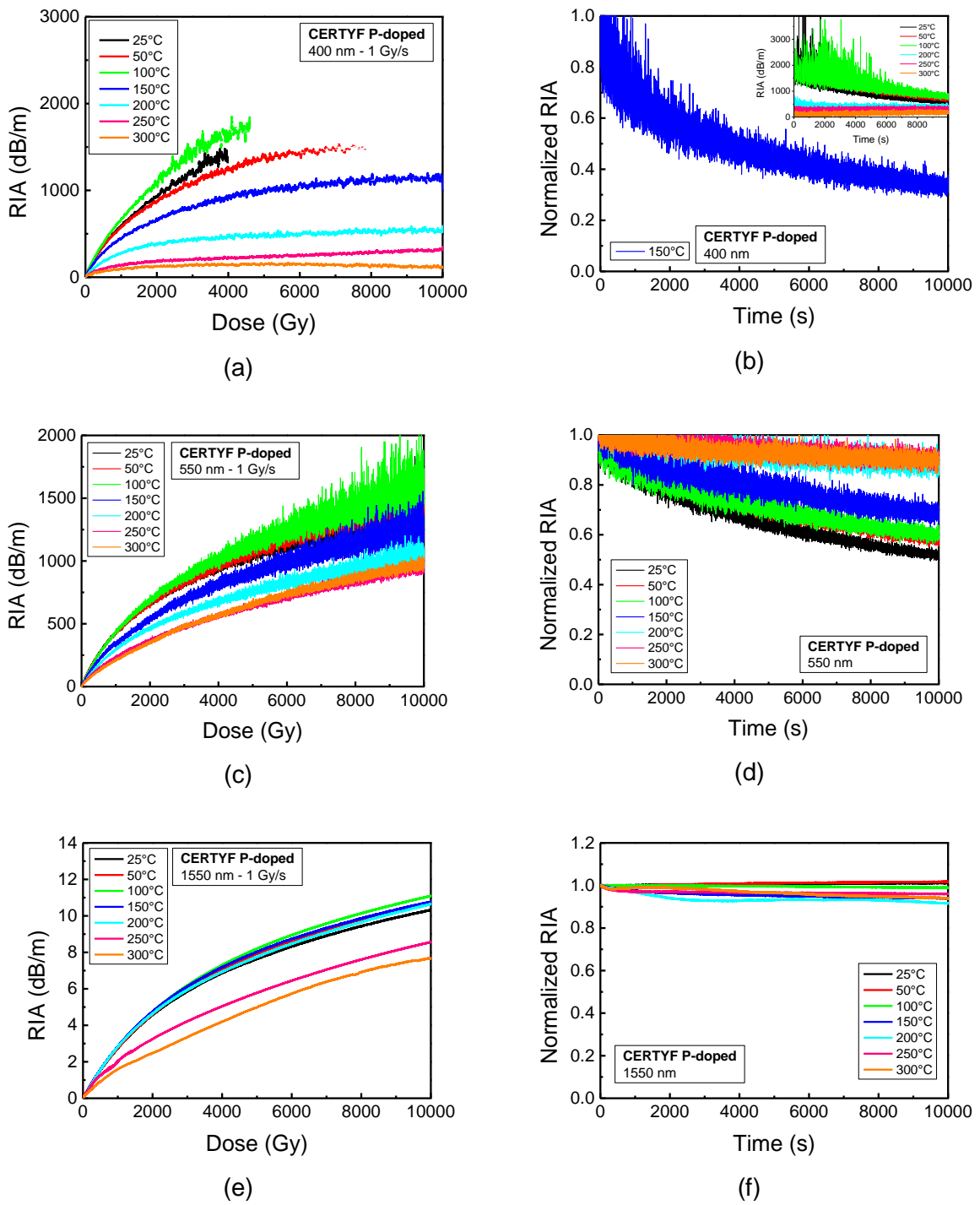


Figure 3.24 RIA growth and normalized (with respect to the value at 10 kGy) recovery kinetics of the CERTYF P-doped OF at three selected wavelengths: 400 nm (a, b), 550 nm (c, d) and 1550 nm (e, f). A smoothing function has been applied to the 400 nm kinetics. Furthermore, since the 400 nm RIA at 10 kGy was out of the detection limit of our experimental setup, the inset of figure (b) reports the non-normalized RIA kinetics at the same wavelength.

On the other hand, for temperatures higher than 100°C, a RIA reduction compared to the one at RT is observed and, generally, the positive effect of the temperature is reduced by the increasing of the accumulated dose. At 650 nm, a different behavior is observed: the

temperature increase has a general positive effect at low doses but, in each case, increasing the accumulated dose leads to a significant RIA increase. Indeed, at the maximum dose of 10 kGy, the RIA at all the investigated temperatures results higher than the one measured at RT. At 1550 nm, a temperature increase up to 200°C has a slight negative effect. Above 200°C the RIA is always lower compared to its RT value.

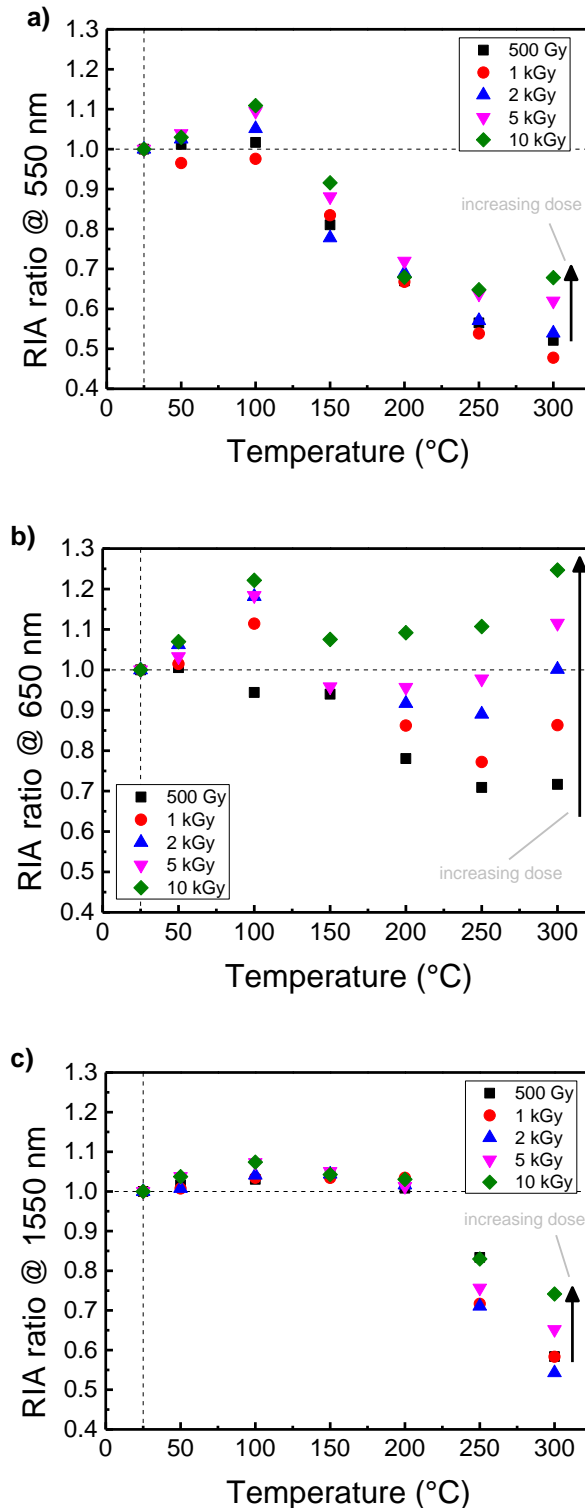


Figure 3.25 Ratio between the RIA values at all the investigated temperatures and the one at RT, at several TIDs during the irradiation and at 550 nm (a), 650 nm (b) and 1550 nm (c).

3.4. Operating temperature range of P-doped OF dosimeters exploiting NIR-RIA

This section presents our study about the temperature dependence of the radiation-sensitivity coefficients at 1550 nm (expressed in dB km⁻¹ Gy⁻¹) of the CERTYF P-doped OF (L28-01) and two others commercially available OFs manufactured by iXblue (details given in section 2.2.2.1). For the measurements, the experimental setup described in Figure 2.12 was used.

Details about the irradiation are given in Table 3.7. It is worth noting that the acrylate coating could be degraded at temperatures above 80°C, however this degradation will not influence the OF guiding properties. For each irradiation run and each type of sample, 2 m long pristine samples have been used.

Table 3.7 Irradiation details for the study about the RIA temperature dependency.

Dose-rate	Total Ionizing Dose in Gy(SiO ₂)	Temperature
1 Gy/s	1 kGy	-80°C
		-40°C
		-20°C
		20°C
		40°C
		80°C
		120°C
		160°C
		200°C
		250°C
		300°C

Furthermore, in order to verify if the RIA is still dose-rate independent at the various temperatures, a 5 m long sample of the P-doped iXblue polyimide coated OF has been irradiated at different dose-rates. Details about the performed irradiation are given in Table 3.8.

Table 3.8 Irradiation details for the study about dose-rate and temperature dependency.

Dose-rate	TID	Temperature			
10 mGy/s	15 Gy	20°C	40°C	80°C	120°C
100 mGy/s		20°C	40°C	80°C	120°C
1000 mGy/s	30 Gy	20°C	40°C	80°C	120°C

Figure 3.26 reports the refractive index profiles of the three tested OFs. As one can see, the two iXblue samples, despite having the same dopant concentration in the core, have different profiles. This is due to the very different drawing conditions, as already described in section 2.2.2.1. Furthermore, the same samples present a F-doped region at the core-cladding interface. As far as concerns the CERTYF sample, from the figure it is possible to see that the drawing conditions are similar to the ones applied to the iXblue polyimide sample. Furthermore, compared to both iXblue samples, the lower index contrast is due to a lower dopant concentration in the core.

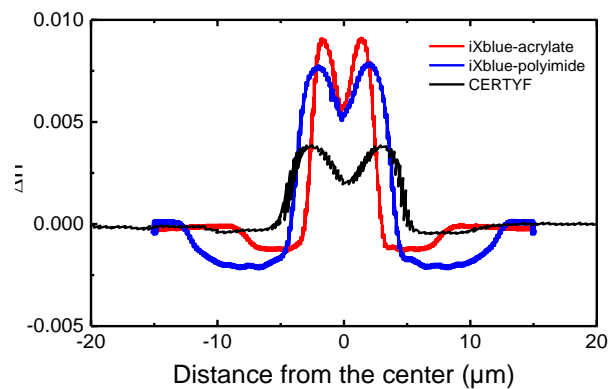


Figure 3.26 Profile of the refractive index contrast of the three P-doped OFs under test

3.4.1. Temperature effects on the radiation sensitivity of P-doped OFs

Figure 3.27 shows the RIA kinetics at 1550 nm as a function of the accumulated dose for the three fibers under test. We report only the kinetics at 1550 nm, instead of the P1 absorption band peak at 1570 nm, because most of commercially-available interrogators that can be used for monochromatic data acquisition operate at this wavelength. The figure reveals that all the samples exhibit a linear behaviour up to ~300 Gy. Moreover, the two fibers from iXblue with different coatings do not have exactly the same calibration curve at high doses: the acrylate coated sample seems slightly more radiation sensitive than the two others.

Figure 3.28, Figure 3.29 and Figure 3.30 report the 1550 nm RIA kinetics of the three samples, as a function of the dose, during the irradiation runs at different irradiation temperatures and as a function of the time after the end of the irradiation (in this case the kinetics are normalized to the RIA at the maximum TID). The linear dependence of RIA with dose is maintained for all samples and temperatures, whereas a small change in the fiber sensitivity (calculated through the slope of the RIA vs Dose curves) is observed. Moreover, for temperatures above 200°C, a clear reduction of the RIA levels during the irradiation and recoveries is observed (as discussed previously).

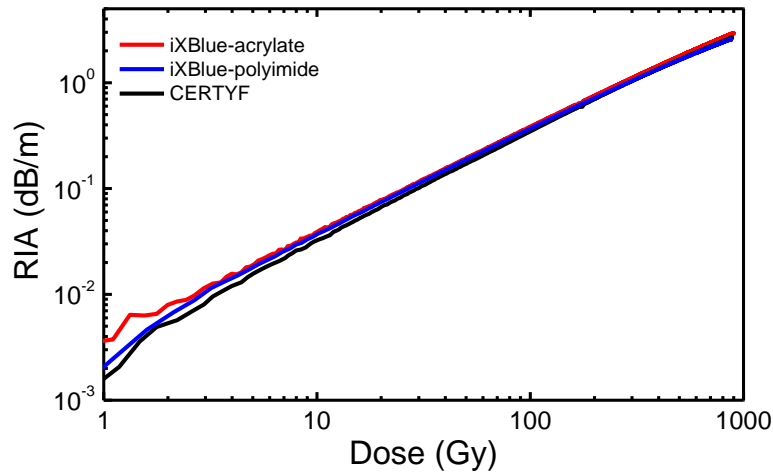


Figure 3.27 RIA kinetics at 1550 nm as a function of the dose, recorded at 20°C and at 1 Gy/s, up to a TID of 1 kGy for the three P-doped samples.

For temperatures up to 120°C, no rapid recovery effect exists after the irradiation end. For some samples, a slight RIA increase (less than 2%) is highlighted after the irradiation end. Such phenomenon has already been reported in the RIA of phosphosilicate OFs and is attributed to the conversion mechanism of the POHC point defects (absorbing in the UV-visible range) to the P1 (absorbing in the IR) [39]. For temperatures above 120°C, it is possible to observe a clear RIA decrease after irradiation: the annealing becomes more efficient as the temperature increases, except for the polyimide coated sample, for which the same RIA recovery has been recorded for temperatures between 200°C and 300°C. This result differs from the one reported by Griscom et al., who observed an increase in the P1 when applying a thermal treatment at temperatures up to 300°C after an irradiation at 77 K [39]. However, it has already been demonstrated by Girard et al. that the combined effects of radiation and temperature on the RIA differs from the one observed by applying a thermal treatment after the irradiation, performed in most cases at RT [36]. In fact, a high irradiation temperature could promote thermal bleaching of point defects, as observed in post-irradiation treatment. However, a higher temperature can also promote defect conversion: from an unstable defect to a more stable one at the investigated temperature, as the case of the conversion of POHCs into P1 defects.

By comparing the kinetics of the CERTYF sample with the ones of both iXblue samples, it can be observed that the former is less temperature-dependent. In this regard, Figure 3.31 reports the radiation sensitivities, calculated for doses lower than 300 Gy (where linear RIA kinetics are observed), at the different investigated temperatures. The sensitivities increase with the temperature from -80°C to 160°C and decrease at higher temperatures. The figure confirms that the temperature dependence of the CERTYF fiber is lower than the one of the other two samples, with variations within 10% at all investigated temperatures between -80°C and 250°C.

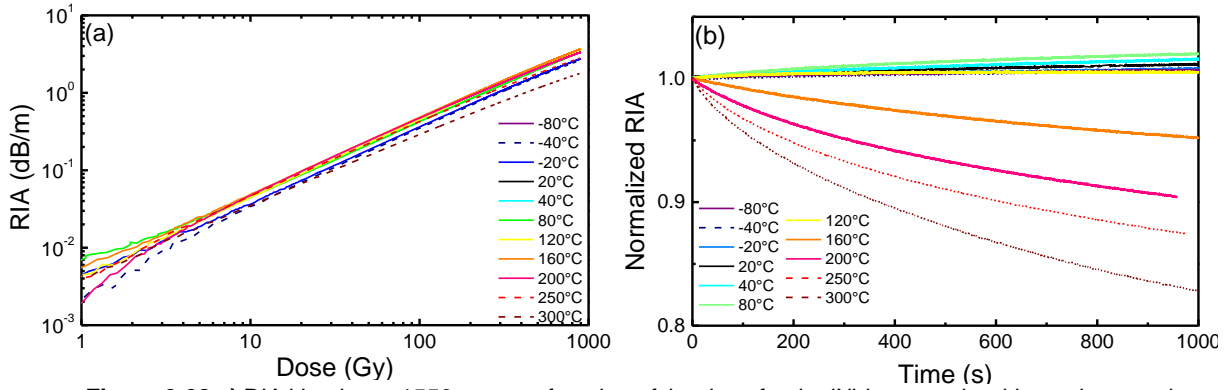


Figure 3.28 a) RIA kinetics at 1550 nm as a function of the dose for the iXblue sample with acrylate coating at different irradiation temperatures, up to TID of 1 kGy and at 1 Gy/s. **b)** RIA kinetics at 1550 nm after the end of the irradiation normalized to the RIA value at the end of the irradiation.

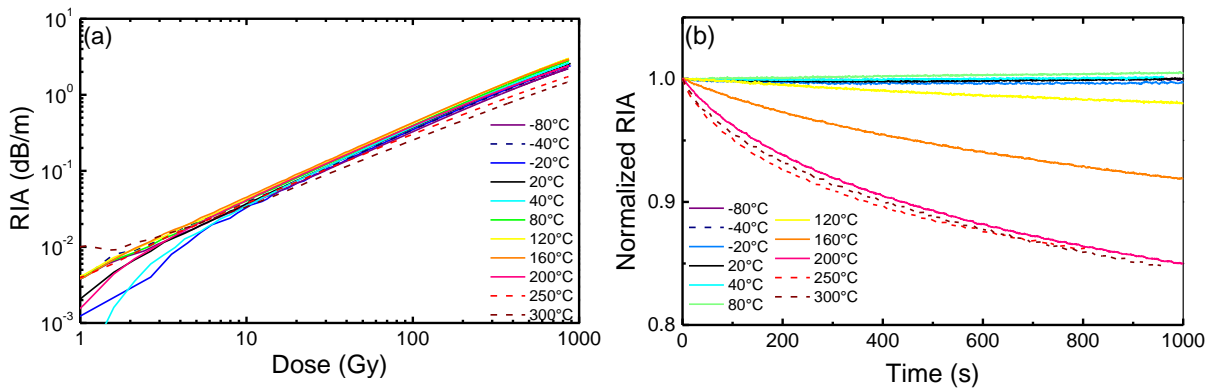


Figure 3.29 a) RIA kinetics at 1550 nm as a function of the dose for the iXblue sample with polyimide coating at different irradiation temperatures, up to TID of 1 kGy and at 1 Gy/s. **b)** RIA kinetics at 1550 nm after the end of the irradiation normalized to the RIA value at the end of the irradiation.

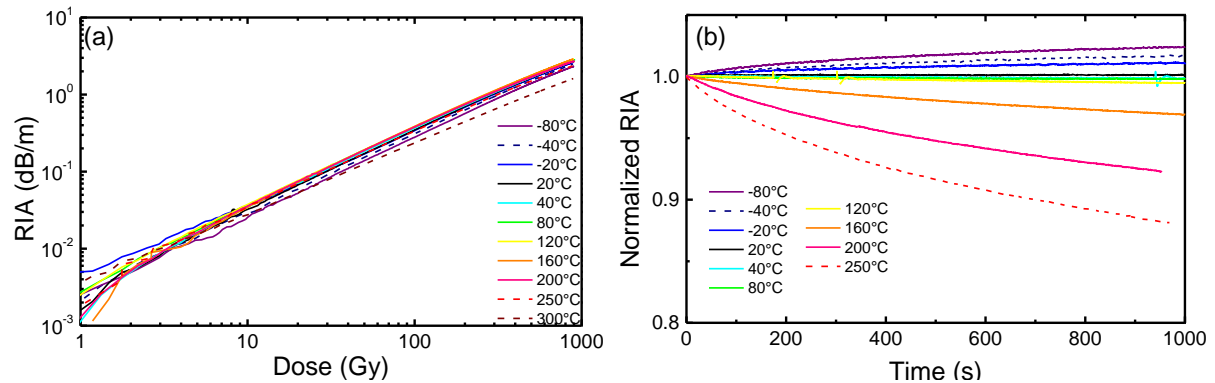


Figure 3.30 a) RIA kinetics at 1550 nm as a function of the dose for the CERTYF sample at different irradiation temperatures, up to TID of 1 kGy and at 1 Gy/s. **b)** RIA kinetics at 1550 nm after the end of the irradiation normalized to the RIA value at the end of the irradiation. On the other hand, for the iXblue samples, the variations are within 10% only in the range -40°C – 80°C. In addition, it is worth noticing that, for the polyimide coated sample, these variations are within the 15% for temperatures between -80°C and 200°C. For dosimetry applications, considering the RT sensitivity for experiments at any other temperature, a “wrong” detected dose will be obtained. However, the relative error induced on the dose measurement will be equal to the one on the sensitivity. Even if our experiments were all performed in the same conditions, it is important to point out that the dosimetry of the MoperiX irradiation chamber has an uncertainty of ~10%.

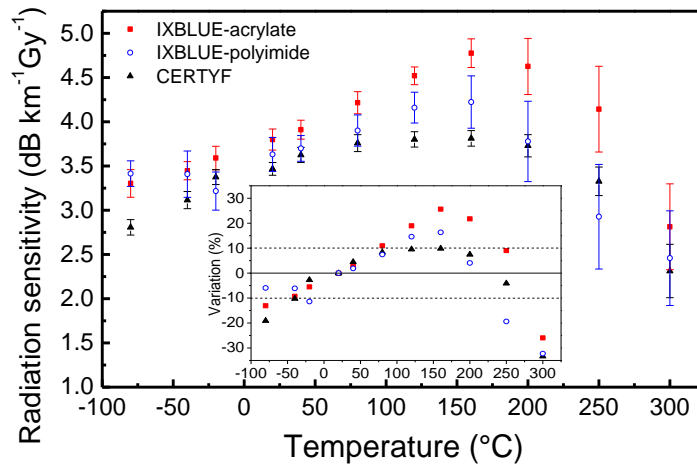


Figure 3.31 Radiation sensitivities of the three examined P-doped samples (calculated for doses below 300 Gy) at the different investigated temperatures. The inset shows the variation of the sensitivities compared to their values at 20°C.

In addition, the uncertainty associated with the CERTYF fiber is smaller than the one of the other two, meaning a more linear dose-dependent RIA curve in the range 0 – 300 Gy. The results here shown for the CERTYF sample agree with the ones reported in section 3.1.1.2, where the same OF has been irradiated at higher doses and dose-rate (up to 100 kGy at 10 Gy/s) and at different temperatures.

In order to highlight the consequences of a calibration performed at different temperatures or in different temperature ranges, Figure 3.32 shows the sensitivity variation evaluated in different temperature ranges. The values have been derived by performing a linear fit on the experimental data set constituted by the ones at the temperatures between the extreme values of the range, whereas the associated bar is the maximal variation between the coefficients related to the considered temperatures. The results obtained at temperatures higher than 120°C have not been considered, since the observed effects of the temperature already invalidate the good performances of the dosimeter.

In all cases, the radiation sensitivities vary in the several temperature ranges and the variation bars increase when the extreme values are taken into consideration, above all -80°C and 120°C. However, in the worst case, all the variations are lower than 15% for each sample.

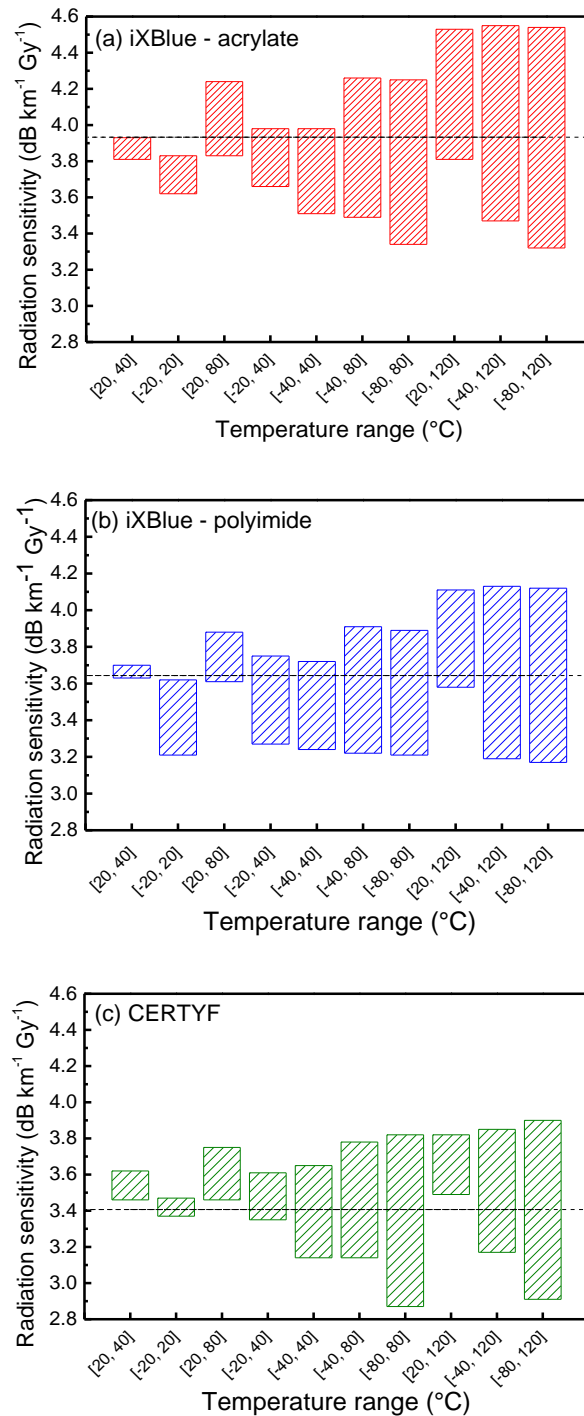


Figure 3.32 Radiation sensitivities evaluated in different temperature ranges, for the iXblue OFs **(a)** with acrylate and **(b)** polyimide coatings and **(c)** for the CERTYF sample. The horizontal line represents the mean value obtained for the widest temperature range [-80, 120] °C. The bars represent the sensitivity variation range.

3.4.2. Dose-rate effects on the radiation sensitivity of P-doped OFs at different temperatures

Finally, the effect of the dose-rate variation combined with the temperature variation has been analysed for the case of the iXblue polyimide coated OF. For the investigation, four temperatures have been considered in the range from 20°C to 120°C. This range is chosen

since it has been already observed that, at low temperatures, the RIA showed a behaviour similar to the one at RT, whereas a strong thermal bleaching at high temperatures prevents to use the fibers as dosimeters in such environments. Figure 3.33 reports the sensitivity coefficients as a function of the dose-rate at four temperatures. From the figure it is possible to observe that the sensitivity is independent from the temperature up to 120°C, within a 10% relative error associated with the irradiator dosimetry.

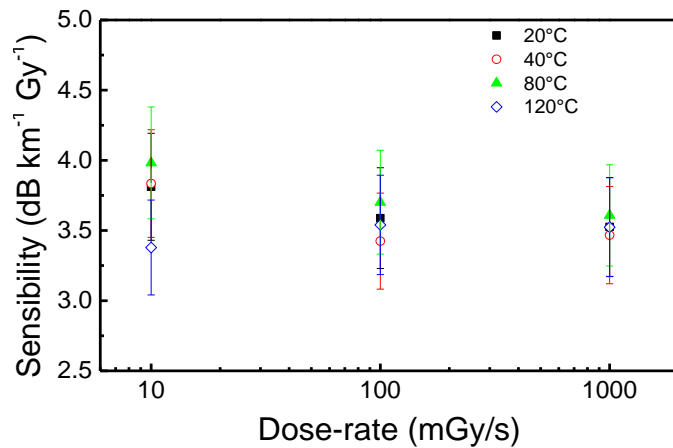


Figure 3.33 Radiation sensitivity coefficients related to the iXblue polyimide coated sample as a function of the dose-rate evaluated at four different temperatures in the range 20°C – 120°C.

3.4.3. Temperature effects on the NIR RIA spectrum

In Figure 3.34 is shown the NIR RIA of the iXblue polyimide coated OF, measured at 100 Gy (within the linearity range) and for different irradiation temperatures. Similar results have been found on the two others samples.

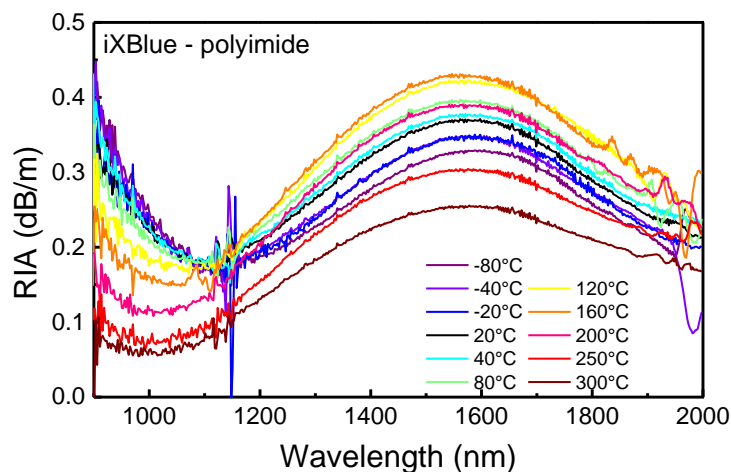


Figure 3.34 Spectral RIA measured at 100 Gy at different irradiation temperatures for the iXblue polyimide coated sample.

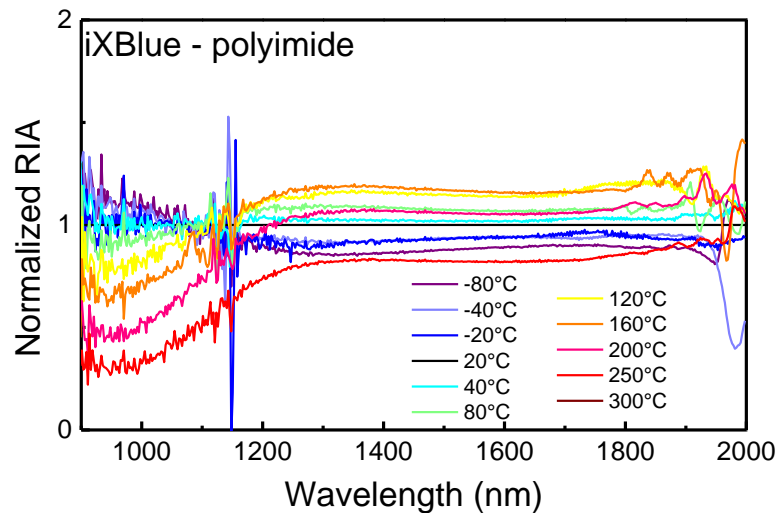


Figure 3.35 Spectral RIA, normalized to the RIA at RT, measured at 100 Gy at different irradiation temperatures for the iXBlue polyimide coated sample.

The RIA in this spectral range is attributed to different contributors [15]: the tail of the POHC absorption band peaked around 500 nm, one or more unknown absorption bands peaked in the range 700 - 1000 nm (that have not been yet attributed to a specific colour center but are typically observed in phosphosilicate OFs) and the P1 absorption band, centred at ~1550 nm. In Figure 3.35 is reported the same spectral RIA but after a normalization to the one obtained at RT. It can be seen that, in the range 1300 nm – 1800 nm, the normalized RIA remains constant, suggesting that the absorption in this region is only due to the P1 point defect.

The RIA variations due to temperature and observed around 1550 nm can be attributed to a different efficiency of the P1 generation or bleaching process during the irradiation. In addition, we should not exclude that the temperature variation could have some effects on the modal propagation inside the fiber. Indeed, the refractive index profile of the P-doped core and pure-silica cladding can be modified with the temperature, altering the radial distribution of the intensity of the guided mode(s) that, in turn, affects the overlap between the fundamental mode and the P-related defects located only in the fiber core, resulting in a variation of the RIA levels at 1550, as reported in [129]. These effects should be further investigated but, from the dosimetry point of view, they cannot be easily mitigated and, in any case, they should have a minor contribution. Indeed, as already said at the beginning of this section, the investigated samples exhibit the same temperature dependence despite the different refractive index profiles (Figure 3.26).

Figure 3.36 shows the generation and bleaching processes related to the P1 defect. Here, the RIA at 1000 nm and 1550 nm, normalized with respect to its value at RT, is reported as a function of the irradiation temperature, for different TIDs and for all the three samples. Assuming that losses at 1000 nm are due to POHCs, from the figure it is possible to see that,

when the temperature increases from -80°C to 160°C , the conversion of POHCs into P1 is increasingly favoured, since the former decreases when the latter increases. However, it is worth noticing that, between -80°C and 80°C , the variations are very small (within 10%) compared to the RIA values measured at RT. Instead, for temperatures above 160°C , the concentration of both color centers decreases, proving that both are thermally bleached. This conclusion is demonstrated by the fact that the efficiency of the two phenomena (interconversion or thermal bleaching) increases at higher doses (corresponding also to longer time of thermal treatments for the radiation induced defects). Finally, we would like to emphasise the same trends have been found in the three fibers, from two different manufacturers, supporting the idea that the temperature dependence is rather related to the fiber composition than to its refractive index profile.

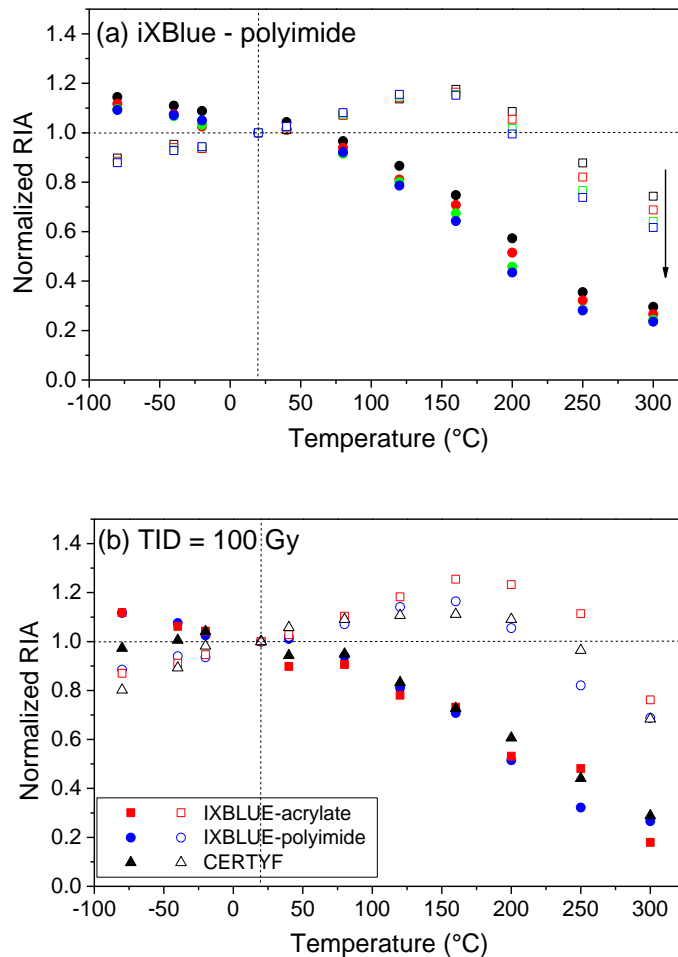


Figure 3.36 a) RIA, normalized to its value at RT, at 1000 nm (full circles) and 1550 nm (empty squares) as a function of the temperature for the iXblue polyimide coated sample at different TID (50 Gy – black, 100 Gy – red, 200 Gy – green, 300 Gy – blue). The arrow indicates the direction of the increasing doses. **b)** RIA, normalized with respect to its value at RT, at 1000 nm and 1550 nm (full and empty symbols, respectively) as a function of the temperature for the different tested OFs (iXblue acrylate – red squares, iXblue polyimide – blue circles, CERTYF – black triangles) at TID of 100 Gy.

3.5. Summary

In this chapter, we presented the response to combined radiation and temperature exposure of different types of radiation-sensitive OFs. RIA kinetics measurements at the telecommunication wavelengths revealed that Al-doped OFs are the most sensitive to radiations while the GeP-codoped ones are the less sensitive. In addition, an excellent reproducibility of the results has been shown, with a relative uncertainty less than 8%.

With regard to Al-doped OFs, the irradiation temperature impacts significantly the RIA in the NIR domain. Indeed, measuring the RIA with two different experimental setup (LD + PM and WLS + spectrometer) and at two different dose-rates and TID ranges, a RIA decrease is observed when the temperature increases. Furthermore, while the RIA in the visible domain is entirely due to Al-OHCs, no evidence of absorption bands in the NIR is found. In addition, the different temperature dependence of Al-OHCs and defects responsible for the NIR absorption suggests that the two color centers are not correlated. Moreover, a linear relationship between the level and dose at which the 1550 nm RIA reaches an equilibrium level highlights a direct generation process of the absorbers responsible for the RIA at this wavelength and, more generally, in the NIR, where the RIA is due to a single and not to multiple absorption components, characterized by a continuum of absorption states.

As far as concerns P-doped OFs, the RIA due to m-POHC absorption bands decreases with the increasing irradiation temperature, whereas the temperature increase has no major impact in the 600 - 700 nm range. Furthermore, a clear decreasing trend with the increasing temperature is observed in the 800 – 1100 nm region, whereas the P1 absorption band is not influenced by the temperature up to 200°C.

P-doped OFs can be used as dosimeters since, thanks to the optical properties of the P1 defect absorbing around 1.6 μm , the RIA linearly increases with the dose up to hundreds of Gy(SiO_2) and does not show any recovery after irradiation, at least for irradiation temperatures up to 120°C. For temperatures exceeding 120°C, the P1 defects start recombining, as proved by our post irradiation RIA recovery measurements. The comparison between the CERTYF sample and other two COTS samples, one acrylate- and one polyimide-coated, revealed, globally, the same performances. From an applicative point of view, the study of the operative temperature of OF-based dosimeters reported that temperature changes, ranging from -80°C to 120°C, do not affect significantly the good performances of the based dosimeters, since the sensitivity variations are within $\pm 15\%$. Finally, the independence of this sensitivity from the dose-rate was also verified between 10 mGy s^{-1} and 1 Gy s^{-1} at temperatures up to 120°C.

Chapter 4: Combined radiation and temperature effects on radiation-tolerant optical fibers

This chapter is devoted to the description and discussion of the results obtained on Ge-doped OFs and is divided into three main sections:

- study of the influence of the 1550 nm probing signal power on the RIA levels of the CERTYF Ge-doped OF and the Corning SMF-28e⁺. In this same section, the NIR RIA at very high TIDs on the SMF-28e⁺ is analysed;
- study of the combined effects of radiation and temperature on the RIA of the Corning SMF-28e⁺ OF at the telecommunication wavelengths;
- study of the combined effects of radiation and temperature on the spectral RIA in the vis/NIR domain on a canonical Ge-doped MM OF.

4.1. Effect of the probing light power level on the RIA of Ge-doped OFs at telecommunication wavelengths

This section reports the results concerning the study on the effects of the probing light power (see section 1.3.2.6) on the RIA at 1550 nm on two Ge-doped OFs: the CERTYF Ge-doped (R27-03) and the Corning SMF-28e⁺. Both samples were investigated up to a TID of 100 kGy and at a dose-rate of 0.4 Gy s⁻¹ (spatial homogeneity being 1%). Afterwards, new pristine samples of SMF-28e⁺ were tested at the same wavelength but at much higher irradiation doses, up to ~9 MGy s⁻¹, with a dose-rate of 6 Gy s⁻¹ (spatial homogeneity of 11%). All the irradiations were performed at RT and with the experimental setup described in section

2.5.2 and with 10 m long samples. The details of the performed irradiation are summarised in Table 4.1.

Table 4.1 Irradiation details of the photobleaching tests on Ge-doped OFs.

Dose-rate	Total Ionizing Dose	Temperature
0.4 Gy s ⁻¹	100 kGy	RT
6 Gy s ⁻¹	~9 MGy	RT

4.1.1. Irradiations at 0.4 Gy s⁻¹

Figure 4.1 shows the RIA kinetics of the SMF-28e⁺ during and after the irradiation at 0.4 Gy s⁻¹ up to a TID of 100 kGy. In order to test four different samples simultaneously, we decided not to save the fourth channel for the monitoring of the source, under the assumption that this one has no fluctuation for a short irradiation period (which was confirmed by the acquisition of the reference signals in others experiments). The 1550 nm probing signals propagating into the four samples range from 1 μW to 2 mW. It should be specified that these power levels are the ones measured at the input of the power meter before the irradiation start.

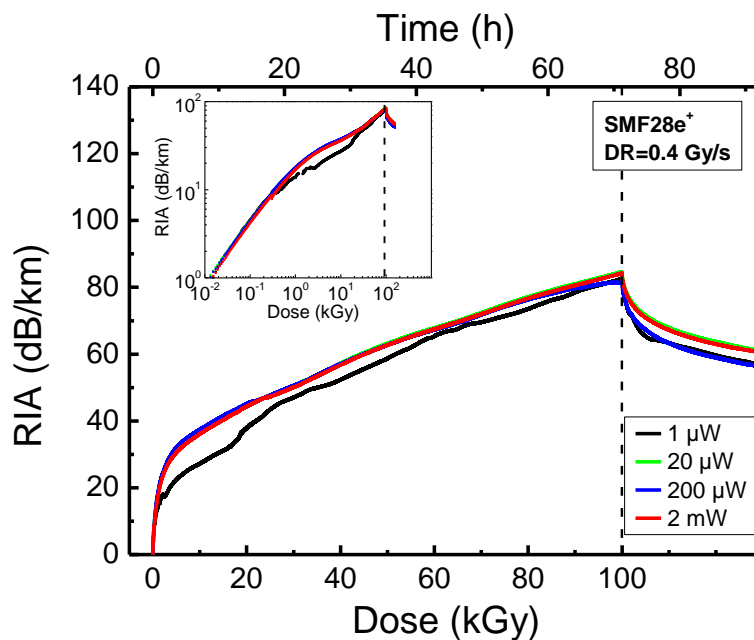


Figure 4.1 RIA kinetics of the Corning SMF-28e⁺ at 0.4 Gy s⁻¹ with different power levels of the 1550 nm probing signal. The dashed vertical line at 100 kGy marks the end of the irradiation. The signal at 1 μW showed some fluctuations during the experiment, which explains the RIA variations. In the inset, the same kinetics are shown on a double logarithmic scale.

All four kinetics show very similar dose dependences: initially the RIA quickly increases up to a TID of ~4 kGy, after it continues to grow but with a lower slope. The inset of Figure 4.1 reports the same curves but in a log-log scale, making it possible to better appreciate the results at low doses. At this dose-rate, the maximum induced attenuation, reached at 100 kGy,

is about 80 dB km^{-1} . It can be observed that the power levels of the probing signal do not affect the RIA kinetics, revealing a variation of less than 3 dB km^{-1} (less than 4% of the absolute value) at 100 kGy TID. Therefore, it is possible to assume that no photobleaching phenomenon takes place in our conditions.

Figure 4.2 shows, instead, the results obtained on the CERTYF sample when exposed to an irradiation in the same conditions. In this case, a longer length of the pre-irradiated P-doped attenuator was used in the first channel in order to investigate lower powers. The fluctuations observed in the 200 nW kinetic are due to the fact that, as the RIA increases during irradiation, the signal to noise ratio decreases and, therefore, the source variations, despite being small, are no longer negligible. Contrary to the SMF-28e⁺ case, the CERTYF sample shows a monotonic RIA decrease when increasing the injected power of the probing signal. Indeed, the kinetics at 200 nW and $280 \text{ }\mu\text{W}$ have different behaviours after a dose of 2 kGy , obtaining a total RIA of 60 dB km^{-1} and 53 dB km^{-1} at 100 kGy , respectively. Furthermore, the 2 mW RIA kinetic shows lower levels over the whole irradiation period, reaching an attenuation of 45 dB km^{-1} at 100 kGy . Moreover, it is worth noticing that the CERTYF sample has a lower RIA than the SMF-28e⁺ at 100 kGy .

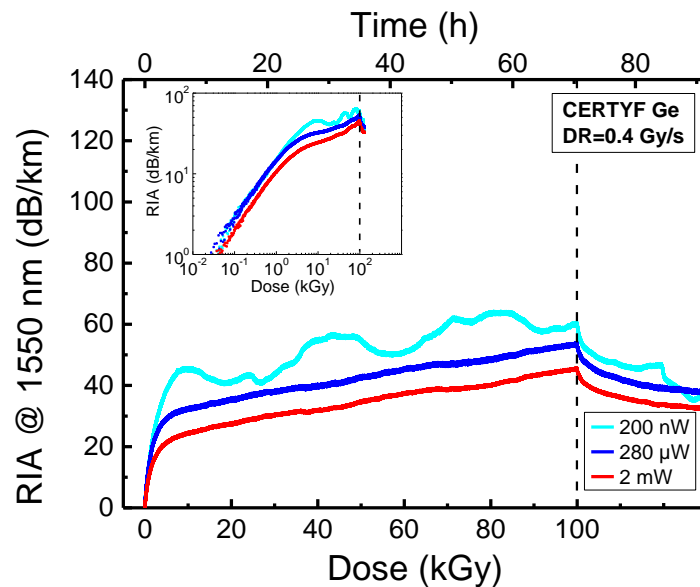


Figure 4.2 RIA kinetics of the CERTYF sample measured with different power levels of the probing signal at 1550 nm , irradiation performed at 0.4 Gy s^{-1} up to 100 kGy . The inset reports the same kinetics but on a log-log scale. The curve related to the second channel (the one devoted to few μW power levels) was omitted due to excessively noisy results.

From both insets of Figure 4.1 and Figure 4.2 it is evident that the shape of the RIAs could not be represented by a single component growth kinetics, revealing a *multiregime* nature of the measured RIA.

4.1.2. Irradiations at 6 Gy s^{-1} for TID at MGy levels

In order to investigate the possibility of a photobleaching phenomenon on the SMF-28e+ at higher doses, this was irradiated up to a TID of $\sim 9 \text{ MGy}$. To minimize the time required for such experiment, the dose-rate was increased to 6 Gy s^{-1} , resulting in a 17 days irradiation run. Moreover, due to the long irradiation, the reference line was restored to monitor the source signal, as shown in Figure 2.14 to correct potential source fluctuation during the analysis. With these conditions, two irradiation runs have been performed in order to investigate additional power levels of the probing signal, by varying the lengths of the P-doped OFs used as attenuators. Furthermore, a spectra RIA measurement was performed on a new pristine sample (experimental setup shown in Figure 2.12), in such a way to compare its RIA kinetics with those resulting from the previous setup. The results are reported in Figure 4.3.

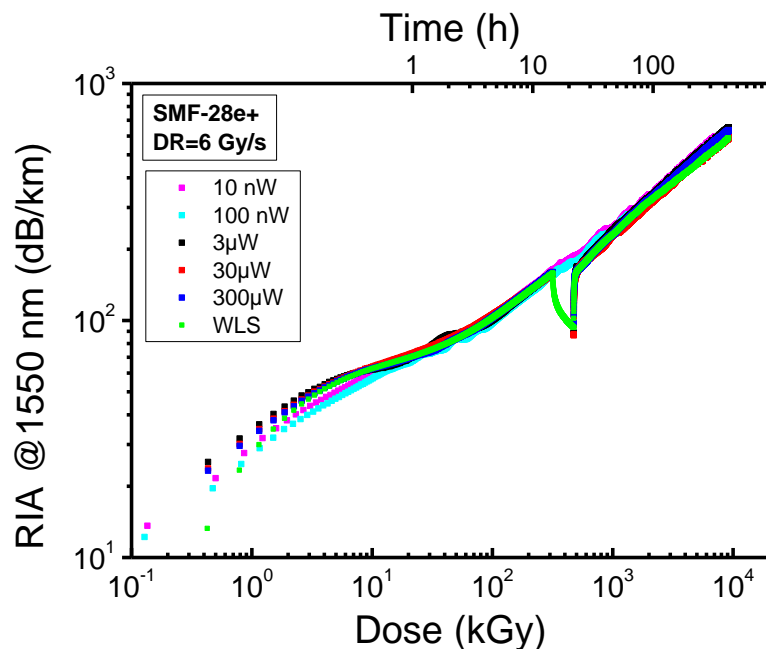


Figure 4.3 1550 nm RIA kinetics at 6 Gy s^{-1} of the SMF-28e+ samples probed with different power level signals and with a white light source (WLS) and a spectrometer. The short RIA decrease around 0.4 MGy is due to a temporary stop of the MoperiX facility.

As illustrated in the figure, the RIA growth still changes its slope at doses of about 4 kGy, despite a different dose-rate. As already reported in [30], [31], in the case of Ge-doped OFs, a higher dose-rate gives rise to a higher RIA, for equal accumulated dose. In this particular case, at a dose-rate of 6 Gy s^{-1} , an increase of 20% in the RIA has been measured at a TID of 100 kGy compared to the value obtained at 0.4 Gy s^{-1} . It was found that, even for doses well above 100 kGy, the considered signal power levels do not affect significantly the behaviour in the RIA growth. In fact, even at extremely high doses, there is no substantial difference ($\sim 10\%$ at the maximum dose) between all the recorded kinetics. This can be said while considering the uncertainty in the dose-rate measurement for each sample which,

despite being very low, leads to more and more significant deviations between the curves after several days of irradiation.

4.1.3. Modelling of the experimental RIA kinetics

Observing the kinetics in Figure 4.1, Figure 4.2 and Figure 4.3, a *multiregime* nature of the RIA is found. The two regimes are constituted by a first part, up to 2-4 kGy, in which the RIA growth with the dose is steep, and a second one, where it continues to increase but with a lower slope. This trend is frequently encountered in Ge-doped OFs since, as already shown by Van Uffelen in [31], the first regime corresponds to a period in which the main RIA contribution arises from precursor sites that are easily transformed into optically-active defects by the radiations. As their concentration is decreasing with the dose, other less-favourable processes start to be able to contribute more to the RIA, becoming the main defect generation process during the second regime. Referring to Figure 4.3, the creation of defects from regular Si-O-Ge bonds under radiation could, for example, justify the quasi-linear growth of the RIA for TID above 1 MGy.

In order to provide a quantitative description of the photobleaching effect on the RIA measured for the CERTYF OF and reported in Figure 4.2, a fitting routine based on the *second-order growth kinetics* model of Griscom [159] was carried out, since kinetics concerning recombination of electrons and holes should be described by a second-order process. In this model, the growth kinetic of a single contribution is expressed by the equation:

$$\text{RIA} = N \cdot \tanh(kx)^\beta \quad (4.1)$$

where N is the saturation level, proportional to the number of absorbers and to the oscillator strength of the defect, k is a parameter linked to the activation rate of the defect and β is an adimensional parameter, with $0 < \beta \leq 1$, which is used to describe the chemical and configurational disorder of the induced colour centers. Finally, x is either the time or the dose. In order to describe the measured kinetics, a two-component fitting function has been identified:

$$\text{RIA} = N_1 \cdot \tanh(k_1x)^{\beta_1} + N_2 \cdot \tanh(k_2x)^{\beta_2} \quad (4.2)$$

which well reproduces the experimental RIA measured for the CERTYF fiber. Based on the best-fit parameters, it is possible to describe the bleaching processes affecting the OF response.

Figure 4.4 reports the experimental measured RIA of the CERTYF Ge-doped OF and the results of the fitting routine obtained using equation (4.2). The relative parameters are listed in Table 4.2.

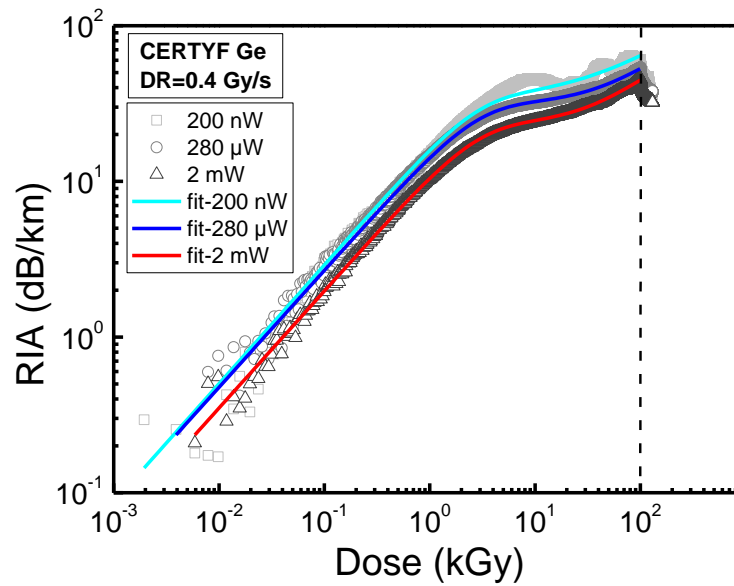


Figure 4.4 Results of the fitting routine using the model described in equation (4.2) concerning the RIAs of the CERTYF Ge-doped OF, at 0.4 Gy s^{-1} and measured with different power levels of the probing signal at 1550 nm (continuous lines). The figure reports also the experimental RIA measured with a 200 nW (empty squares), 280 μW (empty circles) and 2 mW (empty triangles) probing signal.

Table 4.2 Best-fit parameters obtained with the fitting routine on the CERTYF Ge-doped OF 1550 nm RIA kinetics at 0.4 Gy s^{-1} up to 100 kGy.

Fit parameter	200 nW	280 μW	2 mW
N_1 (dB km $^{-1}$)	30	30	20
k_1 (kGy $^{-1}$)	0.4	0.4	0.4
β_1	0.75	0.75	0.75
N_2 (dB km $^{-1}$)	85	45	40
k_2 (kGy $^{-1}$)	2.7×10^{-3}	5.5×10^{-3}	6.3×10^{-3}
β_2	0.7	1	1

According to the experimental data, the RIA remains unaltered up to ~ 2 kGy when measured with probing signal powers of 200 nW and 280 μW , whereas, above 2 kGy, lower radiation-induced losses at 280 μW are detected. The fitting routine well describes this behaviour, since it reports the same values for the parameters referring to the first contribution (the first component of the multi-regime kinetics), with $N_1 = 30 \text{ dB km}^{-1}$, $k_1 = 0.4 \text{ kGy}^{-1}$ and $\beta_1 = 0.75$. Looking at the second contribution (TID > 2 kGy), it is possible to notice that the RIA at 280 μW is smaller than the one at 200 nW, a trend that can also be seen in the fit parameters. Consequently, the bleaching experienced by the curve at 280 μW is limited to the bleaching of the second component. Furthermore, for the RIA curve at 2 mW, a global bleaching is observed in both contributions to the kinetics, as observed in the parameters of the best-fit.

In conclusion, our fitting routine does not provide a single parameter to describe the whole bleaching phenomena, but shows that the observed bleaching is a macroscopic effect

due to all the parameters present in the single-component contribution described by (4.1). Nevertheless, it is important to note how the value of N_1 and N_2 , which represents the saturation value of the RIA and is therefore linked to the number of induced defects, decreases monotonically as bleaching efficiency increases. Moreover, the increase of the β_2 parameter between the 200 nW measurements and the other two measurements (where $\beta_2=1$) would suggest that the photobleaching reduces the configurational disorder of the defects generated during irradiation. Ultimately, the fitting routine based on the second-order model proposed by Griscom [159] could be used as an empirical model to describe the photobleaching effect in OFs.

4.1.4. Spectral NIR RIA at high doses

Figure 4.5 reports the spectral NIR RIA at different selected doses during a 6 Gy s^{-1} irradiation up to a TID of $\sim 9 \text{ MGy}$ at RT and up to 1 day after the end of the irradiation, measured on the Corning SMF-28e⁺ OF. Two separate contributions to the RIA can be distinguished: a first one that is mainly responsible for the absorption at wavelengths lower than $\sim 1100 \text{ nm}$, and a second one absorbing at longer wavelengths. Furthermore, these two contributions show different kinetics with respect to the increasing dose: the first one has a steep growth right after the beginning of the irradiation and up to a TID of $\sim 5 \text{ kGy}$, after which it reaches an equilibrium state; the second contribution appears to have a negligible impact on the RIA at lower doses than 1 kGy , whereas it begins to increase significantly at higher doses. To further highlight the two different RIA evolutions, Figure 4.6 shows the RIA kinetics at 900 nm and 1625 nm , wavelengths that have been chosen as representatives of the two different contributions. The figure highlights that both kinetics have a steep growth right after the start of the irradiation but, while the 900 nm kinetics reaches an equilibrium value at a dose of $\sim 5 \text{ kGy}$, the 1625 nm one continues to grow but with a slower and almost constant slope until the irradiation end. Finally, Figure 4.7 reports the RIA recovery kinetics at the same two wavelengths and after being normalized to their value at the highest TID, as a function of the time up to $\sim 24 \text{ hours}$ after the end of the irradiation. The two RIA contributions show different decays: the one at 900 nm is faster, recovering almost 60% of the RIA after 27 hours, whereas the one at 1625 nm recovers only 20% of the RIA in the same time.

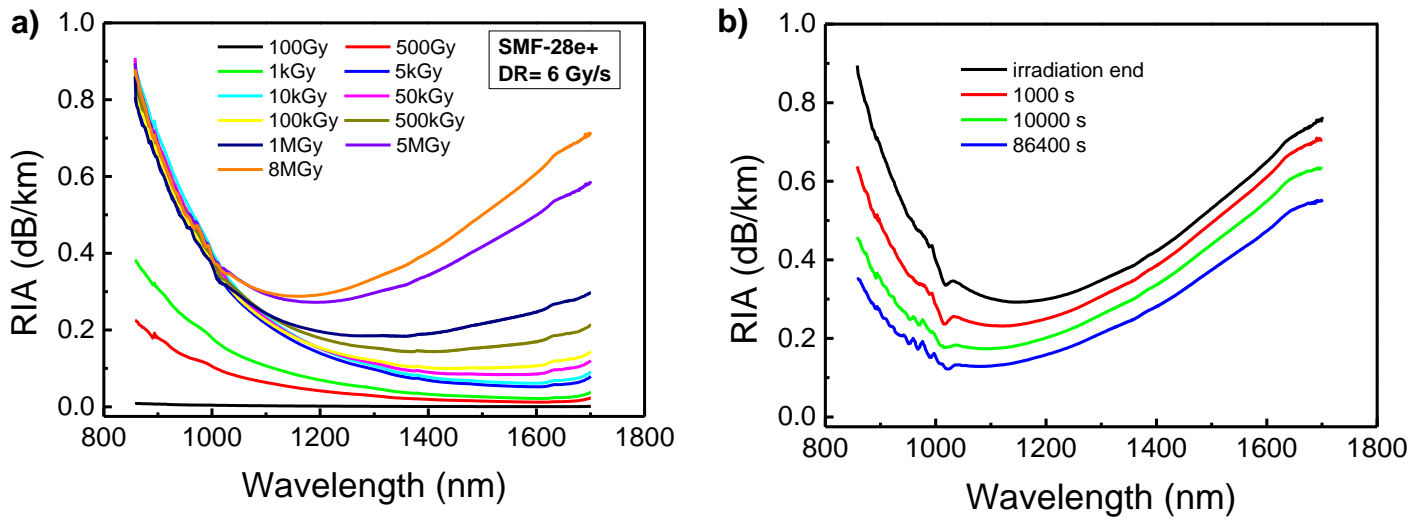


Figure 4.5 Spectral RIA during (a) and after the end of the irradiation (b) up to ~9 MGy with a dose-rate of 6 Gy s⁻¹ and at RT, measured in the NIR domain for the Corning SMF-28e⁺ OF.

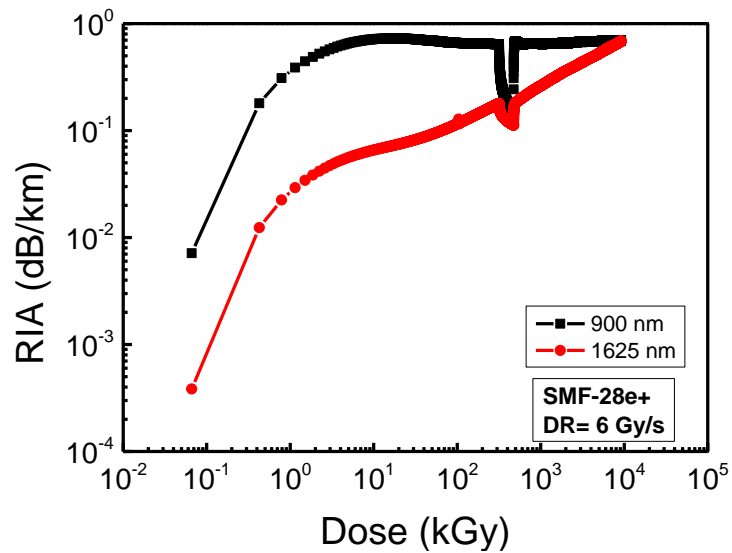


Figure 4.6 RIA kinetics at 900 nm and 1625 nm of the Corning SMF-28e⁺ OF, irradiated up to ~9 MGy at 6 Gy s⁻¹ and RT. The perturbation at ~400 kGy is due to a temporary irradiation shutdown.

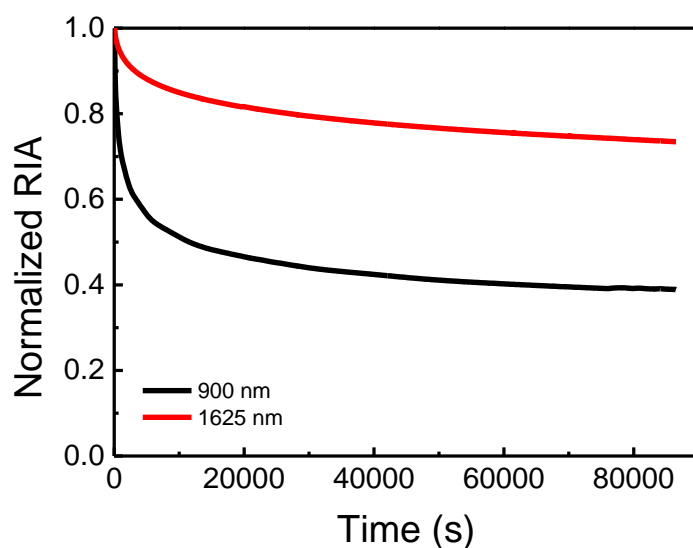


Figure 4.7 Recovery RIA kinetics at 900 nm and 1625 nm, normalized to their values at the end of the irradiation, up to ~24 hours after the irradiation end.

It is known from literature that the GeX and GeY point defects are the main responsible for the optical absorption ranging from the visible to the first part of the NIR domain [15], [38], [122], [127]. In this spectral range, the tail of the Ge(1) optical absorption band has a negligible contribution. For this reason, we performed a spectral decomposition on the RIA taking into account only the GeX and GeY point defects, which were found to be sufficient to reproduce the RIA at short wavelengths. The quality of the obtained fits, for a TID of 100 Gy and 1 MGy, are shown in Figure 4.8.

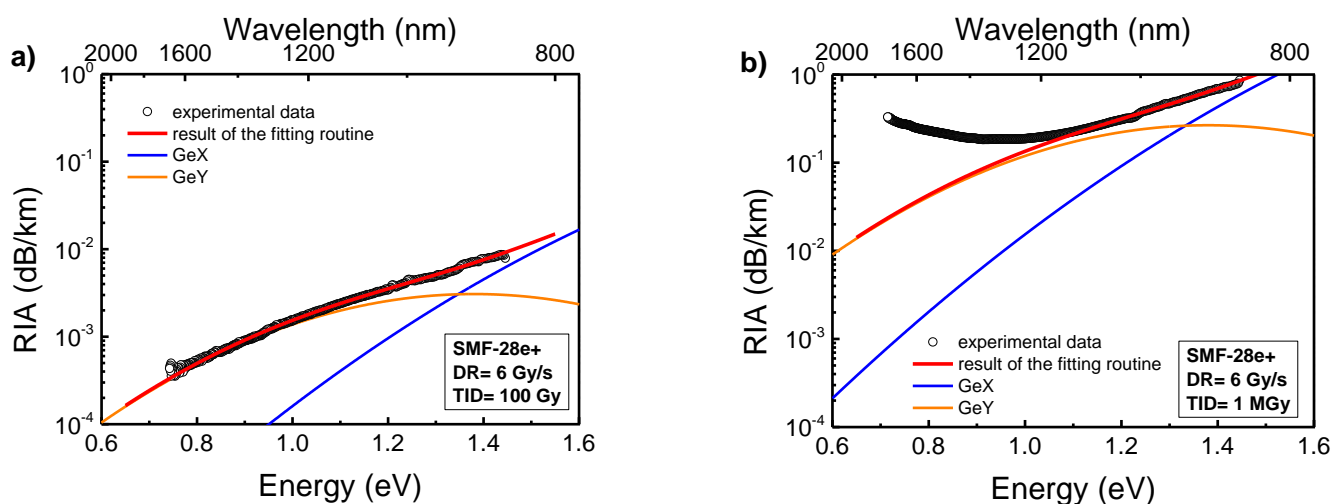


Figure 4.8 Spectral decomposition of the RIA at 100 Gy (a) and 1 MGy (b) of the SMF-28e⁺ irradiated at 6 Gy s⁻¹ and at RT. At 100 Gy, the obtained fit successfully reproduces the whole measured RIA whereas, at 1 MGy, the GeX and GeY point defects allow to fit the RIA only for energies higher than 1.1 eV.

Figure 4.8 demonstrates that the two considered point defects, the GeX and GeY, allow to fully reproduce the RIA at 100 Gy while, at 1 MGy, another contribution is present for

energies lower than 1.1 eV. Moreover, after performing the same type of spectral decomposition to the RIA measured at other selected doses, a direct correlation between the two defects GeX and GeY could be highlighted. Indeed, looking at Figure 4.9, it is possible to observe that the areas of the GeX and GeY optical absorption bands, that are proportional to the concentrations of the corresponding point defects, follow the same trend with respect to the increasing dose. In particular, the concentration of both defects increases up to a TID of 10 kGy and then saturates until the end of the irradiation.

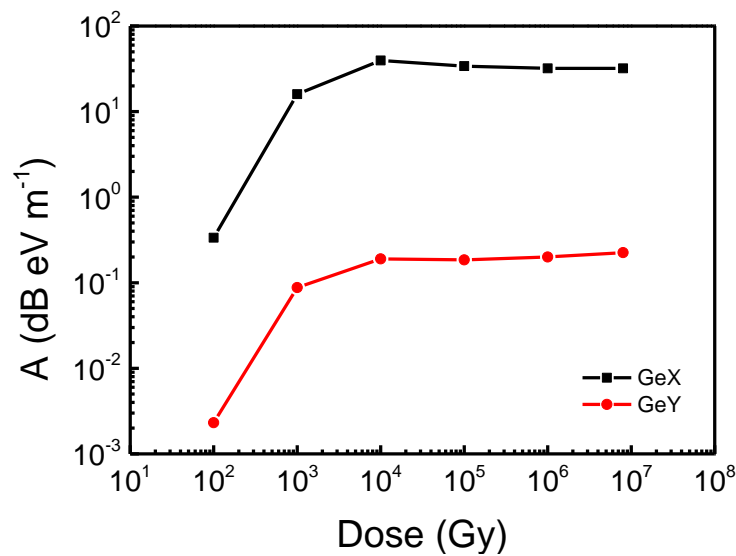


Figure 4.9 Evolution of the area of the optical absorption bands related to the GeX and GeY point defects as a function of the dose, during the irradiation of the SMF-28e⁺ at 6 Gy s⁻¹ and at RT. The two defects follow the same growth kinetic, in particular, their concentration increases up to 10 kGy and then saturates until the end of the irradiation.

This result is consistent with what has been reported by De Michele et al. in [122], where a linear correlation on the decay kinetics of the two defects after a pulsed X-ray irradiation was found. Even if further investigations are necessary in order to assess the nature of this correlation, two types of scenarios can be envisaged: the two defects are generated from the same precursor site or the same defect structure is responsible of their two optical absorption bands.

From literature, the low-energy portion of spectral RIA has been tentatively explained by the generation of Ge-STHs type of defect, in analogy with the work of Chernov in PSC OFs [119]. However, the introduction of this type of optical absorption band cannot explain the measured RIAs of Ge-doped OFs under steady-state irradiations [15], since the defects originating this band are still present ~24 hours after irradiation. For this reason, we deliberately chose not to fit the RIA for energies lower than ~1.1 eV, as it is possible to observe from Figure 4.8b. Moreover, we isolated this “unknown” contribution by subtracting the results of our fitting routine with the measured RIA, as reported in Figure 4.10. The shape of the isolated band is

non-Gaussian and, in addition, since the FUT is a SM OF, the effect of the variation of the confinement factor of the fundamental propagation mode in the core with respect to the wavelength must be considered. Indeed, at shorter wavelengths, the propagation mode results much more confined into the OF core than at longer wavelengths. This phenomenon plays an important role in establishing the shape of the obtained absorption band (that, in fact, result underestimated compared to its “real” value) and, therefore, the RIA should first be corrected according to the confinement factor of the propagation mode before attempting to perform a fitting routine [129]. This type of analysis will be done in future works.

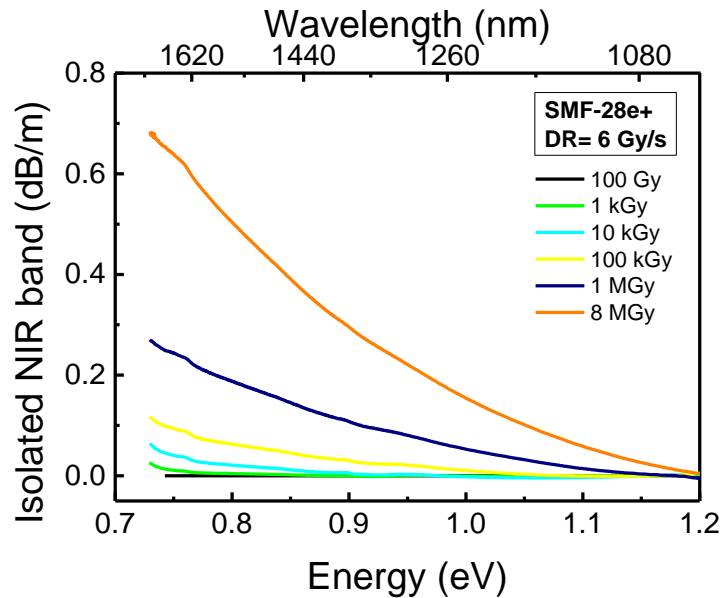


Figure 4.10 Isolated contribution of the optical absorption band in the NIR domain for energies lower than 1.2 eV. To achieve this band, the contribution of the GeX and GeY optical absorption band has been subtracted to the total measured RIA at the selected TIDs.

4.2. Temperature effect on the RIA of the Corning SMF-28e⁺ OF at telecommunication wavelengths

This section presents the results concerning a systematic study on the combined temperature and radiation effects induced on the losses at 1310 nm and 1550 nm of the Corning SMF-28e⁺ (see section 2.2.2.3). For the investigation, several irradiation runs at three different dose-rates and up to 10 kGy were performed, changing the irradiation temperature in the range between -80°C and +80°C. The maximum temperature was limited by the SMF-28e⁺ acrylate coating, which cannot withstand temperatures higher than 80°C. Furthermore, the irradiation temperature was maintained up to 3 hours after the end of irradiation, after which the RT was restored. It is worth pointing out that the target irradiation temperature was reached starting from RT without setting any heating/cooling ramp, but as fast as possible. Moreover, at the end of the three-hours recovery period at the irradiation temperature, the heating/cooling to RT was obtained naturally. In particular, cooling down from high temperatures took approximately one hour, while heating from the lowest temperature to RT took several hours. Details about all the performed irradiations are listed in Table 4.3.

Table 4.3 Details of all irradiation performed and sample length used.

Dose-rate [Gy s ⁻¹]	TID [kGy]	Temperature [°C]	Sample length [m]
0.2	5	-40	20
		20	40
		80	40
0.6	10	-80	15
		-60	15
		-40	15
		-20	15
		0	20
		20	30
		40	30
		60	40
6	10	80	40
		-40	15
		20	20
		80	20

All the experiments were performed with an OTDR (section 2.5.3), working at 1310 nm and 1550 nm with a spatial resolution of 20 cm (fixed by setting the pulse width at 2 ns) and with a 1 minute acquisition.

4.2.1. 1310 nm and 1550 nm RIA kinetics at 0.6 Gy s⁻¹

Figure 4.11 reports the RIA kinetics at 1310 nm and 1550 nm as a function of the time (dose) at the different investigated irradiation temperatures, dose-rate being 0.6 Gy s⁻¹. The

figure highlights a clear trend: the higher the irradiation temperature the lower the RIA. The temperature has a significant impact, indeed the RIA measured at the maximum dose and at -80°C results higher by a factor 38 (19) with respect to the one measured at RT and at 1310 nm (1550 nm). On the other hand, when increasing the temperature up to 80°C , the RIA decreases by a factor ~ 3 with respect to the one measured at RT at both wavelengths.

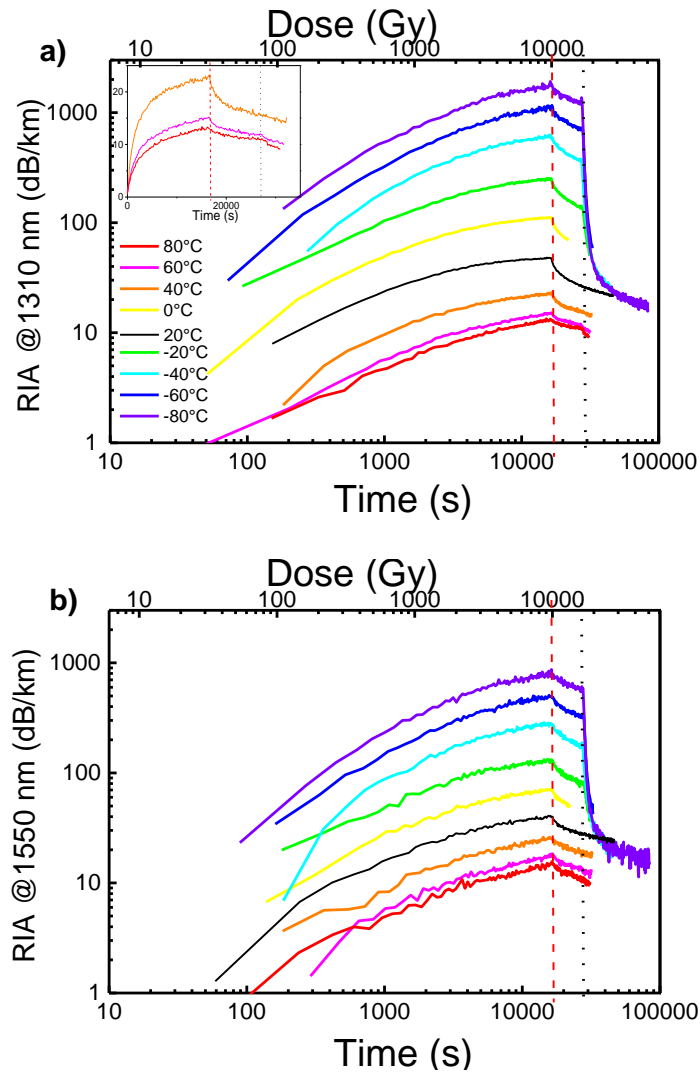


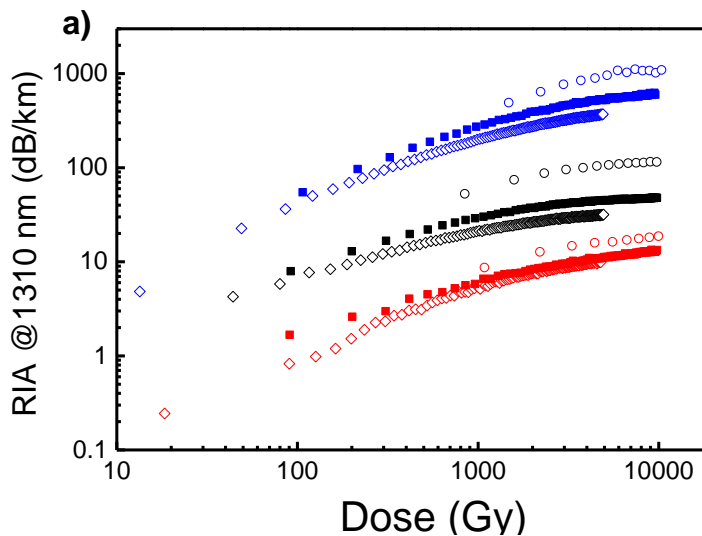
Figure 4.11 Measured RIA at 1310 nm (a) and 1550 nm (b) as a function of the time (bottom axis) or dose (top axis) at the different investigated irradiation temperatures, with a dose-rate of 0.6 Gy s^{-1} and up to 10 kGy. The dashed red vertical line indicates the stop of the irradiation, while the black one indicates the end of the recovery carried out at the same temperature of the irradiation. The inset reports the RIA kinetics at 1310 nm on a double linear scale for irradiation performed at temperatures higher than RT, in order to highlight the small effect induced on the RIA by the cooling down.

Concerning the recoveries, after 3 hours at the same temperature of the irradiation the RIA decreases by 15% or 45%, depending on the wavelength and the temperature. However, at the end of the 3 hours, when the temperature is increased from lower values to RT, the RIA drastically decreases up to values similar to the ones obtained by the irradiation performed at RT, suggesting that the defects at the origin of the RIA are not stable at RT. It is worth pointing out that this last phenomenon can be appreciated only with online RIA measurements, as the

one we performed. On the contrary, when returning to RT after the irradiation/recovery at higher temperatures, a different behaviour is observed: the RIA recovery slightly accelerates, as it is possible to see from the inset of Figure 4.11a. This indicates that, in contrast to what happens at low temperatures, the annealing of defects at high temperatures is not a reversible process. Moreover, the slight recovery acceleration can be due probably to light guiding effects. Indeed, being the silica refractive index dependent on the temperature, a slight variation in the refractive index profile could lead to a different radial distribution of the guided mode propagating inside the OF, changing the overlap between the fundamental mode and the absorbing defects due to the Ge-doping present in the OF core. A study on the subject has been already conducted in [129].

4.2.2. Effect of the dose-rate on the RIA at different irradiation temperatures

Figure 4.12 reports the RIA at 1310 nm and 1550 nm for irradiation performed at three different temperatures and three different dose-rates. With regard to the dose-rate variation, our results confirm the one already reported in literature [30], [31] for Ge-doped OFs: the higher the dose-rate the higher the NIR RIA. However, compared to the effect of the dose-rate, the different irradiation temperatures affect more significantly the RIA values. Furthermore, it can be noticed that the dose-rate effects are less important at higher temperatures.



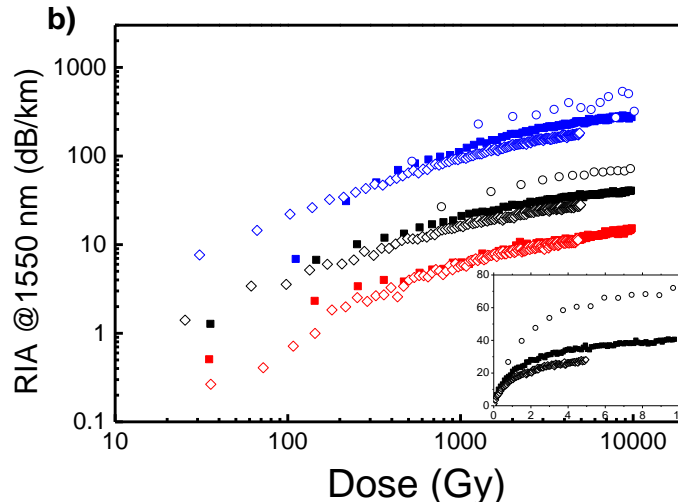


Figure 4.12 RIA kinetics at 1310 nm (a) and 1550 nm (b) as a function of the dose measured at three different irradiation temperatures, -40°C (blue), RT (black) and 80°C (red) and at three different dose-rates, 0.2 Gy s^{-1} (empty diamonds), 0.6 Gy s^{-1} (full squares) and 6 Gy s^{-1} (empty circles). The inset reports the 1550 nm kinetics at RT on a double linear scale, in order to highlight the effect of the dose-rate.

4.2.3. RIA kinetics modelling

For further analysis on the reported kinetics, we performed a fitting routine based on the *second-order growth kinetic model* of Griscom [159], where the RIA is expressed by the equation (4.1). This model differs from the one used by Griscom et al. in [160], known as *first-order growth kinetic model* that, in some cases, can be reconducted to a power law. Since it has been proven by Griscom himself that the *second-order growth model* is suitable for the description of the RIA of Ge-doped OFs [159], we choose this one for our case since it allows to better isolate the temperature dependence. In Figure 4.14 it is possible to appreciate the quality of the best-fit obtained using the model described by equation (4.1) for the RIA growth kinetic, in particular the one at 1550 nm, at RT and with a dose-rate of 0.6 Gy s^{-1} . At first, the fits were calculated independently for each dataset but, given that the value of β was not changing within a 15% range, we decided to fix it at its mean value of ~ 0.6 in order to optimize the other two parameters, N and k .

Figure 4.14 reports the parameter N (the saturation level, proportional to the number of absorbers and to the oscillator strength of the defect) as a function of the temperature for the kinetics at the two investigated wavelengths. As can be seen from the figure, the values derived from the fitting routine are consistent with the experimental results: the RIA saturation level monotonically decreases as the temperature increases and, also, has higher values at higher dose-rates (a feature that is less evident as the temperature increases).

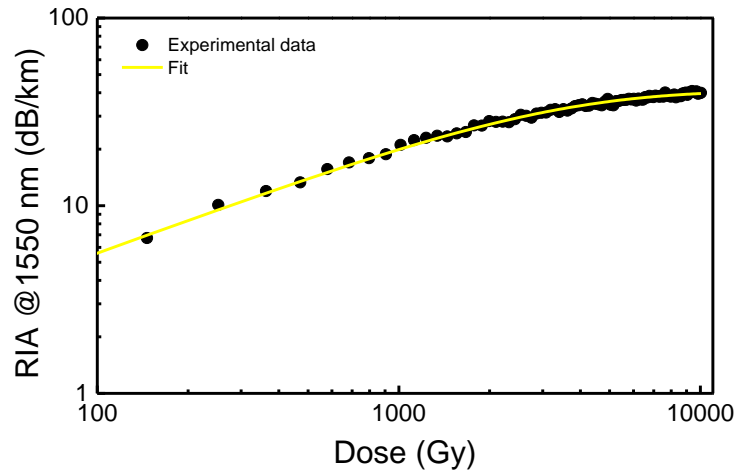


Figure 4.13 Experimental measured RIA at 1550 nm, at RT and for a dose-rate of 0.6 Gy s^{-1} , as a function of the dose. The yellow curve represents the fit obtained with the *second-order growth kinetic model* of Griscom, equation (4.1), by imposing $\beta = 0.6$ and leaving the other two parameters free.

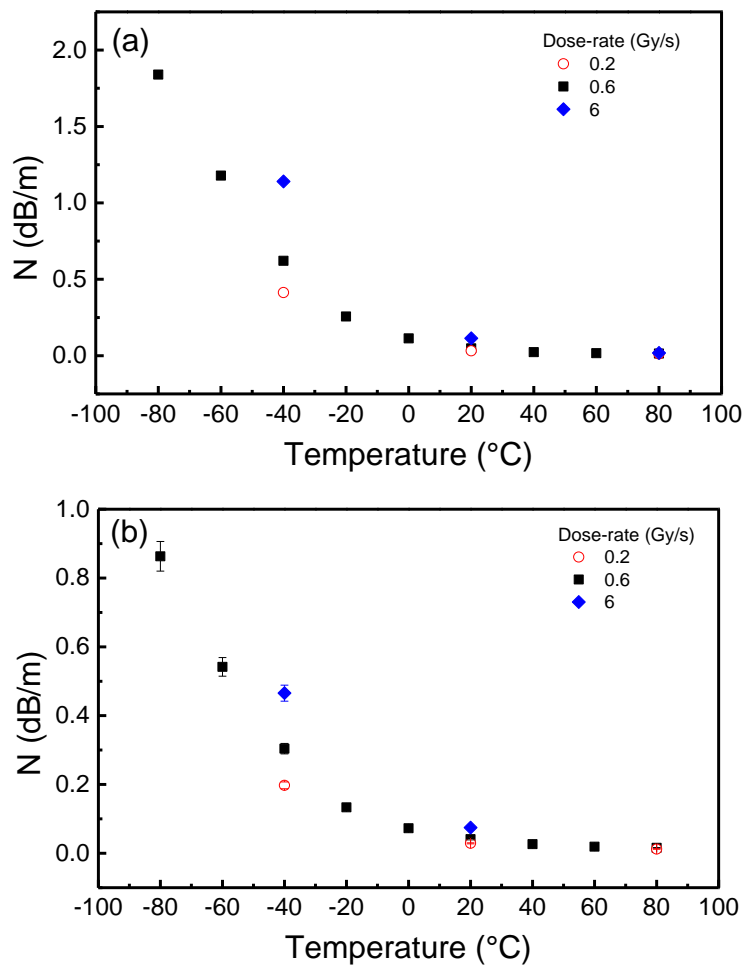


Figure 4.14 Values of the RIA saturation level (N) at 1310 nm (a) and 1550 nm (b), derived from the fitting routine, as a function of the irradiation temperature for the three datasets at different dose-rates. The associated error with N is about 5%.

Furthermore, as reported in Figure 4.15, the saturation level has a temperature dependence that follows the Arrhenius law:

$$N(T, \text{dose} - \text{rate}) = C \cdot e^{\left(\frac{E_a}{k_B T}\right)} \quad (4.3)$$

where E_a is the activation energy, k_B is Boltzmann's constant, T is the temperature (expressed in K) and C is a constant that is independent from the temperature but dependent on the dose-rate. Figure 4.15, reporting the saturation level (in logarithmic scale) as a function of the temperature, shows that the slope of the three datasets at the three different dose-rates is the same. It is worth pointing out that, in the logarithmic scale graph, the slope is proportional to E_a . On the other hand, the three datasets have different intercept with the vertical axis, being this associated to the parameter C that, as already said, is dependent on the dose-rate.

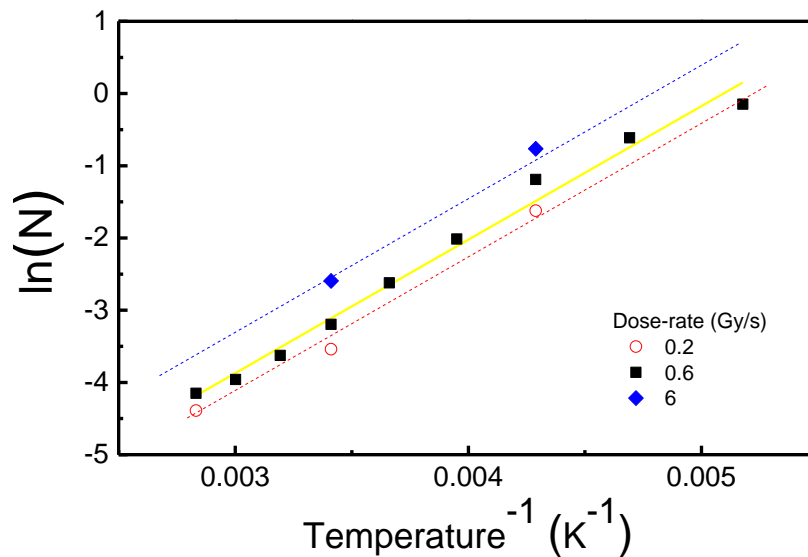


Figure 4.15 RIA saturation values at 1550 nm, obtained from the fitting routine, plotted on a semi-logarithmic scale as a function of the reciprocal of temperature and at three different dose-rates. The straight lines indicate the fits obtained for the three datasets (yellow continuous line – 0.6 Gy s⁻¹; blue dashed line – 6 Gy s⁻¹; red dashed line – 0.2 Gy s⁻¹). The three lines have the same slope (proportional to E_a) but different intercepts (proportional to C).

In Figure 4.16 is reported the dependence of the parameter k , that gives information on the reaction rate, with respect to the temperature and at the two investigated wavelengths. The figure highlights a bell-shaped behaviour of k with respect to the temperature. Since the RIA kinetics illustrated in Figure 4.11 have a monotonic decreasing trend as the temperature increase, we can assess that k is not the most important parameter for the kinetics description. However, its variations are significative, larger than the associated error. As a further investigation, Figure 4.17 illustrates the RIA kinetics at 1550 nm, at all the irradiation temperatures, as a function of the dose and normalized to their values at the maximum TID.

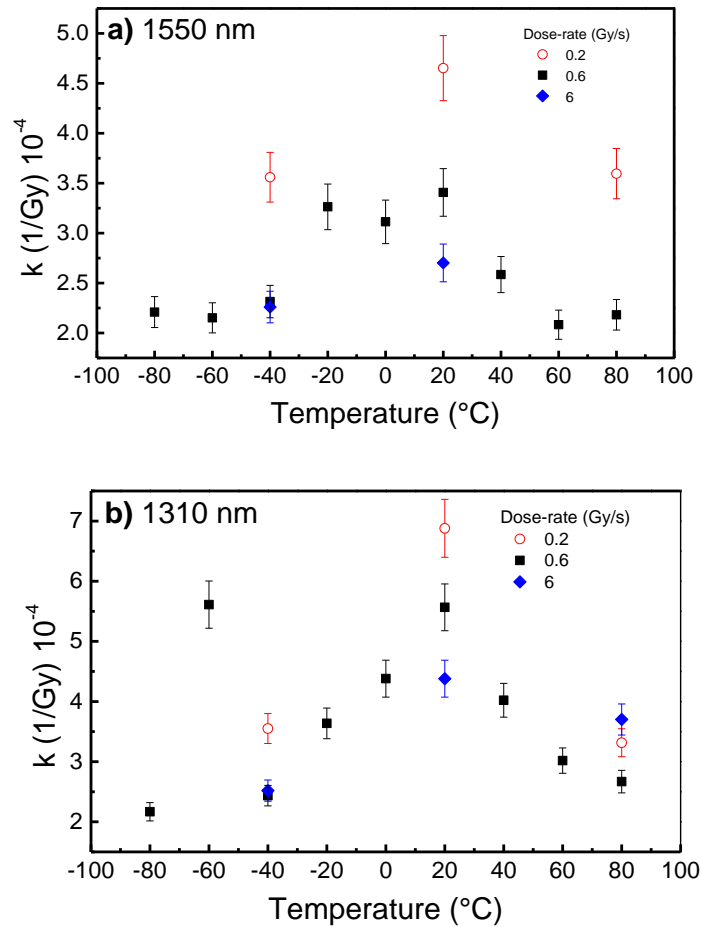


Figure 4.16 Parameter k , obtained from the fitting routines, as a function of the irradiation temperature at different dose-rates and for the two wavelengths: 1550 nm **(a)** and 1310 nm **(b)**. The associated error with the parameter k was found to be about 7%. It was not possible to derive the value of k for the kinetic at 1550 nm, at 80°C and 6 Gy s⁻¹ because of the measurement noise.

The figure highlights that the kinetics are not identical at the different temperatures and, as a consequence, they cannot be described all by unique value of k . Consistently with the observations based on Figure 4.16, from Figure 4.18 we can see that, at temperatures close to RT, the kinetics are faster compared to those at the extreme temperatures. This behaviour is not immediately comprehensible, but we will tentatively give a possible explanation. The bell-shape trend of the parameter k means that, starting from -80°C, as the temperature increases, the generation of the defects responsible for the RIA at the observed wavelengths becomes more probable but, for temperatures above 40°C, this rate decreases. Generally, at low temperatures we expect a lower generation probability, since low temperatures do not encourage the movement of carriers. Consequently, as the temperature increases, we expect the defects generation probability to increase, as in our case for temperatures below 40°C. When the temperature increases even further, the value of k decreases. This can be explained by the fact that, at higher temperatures, thermal recombination becomes more significant. Therefore, it seems as if the rate of thermal bleaching of the defects is faster than that of their generation. This hypothesis is consistent when comparing the values of k obtained at 1310 nm

at the two temperature RT and 80°C (Figure 4.16a). Indeed, it can be observed that the variations of this parameter with the temperature are more important at low dose-rates than at higher ones. In fact, at low dose-rates the time needed to reach a given TID is longer than that required at higher dose-rates, so the effect of thermal bleaching becomes more efficient since the OF is exposed to a high temperature for a longer time. However, more studies are still in progress to confirm this explanation.

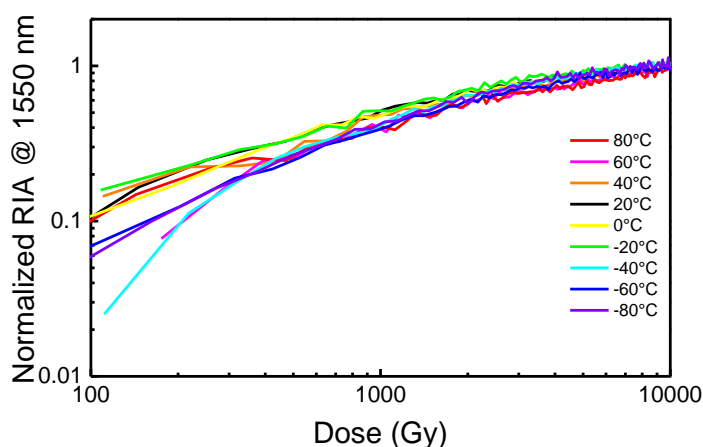


Figure 4.17 RIA kinetics at 1550 nm, normalized to their value at the maximum TID, as a function of the dose and for different irradiation temperatures. The different reaction rate between the curves can be observed at low doses.

Table 4.4 reports the values obtained for the parameters E_a and C for the data at 0.6 Gy s^{-1} . The activation energy values are within their errors (defined as twice the standard deviation). This allows us to conclude that the RIA at both wavelengths is given by the same point defect. Moreover, the value of E_a is in agreement with the one found by Kashaykin et al. for similar Ge-doped OFs [38].

Table 4.4 Parameters of the Arrhenius law relative to the data measured at 0.6 Gy s^{-1} .

Wavelength	E_a [eV]	C [dB m ⁻¹]
1310 nm	0.20 ± 0.03	$\sim 2 \times 10^{-5}$
1550 nm	0.159 ± 0.014	$\sim 8 \times 10^{-5}$

In [38], Kashaykin et al. suggest that at the origin of the absorption in the NIR domain could be mainly due to the GeY defect, for OFs with low Ge concentrations (as the one investigated here), and the GeX, for samples with higher concentration (section 1.3.3.2.3). To better identify the point defects responsible for the IR-RIA, dedicated experiments will be performed on multimode OFs (in order to reduce the impact of guiding properties) using spectrally-resolved attenuation measurements.

4.3. Combined effects of temperature and radiation on the vis/NIR RIA of a canonical MM Ge-doped OF

The present section reports the results concerning the temperature dependence of the spectral RIA of a canonical polyimide-coated MM Ge-doped OF. The use of a MM sample ensures a large portion of the probe signal to be guided within the Ge-doped core and, thus, avoids variation of propagation conditions of guided modes with the variation of the wavelength and, consequently, a more precise evaluation of the light absorption due to material losses. In addition, the polyimide coating has made it possible to extend the temperature range above 80°C, maximum temperature that acrylate coatings can withstand before their degradation.

The investigation consisted on a several irradiation runs, performed with a dose-rate of 0.6 Gy s⁻¹ and up to a TID of 10 kGy, with different irradiation temperatures, ranging from -100°C to 300°C. The spectral RIA in the visible and NIR domains, during the irradiation and up to ~3 hours after its end, was measured. Table 4.5 lists the parameters of all the performed irradiations along with the sample lengths that were used.

Table 4.5 Parameters of the different irradiation runs and length of the sample used.

Dose-rate [Gy s ⁻¹]	TID [kGy]	Temperature [°C]	Sample length [m]	
			vis	NIR
0.6	10	-100	2	15
		-60	2	20
		-30	2	25
		0	2	30
		25	5	30
		50	1	30
		80	1	30
		120	1	40
		160	1	40
		200	1	40
		250	5	40
		300	5	40

4.3.1. Spectral RIA at RT

Figure 4.18 shows the spectral RIA growth, recorded at RT, at different accumulated doses. The RIA grows across the whole spectral domain as the dose increases and, also, its shape remains unaltered, with the highest values in the visible spectrum and lower values at longer wavelengths. This trend is consistent with other Ge-doped OFs RIAs already reported in literature [36], [38], [127]. The higher RIA in the visible is due to the generation of optical absorption bands linked to GeX and GeY point defects (and, at shorter wavelengths, also the tail of the Ge(1) color center), while, for wavelengths longer than ~1100 nm the aforementioned

point defects have a negligible impact, and the RIA in the 1000 – 2000 nm domain is due to the contribution of the absorption band peaked around ~2300 nm and another contribution not identified yet (as already mentioned in 4.1.4).

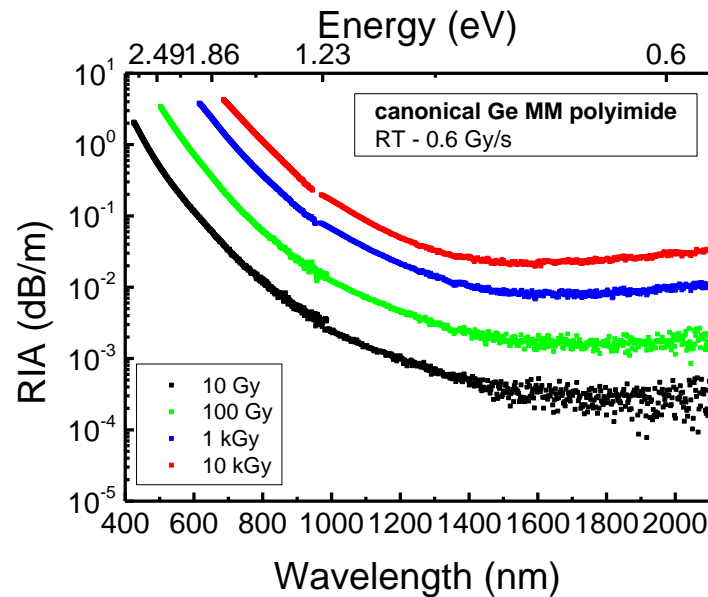


Figure 4.18 Growth of the spectral RIA of the canonical polyimide-coated Ge-doped MM sample, measured in the visible and NIR domains at RT.

4.3.2. Temperature effect on the spectral RIA

Figure 4.19 reports the RIA measured at two TIDs, 100 Gy and 10 kGy, and at three different irradiation temperatures (low, room and high temperature) chosen among the set of irradiation runs carried out during the investigation. It is possible to observe that, at both TIDs and for energies higher than 0.9 eV, the RIA at 25°C is the lowest. In this spectral range, indeed, the RIA does not have a monotonic trend with the increasing of the irradiation temperature: at -100°C it shows the highest value, at 25°C it drops to the lowest value and at 200°C it rises again. On the contrary, at energies below 0.9 eV, RIA values have a definite temperature-dependent behaviour: they reach the highest values at -100°C and decrease as the temperature increases. In addition, the contribution attributable to the absorption band peaked at 0.54 eV is most discernible at 10 kGy, at 25° and 200°C.

In order to better analyse the temperature dependence of the RIA, Figure 4.20 and Figure 4.21 show the kinetics at 750 nm and 1310 nm, respectively, at all the examined irradiation temperatures. At both wavelengths, increasing the temperature from -100°C to 0°C has the same effect: the RIA decreases as the temperature increases over the whole range of TIDs considered. In particular, at 6 kGy, the RIA measured at 750 nm and 1310 nm decreases by a factor of 6 and 35, respectively.

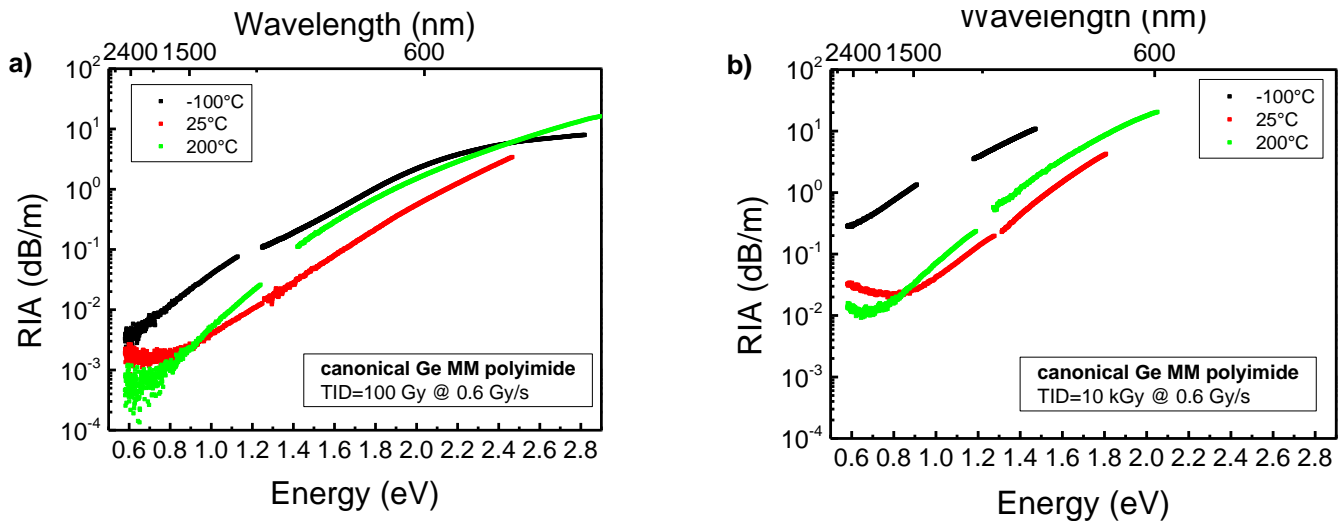


Figure 4.19 RIA as a function of the energy and at three different temperatures (-100°C, RT and 200°C), measured at 100 Gy (a) and 10 kGy (b).

On the other hand, looking at the kinetics for irradiation temperatures higher than 0°C, two different behaviours can be distinguished at 750 nm: the RIA increases (by about a factor 3 at 10 kGy) in the 0°C – 200°C temperature range and, for temperatures above 200°C, starts to decrease again. At 1310 nm, instead, increasing the temperature from 25°C to 300°C has no significant effect.

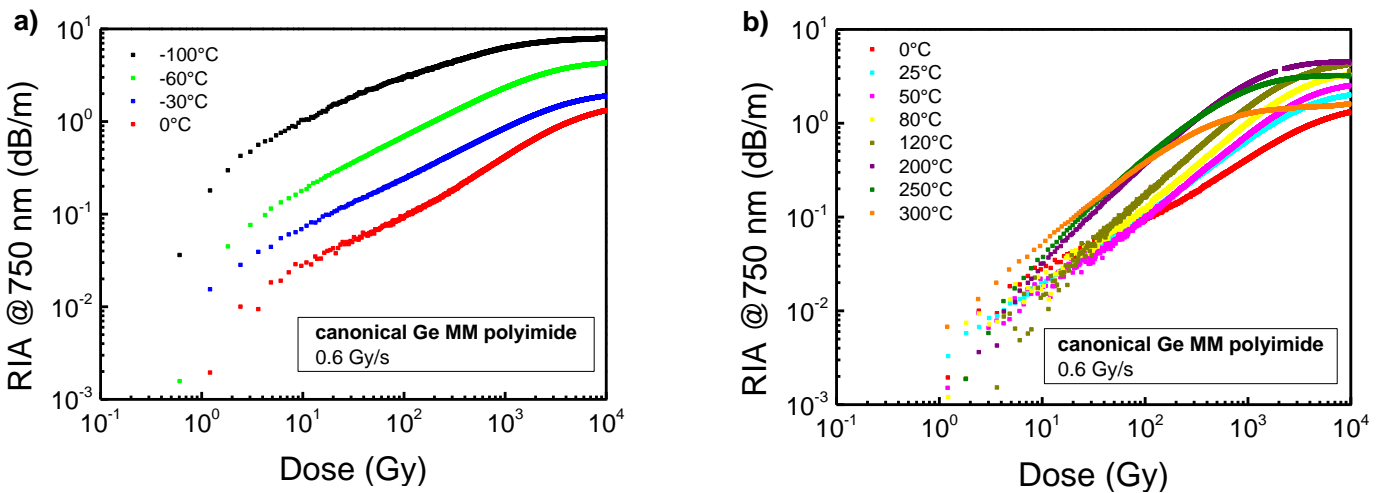


Figure 4.20 RIA kinetics measured at 750 nm for irradiation temperatures ranging from -100°C to 0°C (a) and from 0°C to 300°C (b) for the canonical Ge-doped MM polyimide sample, irradiated at 0.6 Gy s⁻¹ up to 10 kGy. Depending on the temperature range, different effects on the RIA can be observed.

As far the post-irradiation kinetics are concerned, from Figure 4.22a it is possible to observe that the point defects created at lower temperatures are not stable after the end of the irradiation. In particular, at -100°C, the RIA at 750 nm decreases rapidly right after the irradiation stops, recovering almost 95% of the induced RIA after 3 hours.

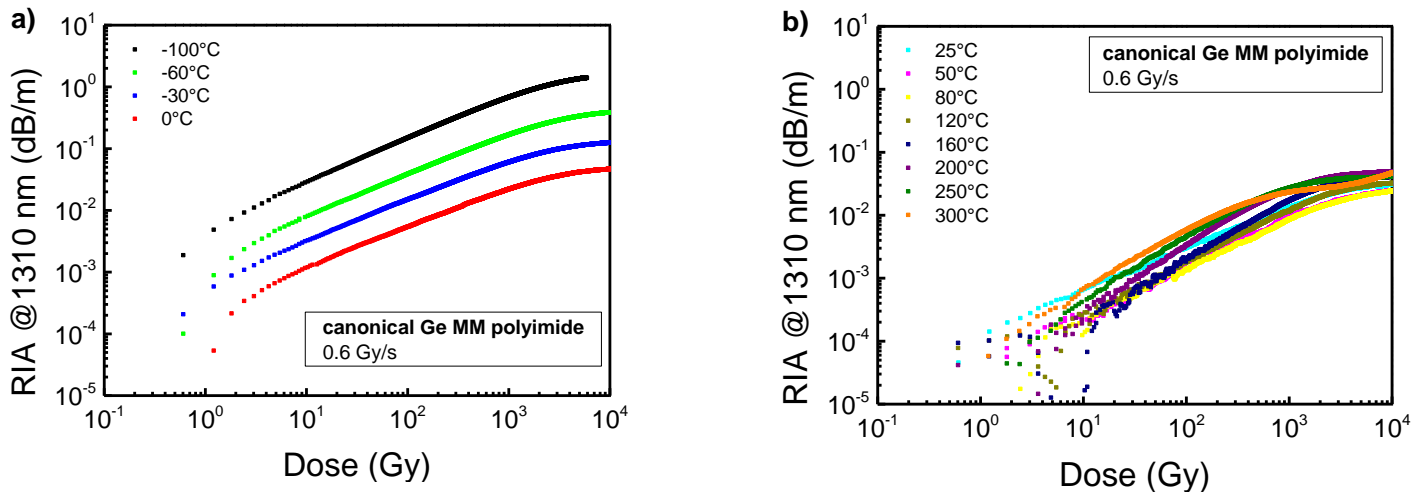


Figure 4.21 RIA kinetics measured at 1310 nm for irradiation temperatures ranging from -100°C to 0°C (a) and from 0°C to 300°C (b) for the canonical Ge-doped MM polyimide sample, irradiated at 0.6 Gy s⁻¹ up to 10 kGy. Depending on the temperature range, different effects on the RIA can be observed.

Increasing the temperature, Figure 4.22b, the post-irradiation annealing seems to become less and less efficient as a function of the time, decreasing from 70% to 8% for temperatures ranging from -60°C to 25°C. It has to be noticed that a lower RIA is observed at higher temperatures in this range, this can be due to a recombination phenomenon taking place during the irradiation or a temperature effect on the defects generation rate. In conclusion, the post-irradiation bleaching is less efficient since the majority of the defects are not present at the irradiation end. Between 50°C and 120°C, no recovery of the signal is measured and, from temperatures higher than 120°C, a phenomenon of thermal annealing of the point defects generated during the irradiation takes place, resulting in a greater amount of recovered RIA as the temperature increases. Comparing the 750 nm RIA growth kinetics at 0°C and 300°C (Figure 4.20) it is possible to observe that, at 10 kGy, their RIA value is very close (~ 1.4 dB m⁻¹ and ~ 1.5 dB m⁻¹ at 0°C and 300°C, respectively) but their growth curves are different: the one at 0°C has a slower increase and does not reach an equilibrium level, whereas the one at 300°C increases much faster at low doses and then reaches an equilibrium state around 2 kGy. From these observations it could be deduced that the temperature increase from 0°C to 300°C acts both by increasing the generation efficiency of the point defect responsible for the absorption at 750 nm and by increasing their recombination efficiency through thermal annealing (an effect that is only noticeable after a while from the start of irradiation). The enhanced thermal bleaching efficiency can also be appreciated by looking at the recovery kinetics at 0°C and 300°C. Indeed, although the RIA values at the end of the irradiation are very close, the decay at 300°C is faster than at 0°C, recovering $\sim 45\%$ of the induced RIA in the first case and only $\sim 15\%$ in the second.

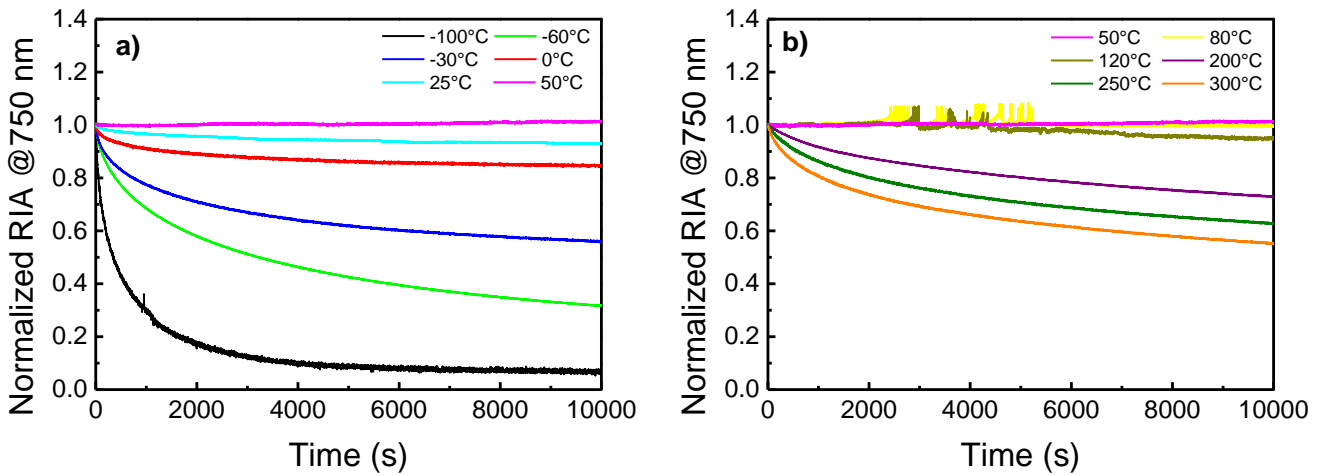


Figure 4.22 RIA recovery kinetics at 750 nm at all the investigated irradiation temperatures, ranging from -100°C to 50°C (a), and from 50°C to 300°C (b). The curves at 80°C and 120°C are noisy due to source fluctuations.

At 1310 nm and low temperatures, a different behaviour is found: varying the temperature in the -60°C – 0°C range does not affect significantly the RIA decay kinetics, recovering about the 40% of the RIA after 3 hours from the irradiation end (Figure 4.23a). Increasing the temperature even more, the recovered portion of the RIA decreases (as for the 750 nm case), being ~30% at 25°C and ~5% for temperatures ranging from 50°C to 160°C. Finally, also at this wavelength, for temperatures above 200°C the effect of thermal annealing becomes significant.

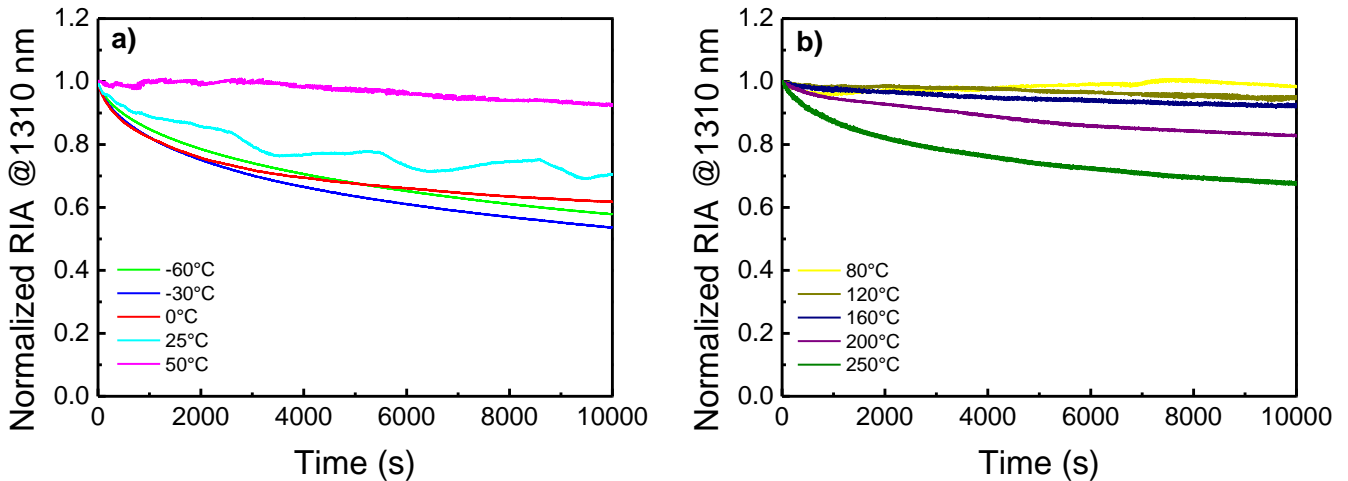


Figure 4.23 RIA recovery kinetics at 1310 nm at all the investigated irradiation temperatures, ranging from -60°C to 50°C (a), and from 80°C to 250°C (b). The curves at -100°C and 300°C have been omitted.

With the available data set, we carried out a further preliminary analysis on the combined effects of radiation and temperature on RIA. Figure 4.24 provide more details on the complex behaviours observed so far, reporting the 750 nm RIA measured at different TIDs (i.e. different time periods since the irradiation start) and normalized to the corresponding RIA value

measured at RT, as a function of the temperature. Therefore, values of the normalization greater than 1 indicate a “negative” effect of the temperature on the RIA, i.e. the RIA measured is higher than the one at RT, on the other hand, values lower than 1 means a “positive” impact on the RIA. For temperatures lower than RT, a clear trend emerges: the greater the accumulated dose, the lower the discrepancy between the measured RIA and the one at RT. This means that, for $T < RT$, the effect of temperature is only significant at low doses, indeed the normalized RIA is about 55, 10, 5 and 2, respectively at -100°C , -60°C , -30°C and 0°C , for a TID of 10 Gy. As seen, the difference becomes less important as the temperature approaches 25°C . As can be noticed, moving away from RT towards higher temperatures, again a higher RIA at low doses can be measured. Whether at low temperatures this phenomenon could be attributed to a lower recombination efficiency of point defects (which becomes more relevant at longer time periods after the irradiation start), at high temperatures this phenomenon could be related to a more efficient conversion between point defects, e.g. due to an increase in the absorption intensity of the GeX centre due to the thermal decay of the Ge(1) centre, as already proposed by Kashaykin et al. in [38]. However, as can be seen from the inset of Figure 4.24, only at 300°C and for doses higher than 4 kGy a lower RIA than the one measured at RT is obtained.

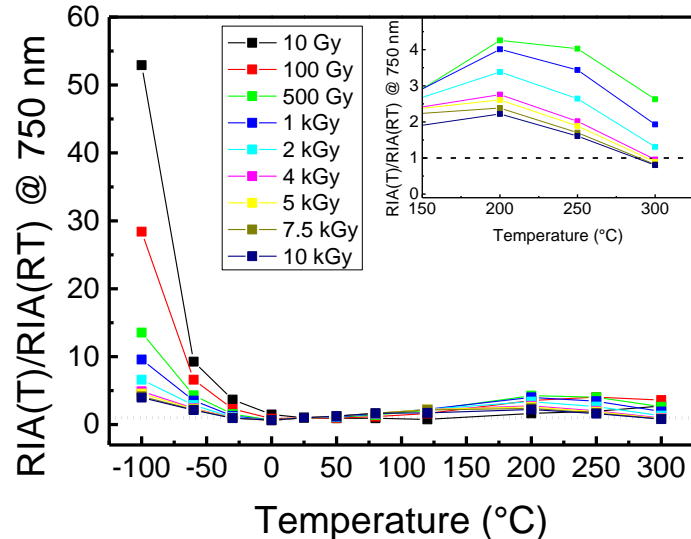


Figure 4.24 Ratio between the 750 nm RIA measured at the different irradiation temperatures and the one measured at RT, at different accumulated doses. The black dashed horizontal line indicates the 1 value. The inset reports a zoom view of the temperatures ranging from 200°C to 300°C ; in this case the ratio at 10 and 100 Gy were omitted since were the ones associated with the greatest uncertainty.

Figure 4.25 reports the same type of analysis considered above, but this time for the 1310 nm RIA. In this case, the combined temperature-radiation action shows a different effect than the one observed at 750 nm. Although, as illustrated in Figure 4.21, higher RIA values result at lower temperatures, here it can be observed that the total accumulated dose (or the

irradiation time) has not a significant influence at temperatures lower than 25°C, indeed all the normalized RIAs are superimposed. This would imply that the recombination rate at low temperatures is the same as at RT and that, subsequently, the higher normalized RIA could be due to a higher generation rate. Furthermore, for temperature ranging from 50°C to 160°C, the normalized RIA increases as the accumulated dose increases. The fact that the concentration of defects at higher dose (longer time) at high temperature is higher could confirm the presence of a conversion phenomenon between defects, as mentioned before in this section. However, as can be observed from Figure 4.21b, this effect is negligible on the RIA values in this temperature range. Finally, for temperatures above 200°C, this behavior is no more present and no definite trend can be found with the present analysis.

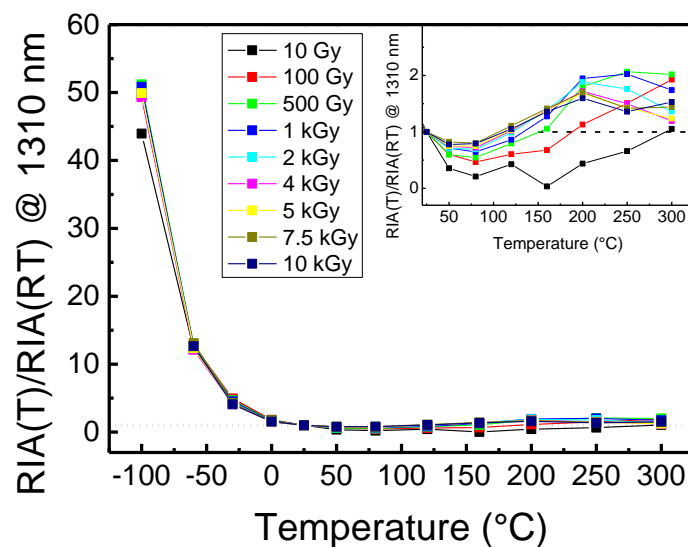


Figure 4.25 Ratio between the 1310 nm RIA measured at the different irradiation temperatures and the one measured at RT, at different accumulated doses. The black dashed horizontal line indicates the 1 value. The inset reports a zoom view of the temperatures ranging from 25°C to 300°C.

Finally, we performed a fitting routine on the RIA at three selected temperatures (-100°C, 25°C and 200°C), at TIDs of 100 Gy, 1 kGy, 10 kGy and, also, 3 hours after the end of the irradiation in such a way to obtain information on the evolution of the population of the point defects. It should be pointed out that the spectral decomposition was carried out by taking into account the point defects responsible for the absorption from the lowest wavelengths recorded in our measurements up to about 1600 nm, i.e. the Ge(1), GeX and GeY centers. An example of a result obtained by our fitting routine is shown in Figure 4.26. It is possible to observe that the GeX- and GeY-related optical absorption bands alone are adequate to describe almost the entire spectral range of the RIA obtained from our measurement. The parameters associated to the absorption centers considered in our fitting routine, as long as the obtained area values, are reported in Table 4.6. As reported by the table, the area values concerning the Ge(1) center, if present, are relatively large. Since the absorption band of the Ge(1) is peaked at

energies that are quite higher compared to those related to our data sets, the found area values are an extrapolation. However, the inclusion of the Ge(1) center in our fitting routine does not affect the area values of the GeX and GeY point defects.

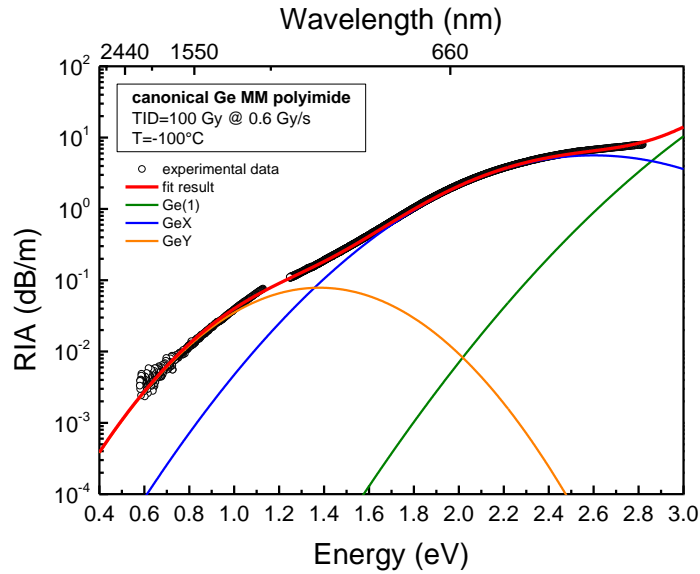


Figure 4.26 Result of the fitting routine performed on the measured spectral RIA at 100 Gy and -100°C. The green, blue and orange lines represent, respectively, the absorption contribution of the Ge(1), GeX and GeY color centers, while the red one represents the resulting fitting curve.

Table 4.6 List of parameters used for optical absorption bands of point defects and relative areas obtained from the fitting routine procedure. The area is given in (dB eV m⁻¹).

Defect	OA band peak (eV)	FWHM (eV)	-100°C				25°C				200°C			
			100 Gy	1 kGy	10 kGy	3 h	100 Gy	1 kGy	10 kGy	3 h	100 Gy	1 kGy	10 kGy	3 h
Ge(1)	4.4	1.20	579				4000	55600			1684	9656		
GeX	2.6	0.97	6	118	289		1.35	8.78	28.83	26.93	4.4	31	55	39
GeY	1.38	0.71	0.059	1.24	2.46		0.005	0.018	0.03	0.015	0.003	0.02	0.04	0.04

The values of the areas of the GeX and GeY absorption bands obtained at the selected dose/temperatures are reported in Figure 4.27. First of all, once again we can assess the correlation between the two defects, as the growth of both areas exhibit the same evolution as the accumulated dose increases, validating the results obtained in [122] and in section 4.1.4. For both absorption bands, areas are higher at -100°C than at the other two temperatures. However, if the GeX has the lowest concentrations at RT, this cannot be said for the GeY, for which the concentrations at RT and 200°C are more or less comparable. Indeed, if for the GeX an increase in temperature from RT to 200°C corresponds to a concentration increase, this does not apply to the GeY. Since the two defects are correlated, the observed increase in the GeX population at 200°C could be due to the thermal decay of the Ge(1) species into GeX,

since, as already reported in [36], at short wavelengths (where the Ge(1) is the major contributor to the optical absorption) the RIA shows a monotonically decreasing trend as the temperature increases. This result could invalidate one of the two hypotheses proposed to explain the correlation between the two absorption bands of GeX and GeY, i.e. that both bands could be related to the same defect structure, and leaning towards the fact that the two defects could be generated by the same precursor site.

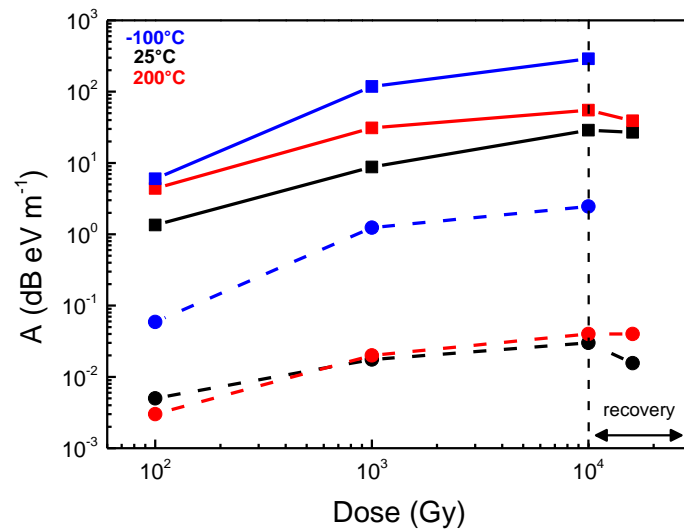


Figure 4.27 Evolution of the area of the absorption bands related to the GeX (full squares) and GeY (full circles) center as a function of the dose and at three selected temperatures: -100°C, 25°C and 200°C.

4.4. Summary

The dependence of the measured RIA of Ge-doped OFs on the power levels of the 1550 nm probing signal, ranging from few nanowatts to few milliwatts, revealed to be not unique. Indeed, while the COTS sample (Corning SMF-28e+) results not affected by photobleaching phenomena (also up to MGy dose levels), the RIA of the CERTYF OF show a dependence on the injected power already for TIDs lower than 100 kGy. This phenomenon was found to be related to a macroscopic effect on the different parameters describing the RIA kinetics. Furthermore, the NIR RIA of the COTS sample irradiated up to high TIDs revealed two separates absorption contributions: the first one, absorbing at wavelengths shorter than 1100 nm and due to GeX and GeY color centers, characterized by a steep growth right after the irradiation start and a saturation at doses of ~5 kGy; and the second one, absorbing at longer wavelengths, which impact increases significant at higher doses without reaching a saturation point.

As far as the combined radiation and temperature effects are concerned, at low temperatures, the SMF-28e+ reported a higher NIR RIA compared to the one measured at RT. The defects at the origin of this attenuation were found to be unstable at RT, since, once the temperature was brought back to RT, the post-irradiation RIA tended to the values measured at RT. A pragmatic model, considering dose, temperature and dose-rate, was proposed to reproduce the RIA growth during irradiation and its temperature dependence. Also the investigations on a canonical MM Ge-doped OF revealed a monotonic dependence of the RIA from the temperature (i.e. lower RIA at higher temperatures) in the range -100°C to 0°C across the whole UV/vis and NIR spectrum, with unstable radiation-induced point defects after the irradiation end. At higher temperatures, instead, the RIA revealed a non-monotonic behavior, a possible manifestation of the more efficient defect conversion of Ge(1) color centers into GeX, as suggested also by our spectral decomposition.

Chapter 5: Radiation effects on radiation-hardened optical fibers

This chapter reports the results obtained for OFs belonging to the radiation-hardened class. In particular, we study the effects of radiation in the visible domain on a set of pure silica core (PSC) multimode (MM) samples drawn from similar preforms but with very different hydroxyl (OH-group) contents. The purpose of this study is to understand how the amount of Si-OH groups governs the OF intrinsic losses and RIA. Furthermore, by means of the spectral decomposition, the role of specific optical absorption bands contributing to the losses was identified.

5.1. Radiation effects on PSC MM OFs: influence of OH groups

In this section, we investigate how the intrinsic and RIA attenuations of MM PSC OFs, in the visible domain, are controlled by their OH amounts. The samples under test differ in OH groups content and are the ones described in section 2.2.2.5. Furthermore, we discuss the H₂ pre-treatment efficiency on the sample with medium-OH content in order to permanently improve both its intrinsic losses in the visible domain and its steady-state radiation response up to 300 kGy dose levels. Finally, we perform the decomposition of the various RIA spectra

in such a way to achieve a better understanding of the basic mechanisms related to the point defects causing the optical loss excess.

Irradiation runs were performed at RT and with a dose-rate of 6 Gy s^{-1} (spatial inhomogeneity below 5% over the sample), up to a total accumulated dose of 300 kGy, with the exception of the medium-OH sample, which underwent an irradiation up to 350 kGy. All the irradiated samples are 1 m long. Under these conditions, online RIA measurements in the visible domain, during and after the irradiation, were performed with the setup illustrated in Figure 2.12. In addition, the radiation-hardened transport OFs were shielded with $\sim 5 \text{ mm}$ thick lead pieces inside the irradiation chamber, making sure that only the samples under test were exposed to X-rays.

Since the medium-OH sample is the one presenting DID defects that are known to be bleachable by molecular hydrogen, it was H_2 loaded using a typical high-pressure reactor, with the procedure described in section 2.3.4. Immediately afterwards the hydrogenation, a thermal treatment was performed on the loaded OF by placing it for one day in an oven at a temperature of 120°C . This last thermal treatment was not intended to anneal the defects but to accelerate the natural outgassing of the residual molecular hydrogen that failed to bond and passivate pre-existing defects in the silica matrix (such as the NBOHCs and E') created during the drawing process. Figure 5.1 shows the attenuation spectrum, measured with the cut-back technique (section 2.5.4), of the medium-OH sample before and after the hydrogen loading and the thermal treatment. The NBOHC absorption band, centered at 630 nm, was completely suppressed. Table 5.1 reports the details of the performed irradiations.

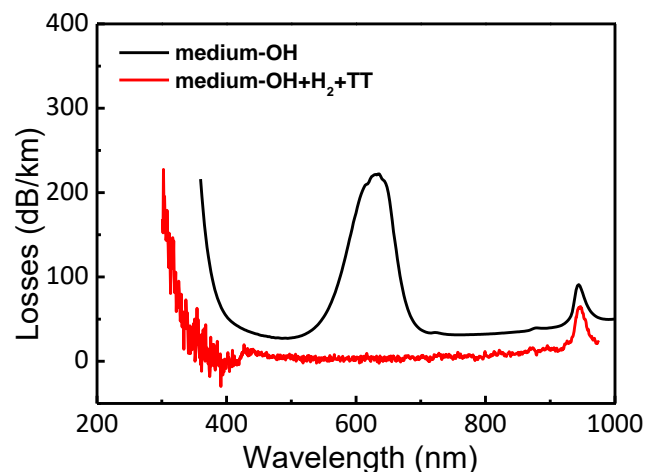


Figure 5.1 Attenuation spectra of the pristine medium-OH sample before and after the H_2 loading and thermal treatment (TT). The NBOHC absorption band (peaked at 630 nm) is completely suppressed in the treated sample.

Table 5.1 Irradiation details.

Sample	Dose-rate [Gy s ⁻¹]	TID [kGy]	Temperature	Sample length [m]
High-OH		300		
Medium-OH	6	350	RT	1
Low-OH		300		
Medium-OH+H ₂ +TT		300		

5.1.1. Online spectral RIA during and after the irradiation

Figure 5.2 shows the spectral RIAs of the high-, medium- and low-OH samples in the 400-900 nm spectral range, during the irradiation and up to 1 hour after its end. In addition, the insets show the RIA growth and recovery kinetics at 450 nm and 650 nm. For all cases, a monotonic increase of the spectral RIA is observed, except for the red wavelength range of the medium-OH OF. Indeed, the 450 nm kinetics increase rapidly at 1 dB m⁻¹ up to ~10 kGy for both the high- and medium-OH samples and at 4 dB m⁻¹ up to ~30 kGy for the low-OH. Instead, the kinetics at 650 nm follow different trends: for the high-OH, it continuously grows with no saturation trend. The medium-OH sample presents an unexpected non-monotonical behaviour, reaching a local maximum RIA value (0.5 dB m⁻¹) at ~5 kGy, after which the RIA decreases before increasing again with a constant slope at higher doses. Finally, the RIA of the low-OH OF follows the trend of the kinetics at 450 nm, since the tendency is dominated by the tail of the UV bands, reaching a very low saturation value (0.02 dB m⁻¹) at ~0.1 kGy. The most resolved features in the spectral measurements are the presence of the ~620 nm centred absorption band (high- and medium-OH content samples) overlapped by the tail of a UV absorption related to point defects absorbing at lower wavelengths. The above-mentioned band is not observed in the low-OH sample for which the UV band is very intense. It is interesting to note how the amplitude of the 620 nm band is coherent with the OH concentration increase in the fibers and in countertendency with the UV tail.

Another spectral characteristic observed in the medium-OH content OF is an unstable wide band centred between 650 and 770 nm, which explains the local maximum at ~10 kGy observed in the RIA kinetics and that disappears at higher doses. Regarding the RIA recovery kinetics, two types of decays are evident: one representing the contribution of the UV tail, which recovers almost all the transmission properties in one hour from the irradiation end, while the defects responsible for the 620 nm band seem more stable in the same time frame at RT.

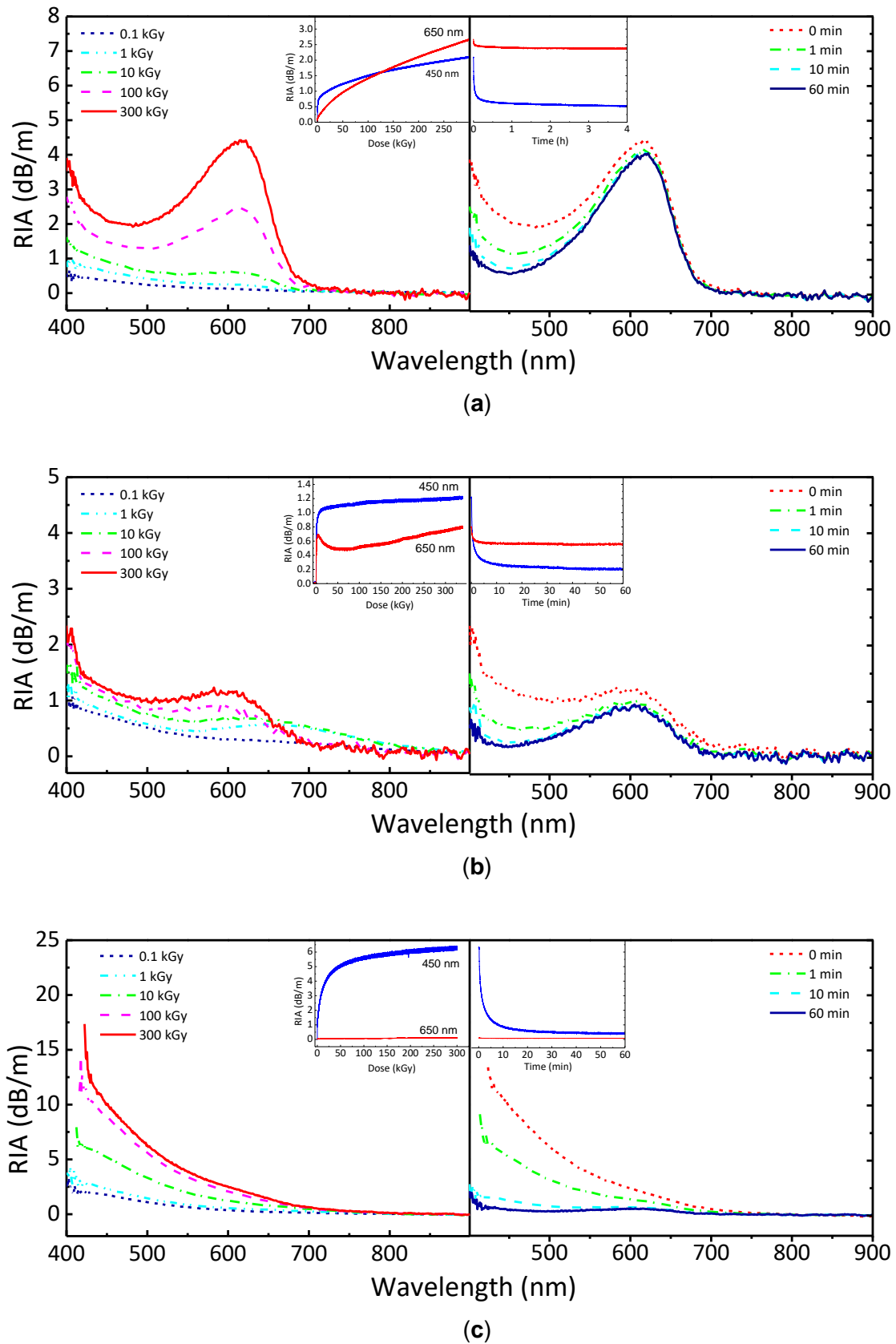


Figure 5.2 RIA spectral growth during the irradiation (left) and spectral decrease during the recovery (right) in the high-OH (a), medium-OH (b) and low-OH (c) sample. All insets show their respective RIA kinetics at 450 nm and 650 nm.

Figure 5.3 reports the RIA spectra during and up to one hour after the irradiation end for the treated medium-OH sample. The two most significant differences with respect to the non-treated counterpart (Figure 5.2b) are: a greater attenuation due to the tail of the band peaked in the UV region and the disappearance of the local maximum in the 650 nm kinetic. Finally, it is worth pointing out that the RIA at 650 nm and at 300 kGy of the treated sample has the same value as the one obtained from the non-treated sample (0.7 dB m^{-1}).

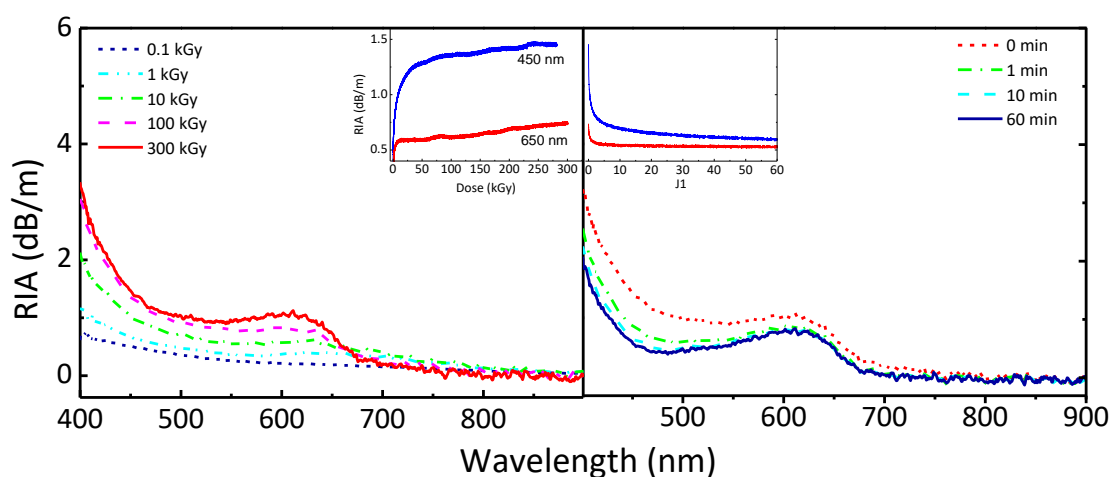


Figure 5.3 RIA spectral growth during the irradiation (left) up to 300 kGy and spectral decrease during the recovery (right) in the medium-OH+H₂+TT sample. Both insets show the respective RIA kinetics at wavelengths of 450 nm and 650 nm.

5.1.2. RIA spectral decomposition

While to date the decomposition of RIA in the UV-visible range of silica-based materials is rather well known and understood, still a number of issues needs to be clarified with regards to certain color centers typically identified in OFs, such as s-a STHs [98], [99], [161]. In order to better understand the basic mechanisms at the origin of the OF losses, we performed a spectral decomposition on the RIA spectra acquired, at the maximum accumulated dose, following the process described in section 2.5.5.

Being all samples PSC, in the fitting routine we considered only intrinsic defects and eventually impurities, such as Cl-related centers [59], [162]. Since the only source of extrinsic processes in the OF under test is attributed to the OH content [163], we started our analysis from the low-OH content sample, being this fiber associated with the lowest probability for the process expressed in (1.20). The result of the fitting routine obtained on the RIA at 300 kGy is shown in Figure 5.4. This analysis highlights the large contribution of the color center peaked at 3.26 eV (380 nm) attributed to Cl⁰, as well as the contributions of the STHs with two absorption bands centered at 2.61 eV (475 nm) and 2.16 (574 nm), corresponding to the STH₁ and STH₂ point defects, respectively. Furthermore, it was deliberately chosen not to introduce in the fitting routine the absorption band related to the Cl₂, given the significant error that would

be committed when assessing its amplitude, considering that is centered at 3.78 eV (328 nm) and then at quite far energies outside the investigated range of wavelengths. All the best-fit parameters of the Gaussian absorption bands of each point defect used in the decomposition of the three OF responses can be found in Table 5.2.

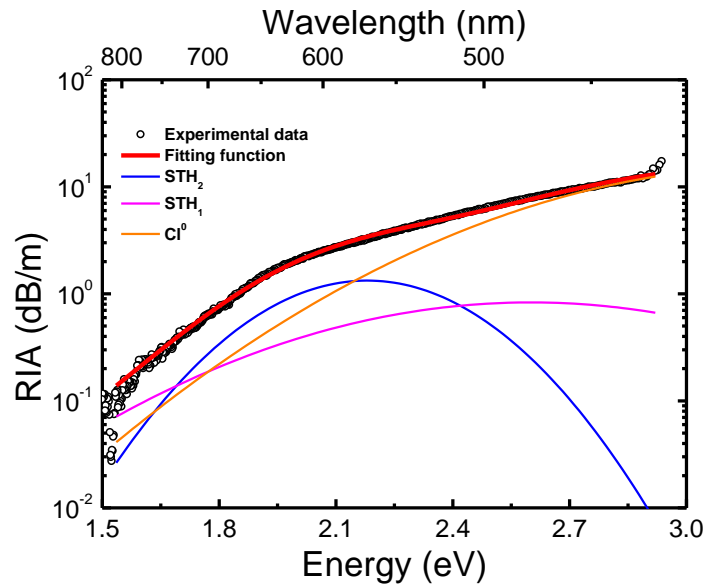


Figure 5.4 Decomposition of the RIA spectrum measured for the low-OH sample at 300 kGy TID. Open circles represent the experimental data while the red line represents the best fitting function obtained by summing the different absorption bands related to single point defects.

To compare the different spectral profiles, we report in Figure 5.5 the spectra normalized to the RIA values measured at 2.8 eV (450 nm). This normalization was done in order to qualitatively highlight the disparity between the three samples. Indeed, the appearance of a new spectral feature in the range 1.7 – 2.7 eV (730 – 460 nm) is evident with analogous spectral characteristics compared to the ones linked to NBOHC centered at ~2.0 eV, strongly supporting the NBOHC generation through the process described in (1.20), in accordance with the OH amount registered in the pristine OFs.

To isolate the NBOHC contribution, we have then decided to perform the fitting routine on the differences between the normalized RIA (Δ RIA) of the high-OH and medium-OH samples with respect to the low-OH sample. It is well known that the NBOHC absorption band around 2 eV is asymmetrical. As a first approximation, it is often considered as a Gaussian band centered at 1.97 eV (FWHM = 0.17 eV). However, when the NBOHC becomes the most important contribution around 2 eV, such approximation cannot be employed. Consequently, the NBOHC absorption band at 2 eV can be described as the sum of three different Gaussian bands with a fixed amplitude ratio, as reported in [95].

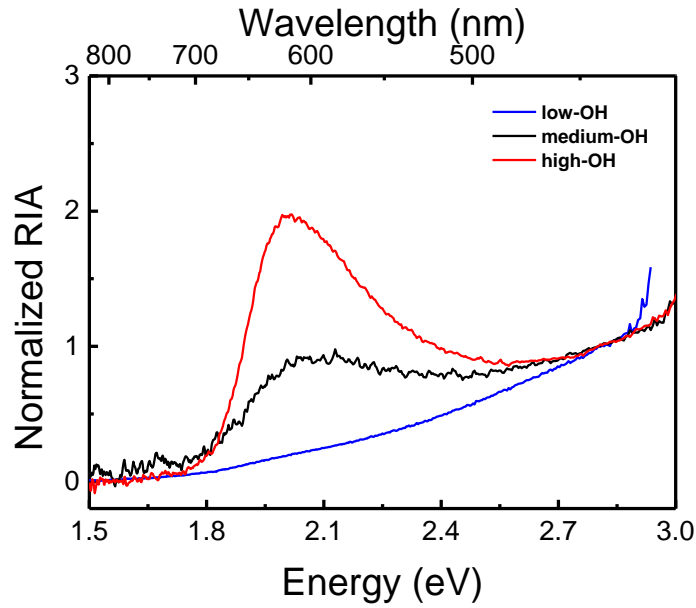


Figure 5.5 RIA spectra, normalized to the value measured at 2.8 eV (450 nm), acquired at 300 kGy TID, for the low-, medium- and high-OH samples.

Table 5.2 Best-fit parameters for the RIA at 300 kGy of the three samples.

Point defect	E_c [eV]	FWHM [eV]	Low-OH ¹	Medium-OH ¹	High-OH ¹
STH ₁	2.6	1.2	1	0.15	0.2
STH ₂	2.16	0.6	0.77	0.36	0.46
NBOHC	1.95, 2.04, 2.21	0.16, 0.27, 0.46	-	0.05, 0.08, 0.06	0.36, 0.55, 0.42
Cl ⁰	3.26	1.17	19.66	2.1	4.1

¹ Parameters refer to the area A [dB eV m⁻¹] of the Gaussian absorption band, necessary to reconstruct the overall RIA spectra.

Figure 5.6a shows the Δ RIA of the high-OH OF and its fitting function. It is possible to observe that the contribution of the NBOHC absorption band stands out and that the considered model well suits the RIA profile. However, to achieve a good quality of the fit, we were obliged to introduce the Gaussian absorption band related to the STH₂ point defect. The introduction of this band is well supported by the literature, where it has been found that a higher OH concentration corresponds to a higher STH₂ relative contribution [99]. In addition, the inset of Figure 5.6a reports the same fitting routine but with the NBOHC considered as a single Gaussian absorption band centered around 2 eV. In this case, it is evident that the result of the fit does not match the experimental data and new absorption bands associated with one or more yet unknown point defects should be introduced. Figure 5.6b reports the fitting function obtained on the overall RIA profile of the high-OH sample at 300 kGy as well as the individual bands of the point defects used for the decomposition.

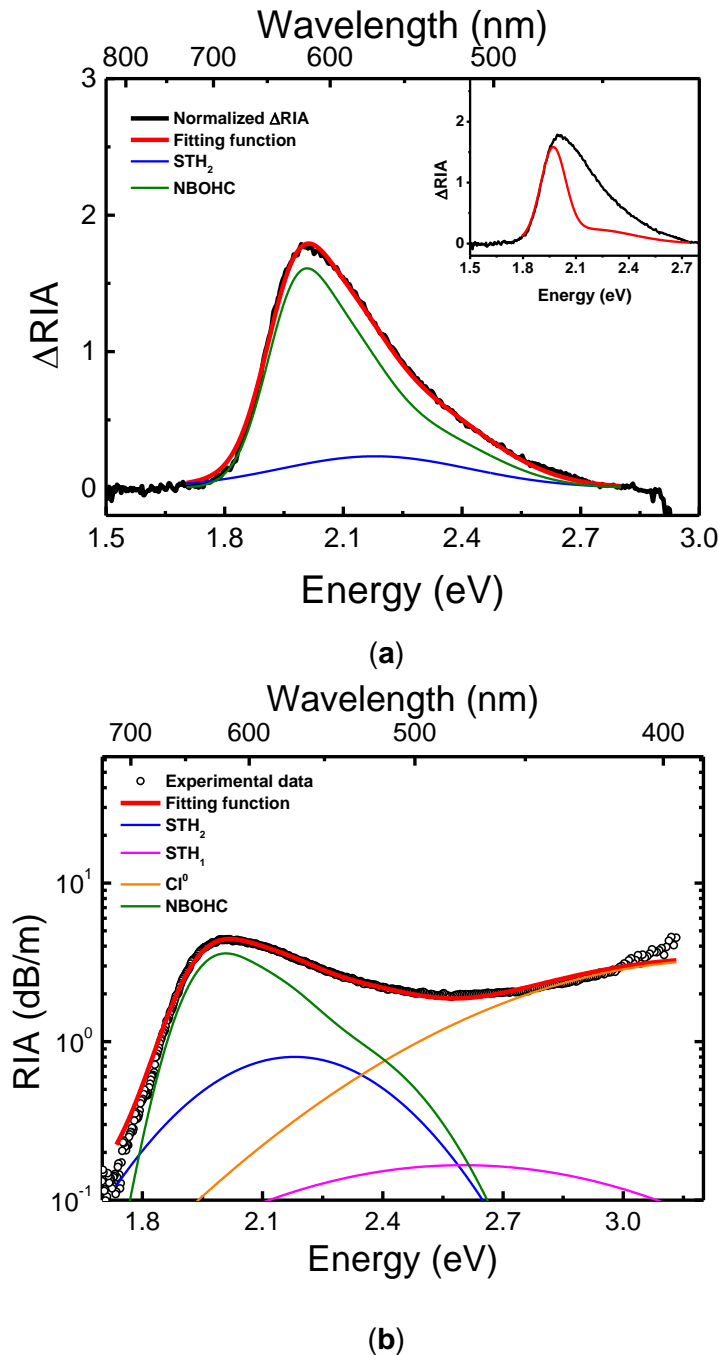
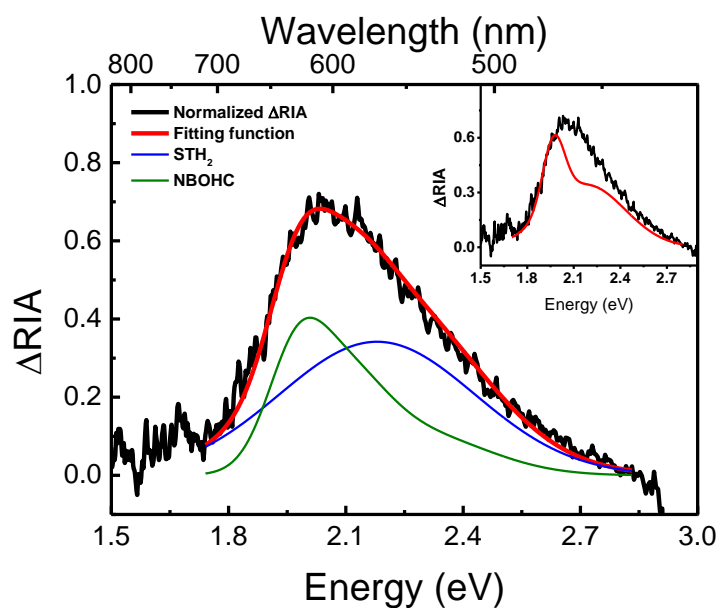
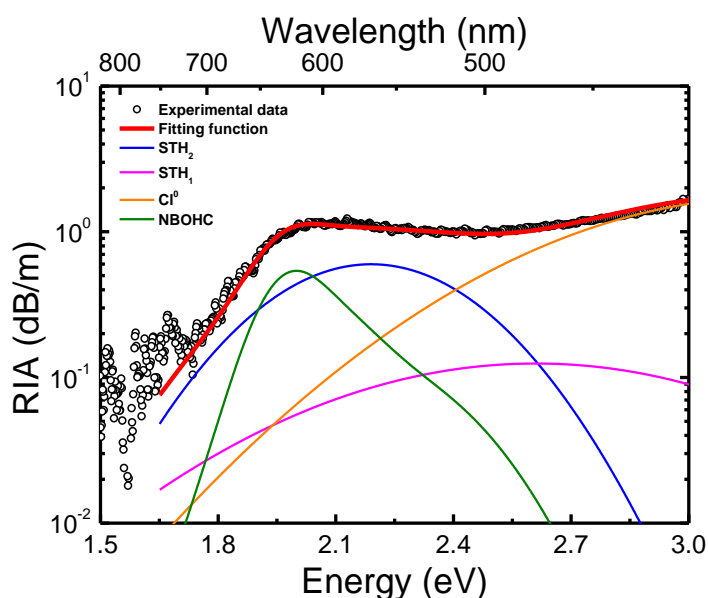


Figure 5.6 (a) Fitting function of the difference between the normalized RIA (ΔRIA) of the high- and low-OH samples, taking into account the mathematical model of the NBOHC described in [95]. The inset shows the attempt to fit the ΔRIA with the NBOHC considered as a single Gaussian band. **(b)** Fitting function of the RIA at 300 kGy of the high-OH sample.

The same approach was used for the analysis of the irradiated medium-OH sample. Figure 5.7a displays the obtained fitting function for the ΔRIA at 300 kGy with respect to the low-OH. In accordance with the process (1.20), in the medium-OH sample we observe a lower content of the NBOHC contribution. Moreover, the inset of Figure 5.7a shows again that, with the classical 1-Gaussian model of the NBOHC, the central region still needs to be completed by some other unknown absorption bands. Figure 5.7b reports the match between the experimental RIA and the fitting function in the medium-OH sample.



(a)

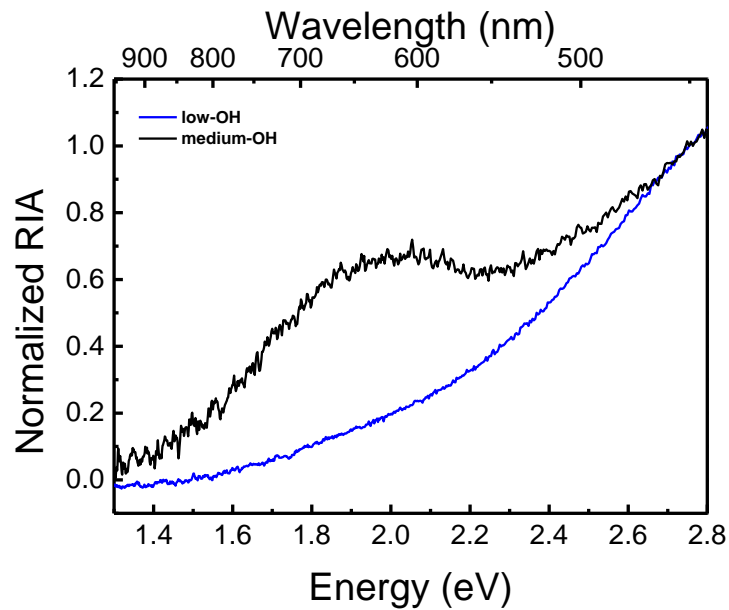


(b)

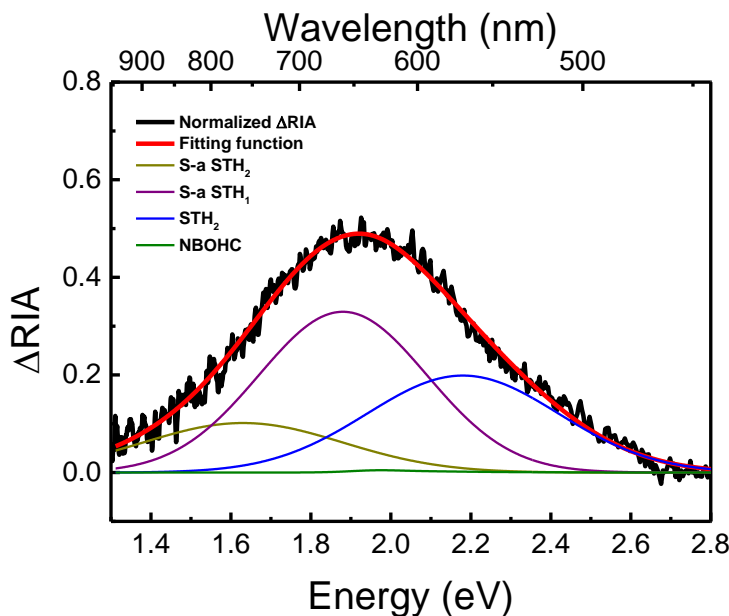
Figure 5.7 (a) Fitting function of the difference between the normalized RIA of the medium- and the low-OH samples, considering the NBOHC model of [95]. The inset shows the attempt to fit the Δ RIA with the NBOHC considered as a single Gaussian band. **(b)** Fitting function of the RIA at 300 kGy of the medium-OH sample.

As in the case of the high-OH, in Figure 5.7a the absorption bands related to NBOHC and STH_2 have been used. In this case, the relative contribution provided by the STH_2 increases in comparison to the high-OH case. The greater contribution of the STH-related bands could also justify the non-monotonic behaviour observed in the RIA kinetics shown in Figure 5.2b, considering their strained assisted variants (s-a STHs) [15], [127], [161]. Indeed, it is possible to notice that, at doses of about 10 kGy, the medium-OH RIA has a broader band covering also energies lower than 1.5 eV compared to the one of the same sample at 300 kGy (Figure 5.5). This band agrees with the s-a STH_1 and s-a STH_2 spectral characteristics,

centered respectively at 1.88 eV (660 nm) and 1.63 eV (760 nm). For this reason, an in-depth analysis of the RIA at 10 kGy of the medium-OH sample has been carried out, being 10 kGy the dose which corresponds to the maximum in the kinetics at 650 nm, as reported in Figure 5.2b. For this purpose, Figure 5.8a reports together the normalized RIA at 2.8 eV of the medium- and low-OH samples. Moreover, Figure 5.8b illustrates the fitting of the Δ RIA, where it becomes evident that the NBOHC contribution at lower doses is negligible and that STH_2 centers are still present.



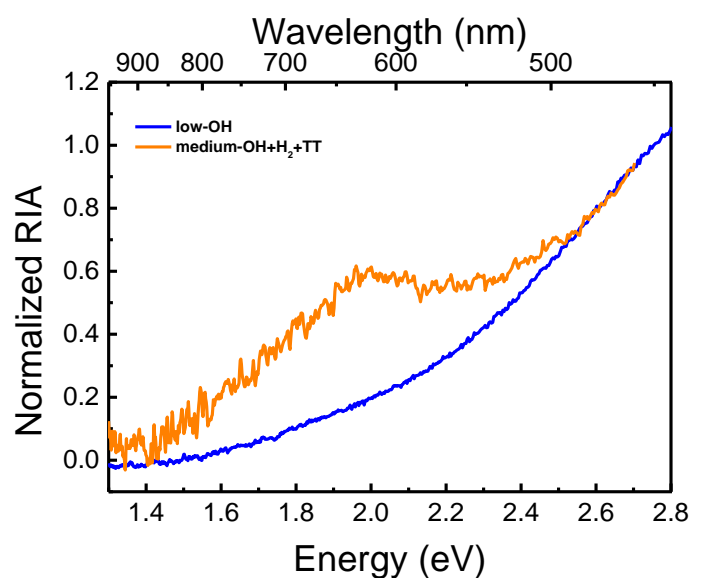
(a)



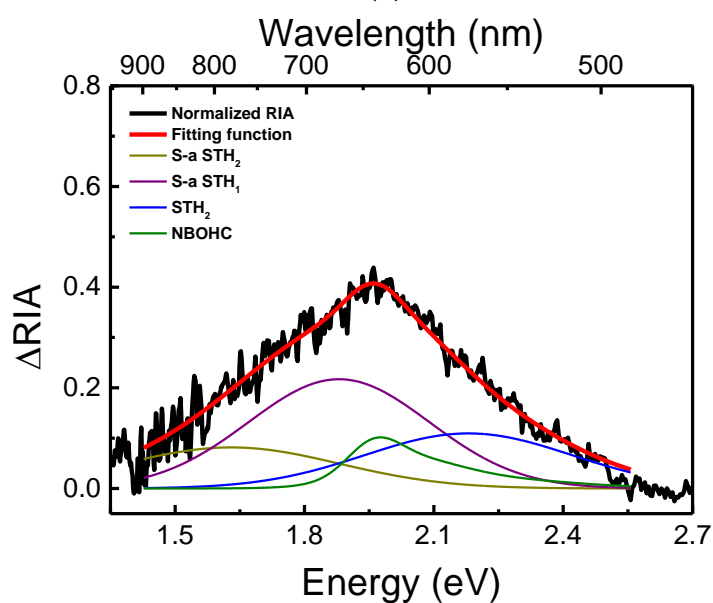
(b)

Figure 5.8 (a) Normalized spectra with respect to the RIA measured at 2.8 eV (450 nm) for the low- and medium-OH samples at 10 kGy dose. **(b)** Fitting function obtained for the difference of the normalized RIA of the medium-OH and low-OH samples measured at a dose of 10 kGy.

As already mentioned in section 5.1, the pristine medium-OH sample was also loaded with H_2 and then thermally treated, in order to eliminate the absorption band centered around 600 nm and mainly due to drawing-induced NBOHCs. Figure 5.9a shows the normalized spectra of the low-OH and the treated medium-OH sample at the dose of 10 kGy. By comparing this figure with Figure 5.8a, we show that the treatment has no significant impact on the shape of the RIA, but it slightly influences the relative magnitudes of the absorption bands used in the decomposition (Figure 5.9b). In particular, the STH_2 band area slightly decreases compared to the case of the non-treated sample and an increase in the NBOHC band is noticed. The best-fit parameters for the treated and non-treated medium-OH sample are listed in Table 5.3.



(a)



(b)

Figure 5.9 (a) Normalized spectra with respect to the RIA measured at 2.8 eV (450 nm) for the low-OH and the treated medium-OH samples at 10 kGy dose. (b) Fitting function obtained for the difference of the normalized RIA of the treated medium- and low-OH samples measured at a dose of 10 kGy.

Table 5.3 Best-fit parameters for the RIA at 10 kGy of the treated and non-treated medium-OH sample.

Point defect	Ec [eV]	FWHM [eV]	Medium-OH ¹	Medium-OH+H ₂ +TT ¹
STH ₁	2.6	1.2	0.24	0.24
STH ₂	2.16	0.6	0.17	0.09
s-a STH ₁	1.88	0.2	0.18	0.13
s-a STH ₂	1.63	0.3	0.07	0.06
NBOHC	1.95, 2.04, 2.21	0.16, 0.27, 0.46	4×10 ⁻⁴ , 6×10 ⁻⁴ , 5×10 ⁻⁴	9.5×10 ⁻⁴ , 14.5×10 ⁻⁴ , 11.2×10 ⁻⁴
Cl ⁰	3.26	1.17	1.74	1.89

¹ Parameters refer to the area A [dB eV m⁻¹] of the Gaussian absorption band, necessary to reconstruct the overall RIA spectra.

Finally, the two RIAs at 300 kGy for the treated and non-treated medium-OH sample are compared in Figure 5.10. It can be seen that, in the treated sample, the magnitude of the RIA increases significantly with respect to the non-treated sample at energies above 2.4 eV. Simultaneously, it is reduced by approximately 10 % in the 1.9 – 2.4 eV range. This last feature could be explained by the slight decrease of the STH₂ magnitude already observed in Figure 5.9b. It is known from literature that STH annealing could be responsible for the creation of the Cl⁰ point defect [58], [99].

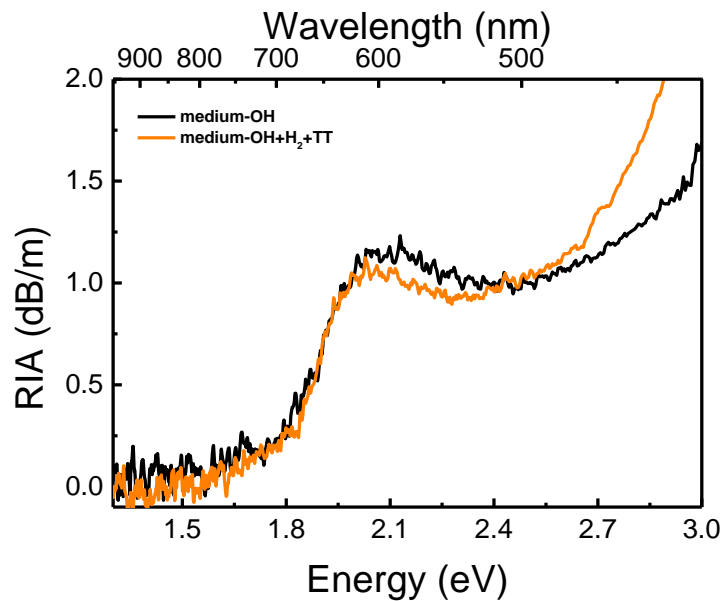


Figure 5.10 Measured RIA of the medium-OH and the treated medium-OH samples at a dose of 300 kGy.

5.2. Summary

This chapter presents the investigation about how the content of Si-OH groups governs the intrinsic losses and the RIA of MM PSC OFs in the vis-NIR spectral range. For the study, three OFs have been drawn from three different preforms with different OH concentrations: the low-OH (0.41 ppm at 1385 nm), the medium-OH (27 ppm at 1240 nm) and the high-OH (873 ppm at 1240 nm). In addition, the effect of a combined H₂ loading added to a thermal-treatment before the irradiation has been studied on the medium-OH sample, in order to eliminate its drawing-induced defects, the main cause of signal degradation in the considered spectral region before irradiation.

The X-ray irradiation at 6 Gy s⁻¹ up to 300 kGy shows a monotonic increase of the RIA for the low- and high-OH samples, while a different behavior was observed for the medium-OH, depending on the spectral range of interest: a monotonic increase of the RIA for wavelengths below ~600 nm and a non-monotonic behavior for wavelengths above ~600 nm.

The spectral decomposition of the RIA highlighted the various point defects that contribute to the optical absorption. In particular, the absorption band peaked at 1.97 eV (~630 nm), attributed to NBOHCs, increases according to the OH amount present in the OF. Moreover, due to its asymmetrical shape, the absorption band associated to NBOHCs has been fitted with two models already presented in literature: a 3-Gaussian model [95], and the “standard” 1-Gaussian model [15], this latter revealing the necessity to include one or more yet unknown contributions in order to match the experimental data.

The non-monotonic trend with the dose of the RIA around 650 nm for the medium-OH sample has been studied by the decomposition of the RIA spectrum at 10 kGy dose at which the maximum value in the kinetics has been measured. Here, the s-a STH contribution is introduced and shown to be the most adapted one to reproduce the experimental data.

Conclusions

Nowadays, the implementation of fiber-based solutions in natural and man-made radiation environment is increasingly promoted thanks to the many advantages offered by silica-based OFs technology, such as immunity to most electromagnetic perturbations, low intrusiveness, high bandwidth, multiplexing capability and an overall good radiation resistance.

When OFs are exposed to radiations, their signal transmission properties are degraded due to the generation of radiation-induced point defects or the conversion of precursor sites into other structures of optically-active defects in the OF silica-based matrix. This phenomenon, named RIA, is the most studied among the radiation-involving processes as is the one with the major impact on the systems performances. RIA levels and kinetics can be affected by many parameters as the irradiation conditions (nature of particles, TID, dose-rate, irradiation temperature), OF composition (glass stoichiometry, impurities concentration), probing light power and whether the OF has been subjected to pre-treatments or not. The knowledge of the RIA dependence on these factors is of fundamental importance for applications such as in-situ diagnostics in nuclear industry or for the monitoring of environmental parameters in nuclear waste dismantling sites. These applications are associated with severe mixed environments characterized by the presence of ionizing radiations, temperature variations and presence of various gases. A typical example is encountered by ANDRA in the framework of the CIGEO project, which led to the conception of the CERTYF consortium, a fundamental research project aiming to improve the current knowledge on the basic mechanisms responsible for the OF degradation in the simultaneous presence of radiation, hydrogen and temperature constraints. The acquired knowledge may contribute to improve the design of radiation-resistant OFs in order to develop radiation-tolerant systems or sensors able to operate in radioactive waste storage facilities or, conversely, to enhance the OF radiation sensitivity in order to improve the performances of dosimetry systems.

The results reported in this thesis cover the online measurement of the RIA related to radiation-sensitive and radiation-tolerant OFs, when exposed simultaneously to X-ray steady-state radiation and temperature variations. In addition, concerning radiation-hardened OFs, the influence of the hydroxyl groups concentration on the visible RIA was investigated. Our experimental setup allowed to evaluate the online RIA, i.e. during the irradiation, enabling the detection also of metastable point defect generation phenomena. Below we summarize the main relevant results obtained during the experimental investigation:

- the RIA in the NIR domain of aluminosilicate OFs is significantly impacted by the irradiation temperature, revealing a level decrease as temperature

Conclusions

increases. Furthermore, while the RIA in the visible domain is entirely due to the contribution of Al-OHCs, no evidence of absorption bands in the NIR is found. In addition, a linear relationship is found between the dose and level at which the 1550 nm RIA reaches an equilibrium level (indicating the same rate of generation and recombination of the point defects responsible for the absorption), suggesting a direct generation process of the absorbers responsible for the RIA at this wavelength and, more generally in the NIR, where the RIA is due to a single and not to multiple absorption components, characterized by a continuum of absorption states.

- In phosphosilicate OFs, the absorption due to m-POHC centers decreases with the increasing irradiation temperature; however, the RIA in the 600 – 700 nm range is independent on the temperature. In the 800 – 1100 nm wavelength range, the temperature increase causes a RIA reduction, showing the presence of an absorption band centered between 1.7 and 1.8 eV. In the future, further investigation will be carried out in order to better isolate the features of the unknown optical absorption bands in this spectral range. Finally, the P1 absorption band is not influenced by the temperature up to 200°C.

For dosimetry application, the comparison between the CERTYF P-doped sample with two other commercially available (C.A.) OFs, one acrylate- and one polyimide-coated, revealed the same performances. Furthermore, studying the operation temperature of these OF-based dosimeters, sensitivity variations within $\pm 15\%$ were reported when varying the temperature in the $-80^\circ\text{C} - 120^\circ\text{C}$ range. Also an independence of the radiation sensitivity on the dose-rate was reported between 10 mGy s^{-1} and 1 Gy s^{-1} , at temperatures up to 120°C .

- By recording the 1550 nm RIA of germanosilicate OFs, no impact of the probing signal power was reported on the C.A. sample (also up to MGy dose levels), contrary to the CERTYF sample. In addition, the NIR RIA of the C.A. OF revealed two distinct absorption contributions characterized by two different kinetics: the first one, due to GeX and GeY color centers, with a steep growth at low doses and a saturation around 5 kGy; and the second one, absorbing at longer wavelengths, with a significant impact at high TIDs.

Combined temperature and radiation experiment on the C.A. sample reported a decreasing trend of the NIR RIA as the temperature increases, caused by unstable color centers at RT. The same trend was obtained from spectral measurement on a MM canonical Ge-doped sample in the $-100^\circ - 0^\circ\text{C}$ temperature range across the UV-vis and NIR spectrum. In addition, it has been observed that when increasing the temperature for values above 0°C , the RIA

does not follow a defined trend, a possible indication of the presence of an interconversion process between point defects.

- The amount of Si-OH groups governs the intrinsic losses and the RIA of MM PSC OFs. In particular, the optical absorption band peaked at ~630 nm, related to drawing- and radiation-induced NBOHCs, increases according to the OH amount present in the sample. Moreover, for the spectral decomposition of the acquired experimental RIA, it was not possible to use the standard 1-Gaussian band model of NBOHC, hence we employed a mathematical model, already reported in literature, in which the asymmetrical NBOHC absorption band is considered as the sum of three different Gaussians with a fixed amplitude ratio. While for the low- and high-OH content sample, the X-ray irradiation reported a monotonic increase of the vis RIA as a function of the accumulated dose, a non-monotonic increase was observed for the medium-OH sample, at wavelengths above ~600 nm. To explain this behavior, the introduction of the absorption bands related to the s-a STHs has shown to be the most adapted one to reproduce our experimental data.

Finally, a combined H₂-loading and thermal-treatment before the irradiation of the medium-OH sample enabled to eliminate the absorption band due to drawing-induced NBOHCs as well as the non-monotonic behavior of the online RIA, modifying the relative magnitudes of the absorption bands used for the decomposition.

List of publications

Articles published on peer-reviewed journals as primary author:

1. C. Campanella, V. De Michele, A. Morana, A. Guttilla, F. Mady, M. Benabdesselam, A. Boukenter, Y. Ouerdane and S. Girard, "Temperature Dependence of Radiation Induced Attenuation of Aluminosilicate Optical Fiber," *IEEE Transactions on Nuclear Science*, 2022, doi: 10.1109/TNS.2022.3150870
2. C. Campanella, A. Morana, V. De Michele, J. Vidalot, E. Marin, A. Boukenter, Y. Ouerdane, P. Paillet, S. Girard, "Photobleaching Effect on the Radiation-Induced Attenuation of an Ultralow Loss Optical Fiber at Telecommunication Wavelengths," *Physica Status Solidi a*, 2021, doi: 10.1002/pssa.202100518
3. C. Campanella, A. Guttilla, A. Morana, V. De Michele, C. Muller, M. Aubry, F. Mady, E. Marin, Y. Ouerdane, A. Boukenter, M. Benabdesselam and S. Girard, "Photobleaching Effect on Infrared Radiation-Induced Attenuation of Germanosilicate Optical Fibers at MGy dose levels", *IEEE Transactions on Nuclear Science*, 68(8), pp 1688-1693 (2021), doi: 10.1109/TNS.2021.3068829
4. C. Campanella, V. De Michele, A. Morana, G. Mélin, T. Robin, E. Marin, Y. Ouerdane, A. Boukenter and S. Girard, "Radiation Effects on Pure-Silica Multimode Optical Fibers in the Visible and Near-Infrared Domains: Influence of OH Groups", *Applied Sciences*, vol.11(7), pp. 2991 (2021), doi: 10.3390/app11072991
5. C. Campanella, A. Morana, S. Girard, A. Guttilla, F. Mady, M. Benabdesselam, H. Desjonqueres, C. Monsanglant-Louvet, C. Balland, E. Marin, Y. Ouerdane, A. Boukenter, S. Delepine-Lesoille, "Combined Temperature and Radiation Effects on Radiation-Sensitive Single-Mode Optical Fibers," *IEEE Transactions on Nuclear Science*, vol. 67, no. 7, pp. 1643-1649, July 2020, doi: 10.1109/TNS.2020.2982280.
6. C. Campanella, L. Mescia, P. Bia, M. A. Chiapperino, S. Girard, T. Robin, J. Mekki, E. Marin, A. Boukenter and Y. Ouerdane, "Theoretical Investigation of Thermal Effects in High Power Er³⁺/Yb³⁺ - Codoped Double-Clad Fiber Amplifiers for Space Applications," *Physica Status Solidi a*, 2019, doi: 10.1002/pssa.201800582

Articles published on peer-reviewed journals as co-author:

7. J. Vidalot, C. Campanella, J. Dachicourt, C. Marcandella, O. Duhamel, A. Morana, D. Poujols, G. Assailit, M. Gaillardin, A. Boukenter, Y. Ouerdane, S. Girard and P. Paillet, "Monitoring of Ultra-High Dose Rate Pulsed X-ray Facilities with Radioluminescent Nitrogen-Doped Optical Fiber," *Sensors*, 22 (9), 3192 (2022), doi: 10.3390/s22093192
8. A. Morana, C. Campanella, M. Aubry, E. Marin, A. Boukenter, Y. Ouerdane and S. Girard, "Temperature Dependence of Low-Dose Radiation-Induced Attenuation of Germanium-Doped Optical Fiber at InfraRed Wavelengths," *IEEE Transactions on Nuclear Science*, 2021, doi: 10.1109/TNS.2021.3133421.
9. V. De Michele, C. Marcandella, A. Morana, C. Campanella, J. Vidalot, P. Paillet, M. Gaillardin, E. Marin, Y. Ouerdane, A. Boukenter and S. Girard, "Pulsed X-Ray Radiation Response of Ultralow Loss Pure-Silica-Core Optical Fibers," *Physica Status Solidi a*, 2021, doi: 10.1002/pssa.202100519
10. A. Guttilla, C. Campanella, M. Benabdesselam, A. Morana, A. Boukenter, Y. Ouerdane, S. Girard, F. Mady, "Investigation by Thermoluminescence of the Ionization and Annealing Processes in Irradiated Ge-Doped Silica Fiber Preform," *IEEE Transactions on Nuclear Science*, vol. 68, no. 8, pp. 1556-1564, Aug. 2021, doi: 10.1109/TNS.2021.3070695.
11. A. Morana, C. Campanella, E. Marin, G. Mélin, T. Robin, G. Li Vecchi, D. Di Francesca, A. Boukenter, Y. Ouerdane, F. Mady, M. Benabdesselam, J. Mekki, N. Balcon and S. Girard, "Operating Temperature Range of Phosphorous-doped Optical Fiber Dosimeters exploiting Infrared Radiation-Induced Attenuation", *IEEE Transactions on Nuclear Science*, 68 (5), pp 906-912 (2021), doi: 10.1109/TNS.2021.3053164
12. M. Royon, F. Vocanson, D. Jamon, F. Royer, E. Marin, A. Morana, C. Campanella, A. Boukenter, Y. Ouerdane, Y. Jourlin and S. Girard, "Impact of γ -rays irradiation on hybrid TiO₂-SiO₂ sol-gel films doped with Rhodamine 6G," *Materials*, 2021, 14, 5754, doi: 10.3390/ma14195754

List of publications

13. G. Li Vecchi, D. Di Francesca, Y. Kadi, D. Ricci, M. Brugger, C. Campanella, A. Alessi, Y. Ouerdane, and S. Girard, "In-situ regeneration of P-doped optical fiber dosimeter," *Optics Letters* 45, 5201-5204 (2020), doi: 10.1364/OL.402382
14. V. De Michele, A. Morana, C. Campanella, J. Vidalot, A. Alessi, A. Boukenter, M. Cannas, P. Paillet, Y. Ouerdane, S. Girard "Steady-State X-Ray Radiation-Induced Attenuation in Canonical Optical Fibers," *IEEE Transactions on Nuclear Science*, vol. 67, no. 7, pp. 1650-1657, July 2020, doi: 10.1109/TNS.2020.2969717
15. A. Morana, C. Campanella, J. Vidalot, V. De Michele, E. Marin, I. Reghioua, A. Boukenter, Y. Ouerdane, P. Paillet and S. Girard, "Extreme Radiation Sensitivity of Ultra-Low Loss Pure-Silica-Core Optical Fibers at Low Dose Levels and Infrared Wavelengths", *Sensors*, 20 (24), 7254 (2020), doi: 10.3390/s20247254
16. S. Girard, A. Morana, C. Hoehr, M. Trinczek, J. Vidalot, P. Paillet, C. Bélanger-Champagne, J. Mekki, N. Balcon, G. Li Vecchi, C. Campanella, D. Lambert, E. Marin, A. Boukenter, Y. Ouerdane and E. Blackmore, "Atmospheric Neutron Monitoring through Optical Fiber-Based Sensing", *Sensors*, 20 (16), 4510, 2020, doi: 10.3390/s20164510
17. M. Aubry, A. Ladaci, S. Girard, L. Mescia, A. Laurent, T. Robin, B. Cadier, M. Boutillier, J. Mekki, A. Morana, C. Campanella, J. Vidalot, E. Marin, Y. Ouerdane and A. Boukenter, "Radiation Effects on WDM and DWDM Architectures of Pre-amplifier and Boost-Amplifier", *IEEE Transactions on Nuclear Science*, 67 (1), 278-283 (2019), doi: 10.1109/TNS.2019.2953645
18. S. Girard, V. De Michele, A. Alessi, C. Marcandella, D. Di Francesca, P. Paillet, A. Morana, J. Vidalot, C. Campanella, S. Agnello, M. Cannas, M. Gaillardin, E. Marin, A. Boukenter and Y. Ouerdane, "Transient and Steady-State Radiation Response of Phosphosilicate Optical Fibers: Influence of H₂ Loading", *IEEE Transactions on Nuclear Science*, 67 (1), 289-295 (2019), doi: 10.1109/TNS.2019.2947583

Conferences contribution

International conferences:

1. **Poster contribution:** M. A. Chiapperino, C. Campanella, L. Mescia, P. Bia, S. Girard, T. Robin, J. Mekki, E. Marin, A. Boukenter and Y. Ouerdane, "Theoretical Investigation of Thermal Effects in High Power Er³⁺/Yb³⁺ - Codoped Double-Clad Fiber Amplifiers for Space Applications", SiO₂ conference, June 2018, Bari, Italy
2. **Oral contribution:** M. Aubry, A. Ladaci, S. Girard, L. Mescia, A. Laurent, T. Robin, B. Cadier, M. Boutillier, J. Mekki, A. Morana, C. Campanella, J. Vidalot, E. Marin, Y. Ouerdane and A. Boukenter, "Radiation Effects on WDM and DWDM Architectures of Preamplifier and Boost-Amplifier", IEEE Nuclear and Space Radiation Effects Conference (NSREC), July 2019, San Antonio, USA
3. **Oral contribution:** S. Girard, V. De Michele, A. Alessi, C. Marcandella, D. Di Francesca, P. Paillet, A. Morana, J. Vidalot, C. Campanella, S. Agnello, M. Cannas, M. Gaillardin, E. Marin, A. Boukenter and Y. Ouerdane, "Transient and Steady-State Radiation Response of Phosphosilicate Optical Fibers: Influence of H₂ Loading", IEEE Nuclear and Space Radiation Effects Conference (NSREC), July 2019, San Antonio, USA
4. **Oral contribution:** C. Campanella, A. Morana, S. Girard, A. Guttilla, F. Mady, M. Benabdesselam, H. Desjonquieres, C. Monsanglant-Louvet, C. Balland, E. Marin, Y. Ouerdane, A. Boukenter and S. Lesoille, "Combined temperature and radiation effects on radiation sensitive single-mode optical fibers", Radiation Effects on Components and Systems (RADECS), September 2019, Montpellier, France (**PRESENTING AUTHOR**)
5. **Poster contribution:** V. De Michele, A. Morana, C. Campanella, J. Vidalot, A. Alessi, A. Boukenter, M. Cannas, Y. Ouerdane and S. Girard, "Characterization of the RIA Induced in Canonical Optical Fibers under Continuous X-ray Irradiation at Room and Liquid Nitrogen Temperatures", Radiation Effects on Components and Systems (RADECS), September 2019, Montpellier, France
6. **Oral contribution:** C. Campanella, A. Guttilla, A. Morana, V. De Michele, C. Muller, F. Mady, E. Marin, Y. Ouerdane, A. Boukenter, M. Benabdesselam and S. Girard, "Infrared Radiation-Induced Attenuation of Germanosilicate Optical Fibers at MGy dose levels", Radiation Effects on Components and Systems (RADECS), October 2020, virtual conference (**PRESENTING AUTHOR**)
7. **Oral contribution:** A. Guttilla, C. Campanella, F. Mady, M. Benabdesselam, A. Morana, A. Boukenter, Y. Ouerdane and S. Girard, "Investigation by Thermoluminescence of the Recombination Process in irradiated Ge-doped Silica Preform", Radiation Effects on Components and Systems (RADECS), October 2020, virtual conference
8. **Oral contribution:** A. Morana, C. Campanella, E. Marin, G. Mélin, T. Robin, G. Li Vecchi, D. Di Francesca, A. Boukenter, Y. Ouerdane, F. Mady, M. Benabdesselam, J. Mekki, N. Balcon and S. Girard, "Operating Temperature Range of Phosphorous-doped Optical Fiber Dosimeters exploiting Infrared Radiation-Induced Attenuation", IEEE Nuclear and Space Radiation Effects Conference (NSREC), July 2021, virtual conference
9. **Oral contribution:** C. Campanella, A. Morana, V. De Michele, J. Vidalot, E. Marin, A. Boukenter, Y. Ouerdane and S. Girard, "Photobleaching Effect on the Radiation-Induced Attenuation of an Ultra-Low Loss Optical Fiber at Telecommunication Wavelength", SiO₂ conference, June 2021, virtual conference (**PRESENTING AUTHOR**)
10. **Oral contribution:** V. De Michele, C. Marcandella, A. Morana, C. Campanella, J. Vidalot, P. Paillet, E. Marin, Y. Ouerdane, A. Boukenter and S. Girard, "Pulsed X-Ray Radiation Response of Ultra-Low Loss Pure-Silica-Core Optical Fiber", SiO₂ conference, June 2021, virtual conference
11. **Oral contribution:** A. Morana, C. Campanella, J. Vidalot, V. De Michele, E. Marin, A. Boukenter, Y. Ouerdane and S. Girard, "Dose-rate dependence of the Radiation-Induced Attenuation of an Ultra-Low Loss Optical Fiber in the Near InfraRed", SiO₂ conference, June 2021, virtual conference
12. **Oral contribution:** F. Fricano, G. Maron, C. Campanella, A. Morana, A. Boukenter, S. Girard, Y. Ouerdane, G. Buscarino, S. Agnello and M. Cannas, "Paramagnetic defects induced in pure and doped optical fibers: influence on the transmission properties", SiO₂ conference, June 2021, virtual conference

National conferences:

13. **Oral contribution:** C. Campanella, L. Mescia, P. Bia, M. A. Chiapperino, S. Girard, T. Robin, J. Mekki, E. Marin, A. Boukenter and Y. Ouerdane, "Theoretical investigation of thermal effects in high power Er³⁺/Yb³⁺-codoped double-clad fiber amplifiers for space applications", Fibre Optiques en

Conferences contribution

Milieu Radiatif (FMR), December 2018, Saint-Etienne, France (**PRESENTING AUTHOR**)

14. **Oral contribution:** C. Campanella, V. De Michele, A. Morana, G. Mélin, T. Robin, E. Marin, Y. Ouerdane, A. Boukenter, and S. Girard, “*Radiation Effects on Pure-Silica Multimode Optical Fibers in the Visible and Near-Infrared Domains: Influence of OH Groups*”, Radiation Effects on Optoelectronics and Photonics Technologies (RADOPT), November 2021, Saint-Etienne, France (**PRESENTING AUTHOR**)
15. **Poster contribution:** C. Campanella, V. De Michele, A. Morana, A. Guttilla, F. Mady, M. Benabdesselam, E. Marin, Y. Ouerdane, A. Boukenter and S. Girard, “*Temperature Dependence of Radiation Induced Attenuation of Aluminosilicate Optical Fiber*”, Radiation Effects on Optoelectronics and Photonics Technologies (RADOPT), November 2021, Saint-Etienne, France (**PRESENTING AUTHOR**)

References

- [1] S. Delepine-Lesoille *et al.*, 'France's State of the Art Distributed Optical Fibre Sensors Qualified for the Monitoring of the French Underground Repository for High Level and Intermediate Level Long Lived Radioactive Wastes', *Sensors*, vol. 17, no. 6, Art. no. 6, Jun. 2017, doi: 10.3390/s17061377.
- [2] *Physique et technologie des fibres optiques - Jean-Pierre Meunier*. Accessed: Dec. 01, 2021. [Online]. Available: <https://www.decitre.fr/livres/physique-et-technologie-des-fibres-optiques-9782746207202.html>
- [3] A. W. Snyder and J. D. Love, 'Weak-guidance approximation', in *Optical Waveguide Theory*, Boston, MA: Springer US, 1983, pp. 623–639. doi: 10.1007/978-1-4613-2813-1_35.
- [4] R. Dorn and C. L. Sergent, 'Technical Note: Preform technologies for optical fibres', *International Journal of Materials and Product Technology*, vol. 4, no. 3, pp. 300–308, Jan. 1989, doi: 10.1504/IJMPT.1989.036751.
- [5] S. R. Nagel, J. B. MacChesney, and K. L. Walker, 'An Overview of the Modified Chemical Vapor Deposition (MCVD) Process and Performance', *IEEE TRANSACTIONS ON MICROWAVE THEORY AND TECHNIQUES*, no. 4, p. 18, 1982.
- [6] C. Yeh, Ed., 'Handbook of Fiber Optics', in *Handbook of Fiber Optics*, San Diego: Academic Press, 1990, pp. 373–382. doi: 10.1016/B978-0-12-770455-5.50023-7.
- [7] A. Guttilla, 'Étude des effets combinés du rayonnement et de la température sur les matériaux à base de silice et les fibres optiques', These de doctorat, Université Côte d'Azur, 2021. Accessed: Jan. 18, 2022. [Online]. Available: <http://www.theses.fr/2021COAZ4038>
- [8] L. Onsager, 'Initial Recombination of Ions', *Phys. Rev.*, vol. 54, no. 8, pp. 554–557, Oct. 1938, doi: 10.1103/PhysRev.54.554.
- [9] T. P. Ma and P. V. Dressendorfer, *Ionizing Radiation Effects in MOS Devices and Circuits*. Wiley. Accessed: Dec. 01, 2021. [Online]. Available: <https://www.wiley.com/en-al/Ionizing+Radiation+Effects+in+MOS+Devices+and+Circuits-p-9780471848936>
- [10] D. L. Griscom, 'Nature Of Defects And Defect Generation In Optical Glasses', in *Radiation Effects on Optical Materials*, Dec. 1985, vol. 0541, pp. 38–59. doi: 10.1117/12.975358.
- [11] H. Henschel, O. Köhn, and H. U. Schmidt, 'Optical fibres as radiation dosimeters', *Nuclear Instruments and Methods in Physics Research Section B: Beam Interactions with Materials and Atoms*, vol. 69, no. 2, Art. no. 2, Jun. 1992, doi: 10.1016/0168-583X(92)96023-R.
- [12] D. D. Francesca, G. L. Vecchi, Y. Kadi, M. Brugger, S. Girard, and A. Alessi, 'Implementation of Optical Fiber based Dosimetry at CERN', in *26th International Conference on Optical Fiber Sensors (2018)*, paper WC1, Sep. 2018, p. WC1. doi: 10.1364/OFS.2018.WC1.
- [13] A. C. Wright, 'Defect-Free Vitreous Networks: The Idealised Structure of SiO₂ and Related Glasses', in *Defects in SiO₂ and Related Dielectrics: Science and Technology*, G. Pacchioni, L. Skuja, and D. L. Griscom, Eds. Dordrecht: Springer Netherlands, 2000, pp. 1–35. doi: 10.1007/978-94-010-0944-7_1.
- [14] W. H. Zachariasen, 'THE ATOMIC ARRANGEMENT IN GLASS', *J. Am. Chem. Soc.*, vol. 54, no. 10, pp. 3841–3851, Oct. 1932, doi: 10.1021/ja01349a006.
- [15] S. Girard *et al.*, 'Overview of radiation induced point defects in silica-based optical fibers', *Reviews in Physics*, vol. 4, p. 100032, Nov. 2019, doi: 10.1016/j.revip.2019.100032.

References

- [16] P. A. Cherenkov, 'Visible luminescence of pure liquids under the influence of γ -radiation', vol. 2, no. 8, pp. 451–454, 1934, doi: 10.3367/UFNr.0093.196710n.0385.
- [17] J. Vidalot *et al.*, 'Optical Fiber-Based Monitoring of X-ray Pulse Series from a Linear Accelerator', *Radiation*, vol. 2, no. 1, pp. 17–32, Dec. 2021, doi: 10.3390/radiation2010002.
- [18] W. Primak and R. Kampwirth, 'The Radiation Compaction of Vitreous Silica', *Journal of Applied Physics*, vol. 39, no. 12, pp. 5651–5658, Nov. 1968, doi: 10.1063/1.1656029.
- [19] C. Muller, 'Conception optique pour les environnements radiatifs et application à une caméra résistante à des doses élevées (MGy)', Université Jean Monnet, Saint Etienne, 2020.
- [20] S. Girard *et al.*, 'Radiation Effects on Silica-Based Optical Fibers: Recent Advances and Future Challenges', *IEEE Transactions on Nuclear Science*, vol. 60, no. 3, Art. no. 3, Jun. 2013, doi: 10.1109/TNS.2012.2235464.
- [21] D. L. Griscom, 'Defect structure of glasses: Some outstanding questions in regard to vitreous silica', *Journal of Non-Crystalline Solids*, vol. 73, no. 1, pp. 51–77, Aug. 1985, doi: 10.1016/0022-3093(85)90337-0.
- [22] D. L. Griscom, 'Intrinsic and Extrinsic Point Defects in a-SiO₂', in *The Physics and Technology of Amorphous SiO₂*, R. A. B. Devine, Ed. Boston, MA: Springer US, 1988, pp. 125–134. doi: 10.1007/978-1-4613-1031-0_15.
- [23] W. Primak, 'Fast-Neutron-Induced Changes in Quartz and Vitreous Silica', *Phys. Rev.*, vol. 110, no. 6, pp. 1240–1254, Jun. 1958, doi: 10.1103/PhysRev.110.1240.
- [24] S. Rizzolo *et al.*, 'Evaluation of Distributed OFDR-Based Sensing Performance in Mixed Neutron/Gamma Radiation Environments', *IEEE Transactions on Nuclear Science*, vol. 64, no. 1, pp. 61–67, Jan. 2017, doi: 10.1109/TNS.2016.2606566.
- [25] G. Cheymol, H. Long, J. F. Villard, and B. Brichard, 'High Level Gamma and Neutron Irradiation of Silica Optical Fibers in CEA OSIRIS Nuclear Reactor', *IEEE Transactions on Nuclear Science*, vol. 55, no. 4, pp. 2252–2258, Aug. 2008, doi: 10.1109/TNS.2008.924056.
- [26] Y. Morita and W. Kawakami, 'Dose rate effect on radiation induced attenuation of pure silica core optical fibres', *IEEE Transactions on Nuclear Science*, vol. 36, no. 1, pp. 584–590, Feb. 1989, doi: 10.1109/23.34505.
- [27] A. Morana *et al.*, 'Extreme Radiation Sensitivity of Ultra-Low Loss Pure-Silica-Core Optical Fibers at Low Dose Levels and Infrared Wavelengths', *Sensors*, vol. 20, no. 24, Art. no. 24, Jan. 2020, doi: 10.3390/s20247254.
- [28] E. J. Friebele, C. G. Askins, and M. E. Gingerich, 'Effect of low dose rate irradiation on doped silica core optical fibers', *Appl. Opt., AO*, vol. 23, no. 23, pp. 4202–4208, Dec. 1984, doi: 10.1364/AO.23.004202.
- [29] P. Lu, X. Bao, K. Brown, and N. Kulkarni, 'Gamma-induced attenuation in normal single-mode and multimode, Ge-doped and P-doped optical fibers: A fiber optic dosimeter for low dose levels', *Can. J. Phys.*, vol. 78, no. 2, pp. 89–97, Mar. 2000, doi: 10.1139/p00-012.
- [30] M. Van Uffelen and P. Jucker, 'Radiation resistance of fiberoptic components and predictive models for optical fiber systems in nuclear environments', *IEEE Transactions on Nuclear Science*, vol. 45, no. 3, Art. no. 3, Jun. 1998, doi: 10.1109/23.685239.
- [31] M. Van Uffelen, 'Modélisation de systèmes d'acquisition et de transmission à fibres optiques destinés à fonctionner en environnement nucléaire', These de doctorat, Paris 11, 2001. Accessed: Dec. 02, 2021. [Online]. Available: <http://www.theses.fr/2001PA112107>
- [32] A. Alessi *et al.*, 'Near-IR Radiation-Induced Attenuation of Aluminosilicate Optical Fibers', *physica status solidi (a)*, vol. 218, no. 15, p. 2000807, 2021, doi: 10.1002/pssa.202000807.

- [33]A. Rosiewicz and M. H. Gray, 'Temperature dependence of radiation- induced loss in optical fibers', in *Integrated Optics and Optical Fiber Communication (1981)*, paper WJ3, Apr. 1981, p. WJ3. doi: 10.1364/OFC.1981.WJ3.
- [34]R. H. West, 'Predicting the radiation induced loss in Ge doped optical fibres at different temperatures', in *1999 Fifth European Conference on Radiation and Its Effects on Components and Systems. RADECS 99 (Cat. No.99TH8471)*, Sep. 1999, pp. 483–490. doi: 10.1109/RADECS.1999.858629.
- [35]A. Alessi *et al.*, 'Irradiation Temperature Influence on the In Situ Measured Radiation Induced Attenuation of Ge-Doped Fibers', *IEEE Transactions on Nuclear Science*, vol. 64, no. 8, pp. 2312–2317, Aug. 2017, doi: 10.1109/TNS.2016.2627598.
- [36]S. Girard *et al.*, 'Combined High Dose and Temperature Radiation Effects on Multimode Silica-Based Optical Fibers', *IEEE Transactions on Nuclear Science*, vol. 60, no. 6, Art. no. 6, Dec. 2013, doi: 10.1109/TNS.2013.2281832.
- [37]D. P. Hawn, C. M. Petrie, T. E. Blue, and W. Windl, 'In-situ gamma radiation induced attenuation in silica optical fibers heated up to 600°C', *Journal of Non-Crystalline Solids*, vol. 379, pp. 192–200, Nov. 2013, doi: 10.1016/j.jnoncrysol.2013.08.013.
- [38]P. F. Kashaykin, A. L. Tomashuk, V. F. Khopin, A. N. Gur'yanov, S. L. Semjonov, and E. M. Dianov, 'New radiation colour centre in germanosilicate glass fibres', *Quantum Electron.*, vol. 48, no. 12, p. 1143, Dec. 2018, doi: 10.1070/QEL16850.
- [39]D. L. Griscom, E. J. Friebele, K. J. Long, and J. W. Fleming, 'Fundamental defect centers in glass: Electron spin resonance and optical absorption studies of irradiated phosphorus-doped silica glass and optical fibers', *Journal of Applied Physics*, vol. 54, no. 7, pp. 3743–3762, Jul. 1983, doi: 10.1063/1.332591.
- [40]P. Borgemans, 'Spectral and kinetic analysis of radiation induced optical attenuation in silica: towards intrinsic fiber optic dosimetry?', PhD. Thesis, Vrije Universiteit, Brussels, Belgium, 2001.
- [41]L. Nuccio, S. Agnello, and R. Boscaino, 'Role of H₂O in the thermal annealing of the E_γ' center in amorphous silicon dioxide', *Phys. Rev. B*, vol. 79, no. 12, p. 125205, Mar. 2009, doi: 10.1103/PhysRevB.79.125205.
- [42]S. Agnello and L. Nuccio, 'Thermal stability of gamma-irradiation-induced oxygen-deficient centers in silica', *Phys. Rev. B*, vol. 73, no. 11, p. 115203, Mar. 2006, doi: 10.1103/PhysRevB.73.115203.
- [43]L. Nuccio, S. Agnello, and R. Boscaino, 'Intrinsic generation of OH groups in dry silicon dioxide upon thermal treatments', *Appl. Phys. Lett.*, vol. 93, no. 15, p. 151906, Oct. 2008, doi: 10.1063/1.2998581.
- [44]P. Martín, M. León, A. Ibarra, and E. R. Hodgson, 'Thermal stability of gamma irradiation induced defects for different fused silica', *Journal of Nuclear Materials*, vol. 417, no. 1–3, pp. 818–821, Oct. 2011, doi: 10.1016/j.jnucmat.2010.12.171.
- [45]M. León *et al.*, 'Thermal stability of neutron irradiation effects on KU1 fused silica', *Journal of Nuclear Materials*, vol. 374, no. 3, pp. 386–389, Mar. 2008, doi: 10.1016/j.jnucmat.2007.09.030.
- [46]E. J. Friebele and M. E. Gingerich, 'Photobleaching effects in optical fiber waveguides', *Appl. Opt.*, AO, vol. 20, no. 19, Art. no. 19, Oct. 1981, doi: 10.1364/AO.20.003448.
- [47]H. Henschel and O. Kohn, 'Regeneration of irradiated optical fibres by photobleaching?', *IEEE Transactions on Nuclear Science*, vol. 47, no. 3, Art. no. 3, Jun. 2000, doi: 10.1109/23.856501.
- [48]G. H. Sigel, E. J. Friebele, M. J. Marrone, and M. E. Gingerich, 'An Analysis of Photobleaching Techniques for the Radiation Hardening of Fiber Optic Data Links', *IEEE*

References

- Transactions on Nuclear Science*, vol. 28, no. 6, pp. 4095–4101, Dec. 1981, doi: 10.1109/TNS.1981.4335681.
- [49] J. J. Koponen, M. J. Söderlund, H. J. Hoffman, and S. K. T. Tammela, 'Measuring photodarkening from single-mode ytterbium doped silica fibers', *Opt. Express, OE*, vol. 14, no. 24, pp. 11539–11544, Nov. 2006, doi: 10.1364/OE.14.011539.
- [50] G. L. Vecchi *et al.*, 'In-situ regeneration of P-doped optical fiber dosimeter', *Opt. Lett., OL*, vol. 45, no. 18, pp. 5201–5204, Sep. 2020, doi: 10.1364/OL.402382.
- [51] H. Henschel, O. Kohn, and H. U. Schmidt, 'Radiation hardening of optical fibre links by photobleaching with light of shorter wavelength', in *Proceedings of the Third European Conference on Radiation and its Effects on Components and Systems*, Sep. 1995, pp. 512–518. doi: 10.1109/RADECS.1995.509830.
- [52] B. Winkler, 'Oxygen-excess related defects in SiO₂-based materials : coupling theory and experiments.', Université de Lyon; niversité de Nova Gorica, 2019.
- [53] A. L. Tomashuk *et al.*, 'Enhanced Radiation Resistance of Silica Optical Fibers Fabricated in High O₂ Excess Conditions', *Journal of Lightwave Technology*, vol. 32, no. 2, pp. 213–219, Jan. 2014, doi: 10.1109/JLT.2013.2285157.
- [54] P. F. Kashaykin *et al.*, 'Radiation-Induced Attenuation in Silica Optical Fibers Fabricated in High O₂ Excess Conditions', *J. Lightwave Technol.*, vol. 33, no. 9, pp. 1788–1793, May 2015, doi: 10.1109/JLT.2015.2394806.
- [55] M. Lancry, E. Régnier, and B. Poumellec, 'Fictive temperature in silica-based glasses and its application to optical fiber manufacturing', *Progress in Materials Science*, vol. 57, no. 1, Art. no. 1, Jan. 2012, doi: 10.1016/j.pmatsci.2011.05.002.
- [56] S. Sakaguchi, S. Todoroki, and S. Shibata, 'Rayleigh Scattering in Silica Glasses', *Journal of the American Ceramic Society*, vol. 79, no. 11, Art. no. 11, 1996, doi: 10.1111/j.1151-2916.1996.tb08714.x.
- [57] E. J. Friebele, G. H. Sigel, and D. L. Griscom, 'Drawing-induced defect centers in a fused silica core fiber', *Appl. Phys. Lett.*, vol. 28, no. 9, Art. no. 9, May 1976, doi: 10.1063/1.88839.
- [58] D. L. Griscom, 'Trapped-electron centers in pure and doped glassy silica: A review and synthesis', *Journal of Non-Crystalline Solids*, vol. 357, no. 8, Art. no. 8, Apr. 2011, doi: 10.1016/j.jnoncrysol.2010.11.011.
- [59] D. L. Griscom, E. J. Friebele, and S. P. Mukherjee, 'Studies of radiation-induced point defects in silica aerogel monoliths', *Cryst. Latt. Def. Amorph. Mat.*, vol. 17, pp. 157–163, 1987.
- [60] I. I. Cheremisin *et al.*, 'Radiation-hard KS-4V glass and optical fiber, manufactured on its basis, for plasma diagnostics in ITER', *Plasma Devices and Operations*, vol. 12, no. 1, Art. no. 1, Mar. 2004, doi: 10.1080/10519990410001652593.
- [61] D. L. Griscom, 'Self-trapped holes in pure-silica glass: A history of their discovery and characterization and an example of their critical significance to industry', *Journal of Non-Crystalline Solids*, vol. 352, no. 23, Art. no. 23, Jul. 2006, doi: 10.1016/j.jnoncrysol.2006.03.033.
- [62] M. Yamaguchi, K. Saito, and A. J. Ikushima, 'Fictive-temperature-dependence of photoinduced self-trapped holes in a - SiO₂', *Phys. Rev. B*, vol. 68, no. 15, p. 153204, Oct. 2003, doi: 10.1103/PhysRevB.68.153204.
- [63] R. P. Wang, N. Tai, K. Saito, and A. J. Ikushima, 'Fluorine-doping concentration and fictive temperature dependence of self-trapped holes in SiO₂ glasses', *Journal of Applied Physics*, vol. 98, no. 2, p. 023701, Jul. 2005, doi: 10.1063/1.1980536.

- [64] J. E. Shelby, 'Radiation effects in hydrogen-impregnated vitreous silica', *Journal of Applied Physics*, vol. 50, no. 5, pp. 3702–3706, May 1979, doi: 10.1063/1.326275.
- [65] S. P. Faile, J. J. Schmidt, and D. M. Roy, 'Irradiation Effects in Glasses: Suppression by Synthesis under High-Pressure Hydrogen', *Science*, vol. 156, no. 3782, pp. 1593–1595, Jun. 1967, doi: 10.1126/science.156.3782.1593.
- [66] J. Stone, 'Interactions of hydrogen and deuterium with silica optical fibers: A review', *Journal of Lightwave Technology*, vol. 5, no. 5, Art. no. 5, May 1987, doi: 10.1109/JLT.1987.1075562.
- [67] B. Brichard *et al.*, 'Radiation assessment of hydrogen-loaded aluminium-coated pure silica core fibres for ITER plasma diagnostic applications', *Fusion Engineering and Design*, vol. 82, no. 15, Art. no. 15, Oct. 2007, doi: 10.1016/j.fusengdes.2007.04.045.
- [68] A. L. Tomashuk, K. M. Golant, and E. M. Dianov, 'Radiation-induced absorption and luminescence in specially hardened large-core silica optical fibers', *IEEE Transactions on Nuclear Science*, vol. 47, no. 3 PART 1, Art. no. 3 PART 1, 2000, doi: 10.1109/23.856500.
- [69] K. V. Zotov, M. E. Likhachev, A. L. Tomashuk, M. M. Bubnov, M. V. Yashkov, and A. N. Gur'yanov, 'Radiation-resistant erbium-doped silica fibre', *Quantum Electron.*, vol. 37, no. 10, pp. 946–949, Oct. 2007, doi: 10.1070/QE2007v037n10ABEH013660.
- [70] K. V. Zotov *et al.*, 'Radiation-Resistant Erbium-Doped Fiber for Spacecraft Applications', *IEEE Trans. Nucl. Sci.*, vol. 55, no. 4, pp. 2213–2215, Aug. 2008, doi: 10.1109/TNS.2008.2001834.
- [71] S. Girard *et al.*, 'Radiation-hard erbium optical fiber and fiber amplifier for both low- and high-dose space missions', *Opt. Lett.*, vol. 39, no. 9, p. 2541, May 2014, doi: 10.1364/OL.39.002541.
- [72] D. Di Francesca *et al.*, 'Influence of O₂-Loading Pretreatment on the Radiation Response of Pure and Fluorine-Doped Silica-Based Optical Fibers', *IEEE Transactions on Nuclear Science*, vol. 61, no. 6, pp. 3302–3308, Dec. 2014, doi: 10.1109/TNS.2014.2357994.
- [73] A. L. Tomashuk *et al.*, 'Role of Inherent Radiation-Induced Self-Trapped Holes in Pulsed-Radiation Effect on Pure-Silica-Core Optical Fibers', *Journal of Lightwave Technology*, vol. 37, no. 3, pp. 956–963, Feb. 2019, doi: 10.1109/JLT.2018.2884078.
- [74] M. C. Paul, D. Bohra, A. Dhar, R. Sen, P. K. Bhatnagar, and K. Dasgupta, 'Radiation response behavior of high phosphorous doped step-index multimode optical fibers under low dose gamma irradiation', *Journal of Non-Crystalline Solids*, vol. 355, no. 28–30, pp. 1496–1507, Aug. 2009, doi: 10.1016/j.jnoncrysol.2009.05.017.
- [75] S. Girard, Y. Ouerdane, C. Marcandella, A. Boukenter, S. Quenard, and N. Authier, 'Feasibility of radiation dosimetry with phosphorus-doped optical fibers in the ultraviolet and visible domain', *Journal of Non-Crystalline Solids*, vol. 357, no. 8, pp. 1871–1874, Apr. 2011, doi: 10.1016/j.jnoncrysol.2010.11.113.
- [76] A. Alessi *et al.*, 'Radiation effects on aluminosilicate optical fibers: spectral investigations from the ultraviolet to near-infrared domains', *physica status solidi (a)*, vol. 216, no. 3, Art. no. 3, 2019.
- [77] G. Beauvois, 'Etude, développement et caractérisation de fibres optiques à haute sensibilité aux radiations ionisantes pour une application de dosimétrie répartie', These de doctorat, Perpignan, 2017. Accessed: Dec. 02, 2021. [Online]. Available: <http://www.theses.fr/2017PERP0068>
- [78] B. Brichard *et al.*, 'Radiation-hardening techniques of dedicated optical fibres used in plasma diagnostic systems in ITER', in *Journal of Nuclear Materials*, Aug. 2004, vol. 329–333, no. 1-3 PART B, pp. 1456–1460. doi: 10.1016/j.jnucmat.2004.04.159.

References

- [79] A. Morana *et al.*, 'Influence of neutron and gamma-ray irradiations on rad-hard optical fiber', *Opt. Mater. Express, OME*, vol. 5, no. 4, pp. 898–911, Apr. 2015, doi: 10.1364/OME.5.000898.
- [80] T. Wijnands, K. Aikawa, J. Kuhnenn, D. Ricci, and U. Weinand, 'Radiation Tolerant Optical Fibers: From Sample Testing to Large Series Production', *J. Lightwave Technol., JLT*, vol. 29, no. 22, pp. 3393–3400, Nov. 2011.
- [81] T. Wijnands, L. K. De Jonge, J. Kuhnenn, S. K. Hoeffgen, and U. Weinand, 'Optical Absorption in Commercial Single Mode Optical Fibers in a High Energy Physics Radiation Field', *IEEE Transactions on Nuclear Science*, vol. 55, no. 4, Art. no. 4, Aug. 2008, doi: 10.1109/TNS.2008.2001859.
- [82] C. Campanella *et al.*, 'Photobleaching Effect on the Radiation-Induced Attenuation of an Ultralow Loss Optical Fiber at Telecommunication Wavelengths', *physica status solidi (a)*, vol. n/a, no. n/a, p. 2100518, doi: 10.1002/pssa.202100518.
- [83] V. De Michele *et al.*, 'Pulsed X-Ray Radiation Response of Ultralow Loss Pure-Silica-Core Optical Fibers', *Physica Status Solidi (a)*, vol. 219, no. 2, p. 2100519, Jan. 2022, doi: 10.1002/pssa.202100519.
- [84] C. Kittel, *Introduction to Solid State Physics*, 1st ed. John Wiley and Sons, 1953.
- [85] P. Wróbel *et al.*, 'Fabrication of corrugated Ge-doped silica fibers', *Opt. Express, OE*, vol. 20, no. 13, pp. 14508–14513, Jun. 2012, doi: 10.1364/OE.20.014508.
- [86] M. Ikeya, M. R. Zimmerman, and N. Whitehead, *New applications of electron spin resonance: dating, dosimetry and microscopy*. Singapore; River Edge, NJ: World Scientific, 1993.
- [87] G. Pacchioni, L. Skuja, and D. L. Griscom, *Defects in SiO₂ and Related Dielectrics: Science and Technology*, Springer, Dordrecht. 2000. [Online]. Available: <https://doi.org/10.1007/978-94-010-0944-7>
- [88] D. L. Griscom, 'Optical Properties and Structure of Defects in Silica Glass', 1991. doi: 10.2109/jcersj.99.923.
- [89] L. Skuja, M. Hirano, H. Hosono, and K. Kajihara, 'Defects in oxide glasses', *physica status solidi (c)*, vol. 2, no. 1, pp. 15–24, 2005, doi: 10.1002/pssc.200460102.
- [90] H. Hosono, Y. Abe, H. Imagawa, H. Imai, and K. Arai, 'Experimental evidence for the Si-Si bond model of the 7.6-eV band in SiO_2 glass', *Phys. Rev. B*, vol. 44, no. 21, pp. 12043–12045, Dec. 1991, doi: 10.1103/PhysRevB.44.12043.
- [91] V. A. Radtsig, 'Reactive intermediates on the surface of solids (SiO₂ and GeO₂): A review of studies and prospects for their development', *Chem. Phys. Reports*, pp. 1206–1245, 1995.
- [92] L. Skuja, 'Optically active oxygen-deficiency-related centers in amorphous silicon dioxide', *Journal of Non-Crystalline Solids*, vol. 239, no. 1, pp. 16–48, Oct. 1998, doi: 10.1016/S0022-3093(98)00720-0.
- [93] M. Stapelbroek, D. L. Griscom, E. J. Friebele, and G. H. Sigel, 'Oxygen-associated trapped-hole centers in high-purity fused silicas', *Journal of Non-Crystalline Solids*, vol. 32, no. 1, pp. 313–326, Feb. 1979, doi: 10.1016/0022-3093(79)90079-6.
- [94] E. J. Friebele, D. L. Griscom, M. Stapelbroek, and R. A. Weeks, 'Fundamental Defect Centers in Glass: The Peroxy Radical in Irradiated, High-Purity, Fused Silica', *Phys. Rev. Lett.*, vol. 42, no. 20, pp. 1346–1349, May 1979, doi: 10.1103/PhysRevLett.42.1346.
- [95] A. Morana *et al.*, 'Origin of the visible absorption in radiation-resistant optical fibers', *Opt. Mater. Express, OME*, vol. 3, no. 10, pp. 1769–1776, Oct. 2013, doi: 10.1364/OME.3.001769.

- [96] D. L. Griscom, 'Self-trapped holes in amorphous silicon dioxide', *Phys. Rev. B*, vol. 40, no. 6, pp. 4224–4227, Aug. 1989, doi: 10.1103/PhysRevB.40.4224.
- [97] D. L. Griscom, 'A Minireview of the Natures of Radiation-Induced Point Defects in Pure and Doped Silica Glasses and Their Visible/Near-IR Absorption Bands, with Emphasis on Self-Trapped Holes and How They Can Be Controlled', *Physics Research International*, vol. 2013, p. e379041, Feb. 2013, doi: 10.1155/2013/379041.
- [98] P. F. Kashaykin, A. L. Tomashuk, M. Yu. Salgansky, A. N. Guryanov, and E. M. Dianov, 'Anomalies and peculiarities of radiation-induced light absorption in pure silica optical fibers at different temperatures', *Journal of Applied Physics*, vol. 121, no. 21, p. 213104, Jun. 2017, doi: 10.1063/1.4984601.
- [99] V. D. Michele *et al.*, 'Pulsed X-Ray Radiation Responses of Solarization-Resistant Optical Fibers', *physica status solidi (a)*, vol. 216, no. 3, p. 1800487, 2019, doi: <https://doi.org/10.1002/pssa.201800487>.
- [100] Y. Sasajima and K. Tanimura, 'Optical transitions of self-trapped holes in amorphous SiO₂', *Phys. Rev. B*, vol. 68, no. 1, p. 014204, Jul. 2003, doi: 10.1103/PhysRevB.68.014204.
- [101] P. W. France, *Fluoride glass optical fibres*. Blackie, 1990. Accessed: Feb. 14, 2022. [Online]. Available: <http://books.google.com/books?id=dxpSAAAAMAAJ>
- [102] O. Humbach, H. Fabian, U. Grzesik, U. Haken, and W. Heitmann, 'Analysis of OH absorption bands in synthetic silica', *Journal of Non-Crystalline Solids*, vol. 203, pp. 19–26, Aug. 1996, doi: 10.1016/0022-3093(96)00329-8.
- [103] J. E. Midwinter, 'Optical fibre telecommunications', *Optics & Laser Technology*, vol. 12, no. 3, p. 160, Jun. 1980, doi: 10.1016/0030-3992(80)90074-2.
- [104] E. Modone and G. Roba, 'OH reduction in preforms by isotope exchange', *Electron. Lett.*, vol. 17, no. 21, p. 815, 1981, doi: 10.1049/el:19810569.
- [105] H. Murata, *Handbook of optical fibers and cables*. New York: Marcel Dekker, 1988.
- [106] J. Stone, 'Interactions of hydrogen and deuterium with silica optical fibers: A review', *J. Lightwave Technol.*, vol. 5, no. 5, pp. 712–733, 1987, doi: 10.1109/JLT.1987.1075562.
- [107] T. Li, *Optical Fiber Communications: Fiber Fabrication*. Saint Louis: Elsevier Science, 2014. Accessed: Feb. 14, 2022. [Online]. Available: <http://qut.eblib.com.au/patron/FullRecord.aspx?p=1154985>
- [108] V. B. Neustruev, 'Colour centres in germanosilicate glass and optical fibres', *J. Phys.: Condens. Matter*, vol. 6, no. 35, pp. 6901–6936, Aug. 1994, doi: 10.1088/0953-8984/6/35/003.
- [109] G. Origlio, 'Properties and radiation response of optical fibers : role of dopants', These de doctorat, Saint-Etienne, 2009. Accessed: Dec. 03, 2021. [Online]. Available: <http://www.theses.fr/2009STET4021>
- [110] D. D. Francesca *et al.*, 'X-ray irradiation effects on fluorine-doped germanosilicate optical fibers', *Opt. Mater. Express, OME*, vol. 4, no. 8, pp. 1683–1695, Aug. 2014, doi: 10.1364/OME.4.001683.
- [111] A. Alessi, S. Girard, M. Cannas, S. Agnello, A. Boukenter, and Y. Ouerdane, 'Evolution of Photo-induced defects in Ge-doped fiber/preform: influence of the drawing', *Opt. Express, OE*, vol. 19, no. 12, pp. 11680–11690, Jun. 2011, doi: 10.1364/OE.19.011680.
- [112] D. Di Francesca *et al.*, 'O₂-Loading Treatment of Ge-Doped Silica Fibers: A Radiation Hardening Process', *Journal of Lightwave Technology*, vol. 34, no. 9, pp. 2311–2316, May 2016, doi: 10.1109/JLT.2016.2533670.

References

- [113] D. L. Griscom, 'On the natures of radiation-induced point defects in GeO₂-SiO₂ glasses: reevaluation of a 26-year-old ESR and optical data set', *Opt. Mater. Express, OME*, vol. 1, no. 3, pp. 400–412, Jul. 2011, doi: 10.1364/OME.1.000400.
- [114] A. Alessi, S. Agnello, and F. M. Gelardi, 'Properties and generation by irradiation of germanium point defects in ge-doped silica', 2012, pp. 75–150.
- [115] L. Giacomazzi, L. Martin-Samos, A. Boukenter, Y. Ouerdane, S. Girard, and N. Richard, 'Ge(2), Ge(1) and Ge-E' centers in irradiated Ge-doped silica: a first-principles EPR study', *Opt. Mater. Express*, vol. 5, no. 5, p. 1054, May 2015, doi: 10.1364/OME.5.001054.
- [116] E. J. Friebele and D. L. Griscom, *Mater. Res. Symp. Proc.*, p. 319, 1986.
- [117] E. V. Anokin, V. M. Mashinsky, V. B. Neustruev, and Y. S. Sidorin, 'Effects of exposure to photons of various energies on transmission of germanosilicate optical fiber in the visible to near IR spectral range', *Journal of Non-Crystalline Solids*, pp. 243–253, 1994.
- [118] A. Alessi *et al.*, 'Effect of irradiation temperature on the radiation induced attenuation of Ge-doped fibers', in *2016 16th European Conference on Radiation and Its Effects on Components and Systems (RADECS)*, Sep. 2016, pp. 1–5. doi: 10.1109/RADECS.2016.8093134.
- [119] P. V. Chernov *et al.*, 'Spectroscopic manifestations of self-trapped holes in silica', *Physica Status Solidi B*, vol. 156, no. 2, pp. 663–675, Dec. 1989.
- [120] S. Girard *et al.*, 'Transient Radiation Responses of Optical Fibers: Influence of MCVD Process Parameters', *IEEE Trans. Nucl. Sci.*, vol. 59, no. 6, pp. 2894–2901, Dec. 2012, doi: 10.1109/TNS.2012.2222440.
- [121] S. Girard, J. Baggio, and J. Bisutti, '14-MeV Neutron, γ -Ray, and Pulsed X-Ray Radiation-Induced Effects on Multimode Silica-Based Optical Fibers', *IEEE Transactions on Nuclear Science*, vol. 53, no. 6, Art. no. 6, Dec. 2006, doi: 10.1109/TNS.2006.886222.
- [122] V. De Michele *et al.*, 'Origins of radiation-induced attenuation in pure-silica-core and Ge-doped optical fibers under pulsed x-ray irradiation', *Journal of Applied Physics*, vol. 128, no. 10, p. 103101, Sep. 2020, doi: 10.1063/5.0014165.
- [123] D. Ehrt, P. Ebeling, and U. Natura, 'UV Transmission and radiation-induced defects in phosphate and fluoride-phosphate glasses', *Journal of Non-Crystalline Solids*, vol. 263–264, pp. 240–250, Mar. 2000, doi: 10.1016/S0022-3093(99)00681-X.
- [124] G. M. Ermolaeva, 'Low-dispersion optical fiber highly transparent in the UV spectral range', *Opt. Eng.*, vol. 43, no. 12, p. 2896, Dec. 2004, doi: 10.1117/1.1814766.
- [125] I. Toccafondo *et al.*, 'Distributed Optical Fiber Radiation Sensing in a Mixed-Field Radiation Environment at CERN', *J. Lightwave Technol., JLT*, vol. 35, no. 16, Art. no. 16, Aug. 2017.
- [126] A. L. Tomashuk, M. V. Grekov, S. A. Vasiliev, and V. V. Svetukhin, 'Fiber-optic dosimeter based on radiation-induced attenuation in P-doped fiber: suppression of post-irradiation fading by using two working wavelengths in visible range', *Opt. Express, OE*, vol. 22, no. 14, Art. no. 14, Jul. 2014, doi: 10.1364/OE.22.016778.
- [127] V. De Michele *et al.*, 'Steady-State X-Ray Radiation-Induced Attenuation in Canonical Optical Fibers', *IEEE Transactions on Nuclear Science*, vol. 67, no. 7, pp. 1650–1657, Jul. 2020, doi: 10.1109/TNS.2020.2969717.
- [128] D. Di Francesca *et al.*, 'Combined Temperature Radiation Effects and Influence of Drawing Conditions on Phosphorous-Doped Optical Fibers', *physica status solidi (a)*, p. 1800553, Dec. 2018, doi: 10.1002/pssa.201800553.

- [129] G. Li Vecchi *et al.*, 'Infrared radiation Induced attenuation of radiation sensitive optical fibers: influence of temperature and modal propagation', *Optical Fiber Technology*, vol. 55, p. 102166, Mar. 2020, doi: 10.1016/j.yofte.2020.102166.
- [130] C. Campanella *et al.*, 'Combined Temperature and Radiation Effects on Radiation-Sensitive Single-Mode Optical Fibers', *IEEE Transactions on Nuclear Science*, vol. 67, no. 7, pp. 1643–1649, Jul. 2020, doi: 10.1109/TNS.2020.2982280.
- [131] A. V. Faustov *et al.*, 'Comparison of Gamma-Radiation Induced Attenuation in Al-Doped, P-Doped and Ge-Doped Fibres for Dosimetry', *IEEE Transactions on Nuclear Science*, vol. 60, no. 4, pp. 2511–2517, Aug. 2013, doi: 10.1109/TNS.2013.2273273.
- [132] M. León *et al.*, 'Ge- and Al-related point defects generated by gamma irradiation in nanostructured erbium-doped optical fiber preforms', *Journal of Materials Science*, vol. 51, pp. 10245–10261, Aug. 2016, doi: 10.1007/s10853-016-0253-5.
- [133] S. Girard *et al.*, 'Proton- and Gamma-Induced Effects on Erbium-Doped Optical Fibers', *IEEE Transactions on Nuclear Science*, vol. 54, no. 6, pp. 2426–2434, Dec. 2007, doi: 10.1109/TNS.2007.910859.
- [134] H. Hideo and K. Hiroshi, 'Radiation-induced coloring and paramagnetic centers in synthetic SiO₂:Al glasses', *Nuclear Instruments and Methods in Physics Research Section B: Beam Interactions with Materials and Atoms*, vol. 91, no. 1, pp. 395–399, Jun. 1994, doi: 10.1016/0168-583X(94)96255-3.
- [135] A. N. Trukhin, J. Teteris, A. Fedotov, D. L. Griscom, and G. Buscarino, 'Photosensitivity of SiO₂-Al and SiO₂-Na glasses under ArF (193nm) laser', *Journal of Non-Crystalline Solids*, vol. 355, no. 18, pp. 1066–1074, Jul. 2009, doi: 10.1016/j.jnoncrysol.2008.11.037.
- [136] A. S. Zyubin, A. M. Mebel, and S. H. Lin, 'Quantum chemical modeling of photoabsorption and photoluminescence of the [AlO₄]⁰ defect in bulk SiO₂', *J. Chem. Phys.*, vol. 119, no. 21, pp. 11408–11414, Dec. 2003, doi: 10.1063/1.1622660.
- [137] 'Home - Photonics by ixblue | Photonics'. <https://photonics.ixblue.com/> (accessed Sep. 30, 2021).
- [138] 'Corning | Materials Science Technology and Innovation'. <https://www.corning.com/worldwide/en.html> (accessed Jan. 13, 2022).
- [139] 'Samsung France | Téléphones Portables | Electroménager | TV', *Samsung fr.* <https://www.samsung.com/fr/> (accessed Jan. 13, 2022).
- [140] D. D. Francesca *et al.*, 'Qualification and Calibration of Single-Mode Phosphosilicate Optical Fiber for Dosimetry at CERN', *J. Lightwave Technol., JLT*, vol. 37, no. 18, Art. no. 18, Sep. 2019.
- [141] 'Corning SMF-28e datasheet'. [Online]. Available: www.corning.com
- [142] D. b. Keck, R. d. Maurer, and P. c. Schultz, 'On the ultimate lower limit of attenuation in glass optical waveguides', *Appl. Phys. Lett.*, vol. 22, no. 7, Art. no. 7, Apr. 1973, doi: 10.1063/1.1654649.
- [143] D. B. Keck and A. R. Tynes, 'Spectral Response of Low-Loss Optical Waveguides', *Appl. Opt., AO*, vol. 11, no. 7, Art. no. 7, Jul. 1972, doi: 10.1364/AO.11.001502.
- [144] P. Kaiser *et al.*, 'Spectral losses of unclad vitreous silica and soda-lime-silicate fibers', *J. Opt. Soc. Am., JOSA*, vol. 63, no. 9, Art. no. 9, Sep. 1973, doi: 10.1364/JOSA.63.001141.
- [145] C. R. Elliott and G. R. Newns, 'Near Infrared Absorption Spectra of Silica: OH Overtones', *Appl. Spectrosc., AS*, vol. 25, no. 3, Art. no. 3, May 1971.

References

- [146] S. Girard *et al.*, 'Growth and Decay Kinetics of Radiation-Induced Attenuation in Bulk Optical Materials', *IEEE Transactions on Nuclear Science*, vol. 65, no. 8, Art. no. 8, Aug. 2018, doi: 10.1109/TNS.2017.2778318.
- [147] R. Bujila, A. Omar, and G. Poludniowski, 'A validation of SpekPy: A software toolkit for modelling X-ray tube spectra', *Physica Medica*, vol. 75, pp. 44–54, Jul. 2020, doi: 10.1016/j.ejmp.2020.04.026.
- [148] G. Poludniowski, A. Omar, R. Bujila, and P. Andreo, 'Technical Note: SpekPy v2.0—a software toolkit for modeling x-ray tube spectra', *Medical Physics*, vol. 48, no. 7, pp. 3630–3637, Jul. 2021, doi: 10.1002/mp.14945.
- [149] S. M. Seltzer, 'Calculation of Photon Mass Energy-Transfer and Mass Energy-Absorption Coefficients', *Radiation Research*, vol. 136, no. 2, p. 147, Nov. 1993, doi: 10.2307/3578607.
- [150] J. H. Hubbel, 'Tables of X-Ray Mass Attenuation Coefficients and Mass Energy-Absorption Coefficients from 1 keV to 20 MeV for Elements Z = 1 to 92 and 48 Additional Substances of Dosimetric Interest'. 1996.
- [151] K. Mochizuki, Y. Namihira, M. Kuwazura, and Y. Iwamoto, 'Behavior of hydrogen molecules adsorbed on silica in optical fibers', *IEEE Journal of Quantum Electronics*, vol. 20, no. 7, pp. 694–697, Jul. 1984, doi: 10.1109/JQE.1984.1072462.
- [152] M. K. Barnoski and S. M. Jensen, 'Fiber waveguides: a novel technique for investigating attenuation characteristics', *Appl. Opt., AO*, vol. 15, no. 9, pp. 2112–2115, Sep. 1976, doi: 10.1364/AO.15.002112.
- [153] S. D. Personick, 'Photon probe — an optical-fiber time-domain reflectometer', *The Bell System Technical Journal*, vol. 56, no. 3, pp. 355–366, Mar. 1977, doi: 10.1002/j.1538-7305.1977.tb00513.x.
- [154] A. H. Hartog, *An Introduction to Distributed Optical Fibre Sensors*, 1st ed. 2018.
- [155] D. Marcuse, *Principles of Optical Fiber Measurements*. 1981.
- [156] C. Campanella *et al.*, 'Photobleaching Effect on Infrared Radiation-Induced Attenuation of Germanosilicate Optical Fibers at MGy Dose Levels', *IEEE Transactions on Nuclear Science*, vol. 68, no. 8, pp. 1688–1693, Aug. 2021, doi: 10.1109/TNS.2021.3068829.
- [157] J. Kuhnhenh, S. K. Hoffgen, and U. Weinand, 'Quality Assurance for Irradiation Tests of Optical Fibers: Uncertainty and Reproducibility', *IEEE Transactions on Nuclear Science*, vol. 56, no. 4, Art. no. 4, Aug. 2009, doi: 10.1109/TNS.2009.2019605.
- [158] V. De Michele, 'Transient optical phenomena related to point defects in pure and doped silica', Jean-Monnet University (Saint-Etienne) and Palermo University, 2021.
- [159] D. L. Griscom, 'Fractal kinetics of radiation-induced point-defect formation and decay in amorphous insulators: Application to color centers in silica-based optical fibers', *Phys. Rev. B*, vol. 64, no. 17, Art. no. 17, Oct. 2001, doi: 10.1103/PhysRevB.64.174201.
- [160] D. L. Griscom, M. E. Gingerich, and E. J. Friebele, 'Model for the dose, dose-rate and temperature dependence of radiation-induced loss in optical fibers', *IEEE Transactions on Nuclear Science*, vol. 41, no. 3, pp. 523–527, Jun. 1994, doi: 10.1109/23.299793.
- [161] A. Tomashuk, 'Inherent and Strain-Assisted Radiation-Induced Self-Trapped Holes in Pure-Silica Optical Fibers', in *Advanced Photonics 2018 (BGPP, IPR, NP, NOMA, Sensors, Networks, SPPCom, SOF) (2018)*, paper BM2A.6, Jul. 2018, p. BM2A.6. doi: 10.1364/BGPPM.2018.BM2A.6.
- [162] L. Skuja, K. Kajihara, K. Smits, A. Silins, and H. Hosono, 'Luminescence and Raman Detection of Molecular Cl₂ and ClClO Molecules in Amorphous SiO₂ Matrix', *J. Phys. Chem. C*, vol. 121, no. 9, pp. 5261–5266, Mar. 2017, doi: 10.1021/acs.jpcc.6b13095.

- [163] L. Vaccaro, M. Cannas, B. Boizot, and A. Parlato, 'Radiation induced generation of non-bridging oxygen hole center in silica: Intrinsic and extrinsic processes', *Journal of Non-Crystalline Solids*, vol. 353, no. 5, pp. 586–589, Apr. 2007, doi: 10.1016/j.jnoncrysol.2006.10.028.